DOCTORAL THESIS

Symmetry Breaking Revealed by THz Spectroscopy of Magnetic Excitations

Kirill Amelin

Symmetry Breaking Revealed by THz Spectroscopy of Magnetic Excitations

KIRILL AMELIN

TAL
TECH
PRESS

TALLINN UNIVERSITY OF TECHNOLOGY
School of Science
Department of Cybernetics

The dissertation was accepted for the defence of the degree of Doctor of Philosophy (Applied Physics) on 22 June 2022

Supervisor: PhD Toomas Rõõm,
                     National Institute of Chemical Physics and Biophysics,
                     Tallinn, Estonia

Co-supervisor: PhD Urmas Nagel,
                     National Institute of Chemical Physics and Biophysics,
                     Tallinn, Estonia

Opponents: Professor Raivo Jaaniso,
                     University of Tartu,
                     Tartu, Estonia

                     Professor Stanislav Kamba,
                     Academy of Sciences of the Czech Republic,
                     Prague, Czech Republic

Defence of the thesis: 30 August 2022, Tallinn

Declaration:
Hereby I declare that this doctoral thesis, my original investigation and achievement, submitted for the doctoral degree at Tallinn University of Technology, has not been submitted for any academic degree elsewhere. The experimental work for this thesis was carried out in the laboratory of Chemical Physics of the National Institute of Chemical Physics and Biophysics (KBFI).

Kirill Amelin

_____
signature

European Union
European Regional
Development Fund

Investing
in your future

Sümmeetriarikkumiste avaldumine magnetergastuste teraherts-spektrites

KIRILL AMELIN

TAL
TECH
KIRJASTUS

Contents

List of publications

The present Ph.D. thesis is based on the following publications that are referred to in the text by Roman numbers.

I K. Amelin, U. Nagel, R. S. Fishman, Y. Yoshida, Hasung Sim, Kisoo Park, Je-Geun Park, and T. Rõõm, "Terahertz absorption spectroscopy study of spin waves in orthoferrite $YFeO_3$ in a magnetic field," *Phys. Rev. B*, vol. 98, p. 174417, Nov 2018.

II Z. Zhang, K. Amelin, X. Wang, H. Zou, J. Yang, U. Nagel, T. Rõõm, T. Dey, A. A. Nugroho, T. Lorenz, J. Wu, and Z. Wang, "Observation of E_8 particles in an Ising chain antiferromagnet," *Phys. Rev. B*, vol. 101, p. 220411, Jun 2020.

III K. Amelin, J. Engelmayer, J. Viirok, U. Nagel, T. Rõõm, and Z. Wang, "Experimental observation of quantum many-body excitations of E_8 symmetry in the Ising chain ferromagnet $CoNb_2O_6$," *Phys. Rev. B*, vol. 102, p. 104431, Sep 2020.

IV K. Amelin, Y. Alexanian, U. Nagel, T. Rõõm, J. Robert, J. Debray, V. Simonet, C. Decorse, Z. Wang, R. Ballou, E. Constable, and S. de Brion "Terahertz magneto-optical investigation of quadrupolar spin-lattice effects in magnetically frustrated $Tb_2Ti_2O_7$," *Phys. Rev. B*, vol. 102, p. 13442, Oct 2020.

Author's contributions to the publications

I In I, I performed the THz measurements and the Laue measurements to confirm the sample orientation. I was the main author, wrote the manuscript, and prepared the figures.

II In II, I performed the THz spectroscopy measurements and analyzed the spectra.

III In III, I performed the THz measurements, analyzed the spectra, and wrote a part of the manuscript.

IV In IV, I performed several THz measurements with various samples, which included filing down samples to make them wedge-shaped, analyzed the spectra, prepared some of the figures, and wrote a part of the manuscript.

Approbation

I presented the results of the thesis at the following conferences:

1. **K. Amelin**, T. Rõõm, U. Nagel, R. Fishman, Je-Guen Park, Hasung Sim, Kisoo Park, and Y. Yoshida. 'THz Absorption Spectroscopy Study of Spin Waves in Orthoferrite $YFeO_3$', APS March Meeting: 5 – 9 March 2018, Los Angeles, CA, USA

2. **K. Amelin**, U. Nagel, R. Fishman, Y. Yoshida, Hasung Sim, Kisoo Park, and Je-Guen Park. 'Spin Structure Models of $YFeO_3$ from THz Spectroscopy Study', APS March Meeting: 3 – 8 March 2019, Boston, MA, USA

3. **K. Amelin**, U. Nagel, R. Fishman, Y. Yoshida, Hasung Sim, Kisoo Park, and Je-Guen Park. 'THz Absorption Spectroscopy Study of Spin Waves in Orthoferrite $YFeO_3$', 4th Grandmaster Early-Career Workshop in Physics: 1 – 8 September 2019, Split, Croatia

4. **K. Amelin**, Y. Alexanian, U. Nagel, T. Rõõm, J. Robert, J. Debray, V. Simonet, C. Decorse, Z. Wang, R. Ballou, E. Constable, and S. de Brion 2. 'THz spectroscopy study of the rare-earth pyrochlore $Tb_2Ti_2O_7$', Graduate School of Functional Materials And Technologies Scientific Conference 2020: 4 – 5 February 2020, Tallinn, Estonia

5. **K. Amelin**, T. Rõõm, U. Nagel, J. Viirok, J. Engelmayer, Z. Zhang, X. Wang, H. Zou, J. Yang, T. Dey, A. A. Nugroho, T. Lorenz, J. Wu, and Z. Wang. 'Experimental observation of E_8 particles in Ising-chain compounds' (Poster), International Conference on Low Energy Electrodynamics in Solids (LEES): 28 June – 8 July 2021, Online

Abbreviations

KBFI	National Institute of Chemical Physics and Biophysics (Keemilise ja Bioloogilise Füüsika Instituut)
INS	Inelastic Neutron Scattering
RIXS	Resonant Inelastic X-ray Scattering
THz	Terahertz
LRO	Long Range Order
SW	Spin Wave
DM	Dzyaloshinskii–Moriya
QCP	Quantum Critical Point
CF	Crystal Field
SIA	Single-Ion Anisotropy
1D	One-Dimensional
3D	Three-Dimensional

Symbols

ε_0	Vacuum permittivity
μ_0	Vacuum permeability
$\hbar$	Reduced Planck constant, $\hbar = (2\pi)^{-1}h$
c_0	Speed of light in vacuum, $c_0 = (\varepsilon_0\mu_0)^{-1/2}$
f	Frequency
ω	Angular frequency, $\omega = 2\pi f$
E	Energy, $E = \hbar\omega$
λ	Wavelength of electromagnetic radiation
$\tilde{\nu}$	Wavenumber, $\tilde{\nu} = f/c_0 = \lambda^{-1}$
$\mathbf{k}$	Wavevector, $|k| = 2\pi/\lambda$
k_B	Boltzmann constant
T	Temperature
T_C	Curie temperature
T_N	Néel temperature
μ_B	Bohr magneton
∇	Del, or nabla operator
δ_{ij}	Kronecker delta
ϵ_{ijk}	Levi-Civita symbol
$[\,,]$	Commutator
$\langle\,\rangle$	Ensemble average

Units

$[f] = \mathsf{THz}$
$[\tilde{\nu}] = \mathsf{cm}^{-1}$
$[E] = \mathsf{meV}$

$1\,\mathsf{THz} = 10^{12}\,\mathsf{Hz} = 33\,\mathsf{cm}^{-1} = 4.1\,\mathsf{meV}$
$1\,\mathsf{cm}^{-1} = 0.03\,\mathsf{THz} = 0.12\,\mathsf{meV}$
$1\,\mathsf{meV} = 0.24\,\mathsf{THz} = 8\,\mathsf{cm}^{-1}$

Introduction

In the 1960s, the scientific community adopted the term "condensed matter" to identify strongly correlated systems, in which physical properties are dictated by collective behavior of interacting atoms [1, 2]. Since then, condensed matter physics has been developing at a rapid pace, having become by far the largest subfield of physics by the end of the twentieth century [3]. A lot of the research is focused specifically on magnetic materials, where the interactions between atoms depend on their magnetic moments. These interactions are commonly studied using spectroscopic techniques such as inelastic neutron scattering (INS) and resonant inelastic X-ray scattering (RIXS), which are great tools for probing magnetic excitations. In these studies, much of attention is directed towards symmetry and, especially, the spontaneous symmetry breaking that accompanies phase transitions in condensed matter [4]. While INS and RIXS provide excellent data on magnetic excitations, including dispersion in momentum space, they lack the sensitivity to separate excitations whose energies are very similar [5]. Additionally, low-energy excitations below 1 meV are inaccessible for RIXS and are rather hard to detect by INS. These limitations make it challenging to study weak interactions that may cause additional symmetry breaking and induce the emergence of novel properties. Here at the National Institute of Chemical Physics and Biophysics (KBFI), we use THz spectroscopy combined with low temperatures and high magnetic fields to fill this gap by studying magnetic excitations in the energy range of 0.4 – 25 meV (3 – 200 cm^{-1}). With the highest spectral resolution of 0.015 meV (0.12 cm^{-1}), our instruments exceed the energy resolution of INS by about an order of magnitude [5]. By combining a Fourier-transform interferometer with a superconducting magnet, we can study magnetic-field dependence of the THz spectrum in a steady-state magnetic field up to 17 T, which is comparable to the strongest steady-state field available for the neutron experiments [6].

In this study, we utilize the precision of THz spectroscopy and its ability to access the low-energy spectrum of single-crystal samples to answer three separate questions: 1) Does the spin-lattice coupling induce symmetry breaking in a frustrated pyrochlore $Tb_2Ti_2O_7$? 2) Can we improve our understanding of magnetic ordering in a rare-earth orthoferrite $YFeO_3$? 3) Can we provide further evidence of the hidden E_8 symmetry near a quantum critical point (QCP) in a quasi-one-dimensional Ising spin chain?

The first question is tightly intertwined with the problem of geometric frustration of spins on a pyrochlore lattice [7], which leads to exotic spin states, such as spin ice and spin liquid. $Tb_2Ti_2O_7$ is an especially puzzling compound, where dynamic interplay between the spins and the lattice is suspected to impede the formation of any kind of long-range order (LRO). If such coupling exists, it would result in very subtle and hard-to-detect features in the excitation spectrum. While earlier studies reported potential observations of the dynamic spin-lattice effects [8, 9, 10], we aim to present unequivocal evidence by studying the magnetic-field dependence of the spectrum, where these features should stand out more clearly.

The second questions is related to the spontaneous symmetry breaking that is responsible for multiferroic properties in certain materials [11]. These properties normally stem from the "weak" Dzyaloshinskii–Moriya (DM) interactions that are rather hard to quantify. Our goal is to study low-energy excitations to provide the most accurate description of the magnetic interactions in $YFeO_3$, which is isostructural to some known multiferroics. A precise description of these interactions opens up possibilities to better model multiferroic compounds, boosting research towards potential future applications.

The final question concerns emergent symmetries close to the quantum critical point of an Ising spin chain. Namely, under certain conditions, the Ising chain is predicted to

feature excitations with the energy ratios from the E_8 affine Toda field theory [12]. Here we focus on two quasi-one-dimensional materials that incorporate Co^{2+} spin chains: a ferromagnetic $CoNb_2O_6$ and an antiferromagnetic $BaCo_2V_2O_8$. Although the E_8 spectrum has been found in $CoNb_2O_6$ by INS, the experiment was only partially successful, as most of the excitation peaks remained obscured in the spectrum [13]. No such attempt has ever been reported for $BaCo_2V_2O_8$. Observation of the full E_8 spectrum, if successful, would not only mark the first ever experimental evidence of highly complex E_8 symmetry, but would also demonstrate the power of integrable field theory to describe the complex symmetry that emerges near the QCP.

The results of this work were published in the American Physics Society's journal *Physics Review B*, as well as presented at various conferences.

1 Experimental setup

All measurements discussed in this work were performed at KBFI in Tallinn, Estonia. The transmission of THz radiation through single-crystal samples was measured using a Martin-Puplett interferometer SPS-200, combined with either a liquid-helium-bath cryostat, or a dilution refrigerator. In this chapter, we introduce both setups and describe the principles of Fourier-transform spectroscopy, specifically with a Martin-Puplett interferometer.

1.1 TeslaFIR

TeslaFIR is a spectrometer that consists of a liquid-helium-bath cryostat and a Martin-Puplett interferometer SPS-200, and is schematically shown in Fig. 1. In TeslaFIR, the sample is placed in a vacuum chamber that is inserted into the bore of a 17-tesla super-conducting magnet. The THz light beam travels from the Martin-Puplett interferometer via light pipes through the sample and onto the detector (bolometer). The polarization of the beam is controlled by a wire-grid polarizer directly in front of the sample, which is rotated by an external motor. To reduce the heat load onto the bolometer, a filter wheel
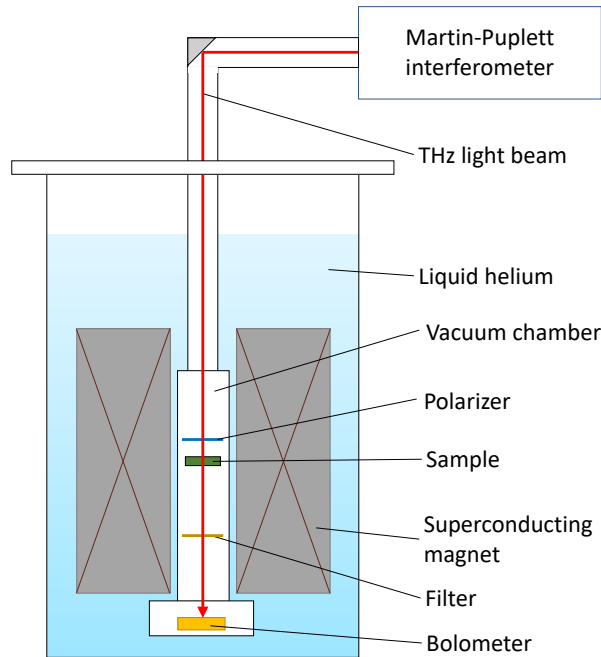
Figure 1: A schematic drawing of TeslaFIR. The temperature of the main bath is reduced by pumping liquid helium through a λ-helix (not shown on the drawing), immersed into the liquid helium above the superconducting magnet.

equipped with a set of low-pass filters with various cutoff frequencies is installed after the sample. The filter wheel is rotated by another external motor, which makes it easy to change the cutoff frequency during the experiment. The bolometer, separated from the liquid helium by a vacuum chamber, operates at the base temperature of 300 mK, which is reached using a separate ^{3}He cooling stage. In this stage, the boiling temperature of liquid ^{3}He is lowered by reducing its pressure with a charcoal sorption pump, kept

at approximately 5 K. The sample temperature can be further reduced to around 2.5 K by pumping on the liquid helium in the main bath of the cryostat through a λ-helix. This also cools the magnet below the liquid helium superfluid transition temperature $T_\lambda = 2.17$ K, which is needed for the operation above 15 T.

In TeslaFIR, we can measure transmission in both Faraday and Voigt configurations, where the applied magnetic field is either parallel or perpendicular to the direction of THz light wavevector **k**. A comparison between Faraday and Voigt configurations is illustrated in Fig. 2. In Voigt configuration, we use two mirrors to change the direction of the incident light beam. An external motor then rotates the sample, which makes it possible to apply the magnetic field in any direction in the plane perpendicular to the **k** vector. Only two incident light polarizations can be used in Voigt configuration, as the reflection off the mirror surface would otherwise ruin the linear polarization.
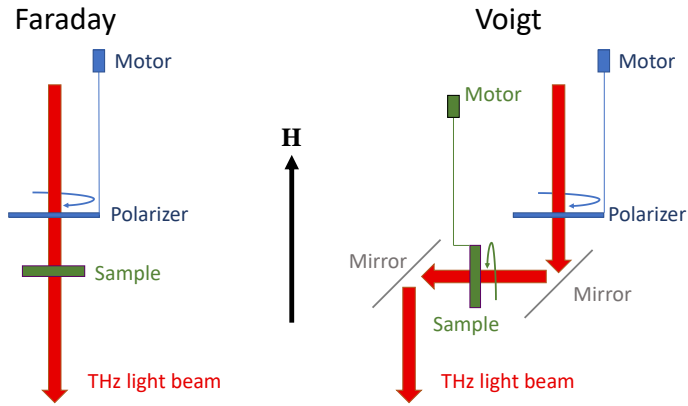
*Figure 2: A comparison between Faraday (left) and Voigt (right) configurations. An external motor rotates the sample in the Voigt configuration, so that the magnetic field **H** can be applied in any direction in the sample plane, perpendicularly to the rotation axis.*

1.2 milliK-TeslaFIR

A schematic diagram of the spectrometer milliK-TeslaFIR, which consists of a dilution refrigerator and a Martin-Puplett interferometer SPS-200, is shown in Fig. 3. In milliK-TeslaFIR, the sample is located at the end of the cold finger, which is inserted into the bore of a 12-tesla superconducting magnet. The cold finger is in contact with the mixing chamber of the ^{3}He/^{4}He cooling circuit, which is located in the inner vacuum chamber, submerged in liquid helium. Below 0.87 K, the ^{3}He/^{4}He mixture in the mixing chamber separates into two phases: a ^{3}He-rich phase at the top, which is almost pure ^{3}He, and a dilute phase with ^{3}He concentration of 6.6% at the bottom [14]. A diffusion pump continuously pumps ^{3}He out of the dilute phase via still, which causes some of ^{3}He to move from the concentrated phase into the dilute phase. The process of ^{3}He crossing the boundary between two phases is endothermic, which means heat is removed from the mixing chamber, thus cooling the cryostat even further. ^{3}He gas that passes through the diffusion pump is subsequently returned into the circuit via heat exchangers, which cool it before it enters the mixing chamber again. Due to the heating effect of the THz beam itself, the lowest possible sample temperature is, to an extent, dependent on the cutoff frequency of a low-pass filter used in the measurement. With the cutoff of 20 cm^{-1}, we can reach a stable sample temperature as low as 150 mK. A separate cooling stage, where the temper-
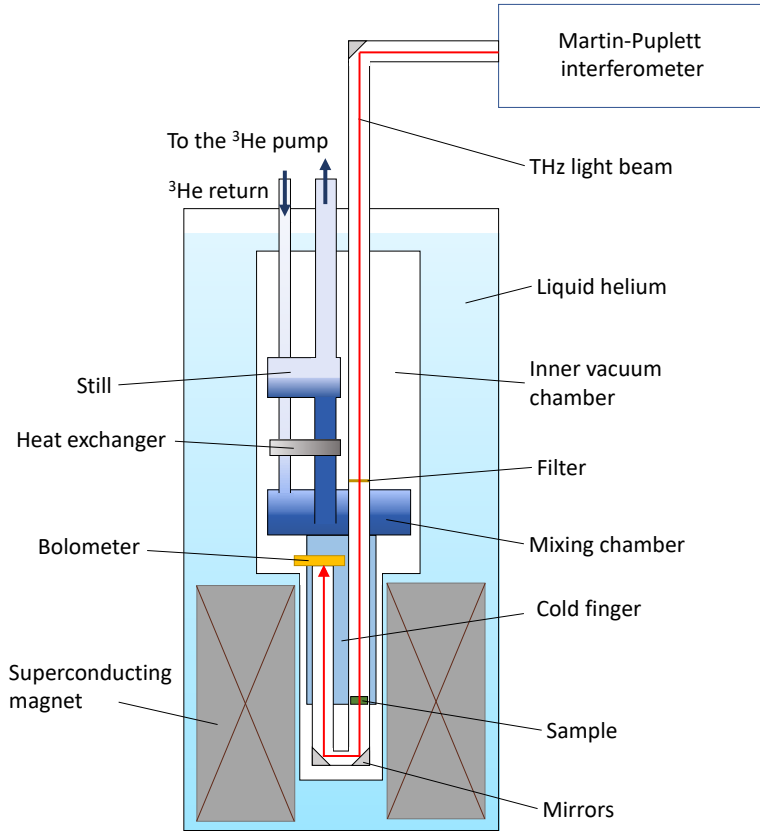
Figure 3: A schematic drawing of milliK-TeslaFIR. The dark blue color in the mixing chamber and still represents the dilute phase of the ^{3}He/^{4}He mixture, the light blue color in the mixing chamber represents the ^{3}He-rich phase. The top part of still and the pumping lines only contain ^{3}He gas.

ature of liquid ^{3}He is reduced by pumping on it with a charcoal absorber at 4.2 K, keeps the bolometer at 400 mK. No polarizer is used in the current setup.

1.3 Martin-Puplett interferometer

The Martin-Puplett interferometer used in all of our measurements is equipped with a mercury lamp, which is the source of THz radiation, a wire-grid polarizer that acts as a beamsplitter, two rooftop mirrors, one stationary and one moving, and two linear polarizers. A photo of the interferometer is shown in Fig. 4. Here, we are going to use Jones vectors and Jones matrices [15] to describe the components and the work principle of the interferometer.

According to Jones calculus, a polarization state of a light beam can be described by a two-component vector

$$\mathbf{E} = \begin{pmatrix} E_V \\ E_H \end{pmatrix}, \tag{1}$$

where and $E_V = E_1 e^{i\phi_1}$ and $E_H = E_2 e^{i\phi_2}$ are the vertical and horizontal electric field components perpendicular to the direction of beam propagation. Linear polarizers that pro-
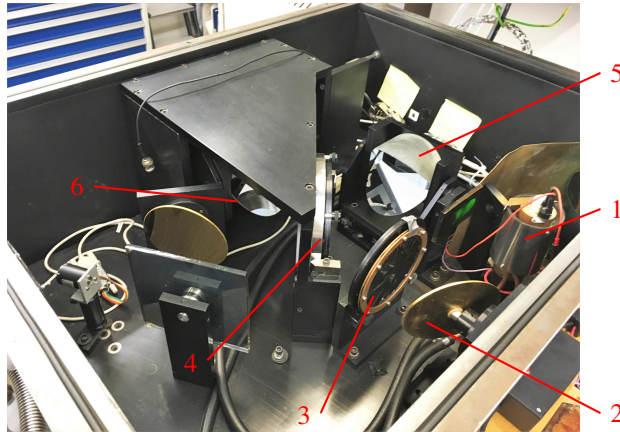
Figure 4: A photo of the Martin-Puplett interferometer used in all of the measurements. The following components are visible in the photo: 1. mercury lamp, 2. off-axis parabolic mirror, 3. linear polarizer, 4. beamsplitter, 5. moving rooftop mirror, 6. stationary rooftop mirror.

duce horizontally and vertically polarized beams are described by transmission matrices

$$T_{\text{VP}} = \begin{pmatrix} 1 & 0 \\ 0 & 0 \end{pmatrix} \qquad T_{\text{HP}} = \begin{pmatrix} 0 & 0 \\ 0 & 1 \end{pmatrix}, \tag{2}$$

such that the resulting polarization state upon transmission is

$$T_{\text{VP}}\mathbf{E} = \begin{pmatrix} 1 & 0 \\ 0 & 0 \end{pmatrix} \begin{pmatrix} E_V \\ E_H \end{pmatrix} = \begin{pmatrix} E_V \\ 0 \end{pmatrix} \tag{3}$$

or

$$T_{\text{HP}}\mathbf{E} = \begin{pmatrix} 0 & 0 \\ 0 & 1 \end{pmatrix} \begin{pmatrix} E_V \\ E_H \end{pmatrix} = \begin{pmatrix} 0 \\ E_H \end{pmatrix}. \tag{4}$$

For a beam reflected off a plane surface, the directions of both E_V and E_H stay the same relative to the instrument, but the direction of propagation changes. The convention we use here is that the vertical axis V is always normal to the instrument plane, with its positive direction "up", and the horizontal axis H is defined relative to V and the direction of propagation according to the right-hand rule, as shown in Fig. 5. Therefore, if the direction of propagation changes, so does the positive direction of the horizontal axis, and E_H needs to be redefined. In our approach, E_H always changes its sign upon reflection. The reflection matrix is then written as

$$R = \begin{pmatrix} 1 & 0 \\ 0 & -1 \end{pmatrix}, \tag{5}$$

which produces the reflected beam

$$R\mathbf{E} = \begin{pmatrix} 1 & 0 \\ 0 & -1 \end{pmatrix} \begin{pmatrix} E_V \\ E_H \end{pmatrix} = \begin{pmatrix} E_V \\ -E_H \end{pmatrix}. \tag{6}$$

Using this notation, we can also define reflection matrices for the polarizers

$$R_{\text{VP}} = \begin{pmatrix} 0 & 0 \\ 0 & -1 \end{pmatrix}, \qquad R_{\text{HP}} = \begin{pmatrix} 1 & 0 \\ 0 & 0 \end{pmatrix}. \tag{7}$$
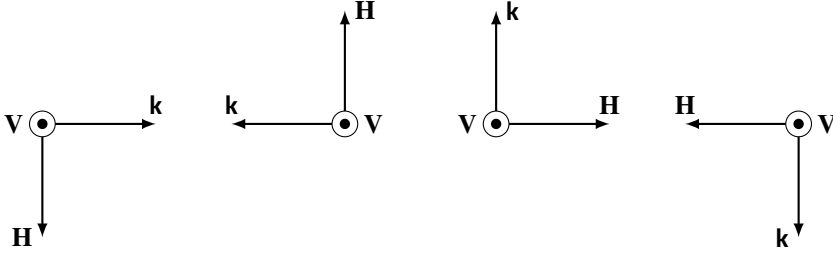
*Figure 5: Dependence of the reference frame orientation on the direction of beam propagation (indicated by the wavevector **k**) in Jones calculus.*

A rooftop mirror consists of two plane mirrors placed at a 90° angle relative to each other, so that the beam is reflected twice, and the direction of propagation is reversed. If the roof line is vertical, the beam reflection is equivalent to two consecutive reflections off a plane surface. The corresponding reflection matrix is the product of two plane surface reflection matrices

$$R_{\mathrm{VRM}} = RR = \begin{pmatrix} 1 & 0 \\ 0 & -1 \end{pmatrix} \begin{pmatrix} 1 & 0 \\ 0 & -1 \end{pmatrix} = \begin{pmatrix} 1 & 0 \\ 0 & 1 \end{pmatrix}. \tag{8}$$

While a vertical rooftop mirror changes the direction of the horizontal component E_H relative to the instrument, the polarization stays the same relative to the direction of propagation, which is why the result is the identity matrix. To describe a rooftop mirror placed with its roof line at an arbitrary angle, we can use the rotation matrix

$$\mathbb{R}(\theta) = \begin{pmatrix} \cos\theta & \sin\theta \\ -\sin\theta & \cos\theta \end{pmatrix}, \tag{9}$$

which projects any vector onto a new coordinate system that is rotated clockwise by θ, as shown in Fig. 6. In this case, we describe the reflection off a rooftop mirror with its roof line at an angle θ as three consecutive procedures: rotation of the coordinate system by θ, reflection off a vertical rooftop mirror, and another rotation back to the original orientation. The result is

$$R_{\mathrm{RM}}^{\theta} = \mathbb{R}(\theta)R_{\mathrm{VRM}}\mathbb{R}(\theta) = \begin{pmatrix} \cos^2\theta - \sin^2\theta & 2\cos\theta\sin\theta \\ -2\cos\theta\sin\theta & \cos^2\theta - \sin^2\theta \end{pmatrix}. \tag{10}$$

The second rotation back to the original orientation happens in the new coordinate system, where the propagation direction is reversed upon reflection, and therefore the same matrix for clockwise rotation $\mathbb{R}(\theta)$ is used instead of $\mathbb{R}(-\theta)$. The horizontal rooftop mirror is equivalent to $\theta = 90°$, which gives

$$R_{\mathrm{HRM}} = \begin{pmatrix} -1 & 0 \\ 0 & -1 \end{pmatrix}. \tag{11}$$

The wire-grid polarizer, which acts as a beamsplitter, is also described by a transmission and a reflection matrix. If we define the angle between E_V and the wires of the beamsplitter as ϕ, then the respective matrices are found in a similar manner: we first rotate the coordinate system by ϕ, then use the transmission/reflection matrix of a horizontal polarizer (with vertical wires), and afterwards perform another rotation. As the
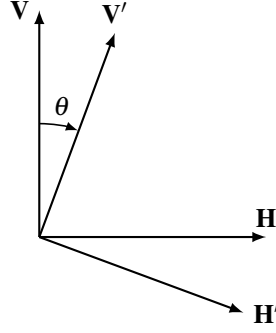
Figure 6: Rotation of a coordinate system by θ with a rotation matrix $\mathbb{R}(\theta)$.

result, we get the matrices

$$T_{\mathrm{BS}}^{\phi} = \mathbb{R}(-\phi)T_{\mathrm{HP}}\mathbb{R}(\phi) = \begin{pmatrix} \sin^2\phi & -\cos\phi\sin\phi \\ -\cos\phi\sin\phi & \cos^2\phi \end{pmatrix} \tag{12}$$

and

$$R_{\mathrm{BS}}^{\phi} = \mathbb{R}(\phi)R_{\mathrm{HP}}\mathbb{R}(\phi) = \begin{pmatrix} \cos^2\phi & \cos\phi\sin\phi \\ -\cos\phi\sin\phi & -\sin^2\phi \end{pmatrix}. \tag{13}$$

Similarly to the case of a rooftop mirror, we multiply the reflection matrix R_{HP} in Eq. (13) by the same clockwise rotation matrix $\mathbb{R}(\phi)$ on the left, which is due to the change in the direction of beam propagation. In case of transmission, however, we need to rotate the coordinate system by $-\phi$ to return to the original reference frame.

The beamsplitter in the Martin-Puplett interferometer is placed at the magic angle, $54.7°$ relative to the vertical axis, so that its projection appears to be at $\phi = \pm 45°$ relative to the polarization axis of the traveling beam. The transmission matrix is therefore

$$T_{\mathrm{BS}}^{\pm 45°} = \frac{1}{2}\begin{pmatrix} 1 & \mp 1 \\ \mp 1 & 1 \end{pmatrix}, \tag{14}$$

and the reflection matrix is

$$R_{\mathrm{BS}}^{\pm 45°} = \frac{1}{2}\begin{pmatrix} 1 & \pm 1 \\ \mp 1 & -1 \end{pmatrix}. \tag{15}$$

Lastly, we need to introduce a matrix that represents the phase change when a beam travels a distance d, which is

$$D(d) = e^{-i\frac{2\pi d}{\lambda}}\begin{pmatrix} 1 & 0 \\ 0 & 1 \end{pmatrix}, \tag{16}$$

where λ is the wavelength.

Now that we have defined Jones matrices for all components of the interferometer, we can describe the work principle according to the schematic diagram in Fig. 7:

① An arbitrarily polarized parallel beam $\mathbf{E}_1 = \begin{pmatrix} E_V \\ E_H \end{pmatrix}$ is created by an off-axis parabolic mirror, which directs the light from the source onto a linear polarizer.

② The beam passes through the linear polarizer, which creates a horizontally polarized light beam

$$\mathbf{E}_2 = T_{\mathrm{HP}}\mathbf{E}_1. \tag{17}$$

Using either vertically or horizontally polarized light leads to the same result, as long as both polarizers in Fig. 7 have the same polarization axis. The horizontally polarized beam then falls onto the beamsplitter, which has the projection of its wires appearing at a $+45°$ angle.

③ Half of the light is reflected off the beamsplitter with the polarization

$$\mathbf{E}_3 = R_{\mathrm{BS}}^{+45°}\mathbf{E}_2 = R_{\mathrm{BS}}^{+45°}T_{\mathrm{HP}}\mathbf{E}_1. \tag{18}$$

④ The reflected beam first travels the distance d_1 between the beamsplitter and the moving rooftop mirror, gets reflected, and then travels the distance d_1 again back to the beamsplitter. Both rooftop mirrors in the interferometer have a horizontal roof line, so the beam that comes back to the beamsplitter is described by

$$\mathbf{E}_4 = D(d_1)R_{\mathrm{HRM}}D(d_1)\mathbf{E}_3 = D(d_1)R_{\mathrm{HRM}}D(d_1)R_{\mathrm{BS}}^{+45°}T_{\mathrm{HP}}\mathbf{E}_1. \tag{19}$$

⑤ While half of the beam is reflected off the beamsplitter, the other half is transmitted through, according to

$$\mathbf{E}_5 = T_{\mathrm{BS}}^{+45°}\mathbf{E}_2 = T_{\mathrm{BS}}^{+45°}T_{\mathrm{HP}}\mathbf{E}_1. \tag{20}$$

⑥ The transmitted beam is described similarly to the reflected one, as it first travels the distance d_2 from the beamsplitter to the stationary rooftop mirror with a phase shift, then gets reflected and travels back, such that

$$\mathbf{E}_6 = D(d_2)R_{\mathrm{HRM}}D(d_2)\mathbf{E}_5 = D(d_2)R_{\mathrm{HRM}}D(d_2)T_{\mathrm{BS}}^{+45°}T_{\mathrm{HP}}\mathbf{E}_1. \tag{21}$$

⑦ For the beam $\mathbf{E}_4$, the beamsplitter wires still appear at a $+45°$ angle. We can check that none of the light gets reflected as the beam comes back to the beamsplitter, since

$$R_{\mathrm{BS}}^{+45°}\mathbf{E}_4 = R_{\mathrm{BS}}^{+45°}D(d_1)R_{\mathrm{HRM}}D(d_1)R_{\mathrm{BS}}^{+45°}T_{\mathrm{HP}}\mathbf{E}_1 = \begin{pmatrix} 0 \\ 0 \end{pmatrix}. \tag{22}$$

Therefore, the initially reflected part of the beam is now transmitted according to $T_{\mathrm{BS}}^{+45°}\mathbf{E}_4$. The originally transmitted beam, however, now approaches the beamsplitter from the opposite direction, which makes the wires appear to be at a $-45°$ angle. We can check that none of the light gets transmitted,

$$T_{\mathrm{BS}}^{-45°}\mathbf{E}_6 = T_{\mathrm{BS}}^{-45°}D(d_2)R_{\mathrm{HRM}}D(d_2)T_{\mathrm{BS}}^{+45°}T_{\mathrm{HP}}\mathbf{E}_1 = \begin{pmatrix} 0 \\ 0 \end{pmatrix}, \tag{23}$$

and the beam is reflected according to $R_{\mathrm{BS}}^{-45°}\mathbf{E}_6$. The two beams from ④ and ⑥ recombine, resulting in

$$\begin{aligned}
\mathbf{E}_7 &= T_{\mathrm{BS}}^{+45°}\mathbf{E}_4 + R_{\mathrm{BS}}^{-45°}\mathbf{E}_6 \\
&= \left[T_{\mathrm{BS}}^{+45°}D(d_1)R_{\mathrm{HRM}}D(d_1)R_{\mathrm{BS}}^{+45°}T_{\mathrm{HP}} + R_{\mathrm{BS}}^{-45°}D(d_2)R_{\mathrm{HRM}}D(d_2)T_{\mathrm{BS}}^{+45°}T_{\mathrm{HP}} \right] \mathbf{E}_1
\end{aligned} \tag{24}$$

(8) Finally, the beam passes through another horizontal polarizer, which gives

$$\mathbf{E}_8 = T_{\text{HP}}\mathbf{E}_7$$
$$= T_{\text{HP}}\left[T_{\text{BS}}^{+45°}D(d_1)R_{\text{HRM}}D(d_1)R_{\text{BS}}^{+45°} + R_{\text{BS}}^{-45°}D(d_2)R_{\text{HRM}}D(d_2)T_{\text{BS}}^{+45°}\right]T_{\text{HP}}\mathbf{E}_1. \tag{25}$$
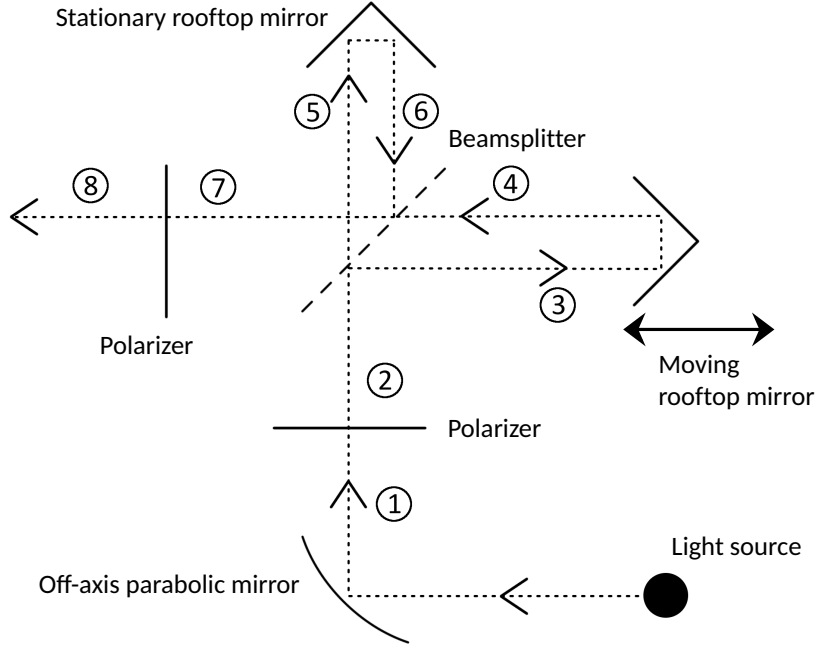
Figure 7: A schematic drawing of a Martin-Puplett interferometer.

Inserting the Jones matrices for the interferometer components from Eqs. (2 – 16) into Eq. (25) results in

$$\mathbf{E}_8 = \begin{pmatrix} 0 & 0 \\ 0 & 1 \end{pmatrix} \times$$

$$\frac{1}{4}\left[\begin{pmatrix} 1 & -1 \\ -1 & 1 \end{pmatrix}\begin{pmatrix} e^{-i\frac{2\pi d_1}{\lambda}} & 0 \\ 0 & e^{-i\frac{2\pi d_1}{\lambda}} \end{pmatrix}\begin{pmatrix} -1 & 0 \\ 0 & -1 \end{pmatrix}\begin{pmatrix} e^{-i\frac{2\pi d_1}{\lambda}} & 0 \\ 0 & e^{-i\frac{2\pi d_1}{\lambda}} \end{pmatrix}\begin{pmatrix} 1 & 1 \\ -1 & -1 \end{pmatrix} + \right.$$

$$\left.\begin{pmatrix} 1 & -1 \\ 1 & -1 \end{pmatrix}\begin{pmatrix} e^{-i\frac{2\pi d_2}{\lambda}} & 0 \\ 0 & e^{-i\frac{2\pi d_2}{\lambda}} \end{pmatrix}\begin{pmatrix} -1 & 0 \\ 0 & -1 \end{pmatrix}\begin{pmatrix} e^{-i\frac{2\pi d_2}{\lambda}} & 0 \\ 0 & e^{-i\frac{2\pi d_2}{\lambda}} \end{pmatrix}\begin{pmatrix} 1 & -1 \\ -1 & 1 \end{pmatrix}\right] \times$$

$$\begin{pmatrix} 0 & 0 \\ 0 & 1 \end{pmatrix}\begin{pmatrix} E_V \\ E_H \end{pmatrix}, \tag{26}$$

which, after performing the matrix multiplications, gives the output of the interferometer

$$\mathbf{E}_{\text{out}} \equiv \mathbf{E}_8 = \frac{1}{2}E_H\begin{pmatrix} 0 \\ e^{-i\frac{4\pi d_1}{\lambda}} + e^{-i\frac{4\pi d_2}{\lambda}} \end{pmatrix}. \tag{27}$$

We can further simplify Eq. (27) by using substitutions $\Delta = d_1 - d_2$ and $\bar{d} = d_1 + d_2$ as

$$\mathbf{E}_{\text{out}} = \frac{1}{2} E_H e^{-i\frac{2\pi\bar{d}}{\lambda}} \begin{pmatrix} 0 \\ e^{-i\frac{2\pi\Delta}{\lambda}} + e^{i\frac{2\pi\Delta}{\lambda}} \end{pmatrix} = E_H e^{-i\frac{2\pi\bar{d}}{\lambda}} \begin{pmatrix} 0 \\ \cos\frac{2\pi\Delta}{\lambda} \end{pmatrix}. \tag{28}$$

Since the intensity of the output light is proportional to the square of the norm of the electric field vector, we get

$$I_{\text{out}} \propto |\mathbf{E}_{\text{out}}|^2 = |E_H|^2 \cos^2 \frac{2\pi\Delta}{\lambda} = \frac{1}{2} |E_H|^2 \left(1 + \cos\frac{4\pi\Delta}{\lambda}\right), \tag{29}$$

which means that at every wavelength λ the intensity is proportional to a cosine function of the total path difference 2Δ between the two beams. The total intensity of the light, which includes all wavelengths that pass through the interferometer simultaneously, is found by integrating I_{out} over the whole wavelength/frequency range [16]. The result is a constant term I_0 plus the variation term, which is a function of the moving mirror position coordinate $x \equiv \Delta$,

$$I(x) = \int_0^\infty I_{\text{out}}(\tilde{\nu}) d\tilde{\nu} = I_0 + \int_0^\infty I(\tilde{\nu}) \cos(4\pi\tilde{\nu}x) d\tilde{\nu}, \tag{30}$$

where $\tilde{\nu} = 1/\lambda$ is the wavenumber, normally expressed in cm^{-1}, and $I(\tilde{\nu})$ is the intensity variation amplitude at a certain wavenumber. Performing a Fourier transform on Eq. (30) results in

$$\int I'(x) \cos(4\pi\tilde{\nu}'x) dx = \int \left[\int_0^\infty I(\tilde{\nu}) \cos(4\pi\tilde{\nu}x) d\tilde{\nu}\right] \cos(4\pi\tilde{\nu}'x) dx$$
$$= \int_0^\infty I(\tilde{\nu}) \delta(\tilde{\nu} - \tilde{\nu}') d\tilde{\nu} = I(\tilde{\nu}'), \tag{31}$$

where $I'(x) = I(x) - I_0$ is a redefined intensity as a function of the moving mirror position without the constant term. The result of Eq. (31) is the light intensity as a function of wavenumber, or, in other words, the recorded spectrum.

The Fourier transform technique combined with a moving mirror that continuously changes the path difference of the two beams makes it possible to detect all frequencies simultaneously. The method increases energy throughput, as compared to spectrometers that are equipped with prisms or gratings to create monochromatic light. Using a wire-grid polarizer as the beamsplitter eliminates the internal reflections, which otherwise occur inside other types of beamsplitters, such as a half-silvered mirror or a dielectric beamsplitter used in the Michelson interferometer. Such internal reflections result in a drop of the beamsplitter's efficiency, which is periodic in frequency, with the period determined by its thickness. A dielectric beamsplitter's efficiency also drops significantly at low frequencies due to low reflectivity. Using a wire-grid beamsplitter, therefore, ensures a uniform efficiency across a wide frequency range [17].

2 Crystal-field excitations in Tb$_2$Ti$_2$O$_7$

Pyrochlore oxides of the type $A_2^{3+}B_2^{4+}O_7$, where A^{3+} is a rare-earth ion and B^{3+} is usually a transition metal, attract immense interest due to the geometrical frustration (Fig. 8) inherent in the lattice of corner-sharing tetrahedra [7]. The frustration often results in the formation of novel phases at low temperature, such as spin glass, spin ice, or spin liquid. Tb$_2$Ti$_2$O$_7$ is a special case of its own: with no LRO down to extremely low temperatures, it
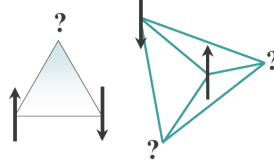
Figure 8: Geometrical frustration of antiferromagnetically coupled spins in a triangle (left) or tetrahedron (right) [7].

has been attributed properties of a spin liquid, spin glass, as well as the so-called quantum spin ice. Additionally, there is clear evidence of the coupling between magnetic and lattice degrees of freedom in Tb$_2$Ti$_2$O$_7$, which produces exotic magnetoelastic excitations modes, and may be important in explaining the absence of the LRO.

In our study, we address the question of coupling between crystal field (CF) excitations and the phonon modes. Our goal is to observe the effect of such vibronic coupling on the THz spectrum of Tb$_2$Ti$_2$O$_7$ by applying the magnetic field in along the $[111]$ direction and thus enhancing the splitting of the ground and the first excited CF doublets. In the following chapter, we, first, show how the absorption coefficient is related to the magnetic susceptibility in electrically insulating magnetic materials, such as Tb$_2$Ti$_2$O$_7$. We then derive the expression for the magnetic susceptibility based on the linear response theory. To calculate the absorption spectrum, it is necessary to determine the energy states of the system under consideration. Therefore, we utilize the crystal-field theory to find the correct Hamiltonian, which is used to calculate the energy states of magnetic Tb^{3+} ions in Tb$_2$Ti$_2$O$_7$. We propose a model that describes the subtle changes in the spectrum and relates them to the vibronic effects, which cause the symmetry breaking in the crystal. Finally, we compare predictions made by the model to the experimental data from spectroscopic measurements of Tb$_2$Ti$_2$O$_7$ to assess its validity.

2.1 Response of a magnetic medium

2.1.1 Solution to Maxwell's equations in an isotropic medium

First of all, we consider an electromagnetic wave propagating through an isotropic medium. Electromagnetic processes in all media are governed by the Maxwell's equations

$$\nabla \cdot \mathbf{D} = \rho \tag{32}$$

$$\nabla \times \mathbf{H} = \mathbf{J} + \frac{\partial \mathbf{D}}{\partial t} \tag{33}$$

$$\nabla \times \mathbf{E} = -\frac{\partial \mathbf{B}}{\partial t} \tag{34}$$

$$\nabla \cdot \mathbf{B} = 0, \tag{35}$$

where $\mathbf{E}$ is the electric field vector, $\mathbf{B}$ is the magnetic flux density, $\mathbf{J} = \hat{\sigma}\mathbf{E}$ is the free charge current density (with $\hat{\sigma}$ being the conductivity tensor), and ρ is the free charge density. $\mathbf{D}$ and $\mathbf{H}$ are macroscopic quantities called the electric displacement and the magnetic field strength vectors, which, in vacuum, are defined according to

$$\mathbf{D} = \varepsilon_0 \mathbf{E}$$
$$\mathbf{H} = \frac{1}{\mu_0}\mathbf{B}. \tag{36}$$

In a medium, however, these quantities are found by spatial averaging of the microscopic charges and current densities, as outlined in [18, Chap. 6.6]. This procedure leads to what is called the constitutive relations

$$\mathbf{D} = \varepsilon_0 \mathbf{E} + (\mathbf{P} + ...)$$
$$\mathbf{H} = \frac{1}{\mu_0}\mathbf{B} - (\mathbf{M} + ...), \tag{37}$$

where the parentheses include spatial averages of the bound charges and currents. Thus, $\mathbf{P}$ is the electric polarization vector, which represents the macroscopically averaged electric dipole, and $\mathbf{M}$ is the magnetization vector, which represents the macroscopically averaged magnetic dipole. Further terms, which include quadrupoles and higher order moment densities, are generally much smaller than $\mathbf{P}$ and $\mathbf{M}$, and, therefore, are omitted in the current approach.

Our goal here is to describe the linear response of a medium, where we assume that the electric polarization and magnetization are strictly proportional to the applied fields. Moreover, we assume that the medium is homogeneous and isotropic, which means that the proportionality factors χ^e and χ^m, called electric and magnetic susceptibilities, are scalars, such that

$$\mathbf{P} = \varepsilon_0 \chi^e \mathbf{E}$$
$$\mathbf{M} = \frac{1}{\mu_0}\chi^m \mathbf{B}. \tag{38}$$

Therefore, $\mathbf{D}$ and $\mathbf{H}$ are then also proportional to $\mathbf{E}$ and $\mathbf{B}$ according to

$$\mathbf{D} = \varepsilon_0 \mathbf{E} + \mathbf{P} = \varepsilon_0 \varepsilon \mathbf{E}$$
$$\mathbf{H} = \frac{1}{\mu_0}\mathbf{B} - \mathbf{M} = \frac{1}{\mu_0 \mu}\mathbf{B}, \tag{39}$$

where we define dielectric permittivity and magnetic permeability of a medium as

$$\varepsilon = 1 + \chi^e$$
$$\mu = \frac{1}{1 - \chi^m}. \tag{40}$$

The effect of magnetization in dia- and paramagnetic materials is small compared to the applied field, so it is usually assumed that $\chi^m \ll 1$ and

$$\mu \approx 1 + \chi^m. \tag{41}$$

In case of magnetic insulating materials that we focus on in this work, it is usually correct to assume that there are no free charges ($\rho = 0$) or free currents ($\mathbf{J} = 0$) present.

This considerably simplifies Eq. (33) and Eq. (34), which then take the form

$$\nabla \times \mathbf{H} = \varepsilon_0 \varepsilon \frac{\partial \mathbf{E}}{\partial t} \tag{42}$$

$$\nabla \times \mathbf{E} = -\mu_0 \mu \frac{\partial \mathbf{H}}{\partial t}. \tag{43}$$

We are going to assume that the electromagnetic radiation propagating through the medium can be decomposed into a set of plane waves with a frequency ω and a wavevector $\mathbf{k}$ of the form

$$\mathbf{H} = \mathbf{H}_0 e^{-i(\omega t - \mathbf{k} \cdot \mathbf{r})}$$

$$\mathbf{E} = \mathbf{E}_0 e^{-i(\omega t - \mathbf{k} \cdot \mathbf{r})}. \tag{44}$$

This allows us to replace $\nabla \times$ by $\mathbf{k} \times$ and $\frac{\partial}{\partial t}$ by $-i\omega$, and rewrite Eqs. (42 – 43) as

$$\mathbf{k} \times \mathbf{H} = -i\omega \varepsilon_0 \varepsilon \mathbf{E} \tag{45}$$

$$\mathbf{k} \times \mathbf{E} = i\omega \mu_0 \mu \mathbf{H}. \tag{46}$$

It is evident from Eqs. (45 – 46) that $\mathbf{E} \perp \mathbf{H} \perp \mathbf{k}$.

Combining Eq. (45) with Eq. (46) results in a wave equation

$$\mathbf{k} \times \mathbf{k} \times \mathbf{H} + \frac{\omega^2}{c_0^2} \varepsilon \mu \mathbf{H} = 0, \tag{47}$$

where $c_0 = \frac{1}{\sqrt{\varepsilon_0 \mu_0}}$ is the speed of light in vacuum. Let us rewrite the equation in tensor form, using Levi-Civita symbol for the vector product,

$$\epsilon_{ijk} k_j \epsilon_{klm} k_l H_m + \frac{\omega^2}{c_0^2} \varepsilon \mu H_i = 0 \tag{48}$$

where H_i stands for the i-th component of the $\mathbf{H}$ vector in Cartesian coordinates. Note the Einstein's notation of repeating indices $a_i b_i \equiv \sum_{i=1}^{3} a_i b_i$ used from now on. We now apply the property of invariance under cyclic permutation of the Levi-Civita symbol $\epsilon_{ijk} = \epsilon_{kij}$ and the identity $\epsilon_{kij} \epsilon_{klm} = \delta_{il} \delta_{jm} - \delta_{im} \delta_{jl}$ to write

$$k_i k_j H_j - k_j k_j H_i + \frac{\omega^2}{c_0^2} \varepsilon \mu H_i = 0. \tag{49}$$

Rewriting $k_j k_j H_i = k^2 H_i = k^2 \delta_{ij} H_j$ and $H_i = \delta_{ij} H_j$ allows us to take the vector component H_j outside of the parentheses to obtain

$$\left[k_i k_j - \left(k^2 + \frac{\omega^2}{c_0^2} \varepsilon \mu \right) \delta_{ij} \right] H_j = 0, \tag{50}$$

which is a set of equations that only has a solution if

$$\det \left[k_i k_j - \left(k^2 + \frac{\omega^2}{c_0^2} \varepsilon \mu \right) \delta_{ij} \right] = 0. \tag{51}$$

Let us now define the refractive index

$$\mathbf{N} = \frac{c_0}{\omega} \mathbf{k}, \tag{52}$$

26

which, in general, is a complex quantity with its components $N_j = n_j + i\kappa_j$. Using this definition, we rewrite Eq. (51) as

$$\det\left[N_i N_j - \left(N^2 + \varepsilon\mu\right)\delta_{ij}\right] = 0, \tag{53}$$

where $N = |\mathbf{N}|$. We can assume without the loss of generality that $\mathbf{N} \parallel \mathbf{z}$ and, therefore,

$$\left(N^2 + \varepsilon\mu\right)\left(N^2 + \varepsilon\mu\right)\varepsilon\mu = 0, \tag{54}$$

which has the solution

$$N = \sqrt{\varepsilon\mu}. \tag{55}$$

As we are going to demonstrate, the absorption coefficient is directly related to the imaginary part of the refractive index. Specifically, in case of magnetic materials the absorption is determined by the imaginary part of the magnetic susceptibility. Using Eq. (40), and assuming $\chi^m \ll 1$, we can write

$$\sqrt{\mu} = \sqrt{\frac{1}{1 - \chi^m}} \approx 1 + \frac{1}{2}\chi^m, \tag{56}$$

which leads to the expression for the refractive index in terms of magnetic susceptibility

$$N \approx \sqrt{\varepsilon}\left(1 + \frac{1}{2}\chi^m\right). \tag{57}$$

2.1.2 Absorption coefficient

The absorption coefficient α is defined through the relation between incident light intensity I_0 and transmitted light intensity I over a distance d

$$I = I_0 e^{-\alpha d}. \tag{58}$$

The light intensity is given by the real part of the Poynting vector [18]

$$\mathbf{S} = \mathbf{E} \times \mathbf{H}, \tag{59}$$

which, according to the cycle-average theorem [19], averages to

$$\bar{\mathbf{S}} = \frac{1}{2}\mathbf{E} \times \mathbf{H}^*, \tag{60}$$

if both $\mathbf{E}$ and $\mathbf{H}$ have time-dependence of the form $e^{-i\omega t}$. Here the star indicates the complex conjugate. From Eqs. (45 – 46) it follows that

$$|\mathbf{E}| = \frac{\omega}{k}\mu_0\mu|\mathbf{H}| = \frac{k}{\omega}\varepsilon_0\varepsilon|\mathbf{H}|, \tag{61}$$

which, using the definition of the phase velocity in the medium, $c = \omega/k$, leads to the expression for the light intensity

$$I = |\bar{\mathbf{S}}| = \frac{1}{2}c\mu_0\mu|\mathbf{H}|^2. \tag{62}$$

For a plane wave propagating along the z axis, the magnetic field strength vector is equal to $\mathbf{H} = \mathbf{H}_0 e^{-i(\omega t - kz)} = \mathbf{H}_0 e^{-i\omega(t - Nz/c_0)}$, where we substitute $k = \omega N/c_0$ from Eq. (52). Therefore, the light intensity of a plane wave is

$$I = \frac{1}{2}c\mu_0\mu|\mathbf{H}_0|^2 e^{-\frac{2\omega}{c_0}\kappa z} = I_0 e^{-\frac{2\omega}{c_0}\kappa z}, \tag{63}$$

where κ is the imaginary part of the refractive index and I_0 is the light intensity at $z = 0$. Comparing the result to the definition of the absorption coefficient in Eq. (58) yields

$$\alpha = \frac{2\omega}{c_0}\kappa. \tag{64}$$

Inserting the expression for the refractive index from Eq. (57) and assuming that ε is a real-valued quantity, we arrive to the expression for the absorption coefficient as a function of the magnetic susceptibility

$$\alpha = \frac{\omega\sqrt{\varepsilon}}{c_0}\chi_I^m. \tag{65}$$

2.2 Linear response theory

The following section is aimed at finding the expression for magnetic susceptibility in Eq. (65) based on the linear response theory, which is outlined in [20, Chap. 3]. In this approach, we assume that the Hamiltonian of a system consists of two parts: a time-independent part that describes the static state of the system, and a time-dependent part that introduces a small perturbation. Any physical observable is then related to the perturbation term in the Hamiltonian via a response function. If we express an observable using the density-operator formalism, we can relate the response function to the time-dependent part of the density operator. To find the explicit time dependence of the density operator, we are going to utilize the Heisenberg and the interaction picture versions of this operator. Once we know the explicit time dependence of the density operator, we can express the response function in terms of the known observables and their eigenvalues. The result is the Kubo formula, from which we can arrive to the expression for the generalized susceptibility of the system. Finally, we will consider a specific case of the magnetic susceptibility, where the external perturbation is the oscillating magnetic field of an incident electromagnetic wave.

2.2.1 Response function

We start with an operator $\hat{B}$ representing a physical observable. The ensemble average of $\hat{B}$ in thermal equilibrium can be expressed in the density-operator formalism as

$$\langle\hat{B}\rangle = \mathrm{Tr}\{\rho\hat{B}\}, \tag{66}$$

with $\mathrm{Tr}\{\ \}$ standing for trace. The density operator is defined as

$$\rho = \frac{1}{\mathscr{Z}}e^{-\beta\hat{H}}, \tag{67}$$

where $\beta = 1/k_B T$, k_B is the Boltzmann constant, T is the temperature, $\mathscr{Z} = \mathrm{Tr}\{e^{-\beta\hat{H}}\}$ is the grand partition function, and $\hat{H}$ is the effective Hamiltonian. We introduce a time-dependent external perturbation $f(t)$ into the system by assuming that the Hamiltonian has the form

$$\hat{H} = \hat{H}_0 + \hat{H}_1, \tag{68}$$

where $\hat{H}_0$ is the time-independent (static) part and

$$\hat{H}_1 = -\hat{A}f(t) \tag{69}$$

is the time-dependent part, which is linear in perturbation $f(t)$. The proportionality factor $\hat{A}$ here is a constant operator. This operator could, for example, be the magnetic moment of the system, which couples to the time-dependent external magnetic field and

introduces a correction to the Hamiltonian. As the result, both the partition function and the density operator become time-dependent, and so does the ensemble average of the physical observable $\hat{B}$. Therefore, Eq. (66) now has the form

$$\langle \hat{B}(t) \rangle = \mathrm{Tr}\{\rho(t)\hat{B}\}. \tag{70}$$

A linear response function φ is defined through the relation between $\langle \hat{B}(t) \rangle$ and $f(t)$

$$\langle \hat{B}(t) \rangle - \langle \hat{B} \rangle = \int_{-\infty}^{t} \varphi_{BA}(t-t')f(t')dt', \tag{71}$$

where $\langle \hat{B} \rangle = \langle \hat{B}(t = -\infty) \rangle$. The response function only depends on the time difference $t - t'$, and the perturbation is assumed to vanish in the limit $\lim_{t' \to -\infty} f(t') = 0$. On the other hand, from Eq. (70) it directly follows that

$$\langle \hat{B}(t) \rangle - \langle \hat{B} \rangle = \mathrm{Tr}\{(\rho(t) - \rho_0)\hat{B}\}, \tag{72}$$

where ρ_0 is the static density operator with $\hat{H} = \hat{H}_0$. This implies that

$$\int_{-\infty}^{t} \varphi_{BA}(t-t')f(t')dt' = \mathrm{Tr}\{(\rho(t) - \rho_0)\hat{B}\}, \tag{73}$$

which is the expression we will use to find the response function φ_{BA}.

Next, to find the expression for $\rho(t)$, we are going to utilize the Heisenberg picture and the interaction picture. A time-dependent operator such as $\hat{B}(t)$ can be written in the Heisenberg picture as

$$\hat{B}(t) = U^\dagger \hat{B} U = e^{i\hat{H}t/\hbar}\hat{B}e^{-i\hat{H}t/\hbar}, \tag{74}$$

where $\hat{B}$ is assumed to have no explicit time dependence. The operator $U \equiv e^{-i\hat{H}t/\hbar}$ is the so-called time-evolution operator, which normally (in the Schrödinger picture) determines the time evolution of an eigenstate. In the Heisenberg picture, however, the time evolution is integrated in the operators, while the wave functions are static. Using the relation between $\hat{B}(t)$ and $\hat{B}$ from Eq. (74), we can rewrite Eq. (70) as

$$\begin{aligned} \langle \hat{B}(t) \rangle &= \mathrm{Tr}\{\rho(t)\hat{B}\} \\ &= \mathrm{Tr}\{\rho(t)e^{-i\hat{H}t/\hbar}\hat{B}(t)e^{i\hat{H}t/\hbar}\} \\ &= \mathrm{Tr}\{e^{i\hat{H}t/\hbar}\rho(t)e^{-i\hat{H}t/\hbar}\hat{B}(t)\} \\ &= \mathrm{Tr}\{\rho_H\hat{B}(t)\}, \end{aligned} \tag{75}$$

where we used the property of trace invariance under cyclic permutations and defined the Heisenberg version of the density operator

$$\rho_H = e^{i\hat{H}t/\hbar}\rho(t)e^{-i\hat{H}t/\hbar}, \tag{76}$$

which has no explicit time dependence,

$$\frac{\partial \rho_H}{\partial t} = 0. \tag{77}$$

The absence of time dependence in ρ_H is expected, because states are stationary in the Heisenberg picture, and the density operator is directly related to the states [21]. Now,

using the Heisenberg version of the density operator, we can find the equation of motion for $\rho(t)$ according to

$$
\begin{aligned}
\frac{d}{dt}\rho(t) &= \frac{d}{dt}\left(-e^{i\hat{H}t/\hbar}\rho_H e^{i\hat{H}t/\hbar}\right) \\
&= -\frac{i}{\hbar}\hat{H}e^{i\hat{H}t/\hbar}\rho_H e^{-i\hat{H}t/\hbar} + e^{i\hat{H}t/\hbar}\rho_H\frac{i}{\hbar}\hat{H}e^{-i\hat{H}t/\hbar} \\
&= -\frac{i}{\hbar}[\hat{H},\rho(t)] \\
&= -\frac{i}{\hbar}[\hat{H}_0,\rho(t)] - \frac{i}{\hbar}[\hat{H}_1,\rho(t)].
\end{aligned}
\tag{78}
$$

In the interaction picture, the density operator is defined as

$$
\rho_I(t) = e^{i\hat{H}_0 t/\hbar}\rho(t)e^{-i\hat{H}_0 t/\hbar},
\tag{79}
$$

where the time-evolution operator is generated using just the static part of the Hamiltonian $\hat{H}_0$, as opposed to the whole Hamiltonian in the Heisenberg picture. Also note that both $\rho_I(t)$ and $\rho(t)$ here are time-dependent. The equation of motion for $\rho_I(t)$ is found according to

$$
\begin{aligned}
\frac{d}{dt}\rho_I(t) &= \frac{d}{dt}\left(e^{i\hat{H}_0 t/\hbar}\rho(t)e^{-i\hat{H}_0 t/\hbar}\right) \\
&= \frac{i}{\hbar}\hat{H}_0 e^{i\hat{H}_0 t/\hbar}\rho(t)e^{-i\hat{H}_0 t/\hbar} + e^{i\hat{H}_0 t/\hbar}\frac{d\rho(t)}{dt}e^{i\hat{H}_0 t/\hbar} + e^{i\hat{H}_0 t/\hbar}\rho(t)\left(-\frac{i}{\hbar}\hat{H}_0\right)e^{-i\hat{H}_0 t/\hbar} \\
&= e^{i\hat{H}_0 t/\hbar}\left(\frac{i}{\hbar}[\hat{H}_0,\rho(t)] + \frac{d\rho(t)}{dt}\right)e^{-i\hat{H}_0 t/\hbar},
\end{aligned}
\tag{80}
$$

which, after including the result from Eq. (78), simplifies to

$$
\frac{d}{dt}\rho_I(t) = -\frac{i}{\hbar}e^{i\hat{H}_0 t/\hbar}[\hat{H}_1,\rho(t)]e^{-i\hat{H}_0 t/\hbar}.
\tag{81}
$$

The equation of motion for the density operator in the interaction picture only depends on the perturbative part of the Hamiltonian, which is exactly what we need to isolate the response to the external perturbation $f(t)$.

To further isolate the linear response, we write the density operator as a sum of two terms

$$
\rho(t) = \rho_0 + \rho_1(t),
\tag{82}
$$

where ρ_0 is the time-independent part defined according to Eq. (67) with $\hat{H} = \hat{H}_0$, and $\rho(t)$ is the additional contribution due to $f(t)$. We insert this expression for $\rho(t)$ into Eq. (81) and get

$$
\begin{aligned}
\frac{d}{dt}\rho_I(t) &= -\frac{i}{\hbar}e^{i\hat{H}_0 t/\hbar}[\hat{H}_1,\rho_0 + \rho_1(t)]e^{-i\hat{H}_0 t/\hbar} \\
&\approx -\frac{i}{\hbar}e^{i\hat{H}_0 t/\hbar}[\hat{H}_1,\rho_0]e^{-i\hat{H}_0 t/\hbar},
\end{aligned}
\tag{83}
$$

where we drop the quadratic term $\hat{H}_1\rho_1 \propto f(t)^2$. If we insert the definition of $\hat{H}_1$ from Eq. (69) and use the commutation relation $[e^{-i\hat{H}_0 t/\hbar},\rho_0] = 0$, we obtain

$$
\begin{aligned}
\frac{d}{dt}\rho_I(t) &= \frac{i}{\hbar}e^{i\hat{H}_0 t/\hbar}[\hat{A},\rho_0]f(t)e^{-i\hat{H}_0 t/\hbar} \\
&= \frac{i}{\hbar}[e^{i\hat{H}_0 t/\hbar}\hat{A}e^{-i\hat{H}_0 t/\hbar},\rho_0]f(t) = \frac{i}{\hbar}[\hat{A}_I(t),\rho_0]f(t),
\end{aligned}
\tag{84}
$$

where we defined a time-dependent version of the operator $\hat{A}$ in the interaction picture $\hat{A}_I(t) = e^{i\hat{H}_0 t/\hbar}\hat{A}e^{-i\hat{H}_0 t/\hbar}$, similar to Eq. (79).

Now that we have the equation of motion for the density operator in the interaction picture, we can go back to our original density operator $\rho(t)$, and, according to the definition of ρ_I in Eq. (79), write

$$
\begin{aligned}
\rho(t) &= e^{-i\hat{H}_0 t/\hbar}\rho_I(t)e^{i\hat{H}_0 t/\hbar} = e^{-i\hat{H}_0 t/\hbar}\left(\int_{-\infty}^{t}\frac{d}{dt'}\rho_I(t')dt' + \rho_0\right)e^{i\hat{H}_0 t/\hbar} \\
&= e^{-i\hat{H}_0 t/\hbar}\rho_0 e^{i\hat{H}_0 t/\hbar} + e^{-i\hat{H}_0 t/\hbar}\left(\frac{i}{\hbar}\int_{-\infty}^{t}\frac{d}{dt'}[\hat{A}_I(t'),\rho_0]dt\right)e^{i\hat{H}_0 t/\hbar} \\
&= e^{-i\hat{H}_0 t/\hbar}e^{i\hat{H}_0 t/\hbar}\rho_0 + \frac{i}{\hbar}\int_{-\infty}^{t}\frac{d}{dt'}[e^{-i\hat{H}_0 t/\hbar}\hat{A}_I(t')e^{i\hat{H}_0 t/\hbar},\rho_0]dt' \\
&= \rho_0 + \frac{i}{\hbar}\int_{-\infty}^{t}[\hat{A}_I(t'-t),\rho_0]f(t')dt',
\end{aligned}
\tag{85}
$$

where we utilized

$$
\int_{-\infty}^{t}\frac{d}{dt'}\rho_I(t')dt' = \rho_I(t')|_{-\infty}^{t} = \rho_I(t) - \rho_0
\tag{86}
$$

and used the time-evolution operator to get

$$
\hat{A}_I(t'-t) = e^{-i\hat{H}_0 t/\hbar}\hat{A}_I(t')e^{i\hat{H}_0 t/\hbar}.
\tag{87}
$$

Note that t is not the integration variable, and the time-evolution operator can be brought inside the integral. We have thus derived the expression for $\rho(t)$, which we plug into Eq. (73) to obtain

$$
\int_{-\infty}^{t}\varphi_{BA}(t-t')f(t')dt' = \frac{i}{\hbar}\text{Tr}\left\{\int_{-\infty}^{t}[\hat{A}_I(t'-t),\rho_0]\hat{B}f(t')dt'\right\}.
\tag{88}
$$

This result allows us to express the response function in terms of operators $\hat{A}$ and $\hat{B}$. We start by rearranging the right-hand side of Eq. (88), using the property of trace invariance under cyclic permutations in addition to the commutation relation $[e^{-i\hat{H}_0 t/\hbar},\rho_0] = 0$, and inserting the expression for $\hat{A}_I(t'-t)$ from Eq. (87) to get

$$
\begin{aligned}
&\text{Tr}\left\{\int_{-\infty}^{t}[\hat{A}_I(t'-t),\rho_0]\hat{B}f(t')dt'\right\} \\
&= \int_{-\infty}^{t}\text{Tr}\{\hat{A}_I(t'-t)\rho_0\hat{B} - \rho_0\hat{A}_I(t'-t)\hat{B}\}f(t')dt' \\
&= \int_{-\infty}^{t}\text{Tr}\{e^{-i\hat{H}_0 t/\hbar}\hat{A}_I(t')e^{i\hat{H}_0 t/\hbar}\rho_0\hat{B} - \rho_0 e^{-i\hat{H}_0 t/\hbar}\hat{A}_I(t')e^{i\hat{H}_0 t/\hbar}\hat{B}\}f(t')dt' \\
&= \int_{-\infty}^{t}\text{Tr}\{\rho_0 e^{i\hat{H}_0 t/\hbar}\hat{B}e^{-i\hat{H}_0 t/\hbar}\hat{A}_I(t') - \rho_0\hat{A}_I(t')e^{i\hat{H}_0 t/\hbar}\hat{B}e^{-i\hat{H}_0 t/\hbar}\}f(t')dt' \\
&= \int_{-\infty}^{t}\text{Tr}\{\rho_0[\hat{B}_I(t),\hat{A}_I(t')]\}f(t')dt'.
\end{aligned}
\tag{89}
$$

Then, we rewrite Eq. (88) as

$$
\begin{aligned}
\int_{-\infty}^{t}\varphi_{BA}(t-t')f(t')dt' &= \frac{i}{\hbar}\int_{-\infty}^{t}\text{Tr}\{\rho_0[\hat{B}_I(t),\hat{A}_I(t')]\}f(t')dt' \\
&= \frac{i}{\hbar}\int_{-\infty}^{t}\langle[\hat{B}_I(t),\hat{A}_I(t')]\rangle_0 f(t')dt',
\end{aligned}
\tag{90}
$$

31

where $\langle\rangle_0$ stands for the ensemble average in thermal equilibrium, determined by $\hat{H}_0$ according to Eq. (66). Finally, since both operators $\hat{B}_I$ and $\hat{A}_I$ in the interaction picture are generated using the time-evolution operator with $\hat{H}_0$ in the exponent, we can drop the indices and write the expression for the response function, also known as the Kubo formula [22],

$$\varphi_{BA}(t-t') = \frac{i}{\hbar}\theta(t-t')\langle[\hat{B}(t),\hat{A}(t')]\rangle. \tag{91}$$

The step function

$$\theta(x) = \begin{cases} 0, & \text{if } x < 0 \\ 1, & \text{if } x \geq 0 \end{cases} \tag{92}$$

is introduced to ensure the causality of the response function, i.e. that the response vanishes for $t' > t$. Note that the response function ϕ_{BA} only depends on the difference $t - t' > 0$, and we can therefore select $t' = 0$, and for $t > 0$ write

$$\varphi_{BA}(t) = \frac{i}{\hbar}\langle[\hat{B}(t),\hat{A}]\rangle = \frac{i}{\hbar}\text{Tr}\{\rho[\hat{B}(t),\hat{A}]\}. \tag{93}$$

To calculate the response function, we need to know the eigenvalues and the eigenstates of the unperturbed Hamiltonian $\hat{H}_0$. Assuming that the states $|\alpha\rangle$ are known, and their corresponding eigenvalues are E_α, we proceed to calculate the response function by inserting the expression for $\hat{B}(t)$ from Eq. (74) into Eq. (93),

$$\begin{aligned} \varphi_{BA}(t) =& \frac{i}{\hbar}\frac{1}{\mathscr{Z}}\text{Tr}\{e^{-\beta\hat{H}}[e^{i\hat{H}t/\hbar}\hat{B}e^{-i\hat{H}t/\hbar},\hat{A}]\} \\ =& \frac{i}{\hbar}\frac{1}{\mathscr{Z}}\sum_\alpha \langle\alpha|e^{-\beta\hat{H}}[e^{i\hat{H}t/\hbar}\hat{B}e^{-i\hat{H}t/\hbar},\hat{A}]|\alpha\rangle \\ =& \frac{i}{\hbar}\frac{1}{\mathscr{Z}}\sum_\alpha e^{-\beta E_\alpha}\langle\alpha|e^{i\hat{H}t/\hbar}\hat{B}e^{-i\hat{H}t/\hbar}\hat{A}|\alpha\rangle - e^{-\beta E_\alpha}\langle\alpha|\hat{A}e^{i\hat{H}t/\hbar}\hat{B}e^{-i\hat{H}t/\hbar}|\alpha\rangle \quad (94) \\ =& \frac{i}{\hbar}\frac{1}{\mathscr{Z}}\sum_{\alpha\alpha'} e^{-\beta E_\alpha}\langle\alpha|e^{i\hat{H}t/\hbar}\hat{B}|\alpha'\rangle\langle\alpha'|e^{-i\hat{H}t/\hbar}\hat{A}|\alpha\rangle \\ & \qquad\qquad - e^{-\beta E_\alpha}\langle\alpha|\hat{A}e^{i\hat{H}t/\hbar}|\alpha'\rangle\langle\alpha'|\hat{B}e^{-i\hat{H}t/\hbar}|\alpha\rangle, \end{aligned}$$

where we used the property of an orthonormal basis $\sum_{\alpha'}|\alpha'\rangle\langle\alpha'| = 1$. If an operator $\hat{\Omega}$ has an eigenstate $|\psi\rangle$, such that $\hat{\Omega}|\psi\rangle = a|\psi\rangle$, then, according to the properties of bra and ket vectors, $\langle\psi|\hat{\Omega}^\dagger = a^*\langle\psi|$. This allows us to write $\langle\alpha|e^{-\beta\hat{H}} = e^{-\beta E_\alpha}\langle\alpha|$ and bring the factor $e^{-\beta E_\alpha}$ out of the bracket in Eq. (94). Furthermore, the time-evolution operator $U = e^{-i\hat{H}t/\hbar}$ satisfies $e^{-i\hat{H}t/\hbar}|\alpha\rangle = e^{-iE_\alpha t/\hbar}|\alpha\rangle$. We therefore apply the operator to the bra vectors according to $\langle\alpha|\left(e^{-i\hat{H}t/\hbar}\right)^\dagger = \left(e^{-iE_\alpha t/\hbar}\right)^*\langle\alpha|$, which gives us $\langle\alpha|e^{i\hat{H}t/\hbar} = e^{iE_\alpha t/\hbar}\langle\alpha|$. Using these relations, we can further simplify the response function as

$$\begin{aligned} \varphi_{BA}(t) =& \frac{i}{\hbar}\frac{1}{\mathscr{Z}}\sum_{\alpha\alpha'} e^{-\beta E_\alpha}\{e^{iE_\alpha t/\hbar}\langle\alpha|\hat{B}|\alpha'\rangle e^{-iE_{\alpha'}t/\hbar}\langle\alpha'|\hat{A}|\alpha\rangle \\ & \qquad\qquad - \langle\alpha|\hat{A}|\alpha'\rangle e^{iE_{\alpha'}t/\hbar}\langle\alpha'|\hat{B}|\alpha\rangle e^{-iE_\alpha t/\hbar}\}. \end{aligned} \tag{95}$$

Since the sum is taken over all of the basis states, we can interchange α and α' in the second term and, defining the population factor $n_\alpha = \mathscr{Z}^{-1}e^{-\beta E_\alpha}$, write

$$\varphi_{BA}(t) = \frac{i}{\hbar}\sum_{\alpha\alpha'}\langle\alpha|\hat{B}|\alpha'\rangle\langle\alpha'|\hat{A}|\alpha\rangle(n_\alpha - n_{\alpha'})e^{i(E_\alpha - E_{\alpha'})t/\hbar}. \tag{96}$$

The result is a specific case of the Kubo formula, which still describes the response of a system to the external perturbation from Eq. (69), but now also includes the existing energy states of the system, and the corresponding thermal populations.

2.2.2 Generalized susceptibility

Susceptibility χ_{BA} is the response to the external perturbation in the frequency domain that satisfies

$$\langle \hat{B}(\omega) \rangle = \chi_{BA}(\omega) f(\omega), \tag{97}$$

where $\langle \hat{B}(\omega) \rangle$ is the generalized Fourier transform defined as

$$\langle \hat{B}(\omega) \rangle = \lim_{\epsilon \to 0^+} \int_{-\infty}^{\infty} \left(\langle \hat{B}(t) \rangle - \langle \hat{B} \rangle \right) e^{i\omega t} e^{-\epsilon t} dt. \tag{98}$$

To find χ_{BA}, we insert the expression for $\langle \hat{B}(t) \rangle - \langle \hat{B} \rangle$ from Eq. (71) and get

$$\langle \hat{B}(\omega) \rangle = \lim_{\epsilon \to 0^+} \int_{-\infty}^{\infty} \left[\int_{-\infty}^{t} \varphi_{BA}(t - t') f(t') e^{\epsilon t'} dt' \right] e^{i\omega t} e^{-\epsilon t} dt. \tag{99}$$

Here we also replaced $f(t)$ by $f(t)e^{\epsilon t}$ with the limit $\epsilon \to 0^+$ to ensure that the external perturbation is added smoothly. Next, we use the substitution $\tau = t - t'$ to write

$$\langle \hat{B}(\omega) \rangle = \lim_{\epsilon \to 0^+} \int_{-\infty}^{\infty} \left[\int_{0}^{\infty} \varphi_{BA}(\tau) f(t - \tau) e^{\epsilon(t - \tau)} d\tau \right] e^{i\omega t} e^{-\epsilon t} dt. \tag{100}$$

Since $f(t - \tau)$ only depends on the difference $t' = t - \tau$, we can make another variable change and separate two integrals

$$\langle \hat{B}(\omega) \rangle = \lim_{\epsilon \to 0^+} \int_{0}^{\infty} \varphi_{BA}(\tau) e^{-\epsilon \tau} e^{i\omega \tau} d\tau \int_{-\infty}^{\infty} f(t') e^{i\omega t'} dt'. \tag{101}$$

Comparing the result to Eq. (97), we obtain the Fourier transform of $f(t)$

$$f(\omega) = \int_{-\infty}^{\infty} f(t) e^{i\omega t} dt \tag{102}$$

and the susceptibility

$$\chi_{BA}(\omega) = \lim_{\epsilon \to 0^+} \int_{0}^{\infty} \varphi_{BA}(t) e^{i\omega t} e^{-\epsilon t} dt, \tag{103}$$

which is the generalized Fourier transform of the response function. The positive integration range makes it possible to use the form of $\varphi_{BA}(t)$ without the step function from Eq. (93), with causality automatically ensured. Inserting the result from Eq. (96) into Eq. (103) and calculating the integral, we obtain the final expression for the susceptibility

$$\chi_{BA}(\omega) = \lim_{\epsilon \to 0^+} \sum_{\alpha \alpha'} \frac{\langle \alpha | \hat{B} | \alpha' \rangle \langle \alpha' | \hat{A} | \alpha \rangle}{E_{\alpha'} - E_{\alpha} - \hbar\omega - i\hbar\epsilon} (n_\alpha - n_{\alpha'}). \tag{104}$$

According to Eq. (65), the absorption coefficient is proportional to the imaginary part of the susceptibility. Thus, the absorption strength is proportional to the matrix elements of the operators $\hat{J}^i$ between the states of a system. We can also see that the more the phonon energy $\hbar\omega$ matches the transition energy $E_{\alpha'} - E_\alpha$, the stronger is absorption.

2.2.3 Magnetic susceptibility

A specific example of the perturbation $f(t)$ and the physical observable $\hat{B}$ is, correspondingly, an oscillating magnetic field and magnetization. If we consider a plane wave of the form $\mathbf{B}^{\omega} = \mathbf{B}_0 e^{-i\omega t}$ interacting with a magnetic atom, which has a magnetic moment $\mathbf{m}$, the perturbation term in the Hamiltonian is

$$\hat{H}_1 = -\mathbf{m} \cdot \mathbf{B}^{\omega}. \tag{105}$$

The magnetic moment of an atom can be expressed thorough the total angular momentum $\mathbf{J}$ as

$$\mathbf{m} = -\frac{g_J \mu_B}{\hbar} \mathbf{J}, \tag{106}$$

in which case

$$\hat{H}_1 = \frac{g_J \mu_B}{\hbar} \mathbf{J} \cdot \mathbf{B}^{\omega}. \tag{107}$$

Comparing this expression for $\hat{H}_1$ to Eq. (69) and taking $f(t) = \mathbf{B}^{\omega}$ gives the form of the operator $\hat{A}$

$$\hat{A}^i = -\frac{g_J \mu_B}{\hbar} \hat{J}^i, \tag{108}$$

where index i indicates the i-th component of a vector in Cartesian coordinates.

Considering the relation between the external perturbation and the physical observable $\hat{B}$ from Eq. (97), and taking into account the relation of the magnetization to the applied field from Eq. (38), we conclude that the correct form of the operator $\hat{B}$ is

$$\hat{B}^i = \mu_0 M^i. \tag{109}$$

Magnetization is defined as the magnetic moment per unit volume,

$$\mathbf{M} \equiv \frac{\mathbf{m}}{V} = -\frac{1}{V} \frac{g_J \mu_B}{\hbar} \mathbf{J}, \tag{110}$$

where V is the unit volume per atom with magnetic moment $\mathbf{m}$. This provides the expression of the physical observable $\hat{B}$ in terms of the angular momentum operator

$$\hat{B}^i = -\frac{1}{V} \frac{\mu_0 g_J \mu_B}{\hbar} \hat{J}^i. \tag{111}$$

Finally, inserting Eq. (108) and Eq. (111) into the expression for general susceptibility in Eq. (104), we obtain the tensor components χ_{ij}^m of the magnetic susceptibility

$$\chi_{ij}^m = \frac{\mu_0 (g_J \mu_B)^2}{V} \lim_{\epsilon \to 0^+} \sum_{\alpha\alpha'} \frac{n_\alpha - n_{\alpha'}}{E_{\alpha'} - E_\alpha - \hbar\omega - i\hbar\epsilon} J_{\alpha\alpha'}^i J_{\alpha'\alpha}^j, \tag{112}$$

where $J_{\alpha\alpha'}^i = \langle\alpha|\hat{J}^i|\alpha'\rangle/\hbar$ is the matrix element of the total angular momentum of an atom between the states $|\alpha\rangle$ and $|\alpha'\rangle$.

2.3 Crystal field theory

Our goal here is to describe the CF Hamiltonian in terms of Steven's operators. We first consider the electrostatic potential in a crystalline environment, which we express in terms of spherical harmonics. We then proceed to substitute the spherical harmonics by the real-valued tesseral harmonics, which we express in Cartesian coordinates. These, in turn, have a direct correspondence to the Steven's operators, which allows us to express the CF

Hamiltonian in the desired form. An alternative approach would be to move directly from spherical harmonics to the spherical tensor operators, and thus arrive to the Wybourne operators, but we are not going to consider this approach here. It is possible to derive Wybourne operators directly from Stevens operators and vice versa, as outlined in [IV, Appendix B].

To describe energy levels of an ion inside a crystalline environment, we approximate ions around it as point charges. Thus the electrostatic potential at the location $\mathbf{r} = (r, \theta, \phi)$ is

$$V(r, \theta, \phi) = \sum_j \frac{q_j}{|(\mathbf{R}_j - \mathbf{r})|}, \tag{113}$$

where q_j are the surrounding point charges at locations $\mathbf{R}_j = (R_j, \theta_j, \phi_j)$. If the angle between $\mathbf{r}$ and $\mathbf{R}_j$ is ω, then we can apply the expansion [23]

$$\frac{1}{|(\mathbf{R}_j - \mathbf{r})|} = \sum_{n=0}^{\infty} \frac{r^n}{R_j^{(n+1)}} P_n^0(\cos \omega), \tag{114}$$

where $R_j > r$ is assumed. P_n^0 are the Legendre polynomials defined as

$$P_n^0(\mu) = \frac{1}{2^n n!} \frac{d^n}{d\mu^n} \left(\mu^2 - 1\right)^n. \tag{115}$$

According to the spherical harmonic addition theorem [24], the Legendre polynomials can also be written as

$$P_n^0(\cos \omega) = \frac{4\pi}{(2n+1)} \sum_{m=-n}^{n} (-1)^m Y_n^{-m}(\theta_j, \phi_j) Y_n^m(\theta, \phi). \tag{116}$$

The spherical harmonics Y_n^m are defined as

$$Y_n^m(\theta, \phi) = (-1)^{(m+|m|)/2} \sqrt{\frac{(2n+1)}{4\pi} \frac{(n-|m|)!}{(n+|m|)!}} P_n^{|m|}(\cos \theta) e^{im\phi}, \tag{117}$$

where, for $m \neq 0$,

$$P_n^{|m|}(\mu) = (1 - \mu^2)^{|m|/2} \frac{d^{|m|}}{d\mu^{|m|}} P_n^0(\mu). \tag{118}$$

Combining Eqs. (113 – 114) and Eq. (116) leads to the expression of the electrostatic potential

$$V(r, \theta, \phi) = \sum_j q_j \sum_{n=0}^{\infty} \frac{r^n}{R_j^{(n+1)}} \sum_{m=-n}^{n} \frac{4\pi}{(2n+1)} (-1)^m Y_n^{-m}(\theta_j, \phi_j) Y_n^m(\theta, \phi). \tag{119}$$

In order to avoid imaginary quantities in the potential, it is convenient to define tesseral harmonics [25] according to

$$\begin{aligned}
Z_{n0} &= Y_n^0 \\
Z_{nm} &= \frac{1}{\sqrt{2}} \left(Y_n^{-m} + (-1)^m Y_n^m\right), \quad m > 0 \\
Z_{nm} &= \frac{i}{\sqrt{2}} \left(Y_n^m - (-1)^m Y_n^{-m}\right), \quad m < 0.
\end{aligned} \tag{120}$$

The Legendre polynomials then take the form

$$P_n^0(\cos\omega) = \frac{4\pi}{(2n+1)} \sum_{m=-n}^{n} Z_{nm}(\theta_j, \phi_j) Z_{nm}(\theta, \phi), \tag{121}$$

and the potential is

$$V(r,\theta,\phi) = \sum_j q_j \sum_{n=0}^{\infty} \frac{r^n}{R_j^{(n+1)}} \sum_{m=-n}^{n} \frac{4\pi}{(2n+1)} Z_{nm}(\theta_j, \phi_j) Z_{nm}(\theta, \phi). \tag{122}$$

We can separate the sum over all surrounding charges into a parameter

$$\gamma_{nm} = \sum_j \frac{4\pi}{(2n+1)} q_j \frac{Z_{nm}(\theta_j, \phi_j)}{R_j^{(n+1)}}, \tag{123}$$

and then rewrite the potential more conveniently as

$$V(r,\theta,\phi) = \sum_{n=0}^{\infty} \sum_{m=-n}^{n} r^n \gamma_{nm} Z_{nm}(\theta, \phi). \tag{124}$$

To use the Stevens' "operator equivalents" method, the tesseral harmonics Z_{nm} (and the potential) are expressed in the Cartesian coordinates

$$V(x,y,z) = \sum_{n=0}^{\infty} \sum_{m=-n}^{n} r^n \gamma_{nm} Z_{nm}(x,y,z). \tag{125}$$

The symmetry of the system determines which terms should be considered in the sum. For example, if the system is symmetric under inversion, then the terms with odd n will all be equal to zero. Some of the more commonly occurring tesseral harmonics are explicitly listed in Table 1. It is clear from the table that all of Z_{nm} have the form

$$Z_{nm} = C \frac{f_{nm}}{r^n}, \tag{126}$$

where C is a constant and $f_{nm}(x,y,z)$ is a function of Cartesian coordinates.

When we consider the Hamiltonian of an ion in a crystal field, we sum up contributions from every optically active electron inside the potential according to

$$\hat{H}_{\mathrm{CF}} = \sum_i q_i V(\hat{x}_i, \hat{y}_i, \hat{z}_i) = -e \sum_i V(\hat{x}_i, \hat{y}_i, \hat{z}_i), \tag{127}$$

where e is the elementary charge, x_i, y_i, and z_i are the coordinates of an i-th electron, and $\hat{x}_i, \hat{y}_i$, and $\hat{z}_i$ are the corresponding position operators. We therefore obtain the Hamiltonian proportional to $\sum_i f_{nm}(\hat{x}_i, \hat{y}_i, \hat{z}_i)$. According to the Stevens' "operator equivalents" method [26], if we evaluate the CF Hamiltonian between states of constant angular momentum J, then there will be a simple relation between the matrix elements of operators $\sum_i f_{nm}(\hat{x}_i, \hat{y}_i, \hat{z}_i)$ and the angular momentum operators $\hat{J}^x$, $\hat{J}^y$, $\hat{J}^z$. Specifically,

$$\left\langle J, m_J' \left| \sum_i f_{nm}(\hat{x}_i, \hat{y}_i, \hat{z}_i) \right| J, m_J \right\rangle \equiv \theta_n \langle r^n \rangle \left\langle J, m_J' \left| O_n^m \right| J, m_J \right\rangle,$$

or

$$\sum_i f_{nm}(x_i, y_i, z_i) \equiv \theta_n \langle r^n \rangle O_n^m, \tag{128}$$

Table 1: Some of the commonly occurring tesseral harmonics Z_{nm} [25] with $r^2 = x^2 + y^2 + z^2$.

$$Z_{20} = \frac{1}{4}\sqrt{\frac{5}{\pi}}\left[\frac{(3z^2 - r^2)}{r^2}\right]$$

$$Z_{22} = \frac{1}{4}\sqrt{\frac{15}{\pi}}\left[\frac{(x^2 - y^2)}{r^2}\right]$$

$$Z_{40} = \frac{3}{16}\sqrt{\frac{1}{\pi}}\left[\frac{(35z^4 - 30z^2r^2 + 3r^4)}{r^4}\right]$$

$$Z_{42} = \frac{3}{8}\sqrt{\frac{5}{\pi}}\left[\frac{(7z^2 - r^2)(x^2 - y^2)}{r^4}\right]$$

$$Z_{43} = \frac{3}{8}\sqrt{\frac{70}{\pi}}\left[\frac{z(x^3 - 3xy^2)}{r^4}\right]$$

$$Z_{4-3} = \frac{3}{8}\sqrt{\frac{70}{\pi}}\left[\frac{z(3x^2y - y^3)}{r^4}\right]$$

$$Z_{44} = \frac{3}{16}\sqrt{\frac{35}{\pi}}\left[\frac{(x^4 - 6x^2y^2 + y^4)}{r^4}\right]$$

$$Z_{4-4} = \frac{3}{16}\sqrt{\frac{35}{\pi}}\left[\frac{4(x^3y - y^3x)}{r^4}\right]$$

$$Z_{60} = \frac{1}{32}\sqrt{\frac{13}{\pi}}\left[\frac{(231z^6 - 315z^4r^2 + 105z^2r^4 - 5r^6)}{r^6}\right]$$

$$Z_{62} = \frac{1}{64}\sqrt{\frac{2730}{\pi}}\left[\frac{(16z^4 - 16(x^2 + y^2)z^2 + (x^2 + y^2)^2)(x^2 - y^2)}{r^6}\right]$$

$$Z_{63} = \frac{1}{32}\sqrt{\frac{2730}{\pi}}\left[\frac{(11z^3 - 3zr^2)(x^3 - 3xy^2)}{r^6}\right]$$

$$Z_{64} = \frac{21}{32}\sqrt{\frac{13}{7\pi}}\left[\frac{(11z^2 - r^2)(x^4 - 6x^2y^2 + y^4)}{r^6}\right]$$

$$Z_{66} = \frac{231}{64}\sqrt{\frac{26}{231\pi}}\left[\frac{(x^6 - 15x^4y^2 + 15x^2y^4 - y^6)}{r^6}\right]$$

where O_n^m are the Stevens' operator equivalents, commonly known as Stevens operators, which are the combinations of operators $\hat{J}^x$, $\hat{J}^y$, $\hat{J}^z$. Some of them are explicitly shown in Table 2. To find the correct form of O_n^m, the position operators in $\sum_i f_{nm}(\hat{x}_i, \hat{y}_i, \hat{z}_i)$ must be replaced by the corresponding angular momentum operators $\hat{J}^x$, $\hat{J}^y$, $\hat{J}^z$, while accounting for their commutation relations. θ_n is a tabulated numerical factor [25], usually called the Stevens factor; it depends on the quantum number n, the angular momentum J, and the number of electrons in the sum of Eq. (127). $\langle r^n \rangle$ is the radial integral of the wave function, which is hard to calculate theoretically, and is usually taken as another numerical parameter.

If we define a parameter

$$A_n^m = -Ce\gamma_{nm}, \tag{129}$$

where C is the same constant as in Eq. (126), then from Eqs. (125 – 128) we obtain the Hamiltonian

$$\hat{H}_{\text{CF}} = \sum_{n=0}^{\infty}\sum_{m=-n}^{n} A_n^m \langle r^n \rangle \theta_n O_n^m. \tag{130}$$

Table 2: Some of the commonly occurring Stevens operators O_n^m [25], where $J_\pm = J_x \pm iJ_y$.

$$O_2^0 = 3J_z^2 - J(J+1)$$

$$O_2^2 = \frac{1}{2}\left[J_+^2 + J_-^2\right]$$

$$O_4^0 = 35J_z^4 - 30J(J+1)J_z^2 + 25J_z^2 - 6J(J+1) + 3J^2(J+1)^2$$

$$O_4^2 = \frac{1}{4}\left[(7J_z^2 - J(J+1) - 5)(J_+^2 + J_-^2) + (J_+^2 + J_-^2)(7J_z^2 - J(J+1) - 5)\right]$$

$$O_4^3 = \frac{1}{4}\left[J_z(J_+^3 + J_-^3) + (J_+^3 + J_-^3)J_z\right]$$

$$O_4^{-3} = \frac{-i}{4}\left[J_z(J_+^3 - J_-^3) + (J_+^3 - J_-^3)J_z\right]$$

$$O_4^4 = \frac{1}{2}\left[J_+^4 + J_-^4\right]$$

$$O_4^{-4} = \frac{-i}{2}\left[J_+^4 - J_-^4\right]$$

$$O_6^0 = 231J_z^6 - 315J(J+1)J_z^4 + 735J_z^4 + 105J^2(J+1)^2J_z^2$$
$$- 525J(J+1)J_z^2 + 294J_z^2 - 5J^3(J+1)^3 + 40J^2(J+1)^2 - 60J(J+1)$$

$$O_6^3 = \frac{1}{4}\left[(11J_z^3 - 3J(J+1)J_z - 59J_z)(J_+^3 + J_-^3)\right.$$
$$\left. + (J_+^3 + J_-^3)(11J_z^3 - 3J(J+1)J_z - 59J_z)\right]$$

$$O_6^4 = \frac{1}{4}\left[(11J_z^2 - J(J+1) - 38)(J_+^4 + J_-^4)\right.$$
$$\left. + (J_+^4 + J_-^4)(11J_z^2 - J(J+1) - 38)\right]$$

$$O_6^6 = \frac{1}{2}\left[J_+^6 + J_-^6\right]$$

Both θ_n and $\langle r^n \rangle$ depend on the shape of the electron cloud around the ion inside the crystal field, while A_n^m describes the crystalline environment created by the surrounding charges. However, all three parameters are often combined into one, which is then numerically fitted to the experimental spectra. Therefore, with the crystal-field parameter $B_n^m = A_n^m \langle r^n \rangle \theta_n$, the Hamiltonian can be expressed in a simple form

$$\hat{H}_{\mathrm{CF}} = \sum_{nm} B_n^m O_n^m. \tag{131}$$

It is possible to determine which terms are equal to zero in Eq. (131) based on the symmetry of the system. The symmetry of the electron cloud of a magnetic ion dictates the symmetry of the Hamiltonian, and so does the distribution of surrounding charges. Thus, if magnetic properties of an ion are determined by the unpaired electrons with the orbital quantum number l, it follows from the Wigner–Eckart theorem [27] that the Stevens factor θ_n is equal to zero, unless $n \leq 2l$ and n is even [28]. For example, only terms $n = 0, 2, 4, 6$ matter for the f-electrons with $l = 3$. Moreover, the Hamiltonian must be invariant under the same symmetry transformations that preserve the system. Therefore, some of the remaining CF parameters B_n^m will also be zero, depending on the symmetry of the surrounding crystal field. The list of non-zero CF parameters up to $n = 6$ for each symmetry group can be found in [29, Table 3].

2.4 Crystal structure and magnetic ordering of $Tb_2Ti_2O_7$

Both Tb^{3+} and Ti^{4+} ions in $Tb_2Ti_2O_7$ individually form a lattice of corner-sharing tetrahedra [30], often referred to as a pyrochlore lattice, shown in Fig. 9. The structure is described by the cubic $Fd\bar{3}m$ space group, and the axes $[111]$, $[\bar{1}\bar{1}1]$, $[1\bar{1}\bar{1}]$, and $[\bar{1}1\bar{1}]$ are all equivalent. The magnetic properties of $Tb_2Ti_2O_7$ are determined by the Tb^{3+} ions, as all the electron shells of Ti^{4+} and O^{2-} are filled and thus are not magnetic.
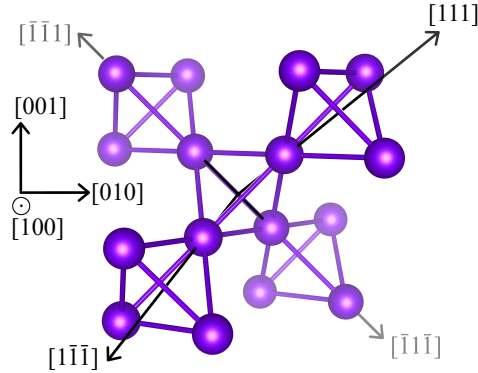
Figure 9: Tb^{3+} ions (spheres) on the pyrochlore lattice of corner-sharing tetrahedra with marked crystallographic axes.

Based on CF calculations [31] and INS studies [32], the strong easy-axis anisotropy confines the magnetic moments **J** of Tb^{3+} ions at low temperatures to point along the cubic $[111]$ axis (or its equivalent), i.e. in our out of the center of a tetrahedron. This effectively makes $Tb_2Ti_2O_7$ an Ising system, where spins can only have two states: pointing parallel or antiparallel to $[111]$. In the presence of the strong easy-axis anisotropy, the macroscopic ordering depends on the sign of the exchange interaction parameter. In case of the ferromagnetic exchange, the ground state of such a system is highly degenerate and features a "two-in-two-out" spin configuration at every tetrahedron (the so-called spin ice), while the antiferromagnetic exchange produces a nondegenerate "all-in/all-out" arrangement [33]. The effective exchange interactions in $Tb_2Ti_2O_7$ are antiferromagnetic, which can be deduced from the negative Curie-Weiss temperature [31]. However, even though $Tb_2Ti_2O_7$ develops short-range correlations below 100 K, it fails to achieve any LRO down to at least 50 mK [34, 35] and, instead, exhibits properties of a spin liquid [36].

One possible explanation why $Tb_2Ti_2O_7$ fails to develop a LRO is that the first excited doublet of the CF levels is separated from the ground state doublet by only 1.5 meV. For comparison, the separation in known spin-ice materials $Ho_2Ti_2O_7$ and $Dy_2Ti_2O_7$ is of the order of 20 meV [37, 38, 39]. The small separation allows for the admixture of the excited and the ground state doublets [40], which effectively turns $Tb_2Ti_2O_7$ into a frustrated Ising ferromagnet with quantum fluctuations transverse to the cubic $[111]$ axis, otherwise referred to as quantum spin ice. It was proposed that the quantum spin ice state would feature a magnetization plateau at 20 mK with magnetic field applied along $[111]$ [41], but so far no experiment has been able to confirm its existence [42, 43, 44, 45, 46].

Additionally, the absence of a LRO could be related to the interplay between magnetic and lattice degrees of freedom. Early studies [47] report large magnetostriction in $Tb_2Ti_2O_7$ at low temperatures. Structural changes upon application of magnetic field have been observed by X-ray diffraction [48] and polarized INS [49]. While magnetostriction can be explained from a single ion perspective, it appears that the situation is more complex,

as the magnetoelastic effects persist in the spin-liquid phase. Remarkably, it has been demonstrated by INS [8, 9] through comparing dispersions of magnetic and phononlike modes in the excitation spectrum that $Tb_2Ti_2O_7$ supports hybrid magnetoelastic excitations. The phenomenon has also been observed in a THz spectroscopy study [10], which addressed the intensity dependence on the incident light polarization of several spectral components in a broad excitation region.

2.5 Vibronic coupling model in $Tb_2Ti_2O_7$

Terbium ions Tb^{3+} in $Tb_2Ti_2O_7$ are in a $^7F_6$ state [31], meaning that there are eight f-electrons, six of which are unpaired. The orbital quantum number of the electron cloud is $L = 3$ and the total spin number from the unpaired electrons is $S = 3$. Therefore, the total angular momentum quantum number is $J = L + S = 6$, according to the LS coupling scheme.

Each terbium ion is surrounded by eight oxygen ions, as shown in Fig. 10, with the local symmetry of the $\bar{3}m$ point group, or D_{3d} in Schoenflies notation. If the cubic $[111]$ axis, which corresponds to the threefold symmetry axis of D_{3d}, is selected to be along z, then the CF Hamiltonian from Eq. (131) that is invariant under all corresponding symmetry transformations is

$$\hat{H}_{CF} = B_2^0 O_2^0 + B_4^0 O_4^0 + B_4^3 O_4^3 + B_6^0 O_6^0 + B_6^3 O_6^3 + B_6^6 O_6^6. \tag{132}$$

The two lowest-energy states of such a system are two doublets with E_g symmetry, separated by 1.5 meV [9].
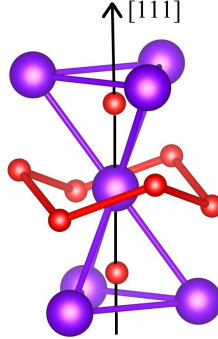
Figure 10: Local D_{3d} oxygen (red) environment around every terbium (purple) ion in $Tb_2Ti_2O_7$, where the cubic $[111]$ axis corresponds the threefold rotation symmetry axis.

When we apply the magnetic field, we introduce a Zeeman interaction term in the Hamiltonian

$$\hat{H}_Z = -g_J \mu_B \mu_0 \mathbf{H} \cdot \mathbf{J}. \tag{133}$$

Under the application of the magnetic field, the magnetic moments of Tb^{3+} ions reorient towards the field. Applying the field along the $[111]$ direction results in a "3-in/1-out, 3-out/1-in" configuration [46] shown in Fig. 11. There are then two types of Tb^{3+} sites in every tetrahedron: site 1 where the magnetic moment is oriented along the field, and three equivalent sites 2, 3, 4 with magnetic moment at an angle relative to the field. The total Hamiltonian for each tetrahedron is

$$\hat{H} = \sum_{k=1}^{4} \hat{H}_{CF}^k + \hat{H}_Z^k, \tag{134}$$

where we assume no interaction between Tb^{3+} ions.
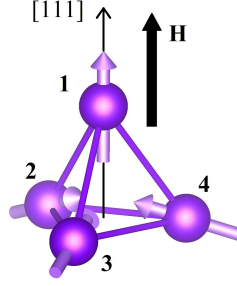
Figure 11: Magnetic moments of Tb^{3+} (shown by arrows) in a tetrahedron at the positions 1, 2, 3, and 4 with the magnetic field applied along the $[111]$ axis.

A low-energy phonon that can couple to the first two doubly degenerate energy levels is an acoustic phonon, which has T_{1u} symmetry of the $m\bar{3}m$ (O_h in Schoenflies notation) point group [9, 10]. The coupling to the acoustic phonon occurs through quadrupolar ($n = 2$) Stevens operators O_2^k, where $k = \pm 1, \pm 2$. Another phonon that can couple to the first excited doublet is an optical phonon of T_{2u} symmetry [10], which couples through a quadrupolar operator O_2^0. Therefore, the symmetry-restricted Hamiltonian associated with the vibronic coupling of phonons to the crystal-field energy levels is [IV]

$$\hat{H}_{\text{vib}} = D_2^0 O_2^0 + D_2^1 (O_2^1 + O_2^{-1}) + D_2^2 (O_2^2 + O_2^{-2}). \tag{135}$$

Note that the operator O_2^0 is already present in the Hamiltonian from Eq. (134), so coupling to the optical phonon does not cause any symmetry breaking of the system, but merely shifts its energy levels. It is the coupling to the acoustic T_{1u} phonon that breaks the symmetry, so that Tb^{3+} ions at the positions 2, 3, and 4 become nonequivalent. As the result, the total Hamiltonian that includes the vibronic coupling,

$$\hat{H} = \sum_{k=1}^{4} \hat{H}_{\text{CF}}^k + \hat{H}_Z^k + \hat{H}_{\text{vib}}^k, \tag{136}$$

will feature different eigenenergies and, hence, new features in the absorption spectrum.

2.6 $Tb_2Ti_2O_7$ results and discussion

A single crystal of $Tb_2Ti_2O_7$ was grown by the floating zone method at ICMMO of the Paris-Saclay University, CNRS. A photo of the sample that was used for the measurement, cut from the larger single crystal, is shown in Fig. 12. We filed down one of the sample surfaces at an angle of $2°$ in order to create a wedge shape and suppress interference fringes in the spectrum. The bottom surface of the sample is perpendicular to the $[111]$ axis, and the average thickness is close to 0.22 mm.

We measured the absorption spectrum using TeslaFIR setup at 3 K and 60 K in the frequency range of 5 – 80 cm^{-1}, with the result shown in Fig. 13. $Tb_2Ti_2O_7$ features very strong absorption above 80 cm^{-1}, with practically no transmitted signal. The signal is already cut off at around 73 cm^{-1} at 60 K, so there is no spectrum plotted in that frequency range. The magnetic field up to 15 T was applied along the $[111]$ crystallographic axis. We observe a strong absorption region ν_1 between 10 cm^{-1} and 20 cm^{-1} in zero field at both temperatures. The absorption gets weaker as the temperature increases. ν_1 shifts
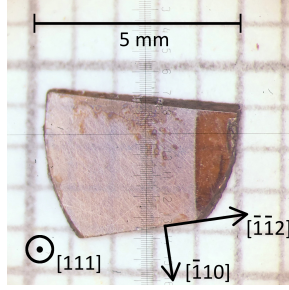
Figure 12: The wedge-shaped $Tb_2Ti_2O_7$ sample used in the measurement. The average sample thickness is close to 0.22 mm, and the bottom surface is perpendicular to the cubic [111] axis.

towards higher energies with the application of the magnetic field, reaching 30 – 40 cm^{-1} in 15 T. Another strong absorption peak ν_2 is visible in the range of 70-80 cm^{-1}, which also seems to shift towards higher energies, as the magnetic field is applied. More peaks are visible above 4 T: two hardening modes ν_3 and ν_4, one softening mode ν_5, and another softening mode ν_6, which is only visible at 60 K. As we see in Fig. 13(a), the difference between two polarizations at 3 K is negligible. There is no visible difference between two polarizations at 60 K, and, therefore, only one of them is plotted.
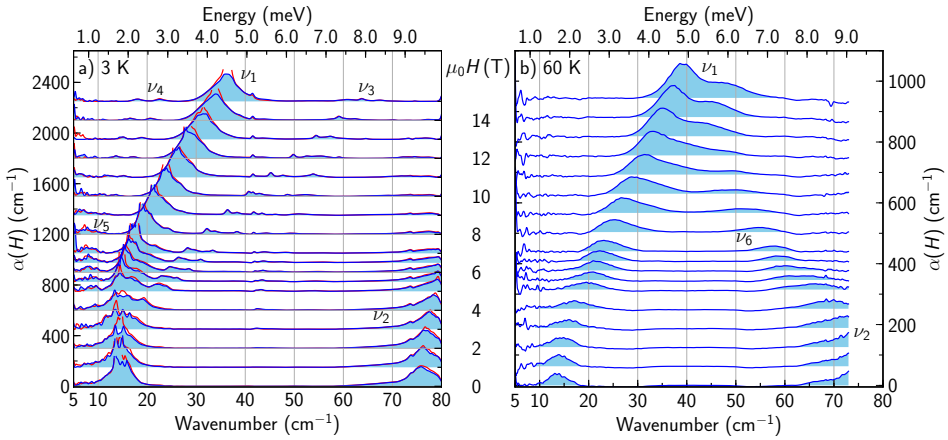
Figure 13: Magnetic-field dependence of the absorption spectrum of $Tb_2Ti_2O_7$ [IV] at a) 3 K and b) 60 K. The visible absorption modes are labeled $\nu_1,...,\nu_6$. Red and blue line colors in panel a) correspond to the two orthogonal incident light polarizations $\mathbf{H}^\omega \parallel [\bar{1}\bar{1}2]$ and $\mathbf{H}^\omega \parallel [\bar{1}10]$, respectively. Only the polarization $\mathbf{H}^\omega \parallel [\bar{1}\bar{1}2]$ is shown in panel b).

We can reproduce the experimental spectrum based on the linear response theory, outlined in Chapter 2.2. First of all, we calculate the absorption coefficient, which is proportional to the imaginary part of the susceptibility from Eq. (112), using the eigenstates of the CF Hamiltonian without any vibronic coupling from Eq. (132). Most of the CF parameters are taken from the literature [9], and only B_2^0 and B_2^4 are adjusted to match the transition frequency at 14 cm^{-1}. The full list of the parameter values is presented in [IV, Table IV]. The theoretically calculated spectrum with the selected linewidth of 2.4 cm^{-1} is shown is Fig. 14. It is clear that the main features of the spectrum, such as the modes $\nu_1,...,\nu_6$ and their field dependence, are very well reproduced. The strongest

absorption mode ν_1 originates from Tb^{3+} ions at positions 2 – 4, which make a transition from the ground CF level to the first excited level. ν_2 is the transition to the second excited
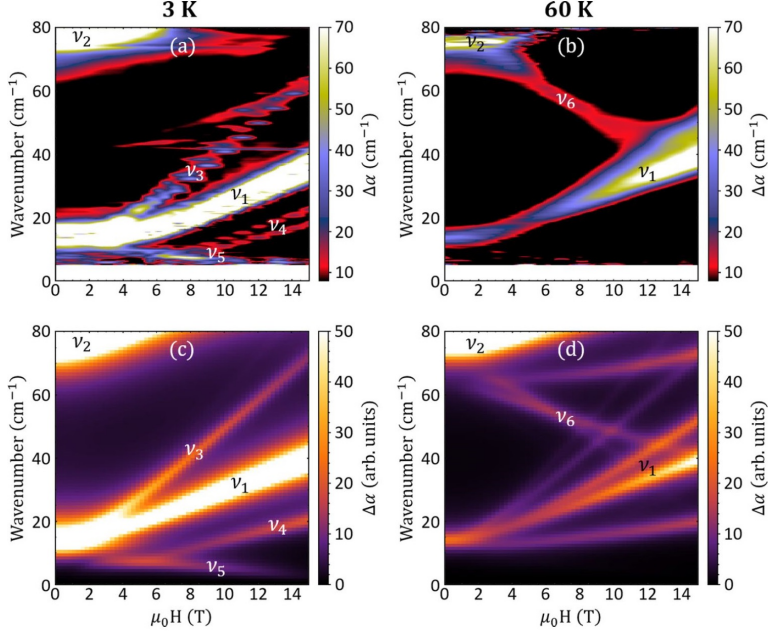
Figure 14: *Theoretically calculated spectrum of $Tb_2Ti_2O_7$ without the vibronic coupling (c)-(d), compared to the measured spectrum (a)-(b). The 3 K result is shown on the left, and the 60 K result is on the right.*

CF level, which includes contributions from all four ions. The weaker modes appear from transitions between different branches of the split CF doublets due to the applied magnetic field, with different contributions from Tb^{3+} ions at position 1 and ions at positions 2 – 4. There are, however, some modes predicted at 60 K, which we do not observe in the measurement. The reason behind their absence could be the combination of their small intensity and weak field dependence, which leads to their disappearance after the baseline subtraction procedure.

To study the vibronic coupling effect on the THz spectrum, we calculate the absorption coefficient using eigenstates of the full Hamiltonian from Eq. (136), which includes $\hat{H}_{vib}$. We use a smaller linewidth of $0.5\,\mathrm{cm}^{-1}$ to better distinguish small features in the spectrum. The contributions from quadrupolar operators $O_2^{\pm1}$ and $O_2^{\pm2}$ are separated by keeping either D_2^1 or D_2^2 equal to zero. The theoretically calculated spectrum with the vibronic coupling through $O_2^{\pm1}$ is shown in Fig. 15, while the effect of $O_2^{\pm2}$ is plotted in Fig. 16. Panels (a) and (b) are same for both figures. With $\hat{H}_{vib}$ added to the total Hamiltonian, Tb^{3+} ions at positions 2 – 4 are no longer equivalent, which results in the splitting of several absorption modes in the spectrum. Specifically, a very clear splitting of the mode ν_4 is visible in Fig. 15 (c) and Fig. 15 (e), and some splitting of the mode ν_3 can be seen in Fig. 15 (c), Fig. 15 (e), Fig. 16 (g), and Fig. 15 (i). $O_2^{\pm1}$ appears to have a larger overall effect on the spectrum than $O_2^{\pm2}$, but the difference is, unfortunately, hard to quantify.

Although the change in the spectrum due to the vibronic coupling is relatively small, we can clearly see from comparison of the calculated absorption spectrum to the experimental result from Fig. 14 (a) that these features are, in fact, present in our measured
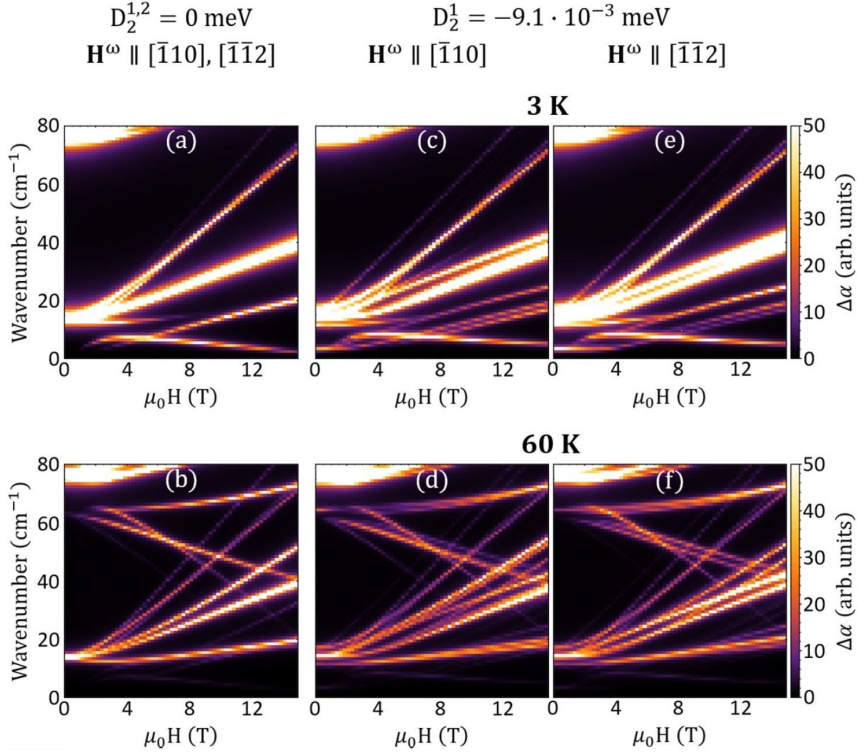
Figure 15: *The effect of the vibronic coupling through O_2^1 on the theoretically calculated spectrum of Tb$_2$Ti$_2$O$_7$ for both polarizations at 3 K (top) and 60 K (bottom) with $D_2^2 = 0$ [IV].*

data. The absorption lines at 60 K are generally wider and less intense, which is probably why the vibronic effect cannot be clearly seen in the measured spectrum at that temperature. The low-temperature THz spectrum of Tb$_2$Ti$_2$O$_7$ is very well reproduces by a rather simple Hamiltonian that includes the CF and Zeeman interaction. However, we can conclude that the spin-lattice effects in the form of the vibronic coupling are clearly present in this material, exhibiting a subtle, but clear influence on the spectrum. The fine features of the spectrum cannot be fully reproduced without including the vibronic coupling. Therefore, we support the evidence that coupling between CF levels with the phonon modes through quadrupolar operators must be considered in the study of the phase diagram of Tb$_2$Ti$_2$O$_7$, and may be important at explaining the lack of magnetic ordering at temperatures below 1 K. Finally, by studying the magnetic-field dependence of the spectrum up to 15 T, we were able to refine the crystal-field parameters in the CF Hamiltonian.

$D_2^{1,2} = 0$ meV
$\mathbf{H}^{\omega} \parallel [\bar{1}10], [\bar{1}\bar{1}2]$

$D_2^2 = -9.1 \cdot 10^{-3}$ meV
$\mathbf{H}^{\omega} \parallel [\bar{1}10]$ $\mathbf{H}^{\omega} \parallel [\bar{1}\bar{1}2]$
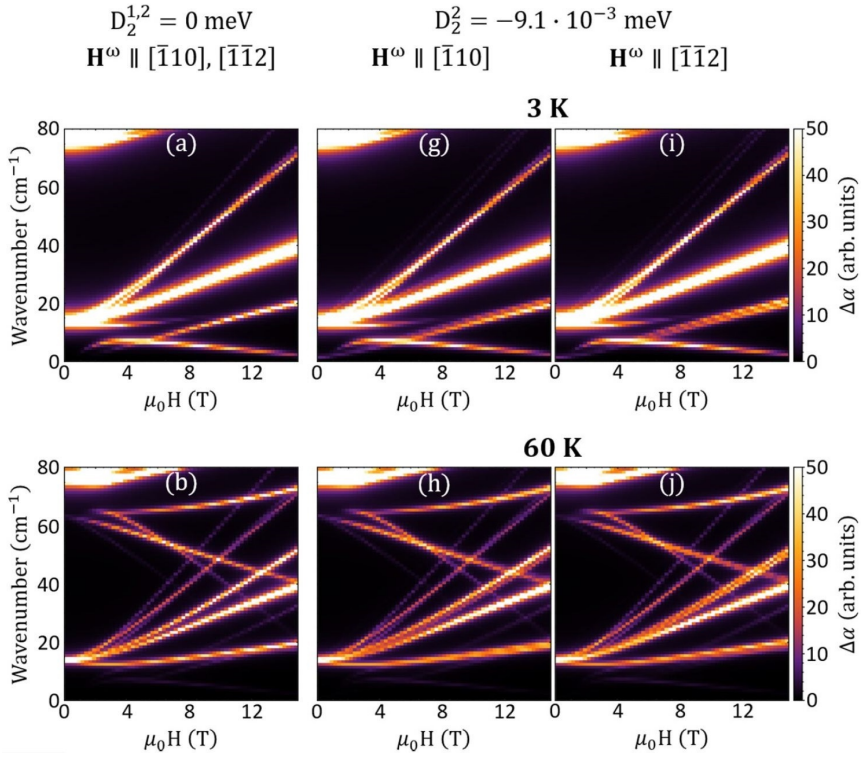
Figure 16: The effect of the vibronic coupling through O_2^2 on the theoretically calculated spectrum of Tb$_2$Ti$_2$O$_7$ for both polarizations at 3 K (top) and 60 K (bottom) with $D_2^1 = 0$ [IV].

3 Spin-wave excitations in $YFeO_3$

Spin-wave (SW) theory often finds its application in the study of multiferroic materials. In these materials, the coupling between electric and magnetic degrees of freedom allow for the magnetic ordering in a material to be tuned by an external electric field, while the electric polarization is sensitive to the applied magnetic field. Multiferroics are important from both scientific and, potentially, industrial point of view, as they may eventually find application in recording devices or spintronics [50, 51]. One class of materials that have been reported to feature multiferroic properties are rare-earth orthoferrites, such as $GdFeO_3$, $Dy_{0.7}Tb_{0.3}FeO_3$, or $Dy_{0.75}Gd_{0.25}FeO_3$ [52, 53]. Using the SW theory, it is possible to model interactions between magnetic moments, and rather precisely describe multiferroic effects.

Here we demonstrate the application of the SW theory to $YFeO_3$, which is not a multiferroic itself, but has the similar orthorhombic structure. It is a relatively simple system with only Fe^{3+} ions carrying a finite magnetic moment. Nevertheless, being able to accurately describe the physics within materials such as $YFeO_3$ is truly important, because they serve as a stepping stone towards understanding isostructural multiferroics. Additionally, $YFeO_3$ features a very high Néel temperature of around $T_N = 644\,K$ [54, 55, 56], which could potentially be key to room-temperature applications. Our aim is to study the magnetic-field dependence of the two low-energy excitations using THz spectroscopy. By applying the magnetic field along all three crystallographic directions and following the magnetic-field dependence of these excitation modes, we are able to determine interaction parameters between spins and the spin configuration of $YFeO_3$ more accurately than it has ever been done before.

3.1 Linear spin-wave theory

3.1.1 Raising and lowering operators of a harmonic oscillator
A classical harmonic oscillator in one dimension is described by the Schrödinger equation

$$\left(\frac{\hat{p}^2}{2m} + \frac{1}{2}m\omega^2\hat{x}^2 \right)\psi = E\psi, \tag{137}$$

with the solution for the energy levels

$$E_n = \hbar\omega\left(n + \frac{1}{2} \right). \tag{138}$$

Here ω is the angular oscillation frequency, m is the mass of a particle, $\hat{p}$ and $\hat{x}$ are the momentum and the position operators, and $n = 0, 1, 2, \ldots$ is called the principle quantum number.

The Hamiltonian can alternatively be expressed as

$$\hat{H} = \frac{\hat{p}^2}{2m} + \frac{1}{2}m\omega^2\hat{x}^2 = \hbar\omega\left[\left(\frac{\hat{x}}{x_0} - i\frac{\hat{p}}{p_0} \right)\left(\frac{\hat{x}}{x_0} + i\frac{\hat{p}}{p_0} \right) + \frac{1}{2} \right], \tag{139}$$

where $x_0 = \sqrt{2\hbar/m\omega}$ and $p_0 = \sqrt{2\hbar m\omega}$ are the characteristic length and momentum for the system. This expression leads to the definition of operators

$$\begin{aligned} \hat{a} &= \frac{\hat{x}}{x_0} + i\frac{\hat{p}}{p_0}, \\ \hat{a}^\dagger &= \frac{\hat{x}}{x_0} - i\frac{\hat{p}}{p_0}, \end{aligned} \tag{140}$$

such that

$$\hat{H} = \hbar\omega\left(\hat{a}^\dagger\hat{a} + \frac{1}{2}\right). \tag{141}$$

Operators $\hat{a}^\dagger$ and $\hat{a}$ satisfy the commutation relations

$$\begin{aligned}
\left[\hat{H}, \hat{a}^\dagger\right] &= \hbar\omega\hat{a}^\dagger \\
\left[\hat{H}, \hat{a}\right] &= -\hbar\omega\hat{a} \\
\left[\hat{a}, \hat{a}^\dagger\right] &= 1
\end{aligned} \tag{142}$$

and define a number operator

$$\hat{a}^\dagger\hat{a} \equiv \hat{N}, \tag{143}$$

which is an observable with its eigenvalue corresponding to the number of particles in a state. If φ_n is an eigenstate of a Hamiltonian $\hat{H}$ such that $\hat{H}\varphi_n = E_n\varphi_n$, and we define a state $\psi = \hat{a}^\dagger\varphi_n$, then acting on that state with the Hamiltonian leads to

$$\begin{aligned}
\hat{H}(\hat{a}^\dagger\varphi_n) &= \left(\left[\hat{H}, \hat{a}^\dagger\right] + \hat{a}^\dagger\hat{H}\right)\varphi_n = \left(\hbar\omega\hat{a}^\dagger + \hat{a}^\dagger\hat{H}\right)\varphi_n \\
&= (\hbar\omega + E_n)\hat{a}^\dagger\varphi_n = (E_n + \hbar\omega)\psi.
\end{aligned} \tag{144}$$

For a state $\psi = \hat{a}\varphi_n$ we similarly get

$$\hat{H}\psi = \hat{H}\hat{a}\varphi_n = ([\hat{H}, \hat{a}] + \hat{a}\hat{H})\varphi_n = (-\hbar\omega + E_n)\hat{a}\varphi_n = (E_n - \hbar\omega)\psi. \tag{145}$$

The energy of the final state is either raised or lowered by $\hbar\omega$ with respect to E_n, which is why $\hat{a}^\dagger$ and $\hat{a}$ are called the raising and the lowering operators. They can also be called the creation and the annihilation operators, as they create or annihilate a quantum of energy.

3.1.2 Spin raising and lowering operators

Given hermitian spin operators $\hat{S}^x$, $\hat{S}^y$, and $\hat{S}^z$, we can define operators

$$\begin{aligned}
\hat{S}^+ &= \hat{S}^x + i\hat{S}^y \\
\hat{S}^- &= \hat{S}^x - i\hat{S}^y
\end{aligned} \tag{146}$$

that satisfy the commutation relations

$$\begin{aligned}
\left[\hat{S}^z, \hat{S}^+\right] &= \hat{S}^+ \\
\left[\hat{S}^z, \hat{S}^-\right] &= -\hat{S}^-.
\end{aligned} \tag{147}$$

The operators are called spin raising and lowering operators, as they increase or decrease the spin projection quantum number m_s by 1. We can demonstrate this effect by acting with $\hat{S}^z$ on a state $\hat{S}^+\varphi_{m_s}$, which is created from an eigenstate of $\hat{S}^z$ that satisfies $\hat{S}^z\varphi_{m_s} = m_s\varphi_{m_s}$, and using the commutation relation above,

$$\hat{S}^z\hat{S}^+\varphi_{m_s} = (\hat{S}^+\hat{S}^z + \hat{S}^+)\varphi_{m_s} = (m_s + 1)\hat{S}^+\varphi_{m_s}. \tag{148}$$

Similarly, considering a state $\hat{S}^-\varphi_{m_s}$, we find

$$\hat{S}^z\hat{S}^-\varphi_{m_s} = (\hat{S}^-\hat{S}^z - \hat{S}^-)\varphi_{m_s} = (m_s - 1)\hat{S}^-\varphi_{m_s}. \tag{149}$$

3.1.3 Holstein-Primakoff approach

The linear SW theory is based on the technique introduced by Holstein and Primakoff [57], which describes the spin waves (magnons) as independent harmonic oscillators. According to this technique, spin operators for a site j can be expressed through $\hat{a}^\dagger$ and $\hat{a}$, which now represent the magnon creation and annihilation operators,

$$\hat{S}_j^+ = \sqrt{2S}\sqrt{1 - \frac{\hat{a}_j^\dagger \hat{a}_j}{2S}}\,\hat{a}_j$$

$$\hat{S}_j^- = \sqrt{2S}\hat{a}_j^\dagger \sqrt{1 - \frac{\hat{a}_j^\dagger \hat{a}_j}{2S}}$$

$$\hat{S}_j^z = \left(S - \hat{a}_j^\dagger \hat{a}_j\right).$$

$$(150)$$

Operators $\hat{a}^\dagger$ and $\hat{a}$ satisfy the commutation relation

$$\left[\hat{a}_j, \hat{a}_k^\dagger\right] = \delta_{jk}.$$

$$(151)$$

We can show that the commutation relations from Eq. (147) still hold, as

$$\left[\hat{S}_j^z, \hat{S}_j^+\right] = \left[S - \hat{a}_j^\dagger \hat{a}_j, \sqrt{2S}\sqrt{1 - \frac{\hat{a}_j^\dagger \hat{a}_j}{2S}}\,\hat{a}_j\right] = -\left[\hat{a}_j^\dagger \hat{a}_j, \left(\sqrt{2S - \hat{a}_j^\dagger \hat{a}_j}\right)\hat{a}_j\right]$$

$$= \left(\sqrt{2S - \hat{a}_j^\dagger \hat{a}_j}\right)\hat{a}_j \hat{a}_j^\dagger \hat{a}_j - \hat{a}_j^\dagger \hat{a}_j \left(\sqrt{2S - \hat{a}_j^\dagger \hat{a}_j}\right)\hat{a}_j$$

$$= \left(\sqrt{2S - \hat{a}_j^\dagger \hat{a}_j}\right)\hat{a}_j \hat{a}_j^\dagger \hat{a}_j - \left(\sqrt{2S - \hat{a}_j^\dagger \hat{a}_j}\right)\hat{a}_j^\dagger \hat{a}_j \hat{a}_j$$

$$\quad - \hat{a}_j^\dagger \hat{a}_j \left(\sqrt{2S - \hat{a}_j^\dagger \hat{a}_j}\right)\hat{a}_j + \left(\sqrt{2S - \hat{a}_j^\dagger \hat{a}_j}\right)\hat{a}_j^\dagger \hat{a}_j \hat{a}_j$$

$$= \left(\sqrt{2S - \hat{a}_j^\dagger \hat{a}_j}\right)\left[\hat{a}_j, \hat{a}_j^\dagger \hat{a}_j\right] - \left[\hat{a}_j^\dagger \hat{a}_j, \sqrt{2S - \hat{a}_j^\dagger \hat{a}_j}\right]\hat{a}_j.$$

$$(152)$$

Knowing that $\left[\hat{a}_j^\dagger \hat{a}_j, \sqrt{2S - \hat{a}_j^\dagger \hat{a}_j}\right] = 0$, and also that

$$\left[\hat{a}_j, \hat{a}_j^\dagger \hat{a}_j\right] = \hat{a}_j \hat{a}_j^\dagger \hat{a}_j - \hat{a}_j^\dagger \hat{a}_j \hat{a}_j$$

$$= \left[\hat{a}_j, \hat{a}_j^\dagger\right]\hat{a}_j = \hat{a}_j$$

$$(153)$$

according to Eq. (151), we find

$$\left[\hat{S}_j^z, \hat{S}_j^+\right] = \left(\sqrt{2S - \hat{a}_j^\dagger \hat{a}_j}\right)\hat{a}_j = \hat{S}_j^+.$$

$$(154)$$

The second commutation relation $\left[\hat{S}^z, \hat{S}^-\right] = -\hat{S}^-$ is proven in a similar way.

Since magnons are collective excitations that occur in coupled spin systems, it is convenient to define Fourier transforms for the raising and lowering operators of a harmonic oscillator

$$\hat{a}_{\mathbf{q}}^\dagger = \frac{1}{\sqrt{N}}\sum_j e^{-i\mathbf{q}\cdot\mathbf{R}_j}\hat{a}_j^\dagger$$

$$\hat{a}_{\mathbf{q}} = \frac{1}{\sqrt{N}}\sum_j e^{i\mathbf{q}\cdot\mathbf{R}_j}\hat{a}_j,$$

$$(155)$$

where the sum is taken over $\mathbf{R}_j$, which is the location of the j-th site, and N is the total number of spins in the system. In this case, $\hat{a}_{\mathbf{q}}^\dagger$ and $\hat{a}_{\mathbf{q}}$ are the creation and annihilation operators of a magnon with a given wavevector $\mathbf{q}$. It is possible to show that in a crystal with a periodic arrangement of spins [58]

$$\frac{1}{N}\sum_j e^{i(\mathbf{q}-\mathbf{q}')\cdot\mathbf{R}_j} = \delta_{\mathbf{q}\mathbf{q}'}.\tag{156}$$

Therefore, in a periodic crystal the magnon creation and annihilation operators satisfy the commutation relation

$$\begin{aligned}\left[\hat{a}_{\mathbf{q}}, \hat{a}_{\mathbf{q}'}^\dagger\right] &= \frac{1}{N}\sum_{j,k} e^{-i\mathbf{q}\cdot\mathbf{R}_j} e^{i\mathbf{q}'\cdot\mathbf{R}_l} \left[\hat{a}_j, \hat{a}_k^\dagger\right] = \frac{1}{N}\sum_{j,k} e^{-i\mathbf{q}\cdot\mathbf{R}_j} e^{i\mathbf{q}'\cdot\mathbf{R}_l} \delta_{jk}\\ &= \frac{1}{N}\sum_j e^{i(\mathbf{q}'-\mathbf{q})\cdot\mathbf{R}_j} = \delta_{\mathbf{q}\mathbf{q}'}.\end{aligned}\tag{157}$$

The inverse Fourier transforms of the two operators are

$$\begin{aligned}\hat{a}_j^\dagger &= \frac{1}{\sqrt{N}}\sum_{\mathbf{q}} e^{-i\mathbf{q}\cdot\mathbf{R}_j}\hat{a}_{\mathbf{q}}^\dagger\\ \hat{a}_j &= \frac{1}{\sqrt{N}}\sum_{\mathbf{q}} e^{i\mathbf{q}\cdot\mathbf{R}_j}\hat{a}_{\mathbf{q}}.\end{aligned}\tag{158}$$

Substituting the spin operators from Eq. (150) into any Hamiltonian results in a rather complex expression that requires a number of approximations to solve. Holstein and Primakoff [57] suggested the following:

1. Replace the square root in Eq. (150) by 1 according to

$$\sqrt{1 - \frac{\hat{a}_j^\dagger \hat{a}_j}{2S}} \approx 1.\tag{159}$$

2. Leave out the terms proportional to $\hat{a}_j^\dagger \hat{a}_j \hat{a}_k^\dagger \hat{a}_k$.

3. Leave out the terms proportional to $\hat{a}_j^\dagger \hat{a}_j \hat{a}_k^\dagger$.

The first approximation is the so-called quasi-saturation condition, which implies that the number of magnons is much smaller than the total number of spins, $\langle n \rangle = \sum \langle \hat{a}_j^\dagger \hat{a}_j \rangle \ll N$. One should keep in mind that this approximation may introduce a significant error at site j in case of a small S. However, the error in the total energy of the whole sample is small [58], as long as

$$\left\langle \sum_j \sqrt{1 - \frac{\hat{a}_j^\dagger \hat{a}_j}{2S}} \right\rangle \approx N.\tag{160}$$

The second approximation corresponds to the assumption that magnons do not interact with each other, as the terms proportional to $\hat{a}_j^\dagger \hat{a}_j \hat{a}_k^\dagger \hat{a}_k$ describe magnon-magnon interactions [5, 58]. We will utilize the first two approximations when we look into the Hamiltonian of a Heisenberg ferromagnet in Chapter 3.1.4. The third approximation is relevant when we encounter terms such as magnetic dipole-dipole interactions [57], which we will not consider here.

The first approximation leads to the simplification of Eq. (150)

$$\hat{S}_j^+ \approx \sqrt{2S}\hat{a}_j$$
$$\hat{S}_j^- \approx \sqrt{2S}\hat{a}_j^\dagger \tag{161}$$
$$\hat{S}_j^z = \left(S - \hat{a}_j^\dagger \hat{a}_j\right).$$

As the result, inserting Eq. (158) into Eq. (161) allows us to rewrite the spin operators as

$$\hat{S}_j^+ \approx \sqrt{\frac{2S}{N}} \sum_{\mathbf{q}} e^{i\mathbf{q}\cdot\mathbf{R}_j}\hat{a}_{\mathbf{q}}$$

$$\hat{S}_j^- \approx \sqrt{\frac{2S}{N}} \sum_{\mathbf{q}} e^{-i\mathbf{q}\cdot\mathbf{R}_j}\hat{a}_{\mathbf{q}}^\dagger \tag{162}$$

$$\hat{S}_j^z = S - \frac{1}{N} \sum_{\mathbf{q},\mathbf{q}'} e^{-i(\mathbf{q}-\mathbf{q}')\cdot\mathbf{R}_j}\hat{a}_{\mathbf{q}}^\dagger \hat{a}_{\mathbf{q}'}.$$

3.1.4 Magnon dispersion in a Heisenberg ferromagnet

We consider a Heisenberg ferromagnet in an external magnetic field as an example of a coupled spin system. The Hamiltonian is a sum of the Heisenberg exchange term and the Zeeman interaction term

$$\hat{H} = \hat{H}_{\text{ex}} + \hat{H}_Z = -J \sum_{\langle j,k \rangle} \mathbf{S}_j \cdot \mathbf{S}_k - g\mu_B \sum_j \mathbf{B} \cdot \mathbf{S}_j, \tag{163}$$

where $J > 0$ determines the strength of the ferromagnetic exchange interaction and $\langle j,k \rangle$ indicates the summation over nearest-neighbor spins. If we choose the magnetic field direction along **z**, the Hamiltonian can be rewritten as

$$\hat{H} = -J \sum_{\langle j,k \rangle} \left[\frac{1}{2}\left(\hat{S}_j^- \hat{S}_k^+ + \hat{S}_j^+ \hat{S}_k^- \right) + \hat{S}_j^z \hat{S}_k^z \right] - g\mu_B B \sum_j \hat{S}_j^z. \tag{164}$$

Inserting the expressions for the spin operators from Eq. (162) gives

$$\hat{H} = -\frac{JS}{N} \sum_{j,\boldsymbol{\delta}} \sum_{\mathbf{q},\mathbf{q}'} \left[e^{-i(\mathbf{q}-\mathbf{q}')\cdot\mathbf{R}_j} e^{i\mathbf{q}'\cdot\boldsymbol{\delta}}\hat{a}_{\mathbf{q}}^\dagger \hat{a}_{\mathbf{q}'} + e^{i(\mathbf{q}-\mathbf{q}')\cdot\mathbf{R}_j} e^{-i\mathbf{q}'\cdot\boldsymbol{\delta}}\hat{a}_{\mathbf{q}}\hat{a}_{\mathbf{q}'}^\dagger \right.$$

$$\left. - e^{-i(\mathbf{q}-\mathbf{q}')\cdot\mathbf{R}_j}\hat{a}_{\mathbf{q}}^\dagger \hat{a}_{\mathbf{q}'} \left(1 + e^{-i(\mathbf{q}-\mathbf{q}')\cdot\boldsymbol{\delta}} \right) \right] - JNZS^2 \tag{165}$$

$$- g\mu_B BNS + \frac{g\mu_B B}{N} \sum_j \sum_{\mathbf{q},\mathbf{q}'} e^{-i(\mathbf{q}-\mathbf{q}')\cdot\mathbf{R}_j}\hat{a}_{\mathbf{q}}^\dagger \hat{a}_{\mathbf{q}'},$$

where Z is the number of nearest neighbors at every spin site, and the higher-order terms proportional to $\hat{a}_{\mathbf{q}}^\dagger \hat{a}_{\mathbf{q}'} \hat{a}_{\mathbf{q}}^\dagger \hat{a}_{\mathbf{q}'}$ were dropped according to the second approximation in Chapter 3.1.3. We also used the fact that for the nearest neighbors $\mathbf{R}_k = \mathbf{R}_j + \boldsymbol{\delta}$, where $|\boldsymbol{\delta}|$ is the nearest-neighbor distance. The Hamiltonian in Eq. (165) can be simplified to

$$\hat{H} = -JS \sum_{\mathbf{q}} \sum_{\boldsymbol{\delta}} \left(e^{i\mathbf{q}\cdot\boldsymbol{\delta}}\hat{a}_{\mathbf{q}}^\dagger \hat{a}_{\mathbf{q}} + e^{-i\mathbf{q}\cdot\boldsymbol{\delta}}\hat{a}_{\mathbf{q}}\hat{a}_{\mathbf{q}}^\dagger - 2\hat{a}_{\mathbf{q}}^\dagger \hat{a}_{\mathbf{q}} \right) - JNZS^2$$

$$- g\mu_B BNS + g\mu_B B \sum_{\mathbf{q}} \hat{a}_{\mathbf{q}}^\dagger \hat{a}_{\mathbf{q}}. \tag{166}$$

Next, we define a parameter

$$\gamma_{\mathbf{q}} = \frac{1}{Z} \sum_{\boldsymbol{\delta}} e^{i\mathbf{q}\cdot\boldsymbol{\delta}}, \tag{167}$$

which, for a centrosymmetric crystal, is real-valued and satisfies [58, 59]

$$\gamma_{\mathbf{q}} = \gamma_{-\mathbf{q}} \tag{168}$$

and

$$\sum_{\mathbf{q}} \gamma_{\mathbf{q}} = 0. \tag{169}$$

Using Eq. (157) with Eqs. (167) – (168) further simplifies the Hamiltonian to

$$\hat{H} = \sum_{\mathbf{q}} \left[2JSZ(1 - \gamma_{\mathbf{q}}) + g\mu_B B \right] \hat{a}_{\mathbf{q}}^\dagger \hat{a}_{\mathbf{q}} - JNZS^2 - g\mu_B BNS. \tag{170}$$

To find the magnon mode frequencies, we are looking for a Hamiltonian term from Eq. (141) of the form

$$\hat{H}' = \sum_{\mathbf{q}} \hbar\omega_{\mathbf{q}} \hat{a}_{\mathbf{q}}^\dagger \hat{a}_{\mathbf{q}}, \tag{171}$$

which gives us

$$\hbar\omega_{\mathbf{q}} = 2JSZ(1 - \gamma_{\mathbf{q}}) + g\mu_B B. \tag{172}$$

Here $\omega_{\mathbf{q}}$ is the frequency of a single ferromagnetic SW mode, which, in the absence of the external magnetic field, has zero frequency at $\mathbf{q} = 0$ (which corresponds to $\gamma_{\mathbf{q}} = 1$), and then grows linearly with B. The energy dependence on the wavevector $\mathbf{q}$ for a two-dimensional Heisenberg ferromagnet on a square lattice with $S = 1/2$ is shown in Fig. 17. The last two terms in Eq. (170) correspond to the exchange energy of all spins in the system and their interaction with the external magnetic field. In the absence of magnons these
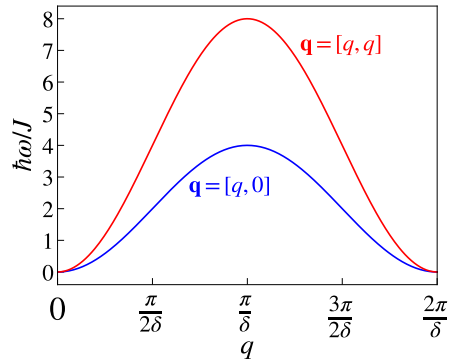
Figure 17: *SW energy dependence on the wave vector $\mathbf{q}$ for a Heisenberg ferromagnet with $S = 1/2$ on a square lattice. The blue line shows the dispersion along one of the edges of the square, while the red line shows the result when the wavevector is pointing along the diagonal. In both cases the result is a cosine function with the periodicity of $2\pi/\delta$, where $\delta = |\boldsymbol{\delta}|$ is the distance between the nearest spins. The energy is shown in units of J.*

two terms combined indicate the total energy of a fully polarized Heisenberg ferromagnet in the magnetic field. If we wish to study higher order processes such as magnon-magnon

interactions, we cannot apply the approximation of Eq. (159). Instead we must expand the spin operators in Eq. (150) and include higher order terms in the Hamiltonian.

Finally, in a crystal with a larger unit cell, the number of modes is equal to the number of spins in that unit cell. Creation and annihilation operators are defined separately for every spin in its local frame, which involves rotations of the coordinate system [5]. Summation in the Hamiltonian then includes summation over the number of possible modes.

3.2 Spin structure of YFeO$_3$

Below T_N, the iron spins $S = 5/2$ in YFeO$_3$ have a G-type antiferromagnetic ordering along the crystallographic a axis, as shown in Fig. 18 (a). Due to the DM interactions, however, the spins are also canted, which results in a weak antiferromagnetism along the b axis, and a weak ferromagnetic moment along c. There are four Fe^{3+} spins in a unit cell of YFeO$_3$,
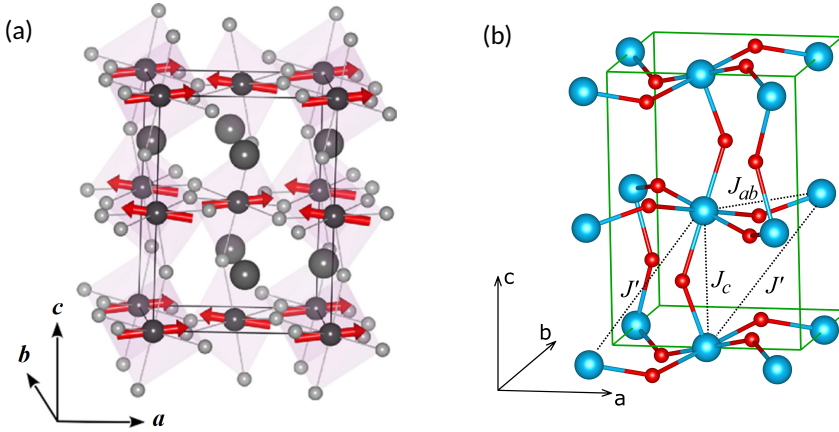
Figure 18: A unit cell of YFeO$_3$. Panel (a) shows the zero-field spin arrangement, with the spins indicated by red arrows [60]. The large dark gray spheres indicate the location of the Y^{3+} ions, and the small light gray spheres correspond to the O^{2-} ions. Panel (b) only shows the location of the magnetic Fe^{3+} ions (blue spheres) and the O^{2-} ions (red spheres) that mediate DM interactions between them [I]. Dotted lines indicate the exchange interaction between the nearest neighbors (J_{ab}, J_c) and the next-nearest neighbors (J'). The unit cell in panel (b) is defined with a $b/2$ shift relatively to panel (a), but the same atoms are shown.

resulting in four spin-wave modes, two of which fall into the THz range with zero-field energies of 1.2 meV (9.8 cm^{-1}) and 2.4 meV (19.3 cm^{-1}). The orientation of each spin is described by two angles ϕ and θ, such that

$$\mathbf{S}_i = S(\sin\theta_i \cos\phi_i,\ \sin\theta_i \sin\phi_i,\ \cos\theta_i). \tag{173}$$

In zero field, the angles satisfy $\theta_1 = \theta_2 = \theta_3 = \theta_4 \equiv \theta$ and $\phi_1 + \pi = -\phi_3 + \pi = -\phi_4 = \phi_2 \equiv \phi$.

The model Hamiltonian for the spins is

$$\hat{H} = -\frac{1}{2}J\sum_{i,j}\mathbf{S}_i \cdot \mathbf{S}_j - \frac{1}{2}J'\sum_{i,j}\mathbf{S}_i \cdot \mathbf{S}_j$$
$$- K_a\sum_i S_{ia}{}^2 - K_c\sum_i S_{ic}{}^2 \qquad (174)$$
$$+ \frac{1}{2}\sum_{i,j}\mathbf{D}_{ij} \cdot (\mathbf{S}_i \times \mathbf{S}_j) - g\mu_B\mu_0\sum_i\mathbf{H} \cdot \mathbf{S}_i,$$

where $J = J_c = J_{ab}$ and J' are the nearest-neighbor and the next-nearest-neighbor exchange interactions, shown in Fig. 18 (b), and the factors of $1/2$ are included to avoid double counting. K_a and K_c are the single-ion anisotropies (SIA) along a and c, $\mathbf{H}$ is the external magnetic field, and $\mathbf{D}_{ij}$ is the DM interaction vector of the form [61]

$$\mathbf{D}_{ij} \propto (\mathbf{R}_i - \mathbf{R}_o) \times (\mathbf{R}_o - \mathbf{R}_j), \qquad (175)$$

where $\mathbf{R}_o$ is the position of O^{2-} ion that couples spins $\mathbf{S}_i$ and $\mathbf{S}_j$. The bonds between Y^{3+} and O^{2-} ions that mediate the DM interactions are shown in Fig. 18 (b). We distinguish two different magnitudes of the DM vectors: the interaction between nearest-neighbor spins in the same ab plane D_{ab}, and the interaction between nearest-neighbors along the c axis D_c.

3.3 YFeO$_3$ results and discussion

Three single-crystal YFeO$_3$ samples, shown in Fig. 19, were prepared at the Center for Correlated Electron Systems of the Institute for Basic Science and at the Department of Physics and Astronomy of the Seoul National University in Korea. Polycrystalline material was prepared by solid-state reaction method, and the single crystals were then grown by the floating zone method, as outlined in [I]. While sample B is not suitable for a Faraday measurement due to its irregular cut, it was still measured in Voigt configuration with $\mathbf{H} \parallel \mathbf{H}^\omega \parallel \mathbf{c}$.
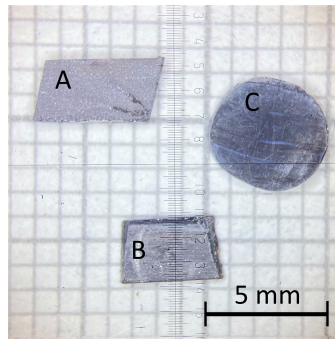
Figure 19: YFeO$_3$ samples with three different cuts, which have the following average thicknesses and orientations: A – 0.86 mm, cut perpendicularly to the a axis; B – 0.54 mm, cut at a 19.75° angle relative to the ac plane, such that the c axis lies in the plane of the cut, C – 0.80 mm, cut perpendicularly to the c axis. All samples are slightly wedge-shaped to avoid interference fringes in the spectrum.

The magnetic-field dependence of the spin-wave absorption coefficient α_{SW}, measured in TeslaFIR at 3 K, is shown in Fig. 20. With the field applied along the a axis, we
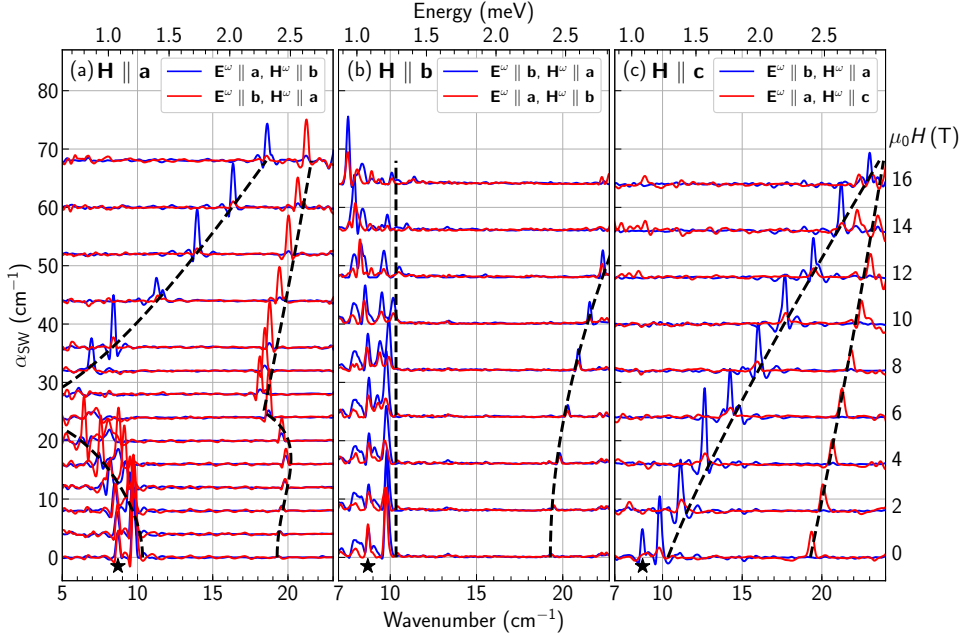
Figure 20: Magnetic-field dependence of the THz absorption spectrum of YFeO$_3$ at $T = 3$ K [I]. The three panels correspond to three different directions of the applied magnetic field. Blue and red spectra correspond to two different polarization of the THz light and the dashed lines show the theoretical fit of the absorption peak positions. The third absorption mode marked by a star is of unknown nature, and is not described by the SW theory.

observe that both modes soften, reach their minimum energies at approximately 6.2 T, and start hardening with the further increase of the magnetic field. This behavior is consistent with the spin-flop transition, which was previously reported above 7 T [62]. We also see a change in the absorption intensity, which increases for one polarization and decreases for the other as the magnetic field goes up, which qualitatively agrees with our theoretical calculations. The picture is quite different for the other two magnetic field directions, where the modes either always harden, or show no change in the energy. There exists a third absorption mode, marked by a star, which is not consistent with the SW theory. It has been previously reported as an "impurity" mode, only present in single crystals grown by the floating zone method [63, 64].

To evaluate the frequencies of the SW modes, we first minimize the energy of the Hamiltonian from Eq. (174), $E = \langle \hat{H} \rangle$, for each direction of the applied magnetic field with respect to eight angles $\{\phi_i, \theta_i\}$. The energy is evaluated assuming that the spins are classical vectors, described by Eq. (173), with the length $S = 5/2$. The SW frequencies are then calculated based on the linear SW theory outlined in Chapter 3.1. The calculated frequencies are compared to the experimentally measured ones, and the loop is repeated with adjusted parameters K_a, K_c, D_{ab}, and D_c until the error is minimized. Note that we are only adjusting the SIA and DM interaction parameter, while the values of J and J' are obtained from an earlier INS work [65] and are kept constant. The exchange interactions are an order of magnitude stronger than the DM interactions, and two to three orders of magnitude stronger than the SIA parameters in YFeO$_3$ [65, 66]. Therefore, J and J' are most accurately determined by studying the dispersion of the higher-energy excitations up to 80 meV (645 cm^{-1}), which is outside of our spectral range. In this study, we focus

exclusively on the two lower-energy excitations, which appear at 9.8 cm^{-1} and 19.3 cm^{-1} in zero field. The positions of the SW absorption modes were simultaneously fitted for all three directions of the external magnetic field, with the result shown by the dashed lines in Fig. 20. The parameters for the spin Hamiltonian in Eq. (174) obtained from the fit are presented in Table 3.

We compare our result with the results from two earlier INS works. Firstly, we observe that the absorption line positions are very well reproduced with the exchange parameters $J = J_c = J_{ab}$ and J' determined by Hahn *et al.* [65], while the parameters used by Park *et al.* [66] result in a worse overall fit. Choosing $J_c = J_{ab}$ is justified because the distances between atoms in the same *ab* plane $\sqrt{a+b}/2 \approx 3.85$ Å is very similar to the distance between two atoms in adjacent planes $c/2 \approx 3.80$ Å. Secondly, we confirm that it is necessary to include the DM interactions between ions in adjacent *ab* planes, as the overall fit improves with nonzero D_c. Finally, we determine all the interaction parameters with greater precision than in the previous works. As a result, we find the angles for the spin configuration in zero field to be $\theta = 0.4966\pi$ and $\phi = 0.0035\pi$, which means that the canting is larger than previously reported by Hahn *et al.* ($\theta = 0.4983\pi$ and $\phi = 0.0010\pi$) and is very close to what was estimated by by Park *et al.* ($\theta = 0.4972\pi$ and $\phi = 0.0032\pi$).

Thus, we have shown that, although INS is currently a perfect technique to quantify the high-energy interactions between spins, THz spectroscopy can be crucial in precisely determining the weaker DM interactions and SIA. Determining these with good accuracy is necessary, as these are the interactions responsible for multiferroic properties of various compounds. We have also been able to model the spin structure and SW excitations in YFeO$_3$, which is a step towards modeling more complex systems, including multiferroics, where Y^{3+} is substituted by magnetic ions. Contrary to the earlier proposed model [65], we determined that there indeed exists a finite DM interaction between neighboring atoms along the c axis, which is important to include for the correct description of YFeO$_3$.

Table 3: Spin Hamiltonian parameter values (meV). The two DM parameters of Hahn et al. [65] are related to D_{ab} as $D_{ab} = \sqrt{D_1^2 + D_2^2}$.

	This work	Hahn *et al.* [65]	Park *et al.* [66]
J_c	-4.77	-4.77	-5.02
J_{ab}	-4.77	-4.77	-4.62
J'	-0.21	-0.21	-0.22
K_a	0.0052	0.0055	0.0091
K_c	0.0044	0.0031	0.0025
$|D_{ab}|$	0.136	0.079	0.121
$|D_c|$	0.189	$-$	0.145

4 Exotic excitations in Ising-chain compounds

The one-dimensional (1D) Ising model is one of the simplest, yet probably one of the most studied models in physics. It provides an insight into a variety of phenomena, such as quantum phase transitions, quantum criticality, or spin dynamics. In reality, however, it is hard to find a material that can effectively be described by the 1D Ising-chain model. Such a material would have to exhibit strong one-dimensionality, which means that the spin chains must be rather well isolated. It is even harder to find a suitable material to study the physics near the QCP, as the exchange interaction must be sufficiently low, so that we can reach the QCP by applying the magnetic field available in laboratory conditions. Two rare examples where it is possible are $CoNb_2O_6$ and $BaCo_2V_2O_8$.

In this study, we measure excitations in both $CoNb_2O_6$ and $BaCo_2V_2O_8$ at different values of the applied magnetic field. By studying the excitation energy dependence on the field, we find a field value that corresponds to the 1D QCP in these compounds. According to the earlier studies [12, 13], the excitation energies then follow specific ratios, which are described by the quantum integrable field theory with the symmetry of the E_8 Lie algebra. Therefore, the goal of this chapter is: 1) to introduce the Ising-chain model and define quantum criticality, 2) to give a basic explanations of what the E_8 Lie algebra is, and what it means for a spectrum to feature E_8 excitations, and 3) to present the THz spectroscopy results of $CoNb_2O_6$ and $BaCo_2V_2O_8$, which provide further evidence of the E_8 symmetry in these systems.

The connection between the E_8 Lie algebra and the perturbed 1D Ising chain near the QCP is, of course, much more intricate than we have the ability to describe here. It is, however, not our goal to study the mathematics of the quantum field theory and asses the relevance of the E_8 Lie algebra in this context. That information can be found in other sources [67, 68].

4.1 The Ising chain model

The Hamiltonian that describes spins in a 1D Ising chain is of the form

$$\hat{H} = -J \sum_{\langle i,j \rangle} S_i^z S_j^z - B_\perp \sum_i S_i^x, \tag{176}$$

where J is the exchange interaction between nearest-neighbor spins that favors their parallel ($J > 0$) or antiparallel ($J < 0$) alignment along the z axis, and B represents the influence of a transverse magnetic field perpendicular to z. For a chain of spins $S = 1/2$, the critical point is at $B_\perp^{c,1D} = J/2$, where no energetically preferred direction for the spins exists. A basic excitation in a 1D Ising chain with no external magnetic field ($B_\perp = 0$) is the creation of a pair of domain walls, called spinons, which can classically be visualized as a spin flip shown in Fig. 21. In a purely 1D system, spinons can freely propagate along the chain, as the configurations featured in Fig. 21 (b – d) are energetically degenerate.

While some of the existing spin systems can relatively accurately be described by the 1D model, they are only quasi-one-dimensional. In reality, the Ising chains are never isolated, but experience some interchain coupling. The weak interchain coupling can be approximated as a local longitudinal magnetic field $B_\parallel$ [13, 69], in which case the Hamiltonian takes the form

$$\hat{H} = -J \sum_{\langle i,j \rangle} S_i^z S_j^z - B_\perp \sum_i S_i^x - B_\parallel \sum_i S_i^z. \tag{177}$$

The ferromagnetic or the antiferromagnetic order in a purely 1D magnet is only present at zero temperature [4], so the interchain coupling stabilizes a three-dimensional (3D)
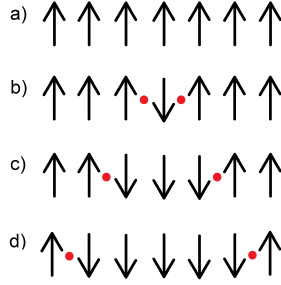
Figure 21: *a) A ferromagnetic 1D spin chain. b) One flipped spin corresponds to the creation of two domain walls called spinons (marked with red dots). c) Three flipped neighboring spins still feature one pair of spinons, now separated from each other. d) Domain walls can be moved further along the chain, which is how spinons are free to propagate without additional energy.*

long-range order for a finite temperature below the critical temperature T_C. If the small longitudinal field acts to preserve the original spin orientation, the QCP is reached at a higher applied field value $B_\perp^{c,3D} > B_\perp^{c,1D}$. The resulting phase diagram is depicted in Fig. 22.
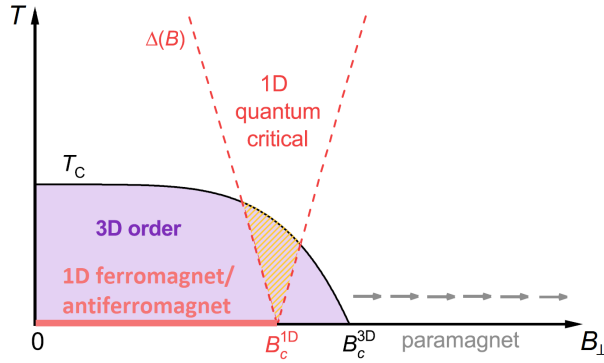
Figure 22: *An illustrative phase diagram of a quasi-one-dimensional Ising chain with $B_\perp^{c,3D} > B_\perp^{c,1D}$ [III].*

With finite interchain coupling, the spinons at $B_\perp = 0$ are no longer free to propagate along the chain. Instead, they are confined into two-spinon bound states by a linear potential $V(x) = \lambda |x|$, where x is the coordinate along the chain, which results in discrete energy levels. The relative motion of spinons is then described by the Schrödinger equation

$$-\frac{\hbar^2}{\mu}\frac{d^2\varphi}{dx^2} + \lambda|x|\varphi = (E - 2E_0)\varphi, \tag{178}$$

where $\lambda = 2B_\parallel \langle S^z \rangle / \tilde{c}$, and $\tilde{c}$ is the lattice constant along the chain [13, 70]. $2E_0$ is the threshold for creating a bound state, above which the excitation energies follow

$$E_j = 2E_0 + z_j \lambda^{2/3} \left(\frac{\hbar^2}{\mu}\right)^{1/3}, \qquad j = 1, 2, 3, ..., \tag{179}$$

where z_j are the negative zeros of the Airy function, $\mathrm{Ai}(z_j) = 0$. Application of a transverse magnetic field $B_\perp$ gradually changes the excitation threshold, as well as the profile of the confining potential [71], which causes changes in the excitation spectrum. As the field approaches the QCP, we expect the emergence of quasiparticles that are described by the E_8 symmetry.

If the 1D Ising chain in a transverse field is near the QCP, it can be described using quantum field theory, which provides an exact solution to the model. When a perturbation in the form of a small longitudinal field is introduced, the model is not exactly solvable any more. However, A. B. Zamolodchikov [12] predicted that in the scaling limit $T \to T_C$ [4], the model is described by a purely elastic scattering matrix of an integrable field theory called "affine Toda field theory". The theory is associated with the E_8 Lie algebra [72] and predicts a spectrum consisting of eight particles with specific mass ratios

$$
\begin{aligned}
m_1 &= m \\
m_2 &= 2m\cos\frac{\pi}{5} = \frac{\sqrt{5}+1}{2}m \approx 1.61803m \\
m_3 &= 2m\cos\frac{\pi}{30} \approx 1.98904m \\
m_4 &= 2m_2\cos\frac{7\pi}{30} \approx 2.40487m \\
m_5 &= 2m_2\cos\frac{2\pi}{15} \approx 2.9563m \\
m_6 &= 2m_2\cos\frac{\pi}{30} \approx 3.21834m \\
m_7 &= 4m_2\cos\frac{\pi}{5}\cos\frac{7\pi}{30} \approx 3.89116m \\
m_8 &= 4m_2\cos\frac{\pi}{5}\cos\frac{2\pi}{15} \approx 4.78339m,
\end{aligned}
\tag{180}
$$

where the first two excitations follow the "golden ratio", $m_2/m_1 = (\sqrt{5}+1)/2$.

Because $CoNb_2O_6$ and $BaCo_2V_2O_8$ are only quasi-one-dimensional, we can model them using the Hamiltonian in Eq. (177), where the interchain interaction is approximated as a small longitudinal field. This longitudinal field acts as the "perturbation" in Zamolodchikov's model, which makes the model applicable in these materials. $B_\perp^{c,3D} > B_\perp^{c,1D}$ also holds for $CoNb_2O_6$ and $BaCo_2V_2O_8$, meaning that we are able to reach the critical field $B_\perp^{c,1D}$ before entering the paramagnetic phase. This condition is necessary to realize the E_8 spectrum, which can only exist in the dashed area shown in Fig. 22.

4.2 E_8 Lie algebra

To give an idea of what it means for a spin system to feature the E_8 spectrum, we review the concept of a Lie algebra. In this chapter, which is based on [73], we define Lie algebras and show how they are described in terms of their root systems, and how root diagrams are constructed. We also demonstrate how a Dynkin diagram fully describes a Lie algebra, and what the Dynkin diagram of the E_8 Lie algebra looks like. Such a diagram can alternatively be represented as a matrix, which is related to the mass ratios we observe in the E_8 spectrum.

4.2.1 Lie groups and Lie algebras

Lie algebras are vector spaces that, as we are going to show, are closely related to Lie groups. Therefore, let us start by defining a group [74]:

1. A group G is a set equipped with a binary operation $\circ$, which takes any two elements of the group and produces another element of the group according to $\circ : G \times G \to G$.

2. There exists an identity element $e \in G$, such that $e \circ f = f \circ e = f, \forall f \in G$.

3. For any element $f \in G$ there exists an inverse $g = f^{-1} \in G$, such that $g \circ f = e$.

4. The binary operation defined above is associative, such that $(f \circ g) \circ h = f \circ (g \circ h)$, $\forall f, g, h \in G$.

A Lie group is, in turn, a group, whose operation $\circ$ is differentiable. In other words, a Lie group is continuous and smooth.

There always exists a vector space $\mathfrak{g}$ that generates the group via a locally invertible exponential map

$$\exp : \mathfrak{g} \to G. \tag{181}$$

$\mathfrak{g}$ is called a Lie algebra, and is defined as a vector space that satisfies the following conditions [75]:

1. It is equipped with a bilinear operation, called the Lie bracket, that preserves the algebra $[\,\cdot\,,\,\cdot\,]: \mathfrak{g} \times \mathfrak{g} \to \mathfrak{g}$.

2. The Lie bracket satisfies $[X, X] = 0, \forall X \in \mathfrak{g}$.

3. The Jacobi identity holds, $[X, [Y, Z]] + [Y, [Z, X]] + [Z, [X, Y]] = 0, \forall X, Y, Z \in \mathfrak{g}$.

Every element of the Lie algebra $X \in \mathfrak{g}$, when exponentiated, generates a unique element of the Lie group [73]

$$\exp(X) = g \in G. \tag{182}$$

The identity element of G is thus generated by the origin (zero) of $\mathfrak{g}$.

A Lie algebra contains all of the necessary information about the Lie group, and it is therefore sufficient to know the Lie algebra to fully describe the corresponding Lie group. In reality, Lie groups usually represent continuous symmetry groups, while elements of Lie algebras correspond to infinitesimal linear transformations. Such transformations can be expressed as matrices acting on a vector space V. According to Ado's theorem [73], any finite-dimensional Lie algebra is linear, which means it is a subalgebra of a general linear algebra $\mathfrak{gl}(V)$, defined over a vector space V. It also means that its elements can be represented with $m \times m$ matrices, where $m = \dim(V)$. The general linear Lie group $GL(V)$ is then a set of invertible $m \times m$ matrices that are generated by the exponential of matrices $X \in \mathfrak{gl}(V)$, which is defined as a Taylor series

$$\exp(X) = 1 + X + \frac{X^2}{2} + \frac{X^3}{6} + \dots . \tag{183}$$

When the elements of a Lie algebra $X, Y \in \mathfrak{g}$ are square matrices, then the Lie bracket that satisfies all of the conditions from the definition of a Lie algebra is the commutator $[X, Y] = XY - YX$.

4.2.2 The adjoint representation

A map φ from one group G to another group H

$$\varphi : G \to H \tag{184}$$

is called a homomorphism if it preserves the structure of a group and satisfies

$$\varphi(g \circ h) = \varphi(g) \circ \varphi(h) \tag{185}$$

for all $g, h \in G$. Since both G and H have their corresponding algebras $\mathfrak{g}$ and $\mathfrak{h}$ that are related to the groups via an exponential map, there must be a corresponding homomorphism,

$$\varphi_* : \mathfrak{g} \to \mathfrak{h}, \tag{186}$$

such that we get a commuting diagram [73]

A representation ρ of a group G is a homomorphism

$$\rho : G \to GL(V). \tag{187}$$

In other words, it is the process of assigning a matrix to each element of the Lie group such that Eq. (185) is satisfied. Since every group has a corresponding Lie algebra, there must exist a representation ρ_* for $\mathfrak{g}$:

$$\rho_* : \mathfrak{g} \to \mathfrak{gl}(V). \tag{188}$$

A particularly important one is the adjoint representation, which we are going to use later in order to define a root system. Since a Lie algebra is a vector space itself, the general linear Lie group can also be defined over that vector space. The adjoint representation of a Lie group is then a homomorphism

$$\mathrm{Ad} : G \to GL(\mathfrak{g}), \tag{189}$$

where $GL(\mathfrak{g})$ is the general linear group over the vector space that is its Lie algebra. The adjoint representation of a Lie algebra Ad_*, more commonly denoted as ad, is similarly

$$\mathrm{ad} : \mathfrak{g} \to \mathfrak{gl}(\mathfrak{g}). \tag{190}$$

The exact form of the adjoint representation of an element $X \in \mathfrak{g}$, applied to an element $Y \in \mathfrak{g}$, is defined as the Lie bracket [75]

$$\mathrm{ad}_X Y = [X, Y]. \tag{191}$$

To prove that ad is a representation, it is possible to show that it satisfies Eq. (185) according to

$$\begin{aligned}
[\mathrm{ad}_X, \mathrm{ad}_Y] Z &= \mathrm{ad}_X \mathrm{ad}_Y Z - \mathrm{ad}_Y \mathrm{ad}_X Z = \mathrm{ad}_X [Y, Z] - \mathrm{ad}_Y [X, Z] \\
&= [X, [Y, Z]] - [Y, [X, Z]] = -[Z, [X, Y]] = [[X, Y], Z] \\
&= \mathrm{ad}_{[X, Y]} Z,
\end{aligned} \tag{192}$$

where we used the Jacobi identity.

4.2.3 Root system

It can be shown that there exist only nine types of so-called simple Lie algebras:

- four classical Lie algebras, $\mathfrak{sl}_{n+1}$, $\mathfrak{so}_{2n+1}$, $\mathfrak{sp}_{2n}$, $\mathfrak{so}_{2n}$, and

- five exceptional Lie algebras, $\mathfrak{g}_2$, $\mathfrak{f}_4$, $\mathfrak{e}_6$, $\mathfrak{e}_7$, $\mathfrak{e}_8$,

where n is an integer called the rank of a Lie algebra. As we are going to demonstrate, n corresponds to the dimension of a root system. Although we do not explicitly indicate it, the implication is that the algebras are defined over complex numbers in all of our examples, such that $\mathfrak{sl}_{n+1} \equiv \mathfrak{sl}_{n+1}\mathbb{C}$.

For any semisimple algebra, i.e. an algebra that is a direct sum of the nine possible simple algebras, there exists a subalgebra $\mathfrak{h} \subset \mathfrak{g}$, which would diagonally act on a vector of a finite-dimensional vector space $v \in V$ according to

$$\rho(H)v = \alpha(H)v \tag{193}$$

for any $H \in \mathfrak{h}$. The eigenvalue $\alpha(H)$ is the weight of the representation $\rho(H)$, and the space V of all possible eigenvectors is the weight space. For the adjoint representation specifically, we can perform a so-called Cartan decomposition into the diagonally acting $\mathfrak{h}$ and weight spaces $\mathfrak{g}_\alpha$

$$\mathfrak{g} = \mathfrak{h} \oplus \left(\bigoplus \mathfrak{g}_\alpha \right), \tag{194}$$

where $\bigoplus$ indicates the summation over all values of α, such that

$$\mathrm{ad}_H X = [H, X] = \alpha(H)X \tag{195}$$

for any $H \in \mathfrak{h}$ and $X \in \mathfrak{g}_\alpha$. The weights of the adjoint representation are called roots, and the weight spaces $\mathfrak{g}_\alpha$ are, accordingly, root spaces. In fact, the root spaces of a semisimple Lie algebra are one-dimensional, meaning that each one of them is only spanned by one eigenvector.

As an example, let us consider a Lie algebra over the complex numbers $\mathfrak{sl}_3$, which consists of 3×3 matrices with a trace equal to zero, and is therefore 8-dimensional. We then know that the diagonalizable subspace $\mathfrak{h} \subset \mathfrak{sl}_3$ must be spanned by traceless matrices of the form

$$H = \begin{pmatrix} a_1 & 0 & 0 \\ 0 & a_2 & 0 \\ 0 & 0 & a_3 \end{pmatrix}, \tag{196}$$

where $a_1 + a_2 + a_3 = 0$. The only matrix X that satisfies Eq. (195) is a matrix of all zeros, except in the position (i, j). We therefore choose matrices E_{ij} with 1 in position (i, j) and zeros everywhere as a basis, in which case

$$\mathrm{ad}_H E_{ij} = [H, E_{ij}] = (a_i - a_j)E_{ij}. \tag{197}$$

Since $a_3 = -a_1 - a_2$ is restricted, we can always express the roots $(a_i - a_j)$ in terms of just two parameters instead of three. This allows us to map all possible roots on a two-dimensional lattice shown in Fig. 23, where the coordinates on the axes k and l correspond to the coefficients for a_1 and a_2 in Eq. (197). For E_{13}, for instance, the equation reads

$$\mathrm{ad}_H E_{13} = \begin{pmatrix} a_1 & 0 & 0 \\ 0 & a_2 & 0 \\ 0 & 0 & a_3 \end{pmatrix} \begin{pmatrix} 0 & 0 & 1 \\ 0 & 0 & 0 \\ 0 & 0 & 0 \end{pmatrix} - \begin{pmatrix} 0 & 0 & 1 \\ 0 & 0 & 0 \\ 0 & 0 & 0 \end{pmatrix} \begin{pmatrix} a_1 & 0 & 0 \\ 0 & a_2 & 0 \\ 0 & 0 & a_3 \end{pmatrix}$$
$$= (a_1 - a_3)E_{13} = (2a_1 + a_2)E_{13}, \tag{198}$$
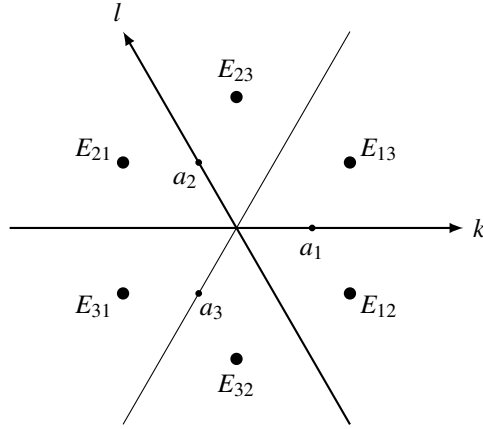
Figure 23: The root system of $\mathfrak{sl}_3$. Large markers correspond to the root spaces E_{ij}, and the small markers indicate where the location of weights a_1, a_2, and a_3 would be.

and the root space spanned by E_{13} is located at $k = 2$, $l = 1$.

A configuration of roots in the Euclidean space $\mathbb{E}$ is called a root system R, and it has to satisfy the following conditions [73]:

1. R is a finite set spanning $\mathbb{E}$.

2. If α is a root, then $-\alpha$ is also a root. However, $k\alpha$ is not a root if $k \neq \pm 1$.

3. If α is a root, then the reflection of any other root in its hyperplane $\alpha^\perp$ is also a root, see Fig. 26.

4. For two roots α, β, the real number

$$n_{\beta\alpha} = 2\frac{(\beta, \alpha)}{(\alpha, \alpha)} \tag{199}$$

is an integer, where $(\,,\,)$ is an inner product defined over the space $\mathbb{E}$.

The inner product in condition 4 is called the *Killing form*, although we will not go into its definition and properties specifically. We would like to mention, however, that we can think of two roots as vectors in $\mathbb{E}$ at an angle ϕ relative to each other. The Killing form is then equivalent to the scalar product of these vectors

$$(\beta, \alpha) \equiv \beta \cdot \alpha = |\beta||\alpha|\cos\phi. \tag{200}$$

If we project vector β onto vector α, as shown in Fig. 24, then the projection β_α is

$$\beta_\alpha = \frac{\beta \cdot \alpha}{|\alpha|}\frac{\alpha}{|\alpha|} = \frac{1}{2}n_{\beta\alpha}\alpha, \tag{201}$$

which is a half-integer times α. Additionally, $n_{\beta\alpha}$ is

$$n_{\beta\alpha} = 2\frac{\beta \cdot \alpha}{\alpha \cdot \alpha} = 2\frac{|\beta|}{|\alpha|}\cos\phi. \tag{202}$$
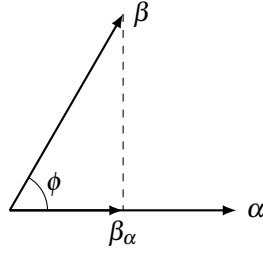
Figure 24: Roots α and β shown as vectors in Euclidean space $\mathbb{E}$, and the projection of β onto α.

Since $n_{\beta\alpha}$ is an integer, and so is $n_{\alpha\beta}$, we know that

$$n_{\beta\alpha}n_{\alpha\beta} = 4\cos^2\phi \tag{203}$$

must be an integer too. It is clear that $\cos^2\phi \neq 1$, because α and β would then be the same root, so we are left with four options: $4\cos^2\phi = 0, 1, 2, 3$. Therefore, there are only seven possible values of the angle between any two roots of a root system:

$$\phi = \frac{\pi}{6}, \frac{\pi}{4}, \frac{\pi}{3}, \frac{\pi}{2}, \frac{2\pi}{3}, \frac{3\pi}{4}, \text{ or } \frac{5\pi}{6}. \tag{204}$$

If we try to sketch a two-dimensional root system, where both conditions from Eq. (201) and Eq. (204) are satisfied, i.e. the angle between any two roots is one of the seven possible angles, and the projection of a root onto any other root is a half-integer of the second root, then we will find that there are only four possible root systems. One of the possibilities turns out to be the aforementioned root system of $\mathfrak{sl}_3$ (that is called A_2), and the other three correspond to Lie algebras $\mathfrak{so}_4$ ($A_1 \times A_1$), $\mathfrak{so}_5$ that is equivalent to $\mathfrak{sp}_4$ (B_2), and the exceptional Lie algebra $\mathfrak{g}_2$ (G_2). All of the possible two-dimensional root systems are shown in Fig. 25.

Turns out that there is an easier way to convey information regarding the lengths of roots and the angles between them than drawing the whole root system. All of that information is contained in what is called a Dynkin diagram.

4.2.4 Dynkin diagram

Now let us come back to the condition 3 of a root system in Chapter 4.2.3, which stated that a reflection in the hyperplane of a root $\alpha^\perp$ maps R onto itself. The consequence of this condition is that we can describe any one of the two-dimensional root systems by just two roots, instead of drawing the whole diagram. For example, the two roots of $\mathfrak{g}_2$ shown in Fig. 26 are sufficient to describe the root system. By condition 3, if we reflect α in the hyperplane $\beta^\perp$, we will generate another root. The same is true for the reflection of β in the hyperplane $\alpha^\perp$. We can then continue the process by reflecting the new roots and eventually arrive to the diagram from Fig. 25 once again. The two roots that are sufficient to describe the whole root system are called the simple roots. There are exactly n simple roots in a Lie algebra, where n is the dimension of the root system (in our examples $n = 2$), which is also called the rank of the Lie algebra.

For any two simple roots it is true that

$$\alpha \cdot \beta \leq 0, \tag{205}$$

which means that they cannot have an acute angle between them. Then, based solely on the number of simple roots in a root system and the angles between them, it is possible to
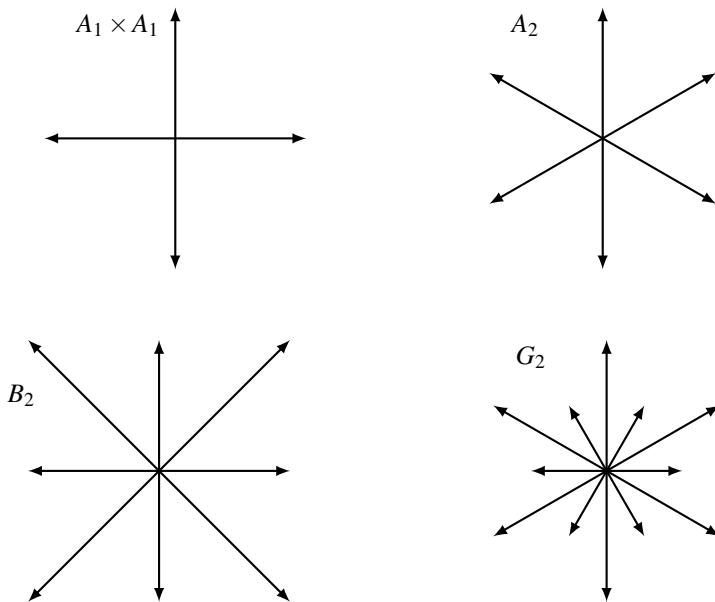
Figure 25: The four existing two-dimensional root systems and their names.
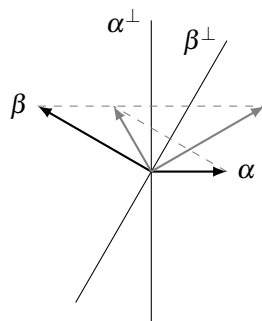
Figure 26: The two simple roots α and β of the Lie algebra $\mathfrak{g}^2$ and their reflections (gray) from the hyperplanes $\alpha^\perp$ and $\beta^\perp$.

construct a Dynkin diagram, which contains all the information regarding the root system. The diagram shows the simple roots as circles and the angle between them is indicated by the number of lines, as shown in Fig. 27, where the arrow indicates the direction from the long to the short root.

Dynkin diagrams are especially useful when dealing with Lie algebras of higher dimensions. The lie algebra $\mathfrak{sl}_7$, for example, has a three-dimensional root system B_3 with eighteen roots, which is quite hard to illustrate. Its Dynkin diagram shown in Fig. 28, however, is rather simple. From that diagram we can read that the first simple root forms an angle of $2\pi/3$ with the second root, as they are connected by one line, and an angle of $\pi/2$ with the third root, as they are not directly connected by any lines. The second root is at an angle of $3\pi/4$ with respect to the third root, and is the longer of the two.

The limited number of possible angles between simple roots results in a number of restrictions on admissible Dynkin diagrams [73]. Consequently, we can list all admissible

$$\phi = \frac{\pi}{2}$$

$$\phi = \frac{2\pi}{3}$$

$$\phi = \frac{3\pi}{4}$$

$$\phi = \frac{5\pi}{6}$$
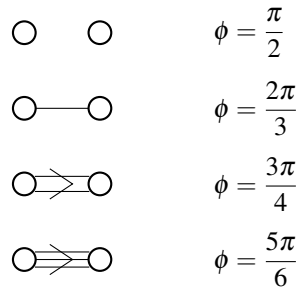
Figure 27: Dynkin diagrams for the Lie algebras of rank 2. The number of lines indicates the angle between two simple roots ϕ, and the arrow shows the direction from a long to a short root.
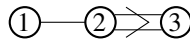
Figure 28: Dynkin diagram of the root system B_3, corresponding to the $\mathfrak{sl}_7$ Lie algebra.

Dynkin diagrams that correspond to irreducible root systems in Fig. 29. By irreducible root systems we mean those that are not a direct sum of simpler root systems. Note that the root system $A_1 \times A_1$ of the Lie algebra $\mathfrak{so}_4$ we mentioned earlier is not irreducible. The first four diagrams in Fig. 29 correspond to the classical Lie algebras or rank n, while the other five belong to the exceptional Lie algebras. We also mentioned that the Lie algebra $\mathfrak{so}_5$ is equivalent to $\mathfrak{sp}_4$. This conclusion can be reached by comparing corresponding Dynkin diagrams in Fig. 29, as B_2 and C_2 would be exactly the same.

4.2.5 E_8 **and its Cartan matrix**

The most complex example of a simple Lie algebra is $\mathfrak{e}_8$. Its root system E_8 is eight-dimensional and contains 240 roots, which makes it impossible to depict fully in two dimensions. It is possible to show a projection of the roots in $\mathbb{R}^8$ onto a plane $\mathbb{R}^2$, which is highly complex, as can be seen in Fig. 31. However, there are only eight simple roots, which can easily be depicted in the Dynkin diagram shown in Fig. 30. The diagram shows that all of the roots that are connected by a line form an angle of $\phi = 2\pi/3$, while the ones that are not connected are at an angle of $\phi = \pi/2$ relative to each other. Thus, root 1 is at an angle of $\phi = 2\pi/3$ relative to root 3, and at an angle of $\phi = \pi/2$ relative to all other roots. Root 4, for instance, forms an angle of $\phi = 2\pi/3$ with roots 2, 3, and 5, and an angle of $\phi = \pi/2$ with the rest of the roots. In fact, using the properties of a root system, it is possible to construct the whole root system with a total of 240 roots from just the Dynking diagram. The root system will, in turn, tell us everything we need to know about the Lie algebra, and, consequently, the 248-dimensional E_8 Lie group.

A Dynkin diagram can alternatively be expressed as a matrix called the Cartan matrix

$$A_{ij} = 2\frac{\alpha_i \cdot \alpha_j}{\alpha_j \cdot \alpha_j}, \tag{206}$$

where α_i and α_j are the simple roots. There diagonal elements of the matrix are always equal to 2, while the rest of the values tell us explicitly what the angles are between simple roots. This way, a Cartan matrix carries all of the information about a Lie algebra in the

A_n		$(n \geq 1)$	$\mathfrak{sl}_{n+1}$
B_n		$(n \geq 2)$	$\mathfrak{so}_{2n+1}$
C_n		$(n \geq 3)$	$\mathfrak{sp}_{2n}$
D_n		$(n \geq 4)$	$\mathfrak{so}_{2n}$
G_2			$\mathfrak{g}_2$
F_4			$\mathfrak{f}_4$
E_6			$\mathfrak{e}_6$
E_7			$\mathfrak{e}_7$
E_8			$\mathfrak{e}_8$
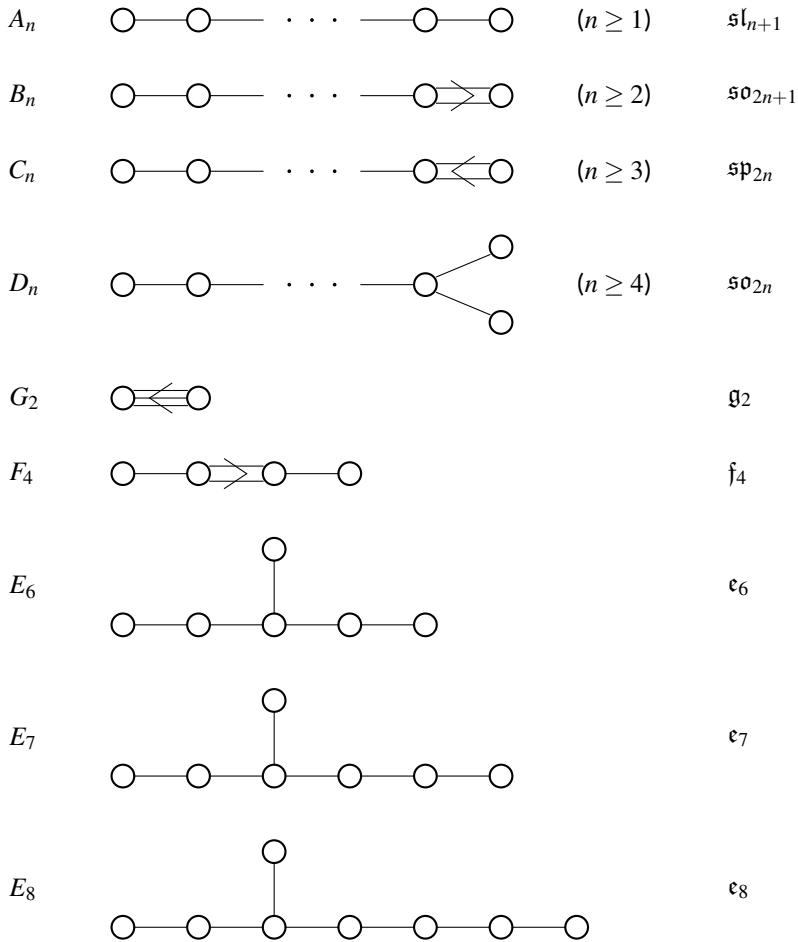
Figure 29: All possible Dynkin diagrams of irreducible root systems and the corresponding Lie algebras.

same way a Dynkin diagram does. For E_8, the matrix is

$$A = \begin{pmatrix} 2 & 0 & -1 & 0 & 0 & 0 & 0 & 0 \\ 0 & 2 & 0 & -1 & 0 & 0 & 0 & 0 \\ -1 & 0 & 2 & -1 & 0 & 0 & 0 & 0 \\ 0 & -1 & -1 & 2 & -1 & 0 & 0 & 0 \\ 0 & 0 & 0 & -1 & 2 & -1 & 0 & 0 \\ 0 & 0 & 0 & 0 & -1 & 2 & -1 & 0 \\ 0 & 0 & 0 & 0 & 0 & -1 & 2 & -1 \\ 0 & 0 & 0 & 0 & 0 & 0 & -1 & 2 \end{pmatrix}. \tag{207}$$

The masses of the E_8 spectrum in Eq. (180) are the real-valued entries of the Perron–Frobenius eigenvector ψ [77], which corresponds to the the lowest eigenvalue a in

$$A\psi = a\psi. \tag{208}$$
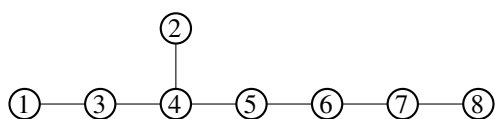
Figure 30: Dynkin diagram of the E_8 root system, showing the eight simple roots of the Lie algebra and the angles between them.
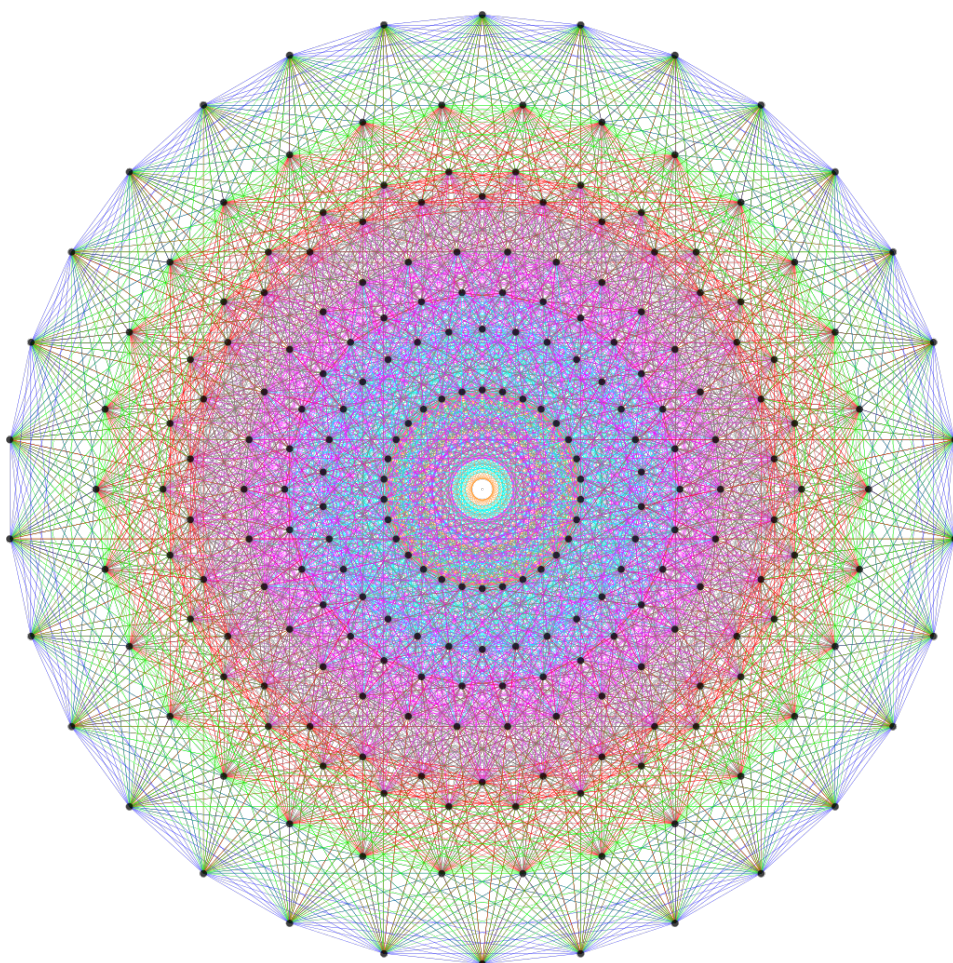
Figure 31: A projection of the eight-dimensional root system E_8 onto a two-dimensional plane [76]. The black vertices correspond to the 240 roots, and the colored edges connect the nearest neighbors in $\mathbb{R}^8$.

4.3 CoNb$_2$O$_6$ results

In CoNb$_2$O$_6$, the Co^{2+} ions are arranged on zigzag chains running along the c axis [78], as shown in Fig. 32. The magnetic easy axis z lies in the ac plane at a 31° angle relative to the c axis [79, 80, 81]. Below $T_C = 2.95$ K [82], the spins order ferromagnetically, and each chain can be modeled with an effective spin-1/2 Hamiltonian in Eq. (176), where z is the magnetic easy axis, and $x \parallel b$ is the hard axis. Due to a finite interchain coupling, CoNb$_2$O$_6$ develops a 3D order below T_C, which can be suppressed by a transverse magnetic field $B_\perp^{c,\mathrm{3D}} = 5.3$ T [83].
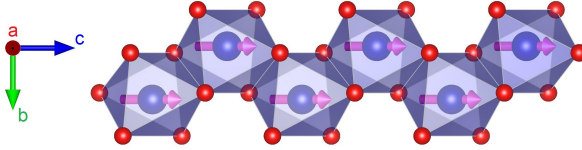
Figure 32: *The crystal structure of CoNb$_2$O$_6$. Co^{2+} ions (blue spheres) are arranged on a zigzag chain running along the c axis, each surrounded by six oxygen ions (red spheres) [13]. The magnetic moments of Co^{2+} (pink arrows) are arranged ferromagnetically in the ac plane.*

The first evidence of the E_8 symmetry in CoNb$_2$O$_6$ was provided by an INS measurement [13], where two excitations were observed with their energies approaching the "golden ratio" at 5 T, which is slightly below $B_\perp^{c,\mathrm{3D}} = 5.3$ T. The higher-energy excitations were not detected, and their absence was explained by the overwhelming multi-particle continuum, which obstructs single-particle excitations above m_2. However, a later numerical study [84] predicted that the single-particle excitations should manifest as sharp peaks and must, therefore, still be visible above a relatively small multi-particle background.

Using the milliK-TeslaFIR spectrometer with the dilution refrigerator, we measured the absorption spectra of CoNb$_2$O$_6$ at 0.25 K in the magnetic field range of 0 – 12 T, applied along the magnetic hard axis. Two single-crystal samples, which are shown in Fig. 33, were grown by the floating zone technique as described in [III] at the University of Cologne, Institute of Physics II. The samples were given a wedge shape with an average thickness of 0.50 mm. They were arranged in a mosaic and measured simultaneously in order to increase the effective surface area and, thus, signal-to-noise ratio. The magnetic-field de-
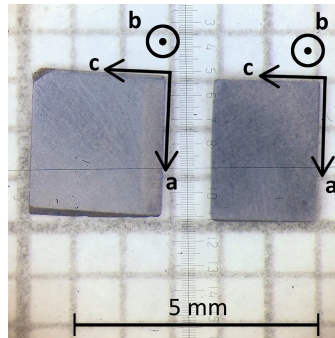
Figure 33: *Two CoNb$_2$O$_6$ samples, both with one surface perpendicular to the b axis, and wedge-shaped with a 2° angle to avoid interference fringes in the spectrum. The samples have a similar average thickness of 0.50 mm.*

pendence of the absorption spectrum is shown in Fig. 34. The lowest-frequency excitation
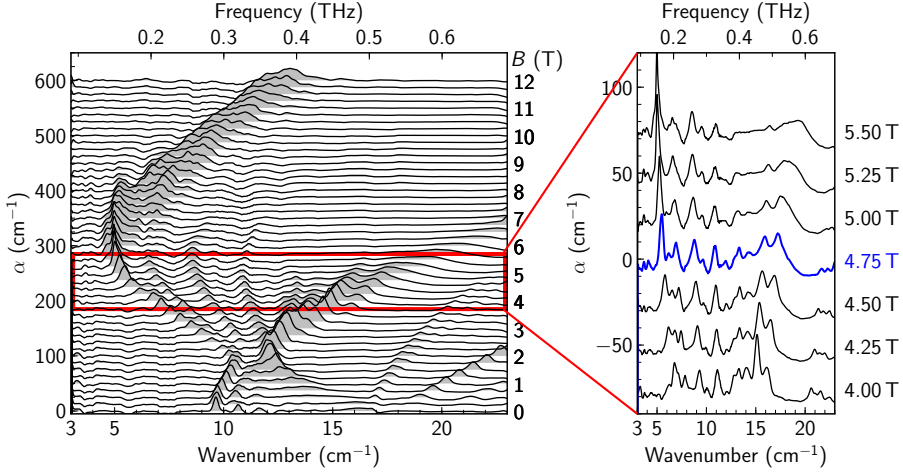
Figure 34: Magnetic-field dependence of the absorption spectrum of CoNb$_2$O$_6$ for **B** ∥ **b** at 0.25 K. The right panel shows only the spectra close to QCP, and the spectrum featuring the E_8 excitations at 4.75 T is plotted in blue.

modes soften and reach their minimum frequency at around 5.5 T, which is in agreement with the critical field of the 3D magnetic order $B_\perp^{c,3D} = 5.3$ T. The critical field of the 1D order $B_\perp^{c,1D} = 4.75$ T was determined by studying the magnetic-field dependence of the E_8 excitations and comparing their energy ratios with respect to m_1 with the theoretically predicted values. Figure 35 shows how the ratios approach the theoretical values close to QCP and almost exactly match them at 4.75 T. This magnetic field value is quite close to the earlier reported 5.0 T [13]. In addition to the two excitations m_1 and m_2, we were also able to detect single-particle excitations up to m_6, as well as the two-particle excitations $m_1 + m_1$ and $m_1 + m_2$, as shown in Fig. 35. The energies of m_3 and $m_1 + m_1$ are practically the same, which makes the two peaks indistinguishable.
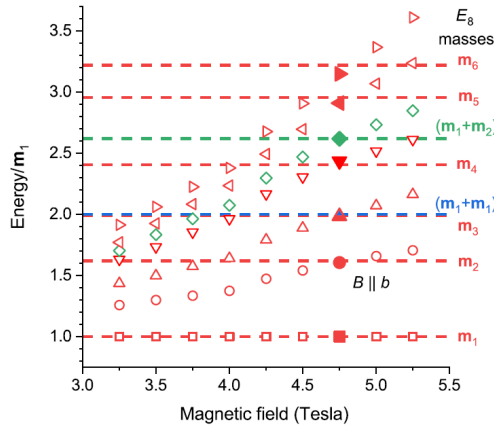
Figure 35: The E_8 spectrum of CoNb$_2$O$_6$ [III]. Measured normalized energies of the E_8 excitations (markers) approach the theoretically predicted values (dashed lines) near the QCP, and match them at 4.75 T (solid markers).

As the result, we report the first experimental observation of the E_8 excitations up to m_6 in CoNb$_2$O$_6$, as well as the two-particle excitations $m_1 + m_1$ and $m_1 + m_2$. We also confirm the numerical predictions that single excitations manifest as sharp peaks and stand out from the relatively weak two-particle-excitation background.

4.4 BaCo$_2$V$_2$O$_8$ results

BaCo$_2$V$_2$O$_8$ features Co^{2+} ions, each surrounded by six oxygens in an octahedral environment, running in screw chains along the crystallographic c axis with a fourfold rotational symmetry [85, 86, 87], as shown in Fig. 36. The arrangement is described by an effective spin-1/2 antiferromagnetic XXZ model [88]. The magnetic moments of Co^{2+} form a 5° angle with the c axis, and the magnetic easy axis z rotates by 90° around c as we move from one ion to the next along the chain [89].
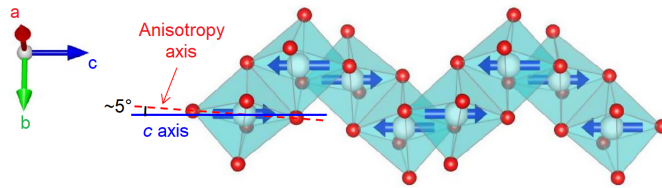
Figure 36: The crystal structure of BaCo$_2$V$_2$O$_8$ [89]. Magnetic moments of Co^{2+} (blue arrows) are antiferromagnetically arranged in a screw chain, each surrounded by six oxygens (red).

Weak interchain coupling induces a 3D antiferromagnetic order with spins aligned along z in BaCo$_2$V$_2$O$_8$ below the Néel temperature $T_N = 5.4$ K [90]. With a transverse magnetic field applied along the crystallographic a (or, equivalently, b) axis, the antiferromagnetic order is suppressed at approximately 10 T [91]. Interestingly, the situation is quite different for the magnetic field applied along the [110] direction, where the antiferromagnetic order is present all the way up to 40 T [92], which is caused by the screw-chain structure of BaCo$_2$V$_2$O$_8$ and the highly anisotropic nature of the effective fields in this material.

A single crystal of BaCo$_2$V$_2$O$_8$ was grown at Institute of Physics II of the University of Cologne by the floating zone method as described in [91]. The sample that was cut out for the measurement, approximately 0.76 mm thick, is shown in Fig. 37. The absorption
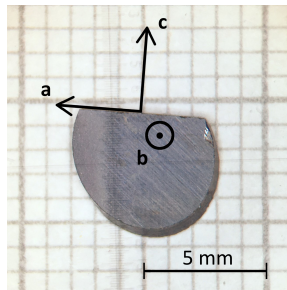
Figure 37: A BaCo$_2$V$_2$O$_8$ sample with the average thickness of 0.76 mm. The sample is wedge-shaped with a 2° angle to avoid interference fringes in the spectrum.

spectra of BaCo$_2$V$_2$O$_8$ were measured in the TeslaFIR setup at 2.7 K with a transverse magnetic field up to 17 T applied along the crystallographic a axis, with the results shown in

Fig. 38. The spectra are measured in the Voigt configuration, with the linearly polarized THz light having the oscillating magnetic field along the applied static field, $\mathbf{h}^\omega \parallel \mathbf{B}_\perp$. We
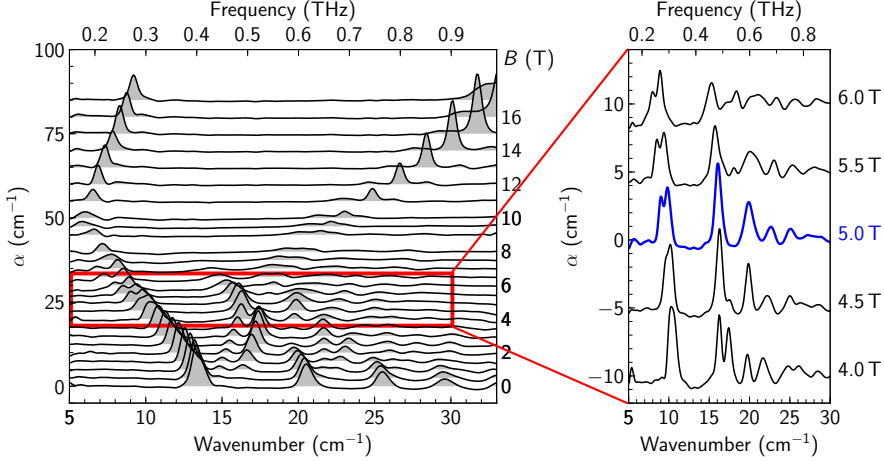
Figure 38: Left panel shows the $BaCo_2V_2O_8$ absorption spectrum dependence on the transverse magnetic field from 0 to 12 T applied along the a axis, measured with the $\mathbf{h}^\omega \parallel \mathbf{B}_\perp \parallel \mathbf{a}$ incident light polarization at 2.7 K. The right panel only shows the spectra close to $B_\perp^{c,1D} = 5.0$ T. The spectrum at 5 T, featuring the E_8 excitations, is shown in blue.

can confirm that the 3D antiferromagnetic ordering is suppressed at approximately 10 T, which is where the lowest-energy excitation reaches its minimum frequency. We determine $B_\perp^{c,1D} = 5.0$ T by following the energy ratios of the excitation peaks and observing how they reach the theoretically predicted values at 5 T, as shown in Fig. 39 (a). A similar critical field value of $B_\perp^{c,1D} = (4.7 \pm 0.3)$ T was recently reported by the nuclear magnetic resonance (NMR) studies of ^{15}V nuclear spin relaxation [93]. Figure 39 (b) shows the frequency-normalized absorption spectrum at the critical field $B_\perp^{c,1D} = 5.0$ T, featuring the single-particle E_8 excitations from m_1 to m_5, as well as the two-particle excitations $m_1 + m_1$ and $m_1 + m_2$. The overall shape of the spectrum matches the shape of the spin dynamic structure factor D_{xx}, shown in 39 (c), which is calculated based on Zamolodchikov's model, as outlined in Supplemental Material of [II]. We also observe that the excitation m_1 is split into two peaks, which can be an indication of a weak orthorhombic anisotropy in the ab plane [II]. The splitting results in each of the two peaks having an area comparable to that of m_2, but when we sum up the two, we get an excitation of higher intensity than m_2 in agreement with the theory. Therefore, we report the first ever experimental observation of the E_8 excitation spectrum in an antiferromagnetic Ising chain, featuring single-particle excitations from m_1 to m_5 and the two-particle excitations $m_1 + m_1$ and $m_1 + m_2$. Studies of the E_8 excitation spectrum in $BaCo_2V_2O_8$ were recently extended by INS spectroscopy and theoretical methods in [93].
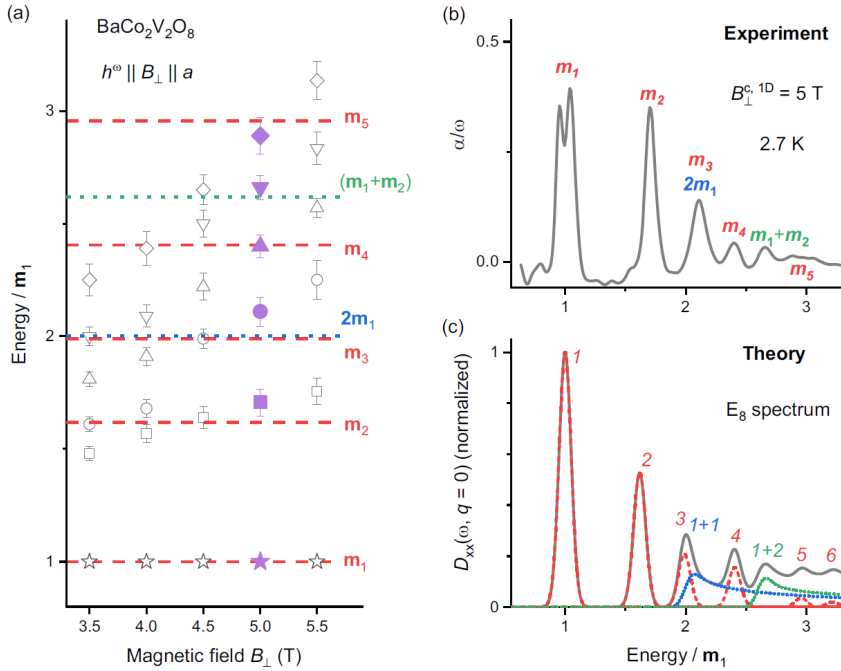
Figure 39: The E_8 spectrum of BaCo$_2$V$_2$O$_8$ compared to the theoretical calculations [II]. (a) Measured excitation energy ratios (symbols) change with the applied magnetic field and simultaneously reach the theoretically predicted values (dashed lines) at $B_\perp^{c,1D} = 5.0\,T$ (solid markers). (b) Measured frequency-normalized absorption spectrum at $B_\perp^{c,1D} = 5.0\,T$ with the indicated E_8 excitations. (c) Theoretically calculated spin dynamic structure factor D_{xx}. The dashed lines show contributions from single-particle excitations (red), $m_1 + m_1$ excitation (blue), and $m_1 + m_2$ excitation (green). The solid line is the sum of all contributions.

Summary

We addressed the question of symmetry and magnetic ordering within three different frameworks:

1. We studied crystal-field excitations of the Tb^{3+} ions in a pyrochlore $Tb_2Ti_2O_7$. By precisely measuring the magnetic-field dependence of these excitations, and comparing the result to the theoretically modeled spectra, we were able to detect entanglement between the ground state and the first excited state via the so-called vibronic coupling. We determined that this dynamic coupling between spin and lattice degrees of freedom lowers the symmetry of the local atomic environment.

2. We utilized the ability of terahertz spectroscopy to track low-energy spin-wave excitations in the applied magnetic field to model the magnetic ordering in an orthoferrite $YFeO_3$. This was done by calculating the excitation frequencies using spin-wave theory and fitting the theoretical values with the experimental data. As the result, we demonstrated the means to accurately quantify "weak" Dzyaloshinskii–Moriya interactions that are responsible for spontaneous symmetry breaking. Moreover, we showed that the correct spin model of $YFeO_3$ must include a Dzyaloshinskii-Moriya interaction between two neighboring Y^{3+} ions along the c axis, which was omitted in one of the earlier proposed models. We also report an overall larger canting of spins in zero field than was previously estimated.

3. We measured the excitation spectra of two quasi-one-dimensional Ising spin chains: $CoNb_2O_6$ and $BaCo_2V_2O_8$. The spectra were measured at different values of the applied transverse field, including those near the quantum critical point. By following the normalized energies of the observed excitations, we were able to determine the value of the one-dimensional critical field for both compounds. At that value, all of the excitations simultaneously reach the theoretically predicted mass ratios from the integrable field theory with the E_8 symmetry. For the first time ever, we were able to observe single-particle excitations of the E_8 spectrum up to m_6 in $CoNb_2O_6$ and up to m_5 in $BaCo_2V_2O_8$, as well as multi-particle excitations. Therefore, we presented strong experimental evidence of the emerging E_8 symmetry near the quantum critical point.

List of Figures

List of Tables

References

[1] J. D. Martin, "What's in a name change?," *Phys. Perspect.*, vol. 17, no. 1, pp. 3–32, 2015.

[2] S. M. Girvin and K. Yang, *Modern Condensed Matter Physics*. Cambridge University Press, 2019.

[3] W. Kohn, "An essay on condensed matter physics in the twentieth century," *Rev. Mod. Phys.*, vol. 71, no. 2, pp. S59–S77, 1999.

[4] S. Sachdev, *Quantum Phase Transitions*. New York: Cambridge University Press, 1999.

[5] R. S. Fishman, J. A. Fernandez-Baca, and T. Rõõm, *Spin-Wave Theory and its Applications to Neutron Scattering and THz Spectroscopy*. 1210 Fifth Avenue, Suite 250, San Rafael, CA, 94901, USA: IOP Concise Physics, Morgan and Claypool Publishers, 2018.

[6] B. L. Winn, C. Broholm, M. Bird, B. C. Breneman, M. Coffey, R. I. Cutler, R. C. Duckworth, R. Erwin, S. Hahn, Y. Hernandez, K. W. Herwig, L. D. Holland, K. M. Lonergan, Z. Melhem, S. J. Minter, C. Nelson, M. P. Paranthaman, J. Pierce, J. Ruff, T. Shen, T. E. Sherline, P. G. Smeibidl, D. Tennant, D. van der Laan, R. J. Wahle, and Y. Zhang, "Ultra-high field magnets for X-ray and neutron scattering using high temperature superconductors," tech. rep., 2017.

[7] J. S. Gardner, M. J. P. Gingras, and J. E. Greedan, "Magnetic pyrochlore oxides," *Rev. Mod. Phys.*, vol. 82, pp. 53–107, 2010.

[8] T. Fennell, M. Kenzelmann, B. Roessli, H. Mutka, J. Ollivier, M. Ruminy, U. Stuhr, O. Zaharko, L. Bovo, A. Cervellino, M. Haas, and R. Cava, "Magnetoelastic excitations in the pyrochlore spin liquid $Tb_2Ti_2O_7$," *Phys. Rev. Lett.*, vol. 112, p. 017203, 2014.

[9] M. Ruminy, E. Pomjakushina, K. Iida, K. Kamazawa, D. T. Adroja, U. Stuhr, and T. Fennell, "Crystal-field parameters of the rare-earth pyrochlores $R_2Ti_2O_7$ ($R =$ Tb, Dy, and Ho)," *Phys. Rev. B*, vol. 94, p. 024430, 2016.

[10] E. Constable, R. Ballou, J. Robert, C. Decorse, J.-B. Brubach, P. Roy, E. Lhotel, L. Del-Rey, V. Simonet, S. Petit, and S. deBrion, "Double vibronic process in the quantum spin ice candidate $Tb_2Ti_2O_7$ revealed by terahertz spectroscopy," *Phys. Rev. B*, vol. 95, p. 020415(R), 2017.

[11] S. Dong, J.-M. Liu, S.-W. Cheong, and Z. Ren, "Multiferroic materials and magnetoelectric physics: symmetry, entanglement, excitation, and topology," *Adv. Phys.*, vol. 64, no. 5-6, pp. 519–626, 2015.

[12] A. B. Zamolodchikov, "Integrals of motion and S-matrix of the (scaled) $T = T_c$ Ising model with magnetic field," *Int. J. Mod. Phys. A*, vol. 04, no. 16, pp. 4235–4248, 1989.

[13] R. Coldea, D. A. Tennant, E. M. Wheeler, E. Wawrzynska, D. Prabhakaran, M. Telling, K. Habicht, P. Smeibidl, and K. Kiefer, "Quantum criticality in an ising chain: Experimental evidence for emergent E_8 symmetry," *Science*, vol. 327, no. 5962, pp. 177–180, 2010.

[14] F. Pobell, *Matter and Methods at Low Temperatures*. Springer-Verlag GmbH, 2007.

[15] J. C. G. Lesurf, *Millimetre-wave Optics, Devices and Systems*. CRC Press, 1990.

[16] H. Kuzmany, *Solid-state spectroscopy*. Springer-Verlag, 2nd ed., 2009.

[17] P. F. Goldsmith, L. T. Greenber, J. E. Harries, G. D. Holah, D. H. Martin, P. L. Richards, and M. V. Schneider, *Infrared and Millimeter Waves: Systems and Components*, vol. 6. Academic Press, 1982.

[18] J. D. Jackson, *Classical Electrodynamics*. John Wiley & Sons, 3rd ed., 1998.

[19] R. Loudon, *The Quantum Theory of Light*. London - New York - Toronto: Oxford University Press, second ed., 1983.

[20] J. Jensen and A. Mackintosh, *Rare Earth Magnetism: Structures and Excitations*. International series of monographs on physics, Clarendon Press, 1991.

[21] C. Cohen-Tannoudji, B. Diu, and F. Laloë, *Quantum Mechanics*. John Wiley & Sons, 2005.

[22] R. Kubo, "Statistical-mechanical theory of irreversible processes. I. General theory and simple applications to magnetic and conduction problems," *J. Phys. Soc. Jpn.*, vol. 12, no. 6, pp. 570–586, 1957.

[23] H. Margenau and G. Murphy, *The Mathematics of Physics and Chemistry*. D. Van Nostrand Company, 1943.

[24] G. Arfken, *Mathematical Methods for Physicists*. Elsevier, 3rd ed., 1985.

[25] M. Hutchings, "Point-charge calculations of energy levels of magnetic ions in crystalline electric fields," *Solid State Phys.*, vol. 16, pp. 227–273, 1964.

[26] K. W. H. Stevens, "Matrix elements and operator equivalents connected with the magnetic properties of rare earth ions," *Proc. Phys. Soc.*, *London*, *Sect. A*, vol. 65, no. 3, pp. 209–215, 1952.

[27] A. R. Edmonds, *Angular Momentum in Quantum Mechanics*. Princeton University Press, 1996.

[28] D. Newman, "Theory of lanthanide crystal fields," *Adv. Phys.*, vol. 20, pp. 197–256, Mar. 1971.

[29] E. Bauer and M. Rotter, *Magnetism of Complex Metallic Alloys: Crystalline Electric Field Effects*. World Scientific, 2009.

[30] S.-W. Han, J. S. Gardner, and C. H. Booth, "Structural properties of the geometrically frustrated pyrochlore $Tb_2Ti_2O_7$," *Phys. Rev. B*, vol. 69, p. 024416, 2004.

[31] M. J. P. Gingras, B. C. den Hertog, M. Faucher, J. S. Gardner, S. R. Dunsiger, L. J. Chang, B. D. Gaulin, N. P. Raju, and J. E. Greedan, "Thermodynamic and single-ion properties of Tb^{3+} within the collective paramagnetic-spin liquid state of the frustrated pyrochlore antiferromagnet $Tb_2Ti_2O_7$," *Phys. Rev. B*, vol. 62, p. 6496, 2000.

[32] M. Kanada, Y. Yasui, M. Ito, H. Harashina, M. Sato, H. Okumura, and K. Kakurai, "Neutron inelastic scattering study on a single crystal of $Tb_2Ti_2O_7$, a magnetically frustrated pyrochlore system," *J. Phys. Soc. Japan*, vol. 68, no. 12, pp. 3802–3805, 1999.

[33] S. T. Bramwell and M. J. Harris, "Frustration in Ising-type spin models on the pyrochlore lattice," *J. Phys.: Condens. Matter*, vol. 10, no. 14, pp. L215–L220, 1998.

[34] J. S. Gardner, S. R. Dunsiger, B. D. Gaulin, M. J. P. Gingras, J. E. Greedan, R. F. Kiefl, M. D. Lumsden, W. A. MacFarlane, N. P. Raju, J. E. Sonier, I. Swainson, and Z. Tun, "Cooperative paramagnetism in the geometrically frustrated pyrochlore antiferromagnet $Tb_2Ti_2O_7$," *Phys. Rev. Lett.*, vol. 82, p. 1012, 1999.

[35] J. S. Gardner, A. Keren, G. Ehlers, C. Stock, E. Segal, J. M. Roper, B. Fåk, M. B. Stone, P. R. Hammar, D. H. Reich, , and B. D. Gaulin, "Dynamic frustrated magnetism in $Tb_2Ti_2O_7$ at 50 mK," *Phys. Rev. B*, vol. 68, p. 180401(R), 2003.

[36] J. P. C. Ruff, B. D. Gaulin, J. P. Castellan, K. C. Rule, J. P. Clancy, J. Rodriguez, and H. A. Dabkowska, "Structural fluctuations in the spin-liquid state of $Tb_2Ti_2O_7$," *Phys. Rev. Lett.*, vol. 99, p. 237202, 2007.

[37] S. Rosenkranz, A. P. Ramirez, A. Hayashi, R. J. Cava, R. Siddharthan, and B. S. Shastry, "Crystal-field interaction in the pyrochlore magnet $Ho_2Ti_2O_7$," *J. Appl. Phys.*, vol. 87, no. 9, pp. 5914–5916, 2000.

[38] Y. Jana, A. Sengupta, and D. Ghosh, "Estimation of single ion anisotropy in pyrochlore $Dy_2Ti_2O_7$, a geometrically frustrated system, using crystal field theory," *J. Magn. Magn. Mater.*, vol. 248, no. 1, pp. 7 – 18, 2002.

[39] A. Bertin, Y. Chapuis, P. D. de Réotier, and A. Yaouanc, "Crystal electric field in the $R_2Ti_2O_7$ pyrochlore compounds," *J. Phys.: Condens. Matter*, vol. 24, no. 25, p. 256003, 2012.

[40] H. R. Molavian, M. J. P. Gingras, , and B. Canals, "Dynamically induced frustration as a route to a quantum spin ice state in $Tb_2Ti_2O_7$ via virtual crystal field excitations and quantum many-body effects," *Phys. Rev. Lett.*, vol. 98, p. 157204, 2007.

[41] H. R. Molavian and M. J. P. Gingras, "Proposal for a [111] magnetization plateau in the spin liquid state of $Tb_2Ti_2O_7$," *J. Phys.: Condens. Matter*, vol. 21, p. 172201, 2009.

[42] S. Legl, C. Krey, S. R. Dunsiger, H. A. Dabkowska, J. A. Rodriguez, G. M. Luke, and C. Pfleiderer, "Vibrating-coil magnetometry of the spin liquid properties of $Tb_2Ti_2O_7$," *Phys. Rev. Lett.*, vol. 109, p. 047201, 2012.

[43] E. Lhotel, C. Paulsen, P. Dalmas de Réotier, A. Yaouanc, C. Marin, and S. Vanishri, "Low-temperature magnetization in geometrically frustrated $Tb_2Ti_2O_7$," *Phys. Rev. B*, vol. 86, p. 020410(R), 2012.

[44] P. J. Baker, M. J. Matthews, S. R. Giblin, P. Schiffer, C. Baines, and D. Prabhakaran, "Unusual field dependence of spin fluctuations on different timescales in $Tb_2Ti_2O_7$," *Phys. Rev. B*, vol. 86, p. 094424, 2012.

[45] L. Yin, J. S. Xia, Y. Takano, N. S. Sullivan, Q. J. Li, and X. F. Sun, "Low-temperature low-field phases of the pyrochlore quantum magnet $Tb_2Ti_2O_7$," *Phys. Rev. Lett.*, vol. 110, p. 137201, 2013.

[46] A. P. Sazonov, A. Gukasov, H. B. Cao, P. Bonville, E. Ressouche, C. Decorse, and I. Mirebeau, "Magnetic structure in the spin liquid $Tb_2Ti_2O_7$ induced by a [111] magnetic field: Search for a magnetization plateau," *Phys. Rev. B*, vol. 88, p. 184428, 2013.

[47] I. V. Aleksandrov, B. V. Lidskii, L. G. Mamsurova, M. G. Neigauz, K. S. Pigal'skiǐ, K. K. Pukhov, N. G. Trusevich, and L. G. Shcherbakova, "Crystal field effects and the nature of the giant magnetostriction in terbium dititanate," *J. Exp. Theor. Phys.*, vol. 62, p. 1287, 1985.

[48] J. P. C. Ruff, Z. Islam, J. P. Clancy, K. A. Ross, H. Nojiri, Y. H. Matsuda, H. A. Dabkowska, A. D. Dabkowski, and B. D. Gaulin, "Magnetoelastics of a spin liquid: X-ray diffraction studies of $Tb_2Ti_2O_7$ in pulsed magnetic fields," *Phys. Rev. Lett.*, vol. 105, p. 077203, 2010.

[49] S. Guitteny, J. Robert, P. Bonville, J. Ollivier, C. Decorse, P. Steffens, M. Boehm, H. Mutka, I. Mirebeau, and S. Petit, "Anisotropic propagating excitations and quadrupolar effects in $Tb_2Ti_2O_7$," *Phys. Rev. Lett.*, vol. 111, p. 087201, 2013.

[50] S. M. Wu, S. A. Cybart, P. Yu, M. D. Rossell, J. X. Zhang, R. Ramesh, and R. C. Dynes, "Reversible electric control of exchange bias in a multiferroic field-effect device," *Nature Mater.*, vol. 9, p. 756, 2010.

[51] C. Binek and B. Doudin, "Magnetoelectronics with magnetoelectrics," *J. Phys.: Condens. Matter*, vol. 17, no. 2, pp. L39–L44, 2005.

[52] M. Tokunaga, Y. Yamasaki, Y. Onose, M. Mochizuki, N. Furukawa, and Y. Tokura, "Novel multiferroic state of $Eu_{1-x}Y_xMnO_3$ in high magnetic fields," *Phys. Rev. Lett.*, vol. 103, no. 18, p. 187202, 2009.

[53] Y. Tokunaga, Y. Taguchi, T. Arima, and Y. Tokura, "Electric-field-induced generation and reversal of ferromagnetic moment in ferrites," *Nat. Phys.*, vol. 8, p. 838, 2012.

[54] V. M. Judin, A. B. Sherman, and I. E. Myl'nikova, "Magnetic properties of $YFeO_3$," *Phys. Lett.*, vol. 22, no. 5, p. 554, 1966.

[55] H. Shen, J. Xu, A. Wu, J. Zhao, and M. Shi, "Magnetic and thermal properties of perovskite $YFeO_3$ single crystals," *Mater. Sci. Eng., B*, vol. 157, no. 1, pp. 77–88, 2009.

[56] D. Treves, "Studies on orthoferrites at the weizmann institute of science," *J. Appl. Phys.*, vol. 36, p. 1033, 1965.

[57] T. Holstein and H. Primakoff, "Field dependence of the intrinsic domain magnetization of a ferromagnet," *Phys. Rev.*, vol. 58, pp. 1098–1113, 1940.

[58] D. D. Stancil and A. Prabhakar, *Spin Waves: Theory and Applications*. Springer, 2009.

[59] R. M. White, *Quantum Theory of Magnetism*. Springer-Verlag Berlin Heidelberg, 2007.

[60] E. Bousquet and A. Cano, "Non-collinear magnetism in multiferroic perovskites," *J. Phys.: Condens. Matter*, vol. 28, no. 123001, p. 28, 2016.

[61] F. Keffer, "Moriya interaction and the problem of spin arrangements in βmns," *Phys. Rev.*, vol. 126, no. 3, p. 896, 1962.

[62] J. Scola, Y. Dumont, N. Keller, M. Vallée, J.-G. Caputo, I. Sheikin, P. Lejay, and A. Pautrat, "Incomplete spin reorientation in yttrium orthoferrite," *Phys. Rev. B*, vol. 84, p. 104429, 2011.

[63] A. M. Balbashov, A. G. Berezin, J. V. Bobryshev, P. J. Marchukov, I. V. Nikolaev, E. G. Rudashevsky, J. Paches, and L. Pům, "Orthogonal magnetic impurity in antiferromagnet YFeO$_3$ single crystal: magnetic resonance and magnetisation measurements," *J. Magn. Magn. Mater.*, vol. 104-107, pp. 1037–1038, 1992.

[64] A. M. Balbashov, G. V. Kozlov, A. A. Mukhin, and A. S. Prokhorov, *Submillimeter spectroscopy of antiferromagnetic dielectrics: Rare-earth orthoferrites*, ch. 2, pp. 56–98. World Scientific, 1995.

[65] S. E. Hahn, A. A. Podlesnyak, G. Ehlers, G. E. Granroth, R. S. Fishman, A. I. Kolesnikov, E. Pomjakushina, and K. Conder, "Inelastic neutron scattering studies of YFeO$_3$," *Phys. Rev. B*, vol. 89, p. 014420, 2014.

[66] K. Park, H. Sim, J. C. Leiner, Y. Yoshida, J. Jeong, S. Yano, J. Gardner, P. Bourges, M. Klicpera, V. Sechovský, M. Boehm, and J.-G. Park, "Low-energy spin dynamics of orthoferrites AFeO$_3$ (A = Y, La, Bi)," *J. Phys.: Condens. Matter*, vol. 30, no. 23, p. 235802, 2018.

[67] D. Borthwick and S. Garibaldi, "Did a 1-dimensional magnet detect a 248-dimensional Lie algebra?," *Not. Amer. Math. Soc.*, vol. 58, pp. 1055–1066, 2011.

[68] M. Oshikawa, "Experimental observations of the universal cascade of bound states in quantum ising chain in a magnetic field and E$_8$ symmetry," *Journal Club for Condensed Matter Physics*, 2020.

[69] S. T. Carr and A. M. Tsvelik, "Spectrum and correlation functions of a quasi-one-dimensional quantum Ising model," *Phys. Rev. Lett.*, vol. 90, p. 177206, 2003.

[70] Z. Wang, M. Schmidt, A. K. Bera, A. T. M. N. Islam, B. Lake, A. Loidl, and J. Deisenhofer, "Spinon confinement in the one-dimensional Ising-like antiferromagnet SrCo$_2$V$_2$O$_8$," *Phys. Rev. B*, vol. 91, p. 140404, Apr 2015.

[71] Z. Wang, J. Wu, S. Xu, W. Yang, C. Wu, A. K. Bera, A. T. M. N. Islam, B. Lake, D. Kamenskyi, P. Gogoi, H. Engelkamp, N. Wang, J. Deisenhofer, and A. Loidl, "From confined spinons to emergent fermions: Observation of elementary magnetic excitations in a transverse-field Ising chain," *Phys. Rev. B*, vol. 94, p. 125130, 2016.

[72] V. Fateev and A. Zamolodchikov, "Conformal field theory and purely elastic S-matrices," *Int. J. Mod. Phys. A*, vol. 05, pp. 1025–1048, 1990.

[73] W. Fulton and J. Harris, *Representation Theory - A First Course*. Springer, 1991.

[74] M. S. Dresselhaus, G. Dresselhaus, and A. Jorio, *Group Theory: Applications to the Physics of Condensed Matter*. Berlin Heidelberg: Springer-Verlag, 2008.

[75] J. E. Humphreys, *Introduction to Lie Algebras and Representation Theory*. Graduate Texts in Mathematics 9, Springer-Verlag New York, 1 ed., 1972.

[76] J. G. Moxness, "3D polytope hulls of E_8 4_{21}, 2_{41}, and 1_{42}," 2020. TheoryOfEverything.org.

[77] G. Mussardo, *Statistical Field Theory: An Introduction to Exactly Solved Models in Statistical Physics*. Oxford Graduate Texts, Oxford University Press, 2009.

[78] T. Hanawa, K. Shinkawa, M. Ishikawa, K. Miyatani, K. Saito, and K. Kohn, "Anisotropic specific heat of $CoNb_2O_6$ in magnetic fields," *J. Phys. Soc. Jpn.*, vol. 63, no. 7, pp. 2706–2715, 1994.

[79] C. Heid, H. Weitzel, P. Burlet, M. Bonnet, W. Gonschorek, T. Vogt, J. Norwig, and H. Fuess, "Magnetic phase diagram of $CoNb_2O_6$: A neutron diffraction study," *Journal of Magnetism and Magnetic Materials*, vol. 151, no. 1, pp. 123–131, 1995.

[80] S. Kobayashi, S. Mitsuda, M. Ishikawa, K. Miyatani, and K. Kohn, "Three-dimensional magnetic ordering in the quasi-one-dimensional ising magnet $CoNb_2O_6$ with partially released geometrical frustration," *Phys. Rev. B*, vol. 60, pp. 3331–3345, 1999.

[81] S. Kobayashi, S. Mitsuda, and K. Prokes, "Low-temperature magnetic phase transitions of the geometrically frustrated isosceles triangular Ising antiferromagnet $CoNb_2O_6$," *Phys. Rev. B*, vol. 63, p. 024415, 2000.

[82] W. Scharf, H. Weitzel, I. Yaeger, I. Maartense, and B. Wanklyn, "Magnetic structures of $CoNb_2O_6$," *Journal of Magnetism and Magnetic Materials*, vol. 13, no. 1, pp. 121–124, 1979.

[83] A. W. Kinross, M. Fu, T. J. Munsie, H. A. Dabkowska, G. M. Luke, S. Sachdev, and T. Imai, "Evolution of quantum fluctuations near the quantum critical point of the transverse field Ising chain system $CoNb_2O_6$," *Phys. Rev. X*, vol. 4, p. 031008, 2014.

[84] J. A. Kjäll, F. Pollmann, and J. E. Moore, "Bound states and E_8 symmetry effects in perturbed quantum Ising chains," *Phys. Rev. B*, vol. 83, p. 020407, 2011.

[85] R. Wichmann and H. Müller-Buschbaum, "Neue Verbindungen mit $SrNi_2V_2O_8$-Struktur: $BaCo_2V_2O_8$ und $BaMg_2V_2O_8$," *Z. anorg. allg. Chem.*, vol. 534, no. 3, pp. 153–158, 1986.

[86] Z. He, D. Fu, T. Kyômen, T. Taniyama, and M. Itoh, "Crystal growth and magnetic properties of $BaCo_2V_2O_8$," *Chem. Mater.*, vol. 17, no. 11, pp. 2924–2926, 2005.

[87] Z. He, T. Taniyama, and M. Itoh, "Large magnetic anisotropy in the quasi-one-dimensional system $BaCo_2V_2O_8$," *Applied Physics Letters*, vol. 88, no. 13, p. 132504, 2006.

[88] S. Kimura, H. Yashiro, K. Okunishi, M. Hagiwara, Z. He, K. Kindo, T. Taniyama, and M. Itoh, "Field-induced order-disorder transition in antiferromagnetic $BaCo_2V_2O_8$ driven by a softening of spinon excitation," *Phys. Rev. Lett.*, vol. 99, p. 087602, 2007.

[89] Q. Faure, S. Takayoshi, S. Petit, V. Simonet, S. Raymond, L.-P. Regnault, M. Boehm, J. S. White, M. Månsson, C. Röegg, P. Lejay, B. Canals, T. Lorenz, S. C. Furuya, T. Giamarchi, and B. Grenier, "Topological quantum phase transition in the Ising-like antiferromagnetic spin chain $BaCo_2V_2O_8$," *Nat. Phys.*, vol. 14, p. 716, 2018.

[90] Y. Kawasaki, J. L. Gavilano, L. Keller, J. Schefer, N. B. Christensen, A. Amato, T. Ohno, Y. Kishimoto, Z. He, Y. Ueda, and M. Itoh, "Magnetic structure and spin dynamics of the quasi-one-dimensional spin-chain antiferromagnet $BaCo_2V_2O_8$," *Phys. Rev. B*, vol. 83, p. 064421, 2011.

[91] S. K. Niesen, G. Kolland, M. Seher, O. Breunig, M. Valldor, M. Braden, B. Grenier, and T. Lorenz, "Magnetic phase diagrams, domain switching, and quantum phase transition of the quasi-one-dimensional Ising-like antiferromagnet $BaCo_2V_2O_8$," *Phys. Rev. B*, vol. 87, p. 224413, 2013.

[92] S. Kimura, K. Okunishi, M. Hagiwara, K. Kindo, Z. He, T. Taniyama, M. Itoh, K. Koyama, and K. Watanabe, "Collapse of magnetic order of the quasi one-dimensional Ising-like antiferromagnet $BaCo_2V_2O_8$ in transverse fields," *Journal of the Physical Society of Japan*, vol. 82, no. 3, p. 033706, 2013.

[93] H. Zou, Y. Cui, X. Wang, Z. Zhang, J. Yang, G. Xu, A. Okutani, M. Hagiwara, M. Matsuda, G. Wang, G. Mussardo, K. Hódsági, M. Kormos, Z. He, S. Kimura, R. Yu, W. Yu, J. Ma, and J. Wu, "E_8 spectra of quasi-one-dimensional antiferromagnet $BaCo_2V_2O_8$ under transverse field," *Phys. Rev. Lett.*, vol. 127, p. 077201, 2021.

[94] E. Jones, T. Oliphant, P. Peterson, *et al.*, "SciPy: Open source scientific tools for Python," 2001–. http://www.scipy.org/ [Online; accessed August 4, 2022].

[95] K. Momma and F. Izumi, "VESTA 3 for three-dimensional visualization of crystal, volumetric and morphology data," *J. Appl. Cryst.*, vol. 44, pp. 1272–1276, 2011.

Acknowledgements

First and foremost, I would like to thank Michelle Mueller, who has been by my side this whole time, and offered unconditional support throughout my PhD journey. I am also extremely grateful to my friends and family, who always back me and keep me positive.

I would like to thank my supervisors Toomas Rõõm and Urmas Nagel, without whom none of this would have been possible. Thank you for your support and invaluable contribution to this work. I also wish to thank all of the members of the THz group at KBFI for all your help and good time working together.

I am grateful to all of the collaborators, especially Randy Fishman, Yann Alexanian, Rafik Ballou, Sophie de Brion, Zhao Zhang, and Jianda Wu for their theoretical work and calculations, as well as Hasung Sim, Kisoo Park, Je-Geun Park, Claudia Decorse, and Thomas Lorenz for growing high-quality crystals for the THz measurements. Special thanks to Zhe Wang, who started most of the fruitful collaborations that led to the results of this work. Finally, I am thankful to everyone who I have had pleasure to work with, whether on the projects presented here, or the ones whose results are yet to be published.

I would like to acknowledge the open-source SciPy library [94] for Python that was used to analyze and visualize the experimental results of this work, and Vesta software [95] that was used to model crystal structures of the studied materials.

Abstract
Symmetry breaking revealed by THz spectroscopy of magnetic excitations

Magnetic excitations provide valuable information on interactions within various magnetic materials, giving insight into magnetic ordering, symmetry, and spontaneous symmetry breaking upon phase transitions. A powerful technique to study magnetic excitations is THz spectroscopy, which not only has superior spectral resolution to some widely used spectroscopic techniques, such as inelastic neutron scattering or resonant inelastic X-ray scattering, but can also probe low-energy excitations below 1 meV. In this work, we use two THz spectrometers at the National Institute of Chemical Physics and Biophysics in Tallinn to study magnetic excitations in a pyrochlore $Tb_2Ti_2O_7$, an orthoferrite $YFeO_3$, and two quasi-one-dimensional Ising spin chains $CoNb_2O_6$ and $BaCo_2V_2O_8$. Our setup combines a Martin-Puplett interferometer with either a liquid-helium-bath cryostat and a 17-tesla superconducting magnet, or a dilution refrigerator, equipped with a 12-tesla superconducting magnet. The available range of energies, temperatures, and magnetic fields gives access to low-energy spin-wave modes in $YFeO_3$ below and above the spin-flop transition field, crystal-field excitations in $Tb_2Ti_2O_7$, including transitions from the ground state and between excited states, as well as confined spinons and other magnetic excitations in Ising spin chains $CoNb_2O_6$ and $BaCo_2V_2O_8$ in close proximity to and far away from the quantum critical point.

Magnetic Tb^{3+} ions in $Tb_2Ti_2O_7$ are arranged on a pyrochlore lattice of corner-sharing tetrahedra. $Tb_2Ti_2O_7$ fails to develop any long-range magnetic order down to 50 mK, and features a fluctuating spin-liquid state instead. Recent INS and THz spectroscopy studies showed that $Tb_2Ti_2O_7$ supports hybrid magnetoelastic excitations, which indicate an interplay between spin and lattice degrees of freedom, resulting in dynamic symmetry breaking of the local crystal field environment at the Tb^{3+} site. To confirm the local symmetry breaking, we study magnetic-field dependence of the crystal-field excitations of Tb^{3+} ions in the temperature range 3 – 60 K, with the magnetic field applied along the cubic $[111]$ axis. We propose a model Hamiltonian that incorporates such vibronic coupling and reproduces experimentally observed features in the absorption spectrum in the applied magnetic field, thus providing strong evidence of the dynamic symmetry breaking in $Tb_2Ti_2O_7$.

$YFeO_3$ is isostructural to some known multiferroics with an orthorhombic structure. With only Fe^{3+} ions carrying a finite spin $S = 5/2$, it is a great model component that gives insight into magnetic interactions and magnetic ordering in multiferroic materials. In these materials, the relatively weak, as compared to the exchange couplings, Dzyaloshinskii–Moriya interactions are responsible for additional symmetry breaking, and the arising multiferroic properties. Therefore, it is highly important to model them accurately. Previous inelastic neutron scattering works proposed two distinct models to describe the Dzyaloshinskii–Moriya interaction in $YFeO_3$ with different values of the exchange interaction parameters and single-ion anisotropies. We study the magnetic-field dependence of the spin-wave modes in $YFeO_3$ at 3 K with the magnetic field applied along all three crystallographic directions. Using the linear spin-wave theory, we calculate the spin-wave excitation energies and fit them to the experimentally measured ones to find the correct values of Dzyaloshinskii–Moriya interaction and single-ion anisotropy parameters. As the result, we determine which model describes the interactions more accurately, as well as refine the zero-field spin structure of $YFeO_3$.

Exotic states of matter and complex symmetries often emerge in the proximity of the

quantum critical point. In 1989, A. B. Zamolodchikov proposed that an Ising spin chain in a transverse magnetic field near the quantum critical point, if perturbed by a small longitudinal field, can be described by an integrable quantum field theory with the symmetry of the E_8 Lie algebra. The theory provides an exact solution, which features an excitation spectrum of eight particles that follow specific mass ratios. The earlier attempt to experimentally measure the E_8 spectrum by inelastic neutron scattering only featured two of the possible eight excitations in $CoNb_2O_6$. $CoNb_2O_6$ is a realization of a quasi-one-dimensional Ising spin chain, with a ferromagnetic arrangement of Co^{2+} spin. We measured the THz absorption spectrum of $CoNb_2O_6$ at 250 mK in the applied transverse magnetic field up to 12 T. Close to the quantum critical point, we report the observation of the E_8 spectrum with the single-particle excitations up to m_6, as well as multi-particle excitations. Additionally, we studied the absorption spectrum of $BaCo_2V_2O_8$, which incorporates antiferromagnetic Co^{2+} spin chains. We performed the measurement at 2.7 K in the applied transverse magnetic field up to 17 T. Near the quantum critical point, we observe the E_8 spectrum with the single-particle excitations up to m_5 together with the multi-particle excitations. We, therefore, report strong evidence of the emergent E_8 symmetry in both $CoNb_2O_6$ and $BaCo_2V_2O_8$.

Kokkuvõte
Sümmeetriarikkumiste avaldumine magnetergastuste terahertsspektrites

Magnetiliste ergastuste uurimine annab väärtuslikku teavet aine magnetmomentide vaheliste vastasmõjude, magnetilise korrapära ning sellega seotud sümmeetriarikkumiste kohta faasisiiretel. Antud töös kasutatakse teraherts spektroskoopiat, mis võrreldes teiste meetoditega, nagu mitteelastne neutronhajumine või mitteelastne röntgenkiirguse hajumine, annab parema energialahutuse ning lisaks on võimeline mõõtma ergastusi energiatel alla 1 meV (0.24 THz). Keemilise ja Bioloogilise Füüsika Instituudis kasutatavad teraherts-piirkonna spektromeetrid võimaldavad teha mõõtmisi magnetväljades kuni 17 teslat ja väga madalatel temperatuuridel kuni mõnisada millikelvinit. Selline energia-, magnetvälja- ja temperatuurivahemik annab juurdepääsu kristallväljaergastustele terbium titanaadis $Tb_2Ti_2O_7$, spinnlainetele ütrium ortoferriidis $YFeO_3$ ning Isingi spinnahela ergastustele kvantkriitilise punkti lähedal.

Terbium titanaadis $Tb_2Ti_2O_7$ paiknevad magnetilised Tb^{3+} ioonid tetraheedri tippudes moodustades pürokloori tüüpi kristallvõre. Tb magnetmomendid ei korrastu ka ülimadalal temperatuuril, kuni 50 mK, vaid viibivad fluktueerivas spinnjää olekus. Hiljutised mitteelastse neutronhajumise ja teraherts-uuringud näitasid, et $Tb_2Ti_2O_7$-s on hübriidsed magnetelastsed ergastused, mis viitavad magnetmomentide ja kristallvõrevõnkumiste vastasmõjule. Meie mõõtsime $Tb_2Ti_2O_7$ neeldumisspektrite magnetväljasõltuvuse temperatuurivahemikus 3 – 60 K. Mõõdetud spektrite modelleerimiseks koostasime hamiltoniaani, mis kirjeldab magnetmomentide ja kristallvõrevõnkumiste vastasmõju kristallvälja kaudu. Võrreldes teoreetilist tulemust mõõdetud spektriga, kinnitame võrevõnkumistest põhjustatud lokaalse kristallvälja dünaamilist sümmeetriarikkumist.

Ütrium ortoferriidi $YFeO_3$ struktuur on sarnane mõnede multiferroidide struktuurile. Arvestades, et selles aines on ainult Fe^{3+} ioonidel nullist erinev spinn $S = 5/2$, võimaldab $YFeO_3$ magnetiste vastasmõjude ning korrastatuse uurimine paremini mõista keerulisema struktuuriga multiferroidide omadusi. Olulised on vahetusvastasmõjudega võrreldes suhteliselt nõrgad Dzyaloshinskii–Moriya vastasmõjud, mis põhjustavad magnetilise struktuuri sümmeetria rikkumist ja multiferroidsete omaduste tekkimist. Seega on nende täpne modelleerimine eriti tähtis. Varasemad mitteelastse neutronhajumise uuringute poolt pakutud kaks mudelit ei olnud kooskõlalised, sest sisaldasid erinevaid Dzyaloshinskii–Moriya vastasmõjusid ja ühe iooni anisotroopia parameetreid. Meie uurisime kahe madalal energial oleva spinnlaine sageduste sõltuvust magnetväljast temperatuuril 3 K, rakendades magnetvälja kolme erineva kristalltelje suunas. Kasutades lineaarset spinnlaine teooriat arvutasime ergastuste sagedused ning lähendasime tulemust eksperimentaalselt mõõdetud väärtustega. Lõpptulemuseks tegime kindlaks, milline mudel kirjeldab Dzyaloshinskii–Moriya vastasmõjusid paremini, määrasime täpsemalt vastasmõju parameetrid ning täpsustasime spinnide kõrvalekaldenurkasid ideaalsest antiferromagnetilisest struktuurist.

Kvantkriitilise punkti lähedal tekivad tihti eksootilised aineolekud ning ilmuvad komplekssed sümmeetriad. 1989. aastal näitas A. B. Zamolodchikov, et Isingi spinnahelat ristises magnetväljas kvantkriitilise punkti lähedal ja väikese pikimagnetvälja häiritusega kirjeldab integreeritav kvantväljateooria, millel on E_8 Lie algebra sümmeetria. Teooria on täpselt lahendatav ning ennustab ergastusspektri, mis koosneb kaheksast osakesest kindlate massisuhetega. E_8 spekter mõõdeti esimest korda koobalt niobaadi $CoNb_2O_6$ ferromagnetilises Co^{2+} spinnide ahelas mitteelastse neutronhajumisega. Kahjuks oli siis võimalik näha vaid kaht ergastust kaheksast. Meie mõõtsime $CoNb_2O_6$ spektrit temperatuuril 250 mK kuni

12 T ristimagnetväljas. Kvantkriitilise punkti lähedal leidsime kuus ergastust E_8 teooriaga määratud massisuhetega ning ka nende mitmeosakese ergastused. Lisaks sellele uurisime ka antiferromagnetilise Co^{2+} spinnide ahelaga $BaCo_2V_2O_8$ spektrit temperatuuril 2.7 K magnetväljas kuni 17 T. $BaCo_2V_2O_8$-s leidsime viis E_8 osakest ja mitmeosakese ergastusi. Meie töö kinnitab veenvalt, et mõlemas aines kvantkriitilise punkti lähedal tekib E_8 sümmeetria.

Appendix 1

I

K. Amelin, U. Nagel, R. S. Fishman, Y. Yoshida, Hasung Sim, Kisoo Park, Je-Geun Park, and T. Rõõm, "Terahertz absorption spectroscopy study of spin waves in orthoferrite YFeO$_3$ in a magnetic field," *Phys. Rev. B*, vol. 98, p. 174417, Nov 2018

Terahertz absorption spectroscopy study of spin waves in orthoferrite YFeO₃ in a magnetic field

K. Amelin,[1] U. Nagel,[1] R. S. Fishman,[2] Y. Yoshida,[3] Hasung Sim,[4,5] Kisoo Park,[4,5] Je-Geun Park,[4,5] and T. Rõõm[1]

[1]*National Institute of Chemical Physics and Biophysics, Tallinn 12618, Estonia*
[2]*Materials Science and Technology Division, Oak Ridge National Laboratory, Oak Ridge, Tennessee 37830, USA*
[3]*National Institute of Advanced Industrial Science and Technology, Tsukuba, Ibaraki 305-8565, Japan*
[4]*Center for Correlated Electron Systems, Institute for Basic Science, Seoul 08826, Korea*
[5]*Department of Physics and Astronomy, Seoul National University, Seoul 08826, Korea*

We measured absorption of THz radiation in YFeO₃ single crystals at a temperature of 3 K in the magnetic field up to 17 T applied in all three crystallographic directions. Two spin-wave modes were observed at the Γ point with energies 1.2 meV (9.8 cm^{-1}) and 2.4 meV (19.3 cm^{-1}) in zero field. From the magnetic-field dependence of mode energies, we have refined the previously proposed model [S. E. Hahn *et al.*, Phys. Rev. B **89**, 014420 (2014)] and quantified the parameters of Dzyaloshinskii-Moriya interactions and single-ion anisotropies.

I. INTRODUCTION

Strong coupling between electric and magnetic orders in multiferroic materials is an interesting phenomenon that allows for tuning of magnetic properties with the applied electric field, and it can find applications in future recording devices and spintronics [1,2]. Such a magnetoelectric effect has been observed in rare-earth orthoferrites R FeO₃, where R is a rare-earth element. GdFeO₃, for example, obtains a magnetically induced ferroelectric ground state below 2.5 K, in which the magnetic moment can be controlled with the electric field [3]. The same possibility has been reported [4] for compounds Dy₀.₇Tb₀.₃FeO₃ and Dy₀.₇₅Gd₀.₂₅FeO₃. While GaFeO₃ and AlFeO₃ do not belong to the group of rare-earth orthoferrites, their rather similar noncentrosymmetric orthorhombic structure also allows for spontaneous electric polarization and results in multiferroic properties [5].

To fully understand such multiferroic behavior, it is necessary to be able to accurately describe and quantify the interactions inside these materials. Here we focus on an orthoferrite YFeO₃ with a distorted perovskite structure of the *Pbnm* symmetry group. Although the inversion symmetry of this structure does not allow for multiferroicity, YFeO₃ is a perfect model system for studying magnetic interactions. In particular, all electron shells in Y³⁺ are completely filled, which means that the magnetic ordering comes exclusively from the Fe³⁺ ions. Thus, modeling this compound allows us to lay the foundation for understanding the magnetoelectric mechanisms and spin dynamics in materials that exhibit more complex behavior.

The striking feature of orthoferrites is their high Néel temperature T_N, which for YFeO₃ is reported [6–8] to be approximately 644 K. This property could, in principle, result in room-temperature applications. Below T_N, the iron spins $S = 5/2$ order in an antiferromagnetic (AFM) state $\Gamma_4(G_a, F_c, A_b)$, where the spins are canted, resulting in a weak ferromagnetic (FM) component along the c axis [9,10]. This spin structure is described by a combination of exchange interactions, Dzyaloshinskii-Moriya (DM) interactions that result in weak FM order, and single-ion anisotropies (SIA). It has been shown [11] that with the magnetic field applied along the a axis, the weak FM moment rotates away from the c axis toward the field by 80° at around 7.0 T.

There are four spin-wave (SW) modes associated with the four magnetic ions per unit cell in YFeO₃. Two modes have been observed at about 10 and 20 cm^{-1} at the Γ point with Raman spectroscopy [12] and quasioptical techniques [13,14]. Combining these observations with inelastic neutron scattering (INS) measurements of SW dispersion at higher energies led to the development of a simplified spin-state model [15]. There the spin Hamiltonian had two types of exchange interactions (those between nearest-neighbor and next-nearest-neighbor spins), two DM coupling parameters between atoms located in the ab plane, and two SIA constants. From a later structural analysis with INS study of low-energy excitations around a magnetic Brillouin zone center [16], it followed that the model had to be improved by including additional DM interactions between adjacent planes. However, no extensive study of the magnetic-field dependence of SW modes has been performed until now.

The current reexamination of YFeO₃ has two motivations. First, THz spectroscopy has far greater sensitivity in frequency than does inelastic neutron scattering. So it is much better suited to study the low-frequency spin dynamics produced by spin-orbit coupling and to estimate the weak, as compared to exchange couplings, DM and SIA interactions in YFeO₃. Second, we use this opportunity to incorporate the more complex structure of the DM vectors. By applying
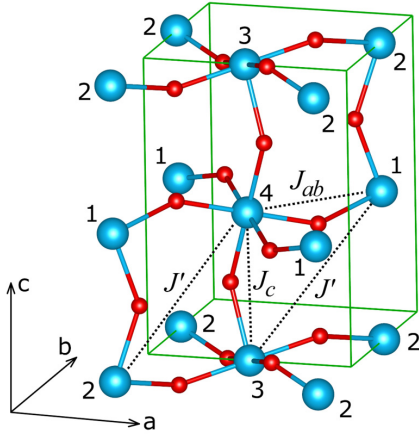
FIG. 1. Magnetic interactions in YFeO₃. Magnetic Fe ions are blue and labeled 1 through 4; oxygen ions are red.

the magnetic field in the three crystallographic directions, we obtain much more precise values for the DM and SIA interactions in YFeO₃ than was previously possible.

II. THEORY

The magnetic unit cell of YFeO₃ contains four $S = 5/2$ Fe^{3+} ions. A sketch of the magnetic unit cell and the exchange interactions between the spins is shown in Fig. 1. We include three exchange interactions: J_{ab} couple pairs of spins {1, 4} and {2, 3} within the ab plane, J_c couple pairs {1, 2} and {3, 4} along c, and J' couple pairs {1, 3} and {2, 4} in different layers separated by $c/2$.

In the absence of DM interactions, the exchange interactions and SIA would stabilize a simple AFM state with spins 1 and 3 aligned along $-\mathbf{a}$ and spins 2 and 4 aligned along $\mathbf{a}$. An earlier work by Hahn *et al.* [15] assumed a simplified model where two DM vectors were taken along $\mathbf{b}$ and $\mathbf{c}$. Each DM interaction was assumed to couple only nearest-neighbor spins, $\{i, j\} = \{2, 3\}$ and $\{1, 4\}$, in the ab plane. The DM vector $\mathbf{D}_2$ then produces the tilt of the spins in the ab plane away from the a axis, and $\mathbf{D}_1$ produces the tilt of the spins toward the c axis [10]. They also included easy-axis SIA K_a and K_c along the a and c axes, respectively. The spin state can be written as

$$\mathbf{S}_i = S(\sin\theta_i \cos\phi_i, \ \sin\theta_i \sin\phi_i, \ \cos\theta_i). \quad (1)$$

In zero field the angles are $\theta_1 = \theta_2 = \theta_3 = \theta_4 \equiv \theta$ and $\phi_1 + \pi = -\phi_3 + \pi = -\phi_4 = \phi_2 \equiv \phi$. This state has a net spin c-component $F_c = (\mathbf{S}_1 + \mathbf{S}_2 + \mathbf{S}_3 + \mathbf{S}_4)_c = 4S\cos\theta$ per magnetic unit cell. It has no spin component perpendicular to the c axis, but it has AF components along the a axis, $G_a = (\mathbf{S}_1 - \mathbf{S}_2 + \mathbf{S}_3 - \mathbf{S}_4)_a$, and the b axis, $A_b = (\mathbf{S}_1 - \mathbf{S}_2 - \mathbf{S}_3 + \mathbf{S}_4)_b$. The relations between spin vectors and angles are $A_b/G_a = \tan\phi$ and $F_c/G_a = (\cos\phi\tan\theta)^{-1}$.

Hahn *et al.* [15] fit the SW spectrum to obtain the exchange interactions, SIA, and DM vectors. The set of parameters was constrained to produce the zero-field spin state with

$\theta = 0.498\pi$ and $\phi = 0.001\pi$. Because J_{ab} and J_c couple sites that are bridged by one anion and separated by distances $\sqrt{a^2 + b^2}/2 \approx 3.85$ Å and $c/2 \approx 3.80$ Å, respectively, these two antiferromagnetic coupling constants were set equal to the single exchange constant J. By contrast, J' couples sites that are bridged by two anions and by distance $\sqrt{a^2 + b^2 + c^2}/2 \approx 5.41$ Å. So $|J'|$ is expected to be much smaller than $|J|$. Hahn *et al.* estimated that $J = -4.77$ meV and $J' = -0.21$ meV. The SIA $K_a = 0.0055$ meV and $K_c = 0.0035$ meV favor the spins to lie perpendicular to the b axis. The DM vectors had estimated magnitudes $D_1 = 0.074$ meV and $D_2 = 0.028$ meV.

However, a symmetry analysis of the perovskite crystal structure [17] revealed that the DM vectors are more complex than assumed by Hahn *et al.* [15]. Rather than just two DM vectors, each oxygen atom-mediated bond (Fig. 1) carries its own local DM vector, including nearest neighbors {1, 2} and {3, 4} on adjacent ab planes separated by $\pm c/2$. While there are still only two overall magnitudes for the DM vectors, this more complex interaction structure could modify the estimates for the microscopic parameters in YFeO₃.

With the magnetic field $\mathbf{H}$ along $\mathbf{m}$, the Hamiltonian of YFeO₃ can be written as

$$\mathcal{H} = -\frac{1}{2}J \sum_{i,j} \mathbf{S}_i \cdot \mathbf{S}_j - \frac{1}{2}J' \sum_{i,j} \mathbf{S}_i \cdot \mathbf{S}_j$$
$$- K_a \sum_i S_{ia}^2 - K_c \sum_i S_{ic}^2$$
$$+ \frac{1}{2} \sum_{i,j} \mathbf{D}_{ij} \cdot (\mathbf{S}_i \times \mathbf{S}_j) - \mu_B \mu_0 H \sum_i \mathbf{m} \cdot \mathbf{S}_i, \quad (2)$$

where the exchange interactions couple the spins indicated in Fig. 1, and $J_{ab} = J_c \equiv J$. The factors of $1/2$ avoid double counting. Because the spectroscopic modes are evaluated at wave vector $\mathbf{q} = 0$, we do not include interactions between spins in neighboring unit cells, e.g., between $\mathbf{S}_1$ and $\mathbf{S}_1$, although these are next-nearest-neighbor interactions.

The orientation of the local vectors $\mathbf{D}_{ij}$ is determined by the condition that [18]

$$\mathbf{D}_{ij} \propto (\mathbf{R}_i - \mathbf{R}_o) \times (\mathbf{R}_o - \mathbf{R}_j), \quad (3)$$

where $\mathbf{R}_o$ is the position of the oxygen atom that couples spins i and j. Consequently, the DM vectors are given by [17]

$$\mathbf{D}_{32} = D_{ab}(-\alpha_{ab}, \beta_{ab}, \gamma_{ab}), \ \Delta\mathbf{R} = \pm(a/2, b/2, 0), \quad (4)$$

$$\mathbf{D}'_{32} = D_{ab}(\alpha_{ab}, \beta_{ab}, \gamma_{ab}), \ \Delta\mathbf{R} = \pm(-a/2, b/2, 0), \quad (5)$$

$$\mathbf{D}_{41} = D_{ab}(-\alpha_{ab}, -\beta_{ab}, \gamma_{ab}), \ \Delta\mathbf{R} = \pm(-a/2, b/2, 0), \quad (6)$$

$$\mathbf{D}'_{41} = D_{ab}(\alpha_{ab}, -\beta_{ab}, \gamma_{ab}), \ \Delta\mathbf{R} = \pm(a/2, b/2, 0), \quad (7)$$

$$\mathbf{D}_{12} = D_c(-\alpha_c, \beta_c, 0), \ \Delta\mathbf{R} = \pm(0, 0, c/2), \quad (8)$$

$$\mathbf{D}_{34} = D_c(\alpha_c, \beta_c, 0), \ \Delta\mathbf{R} = \pm(0, 0, c/2), \quad (9)$$

where $\Delta\mathbf{R} = \mathbf{R}_i - \mathbf{R}_j$ for $\mathbf{D}_{ij} = -\mathbf{D}_{ji}$. The vectors are all normalized so that $\alpha_{ab}^2 + \beta_{ab}^2 + \gamma_{ab}^2 = 1$ and $\alpha_c^2 + \beta_c^2 = 1$.
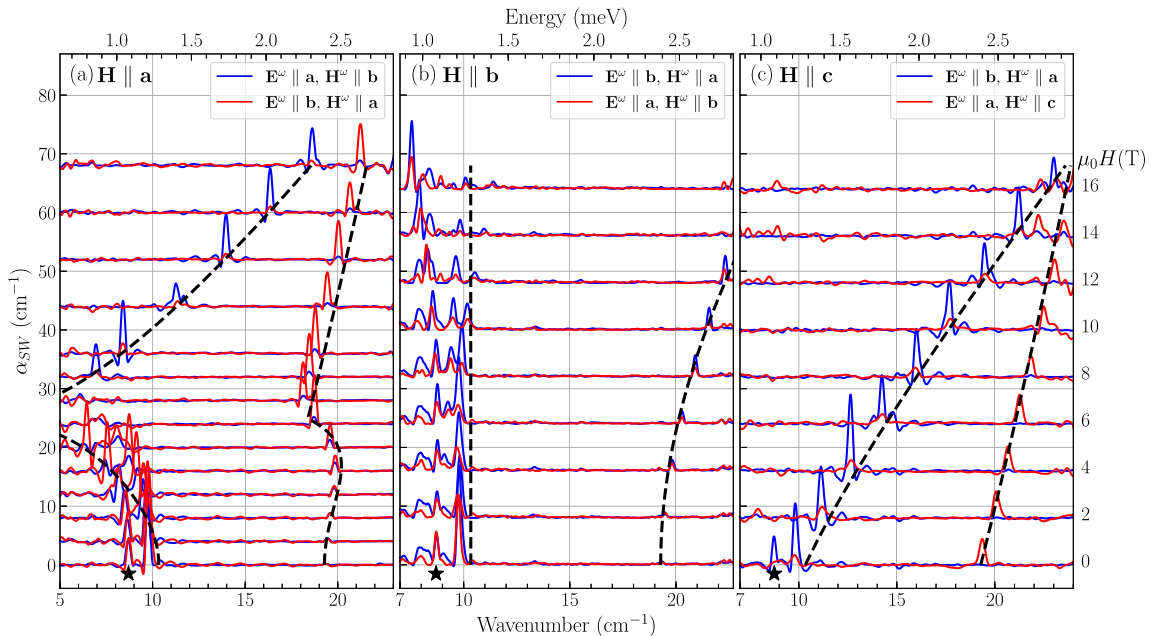
FIG. 2. Magnetic-field dependence of SW absorption spectra of YFeO$_3$ at 3 K. Panels (a), (b), and (c) correspond to the magnetic field **H** applied along crystallographic axes a, b, and c, respectively. The spectra are shifted vertically in proportion to the magnitude of the applied magnetic field, marked on the right side of the plot. In each panel, blue and red solid lines denote two orthogonal incident light polarizations, where the oscillating electric- and magnetic-field vectors **E**$^\omega$ and **H**$^\omega$ are aligned along different crystallographic axes. Dashed lines show the absorption peak positions obtained from the theoretical fit. The impurity peak position in zero field is marked with a star.

Based on Eq. (3) and the structural analysis [16], $\alpha_{ab} = 0.517$, $\beta_{ab} = 0.488$, $\gamma_{ab} = 0.703$, $\alpha_c = 0.346$, and $\beta_c = 0.938$.

III. EXPERIMENT

We prepared polycrystalline YFeO$_3$ using Y$_2$O$_3$ and Fe$_2$O$_3$ by a standard solid-state reaction method. All the starting materials were prepared in a stoichiometric ratio and mixed, pelletized, and sintered several times. The final sintering condition was set to 1400 °C for 24 h. Single crystals were subsequently grown with a 4-mm-diameter feed rod of a correct composition by a floating-zone furnace (Crystal Systems, Japan) under an oxygen atmosphere at a growth speed of 3 mm/h. We checked the quality of the samples using a single-crystal diffractometer and bulk property measurements.

Three cuts of YFeO$_3$ single crystals, (100), (010), and (001), with thicknesses slightly under 1 mm were prepared. The intensity of transmitted THz radiation was detected in the range from 5 to 40 cm^{-1} using a Martin-Puplett interferometer, a mercury discharge lamp as a light source, and a Si bolometer operated at $T = 0.3$ K. The polarization of incident radiation was controlled by a wire-grid polarizer. Measurements were performed in Faraday and Voigt configurations, where the THz radiation propagates parallel or perpendicular to the applied magnetic field, respectively. In a Voigt configuration, the SW mode frequencies were measured as a function of the sample orientation in fields just below and above the observed spin-flop (SF) transition (i.e., 5 and 7 T). The sample was rotated around the c axis such that

the magnetic-field vector was in the ab plane. The exact alignment **H** ∥ **a** was achieved by finding the orientation that corresponds to the lowest frequency of the resonance peak.

Differential absorbance spectra were calculated from the ratios of transmitted light intensities measured with and without the applied magnetic field in the following way. In a sample with negligible interference (i.e., wedged or with high enough absorption), the transmitted light intensity I is related to the incident light intensity I_0 via $I = I_0(1 - R)^2 \exp(-\alpha d)$, where R is the reflection coefficient, α is the absorption coefficient, and d is the sample thickness. Therefore, the absorption coefficient is defined as $\alpha = -d^{-1} \ln[(1 - R)^{-2} I/I_0]$. If we assume that R does not depend on the applied magnetic field, we can calculate the differential absorbance $\alpha_{SW} \equiv \alpha(H) - \alpha(0) = -d^{-1} \ln[I(H)/I(0)]$ by dividing the transmitted intensity spectrum measured in the magnetic field $I(H)$ by the zero-field spectrum $I(0)$. Finally, a baseline, statistically calculated from negative values of α_{SW}, is subtracted to reveal absorption peaks in the zero-field spectrum.

IV. RESULTS

Using THz spectroscopy, we have measured two lowest spin-wave modes at $\mathbf{q} = \mathbf{0}$ for the magnetic field along the a, b, and c axes, with results shown in Fig. 2. YFeO$_3$ undergoes a spin-flop transition when the field is applied along the a axis. While the spins are almost parallel to the a axis below H_{SF}, they are almost parallel to the c axis above H_{SF}.
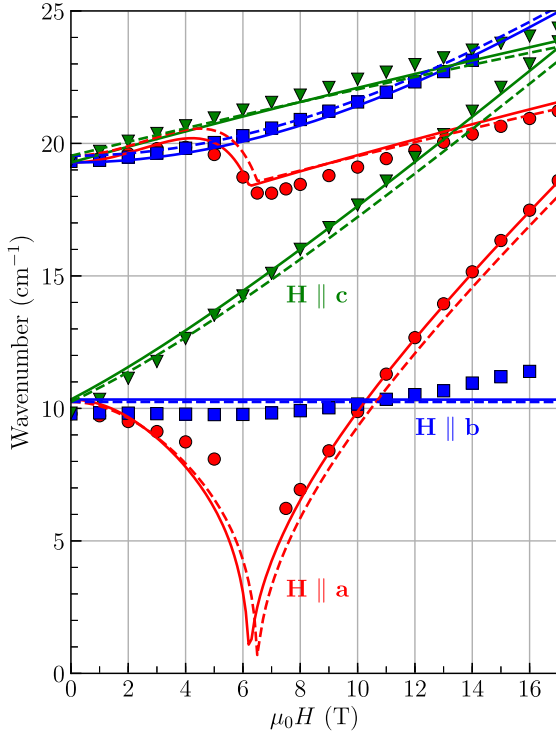
FIG. 3. Magnetic-field dependence of the absorption peak positions (symbols) with the field applied along the three crystallographic axes and the theoretical fit result (solid lines). Dashed lines show the fit with the simplified model, where $D_c = 0$.

TABLE I. Spin Hamiltonian parameter values (meV). The two DM parameters of Hahn *et al.* [15] are related to D_{ab} as $D_{ab} = \sqrt{D_1^2 + D_2^2}$.

	This work	$D_c = 0$	Hahn *et al.* [15]	Park *et al.* [16]
J_c	−4.77	−4.77	−4.77	−5.02
J_{ab}	−4.77	−4.77	−4.77	−4.62
J'	−0.21	−0.21	−0.21	−0.22
K_a	0.0052	0.0055	0.0055	0.0091
K_c	0.0044	0.0038	0.0031	0.0025
$|D_{ab}|$	0.136	0.147	0.079	0.121
$|D_c|$	0.189	0		0.145

earlier reports. The resulting values of K_a and K_c are quite close to those predicted by Hahn *et al.* [15]. Not surprisingly, considering that the DM vectors are oriented away from the c and b axes, the values for D_{ab} and D_c are larger than $\sqrt{D_1^2 + D_2^2}$ estimated by Hahn *et al.* [15]. These parameters correspond to the zero-field canted state with $\theta = 0.4966\pi$ and $\phi = 0.0035\pi$, which is more canted than previously predicted. When the field is applied along the a axis, these parameters produce a SF field $\mu_0 H_{SF} = 6.2$ T.

We evaluated the validity of the more complex DM model by also fitting the experimental data using a simplified model from Hahn *et al.* [15], with $D_c = 0$ and $\alpha_{ab} = 0$. In this case the four fitting parameters are D_1, D_2, K_a, and K_c. The result is plotted in Fig. 3 with dashed lines. While it is still possible to fit the spectrum rather well with fixed $D_c = 0$, it does not match the experimental data as closely as the more complex model that includes DM interaction between adjacent planes. This is confirmed by the difference in χ^2 (0.462 against 0.168). The corresponding fit parameters are specified in Table I in the second column. The values of D_1 and D_2 are 0.139 and 0.048 meV, respectively.

In addition to the two SW modes, there exists another mode below 9 cm^{-1}, which is especially pronounced in Figs. 2(a) and 2(b), and it has been indicated with a star. This mode has previously been reported [19,20] to be an impurity mode only present in single crystals grown by the floating zone method. The mode was assigned to Fe^{3+} atoms occupying Y^{3+} sites, and is not accounted for in the present model.

Since THz spectroscopy only measures the two low-frequency modes below 3 meV, we use the SW spectrum measured with INS [15] for frequencies up to 80 meV to fix the exchange interactions $J_c = J_{ab} = -4.77$ meV and $J' = -0.21$ meV. That leaves the four "small" spin-orbit parameters K_a, K_c, D_{ab}, and D_c to be determined by optical spectroscopy.

For each field direction and magnitude and set of parameters, we minimize the energy $E = \langle \mathcal{H} \rangle$ as a function of the eight angles θ_i and ϕ_i for the four spins in the magnetic unit cell. Based on the linear SW theory, we then evaluate the frequencies of the two lowest SW modes for comparison with the measured spectroscopic mode frequencies. This loop is repeated until we achieve a minimum of χ^2.

The result of this procedure is presented in Fig. 3, which shows a rather good agreement between the theory and the experimental data. All of the coupling parameters are summarized in Table I, where the values are compared to those from

FIG. 4. Zero-field spectra measured in six different polarizations qualitatively showing the selection rules. The spectra are grouped according to the direction of the oscillating magnetic field $\mathbf{H}^\omega$. For each direction, only one mode is visible. The dashed lines show arbitrarily scaled theoretical spectra. The impurity mode is marked with a star.

Figure 4 qualitatively shows the selection rules for $YFeO_3$. It is clear that the absorption intensity depends on the direction of the oscillating magnetic field $\mathbf{H}^\omega$ rather than the electric field $\mathbf{E}^\omega$. The selection rules are well reproduced by the theory, where in zero field the lower-frequency mode is visible in polarizations with $\mathbf{H}^\omega \parallel \mathbf{a}$ and $\mathbf{H}^\omega \parallel \mathbf{b}$, while the higher-frequency mode occurs exclusively with $\mathbf{H}^\omega \parallel \mathbf{c}$. While the theory qualitatively matches the experiment in the whole magnetic-field range (selection rules change after the spin flop), we have not been able to accurately reproduce the absorption intensities. Thus, in Fig. 4 the higher-frequency mode is predicted to have much higher intensity, while in reality the intensities of the two modes are comparable. The cause of this discrepancy remains unknown.

V. CONCLUSION

Two SW modes were measured by THz absorption spectroscopy and modeled by the Hamiltonian, Eq. (2). Our result shows that it is necessary to account for the more complex DM structure to accurately model the magnetic interactions in $YFeO_3$, which is confirmed by the overall quality of the fits. With that in mind, we were able to fit the magnetic-field dependence of the absorption spectra up to 17 T, from which we precisely quantified the SIA and DM interactions. These values are in good agreement with earlier reported INS data, and are only slightly modified.

The obtained canting, with angles $\theta = 0.4966\pi$ and $\phi = 0.0035\pi$, is considerably larger than that previously reported by Hahn *et al.* [15] (0.4983π and 0.0010π) and is very close to what was estimated by Park *et al.* [16] (0.4972π and 0.0032π). This larger canting results from the higher magnitudes of the DM interaction vectors than previously predicted. The new values of canting angles correspond better to the experimentally observed [10] ratios $F_c/G_a = 0.0129$ and $A_b/G_a = 0.0159$ that correspond to $\theta = 0.4959\pi$ and $\phi = 0.0051\pi$.

It is worth noting that the spin flop occurs at $\mu_0 H_{SF} = 6.2$ T with the current set of parameters, which is lower than the previously reported value of 7.0 T. Unfortunately, it is hard to unambiguously determine the exact SF field from the experimental data alone, as the lower SW mode does not soften completely. Why does the lower, experimental mode frequency not soften as much as predicted near H_{SF}?

There might be several explanations for this discrepancy. SW theory does not include higher-order fluctuations that could enhance the SW frequencies near H_{SF}. Because the predicted drop in the lowest mode frequency is very steep, it will be significantly lifted by crystal domains with slightly different spin-flop fields. However, 6.2 T clearly matches the SF field we observed much better than what is estimated using sets of parameters from Hahn *et al.* [15] or Park *et al.* [16], which is 9.0 and 15.9 T, respectively. This is a good indication that fitting the magnetic-field dependence of THz spectra provides a better estimation of the SIA and DM interaction parameters.

Therefore, we have shown that while INS is better suited to estimate the stronger exchange couplings based on the SW dispersion at high frequencies, THz spectroscopy is better suited to study the "weak" spin-orbit induced DM and SIA couplings at low frequencies and $\mathbf{q} = \mathbf{0}$. Since these "weak" interactions are responsible for a material's multiferroic behavior, THz spectroscopy should prove useful in the future, when this approach is extended to materials where Y^{3+} is substituted by other, possibly magnetic ions.

One of the challenges of our method is currently the limited availability of large enough high-quality single crystals for transmission measurements. The other limitation is the fact that we cannot very well detect low-frequency modes that soften close to the spin flop, as it is hard to measure below 5 cm^{-1} with THz spectroscopy. While we are currently not able to determine the cause of the discrepancy between the theoretical and the measured absorption intensities, we hope to find the answer in future measurements that would include other orthoferrites.

[1] S. M. Wu, S. A. Cybart, P. Yu, M. D. Rossell, J. X. Zhang, R. Ramesh, and R. C. Dynes, Nat. Mater. **9**, 756 (2010).

[2] C. Binek and B. Doudin, J. Phys.: Condens. Matter **17**, L39 (2005).

[3] Y. Tokunaga, N. Furukawa, H. Sakai, Y. Taguchi, T. Arima, and Y. Tokura, Nat. Mater. **8**, 558 (2009).

[4] Y. Tokunaga, Y. Taguchi, T. Arima, and Y. Tokura, Nat. Phys. **8**, 838 (2012).

[5] R. Saha, A. Shireen, S. N. Shirodkar, U. V. Waghmare, A. Sundaresan, and C. N. R. Rao, Solid State Commun. **152**, 1964 (2012).

[6] V. M. Judin, A. B. Sherman, and I. E. Myl'nikova, Phys. Lett. **22**, 554 (1966).

[7] H. Shen, J. Xu, A. Wu, J. Zhao, and M. Shi, Mater. Sci. Eng., B **157**, 77 (2009).

[8] D. Treves, J. Appl. Phys. **36**, 1033 (1965).

[9] D. Treves, Phys. Rev. **125**, 1843 (1962).

[10] V. P. Plakhty, Y. P. Chernenkov, and M. N. Bedrizova, Solid State Commun. **47**, 309 (1983).

[11] J. Scola, Y. Dumont, N. Keller, M. Vallée, J.-G. Caputo, I. Sheikin, P. Lejay, and A. Pautrat, Phys. Rev. B **84**, 104429 (2011).

[12] R. M. White, R. J. Nemanich, and C. Herring, Phys. Rev. B **25**, 1822 (1982).

[13] A. A. Volkov, Y. G. Goncharov, G. V. Kozlov, S. P. Lebedev, and A. M. Prokhorov, Infr. Phys. **25**, 369 (1985).

[14] A. A. Mukhin, A. N. Lobanov, and M. Gorian, J. Magn. Res. **195**, 60 (2008).

[15] S. E. Hahn, A. A. Podlesnyak, G. Ehlers, G. E. Granroth, R. S. Fishman, A. I. Kolesnikov, E. Pomjakushina, and K. Conder, Phys. Rev. B **89**, 014420 (2014).

[16] K. Park, H. Sim, J. C. Leiner, Y. Yoshida, J. Jeong, S. Yano, J. Gardner, P. Bourges, M. Klicpera, V. Sechovský, M. Boehm, and J.-G. Park, J. Phys.: Condens. Matter **30**, 235802 (2018).

[17] M. Mochizuki and N. Furukawa, Phys. Rev. B **80**, 134416 (2009).

[18] F. Keffer, Phys. Rev. **126**, 896 (1962).

[19] A. M. Balbashov, A. G. Berezin, J. V. Bobryshev, P. J. Marchukov, I. V. Nikolaev, E. G. Rudashevsky, J. Paches, and L. Půst, J. Magn. Magn. Mater. **104-107**, 1037 (1992).

[20] A. M. Balbashov, G. V. Kozlov, A. A. Mukhin, and A. S. Prokhorov, in *High Frequency Processes in Magnetic Materials*, edited by G. Srinivasa and A. N. Slavin (World Scientific, Singapore, 1995), Chap. 2, pp. 56–98.

Appendix 2

II

Z. Zhang, K. Amelin, X. Wang, H. Zou, J. Yang, U. Nagel, T. Rõõm, T. Dey, A. A. Nugroho, T. Lorenz, J. Wu, and Z. Wang, "Observation of E_8 particles in an Ising chain antiferromagnet," *Phys. Rev. B*, vol. 101, p. 220411, Jun 2020

Observation of E_8 particles in an Ising chain antiferromagnet

Zhao Zhang,[1] Kirill Amelin ⊙,[2] Xiao Wang,[1] Haiyuan Zou,[1] Jiahao Yang,[1] Urmas Nagel ⊙,[2] Toomas Rõõm,[2]
Tusharkanti Dey,[3,4] Agustinus Agung Nugroho,[5] Thomas Lorenz,[3] Jianda Wu ⊙,[1,*] and Zhe Wang ⊙[3,†]

[1]*Tsung-Dao Lee Institute and School of Physics & Astronomy, Shanghai Jiao Tong University, Shanghai 200240, China*
[2]*National Institute of Chemical Physics and Biophysics, 12618 Tallinn, Estonia*
[3]*Institute of Physics II, University of Cologne, 50937 Cologne, Germany*
[4]*Department of Physics, Indian Institute of Technology (Indian School of Mines), Dhanbad 826004, Jharkhand, India*
[5]*Faculty of Mathematics and Natural Sciences, Institut Teknologi Bandung, 40132 Bandung, Indonesia*

Near the transverse-field-induced quantum critical point of the Ising chain, an exotic dynamic spectrum consisting of exactly eight particles was predicted, which is uniquely described by an emergent quantum integrable field theory with the symmetry of the E_8 Lie algebra, but rarely explored experimentally. Here we use high-resolution terahertz spectroscopy to resolve quantum spin dynamics of the quasi-one-dimensional Ising antiferromagnet $BaCo_2V_2O_8$ in an applied transverse field. By comparing to an analytical calculation of the dynamical spin correlations, we identify E_8 particles as well as their two-particle excitations.

Exotic states of matter, such as high-temperature superconductivity or magnonic Bose-Einstein condensation, can emerge in the vicinity of a quantum critical point [1], which identifies a zero-temperature phase transition tuned by an external parameter, e.g., chemical substitution or applied magnetic field [2,3]. Quantum critical points are often characterized by enhanced many-body fluctuations together with divergence of correlation length and complex emergent symmetry [1,4–8]; thus it is generally a formidable task to precisely describe the quantum many-body physics near a quantum critical point. Exactly solvable models play a crucial role in this regard, because a precise understanding of the quantum many-body physics can be gained by rigorously analyzing these models [4,6]. The one-dimensional (1D) spin-1/2 Ising model in a transverse magnetic field is such a paradigmatic example [1,4–9]. Considering only the exchange interaction between the nearest-neighbor spins on a chain [10,11], this model has been investigated most broadly in quantum magnetism, which provides deep insights into the fundamental aspects of the quantum many-body physics [1,6–8]. In particular, highly unconventional dynamic properties have been theoretically predicted to emerge near the transverse-field Ising quantum critical point, either for equilibrium states upon constant perturbations or for states far from equilibrium after a quantum quench (see, e.g., Refs. [12–18]). Moreover, the study of the transverse-field Ising quantum critical point is of importance also in the context of quantum information [5,8] and quantum simulation using ultracold atoms [19].

A remarkable prediction of an exotic dynamic spectrum was made three decades ago for the transverse-field Ising

chain perturbed by a small longitudinal field [12]. It is described by the Hamiltonian

$$H = -J \sum_i S_i^z S_{i+1}^z - B_\perp \sum_i S_i^x - B_\parallel \sum_i S_i^z, \qquad (1)$$

with the x and z components S_i^x and S_i^z, respectively, of the spin-1/2 magnetic moment at the ith site on a 1D chain. The first term is the Ising term with the ferromagnetic exchange $J > 0$ between the nearest-neighbor spins. The second and third terms describe the interactions of the spins with the transverse field $B_\perp$ and the perturbative longitudinal field $B_\parallel$, respectively. Close to the transverse-field Ising quantum critical point [see Fig. 1(b)], the excitation spectrum of this model was predicted to be governed by a complex symmetry which is described by a quantum integrable field theory with the E_8 symmetry (an exceptional simple Lie algebra of rank 8) [12], which, however, is rarely explored experimentally. An analytical solution of the E_8 excitation spectrum delivered exactly eight particles ($\mathbf{m}_1$ to $\mathbf{m}_8$), the existence of which is uniquely determined by the specific ratios of their masses (Table I) with the lowest mass scaling with the perturbative longitudinal field; i.e., $\mathbf{m}_1 \propto |B_\parallel|^{8/15}$ [12]. Further analysis on the dynamic characteristics of the eight particles showed that the single-particle spectral weight decreases monotonically and drastically with increasing energy [Fig. 1(a)] [13,14]. Despite the apparent simplicity of the spin Hamiltonian in Eq. (1), an experimental realization of the E_8 spectrum, however, is very difficult, because several crucial criteria must be simultaneously fulfilled: one-dimensionality of spin interactions, strong Ising anisotropy, and a perturbative longitudinal field.

In this work, we use high-resolution terahertz (THz) spectroscopy to resolve E_8 particles in an antiferromagnetic Ising spin-chain material $BaCo_2V_2O_8$, where all the crucial criteria are found to be realized. By performing analytical

FIG. 1. (a) Normalized dynamical structure factor $D_{xx}(m_i, q = 0)$ at zero momentum transfer for the eight particles with specific ratios $\mathbf{m}_i/\mathbf{m}_1$ ($i = 1, 2, \ldots, 8$) [see Table I and Eq. (2)]. (b) Illustrative phase diagram of a quasi-one-dimensional Ising antiferromagnet in a transverse magnetic field. In zero field a three-dimensional (3D) Néel order is stabilized below T_N due to perturbative interchain couplings. The quantum critical point of the transverse-field Ising chain at $B_\perp^{c,1D}$ [corresponding to the vanishing spin gap $\Delta(B_\perp)$] is masked under the 3D Néel order ($B_\perp^{c,1D} < B_\perp^{c,3D}$). A paramagnetic phase is reached when the long-range order is suppressed by $B_\perp > B_\perp^{c,3D}$. The possible region to realize the E_8 dynamic spectrum is indicated by the dashed area. (c) The spin chain in the quasi-one-dimensional Ising antiferromagnet BaCo$_2$V$_2$O$_8$ is constituted by edge-sharing CoO$_6$ octahedra, running with a fourfold screw axis along the crystallographic c axis. In BaCo$_2$V$_2$O$_8$, the 3D Néel order is formed below $T_N \approx 5.5$ K and $B_\perp^{c,3D} = 10$ T [21].

calculation of the spin dynamic structure factor using the quantum integrable field theory of the E_8 spectrum, we unambiguously identify E_8 single particles as well as their two-particle excitations.

BaCo$_2$V$_2$O$_8$ is a magnetic insulator with a tetragonal crystal structure [20,21]. Based on the magnetic cobalt ions, the

spin chains in BaCo$_2$V$_2$O$_8$ are constituted by edge-sharing CoO$_6$ octahedra, running with a fourfold screw axis along the crystallographic c axis [Fig. 1(c)]. High-quality single crystals of BaCo$_2$V$_2$O$_8$ were grown using the floating-zone method [21]. The crystal structure and magnetic properties were characterized by x-ray diffraction, magnetization, heat capacity, and dilatometry measurements [21]. For the optical experiment, single crystals were oriented at room temperature using x-ray Laue diffraction and cut perpendicular to the tetragonal a axis with a typical surface area of $4 \times 4 \, \text{mm}^2$ and a thickness of 0.76 mm. Using a Sciencetech SPS200 Martin-Puplett type spectrometer with a 0.3 K bolometer, THz transmission measurements were carried out down to 2.7 K (below $T_N \approx 5.5$ K) in a cryostat equipped with a superconducting magnet for applying fields up to 17 T. An external field $B_\perp$ was applied parallel to the tetragonal a axis, while the THz electromagnetic waves propagated along the other tetragonal a axis in Voigt configuration. A rotatable polarizer was placed in front of the sample for tuning polarization of the THz waves. The change of absorption coefficient $\Delta\alpha$ due to magnetic excitations was derived by taking the zero-field transmission spectrum at 10 K (slightly above T_N) as a reference spectrum; see the Supplemental Material [22].

An easy-axis anisotropy along the c axis in BaCo$_2$V$_2$O$_8$ was evidenced by magnetization measurements [21], and further confirmed by investigations of quantum spin dynamics [23–26]. By precisely comparing to the exact results of Bethe ansatz, the quantum spin dynamics in BaCo$_2$V$_2$O$_8$ can be nicely described by a 1D spin-1/2 antiferromagnetic Heisenberg-Ising model with a strong Ising anisotropy [23,24]. Below $T_N \approx 5.5$ K, a three-dimensional (3D) Néel-type antiferromagnetic order [Fig. 1(b)] is stabilized due to the presence of small perturbative interchain couplings [21,24,27–29]. In an applied transverse magnetic field along the a axis, the 3D order is suppressed above $B_\perp^{c,3D} = 10$ T [see Fig. 1(b)] [21].

The interchain couplings strongly influence the quantum spin dynamics below T_N. As illustrated in Fig. 2(a), a spin-flip excitation, which corresponds to $\Delta S = \pm 1$, fractionalizes into two spinons each with a fractional quantum number of spin-1/2. In the Néel-ordered phase, the spinons cannot propagate freely on the chain, but are confined into two-spinon bound states due to the inter-chain couplings. The confining potential increases linearly with the distance between the two spinons [Fig. 2(b)], leading to the discrete levels of spinon-pair bound states, in contrast to spinon continuum of a decoupled chain. Figure 2(c) shows the zero-field absorption spectrum of BaCo$_2$V$_2$O$_8$ below a strong optical phonon band [22,24]. The absorption spectrum exhibits five sharp peaks with their eigenenergies following a linear dependence on

TABLE I. Analytically predicted mass ratios of the E_8 particles ($\mathbf{m}_1$ to $\mathbf{m}_8$) and the derived onsets of the multiparticle continua ($\mathbf{2m}_1$, $\mathbf{m}_1 + \mathbf{m}_2$, $\mathbf{m}_1 + \mathbf{m}_3$, $\mathbf{3m}_1$, and $\mathbf{2m}_2$) [12,13,14].

Single	$\mathbf{m}_2$	$\mathbf{m}_3$		$\mathbf{m}_4$		$\mathbf{m}_5$			$\mathbf{m}_6$		$\mathbf{m}_7$	$\mathbf{m}_8$
Multi			$\mathbf{2m}_1$		$\mathbf{m}_1 + \mathbf{m}_2$		$\mathbf{m}_1 + \mathbf{m}_3$	$\mathbf{3m}_1$		$\mathbf{2m}_2$		
$\mathbf{m}_i/\mathbf{m}_1$	1.618	1.989	2	2.405	2.618	2.956	2.989	3	3.218	3.236	3.891	4.783

FIG. 2. (a) The interchain couplings in the 3D Néel-ordered phase effectively exert a staggered perturbative longitudinal field $(-1)^i B_\parallel$ on the ith spin of the neighboring chain. The two-spinon excitations (red sphere) are confined due to the staggered field. (b) The corresponding confining potential increases linearly with the distance between the two spinons, which leads to the discrete levels of two-spinon bound states with energies $m_1, m_2, m_3, \cdots$. (c) The zero-field absorption spectrum exhibits a series of peaks, measured with $h^\omega \| a$. $\Delta\alpha$ and ω denote absorption coefficient and wave number, respectively. (d) The energies of the peaks follow a linear dependence on ζ_i, the negative zeros of the Airy function $A_i(-\zeta_i) = 0$, which evidences the confinement of spinons due to the staggered longitudinal fields [24,27,28,30]. (e) Evolution of the absorption spectra in finite transverse fields $B_\perp \| h^\omega$. The spectra are shifted vertically by constants proportional to the transverse fields for clarity. The spectra below $B_\perp^{c,3D} = 10$ T in the Néel-ordered phase are complex and exhibit several peaks, while above $B_\perp^{c,3D}$ in the field-induced paramagnetic phase [see Fig. 1(b)] the main features of the spectra are two sharp peaks.

ζ_i [see Fig. 2(d)]; the negative zeros of the Airy function $A_i(-\zeta_i) = 0$, which nicely confirms the confined spinon-pair excitations reported previously [24,27,28,30]. Another important implication of this observation is that the interchain couplings provide an effective longitudinal field, which is perturbative and staggered with the peculiar form of $(-1)^i B_\parallel$ corresponding to the spin S_i^z on the ith site of the chain. Such a staggered longitudinal field is crucial for the realization of the E_8 spectrum, because via the transformation $S_i^z \rightarrow (-1)^i S_i^z$, we can map our antiferromagnetic chain into the ferromagnetic model in Eq. (1).

While all the aforementioned criteria are found to be fulfilled in $BaCo_2V_2O_8$ at zero field, it is necessary that they remain fulfilled when applying an external transverse field. In particular, to maintain the collective effects of the staggered fields, the 3D order should not be suppressed before the 1D quantum critical point is reached, i.e., $B_\perp^{c,1D} < B_\perp^{c,3D}$, as illustrated in Fig. 1(b). As we will show below, this condition is indeed realized in $BaCo_2V_2O_8$.

In a transverse field applied along the crystallographic a axis ($B_\perp \| a$), we measured the absorption spectra at 2.7 K below T_N with the linearly polarized THz magnetic field h^ω along the same orientation (i.e., $h^\omega \| B_\perp \| a$), see Fig. 2(e) (also see Supplemental Material [22]). As indicated by the arrows in Fig. 2(e), the $\mathbf{m}_1$ mode observed at 0.4 THz in zero field softens monotonically with increasing field until reaching the minimum frequency of 0.18 THz at 10 T, which is followed by a continuous increase in higher fields (e.g., 0.22 THz at 13 T). The evolution of the lowest-lying mode $\mathbf{m}_1$ reflects the field dependence of the spin excitation gap, which provides the spectroscopic evidence for the suppression of the long-range order above $B_\perp^{c,3D} = 10$ T, consistent with previous thermodynamic measurements [21]. The Néel-ordered and the paramagnetic phases are contrasted by their spin dynamic spectra, which is similar to the behavior reported in an isostructural compound [31]. Below $B_\perp^{c,3D}$, the low-field spectra are characterized by several peaks with different intensities at different energies [22]. In contrast, in the field-
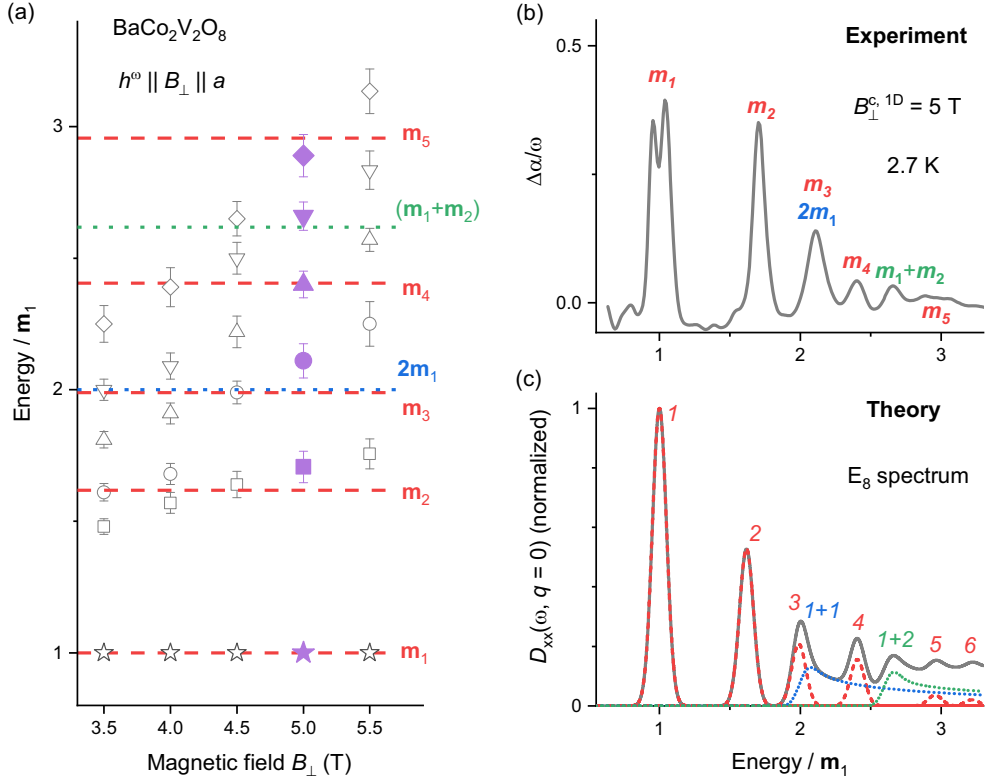
FIG. 3. (a) The ratios of the excitation energies (symbols) increase monotonically as the transverse field approaches 5 T from below, and at 5 T simultaneously reach the theoretically expected values (dashed and dotted lines) for the E_8 single- and two-particle excitations $\mathbf{m}_2$, $\mathbf{m}_3$, $2\mathbf{m}_1$, $\mathbf{m}_4$, $\mathbf{m}_1 + \mathbf{m}_2$, and $\mathbf{m}_5$ (see Table I). At $B_\perp^{c, 1D} = 5$ T, the absorption spectrum in (b) is in excellent agreement with (c) the analytically calculated spin dynamic structure factor $D^{xx}(\omega, q = 0)$ for the quantum integrable model of the E_8 dynamic spectrum (solid line) [see Eq. (2)]. The dashed and dotted lines show the separate contributions of the single-particle ($\mathbf{m}_1$ to $\mathbf{m}_6$) and two-particle ($2\mathbf{m}_1$ and $\mathbf{m}_1 + \mathbf{m}_2$) excitations, respectively [22]. Due to a strong phonon band [24], the spectrum in (b) cannot be resolved at higher energies for $\mathbf{m}_6$ to $\mathbf{m}_8$. The spectra in (c) are broadened with a full width at half maximum of $0.1\mathbf{m}_1$.

induced paramagnetic phase the spectra are dominated by two sharp peaks (e.g., 0.26 and 0.99 THz at 16 T). In addition, a small splitting of the $\mathbf{m}_1$ peak (about 0.1 meV) is resolved above 5 T but disappears above 10 T, indicating the existence of a weak orthorhombic *ab*-plane anisotropy in the 3D ordered phase [21,32], while no splitting of the higher-energy peaks can be resolved.

The transverse-field dependence of the spin dynamics in the Ising chain systems has been the subject of previous reports, based on experimental studies and/or on numerical simulations; see, e.g., Refs. [29,31,33]. Here, we focus on the discussion of the E_8 dynamics that was predicted to emerge only in the vicinity of the transverse-field Ising quantum critical point. Figure 3(a) shows the energy ratios of the higher-frequency excitations with respect to the corresponding $\mathbf{m}_1$ mode at each field. With increasing field, we observe a continuous increase of all the ratios, and at 5 T, they simultaneously reach the expected values for $\mathbf{m}_2$, $\mathbf{m}_3$ and $2\mathbf{m}_1$, $\mathbf{m}_4$, $\mathbf{m}_1 + \mathbf{m}_2$, and $\mathbf{m}_5$ of the E_8 dynamic spectrum (see Table I), as indicated

by the dashed and dotted lines. Above 5 T, the ratios deviate again from those values of the E_8 spectrum. This strongly indicates that we have experimentally realized the E_8 spectrum at 5 T [Fig. 3(b)], which also provides the dynamic evidence that $B_\perp^{c, 1D} = 5$ T corresponds to the 1D quantum critical field, with the required condition $B_\perp^{c, 1D} < B_\perp^{c, 3D}$ consistently fulfilled. The value of the 1D critical field agrees with the result of a detailed numerical simulation [33]. At the same time, Fig. 3(b) presents a very crucial feature that the two-particle continua ($2\mathbf{m}_1$ and $\mathbf{m}_1 + \mathbf{m}_2$) are characterized by a relatively narrow peak at the onset energies. This observation shows that the continua are not so overwhelming that the higher-energy E_8 particles ($\mathbf{m}_3$, $\mathbf{m}_4$, and $\mathbf{m}_5$) can still be resolved, in contrast to the conventional intuitive understanding that the high-energy E_8 particles are hidden in a featureless $2\mathbf{m}_1$ continuum [34].

To further elaborate on the dynamic characteristics, we perform analytical calculations of the quantum integrable model of the E_8 dynamic spectrum [6,12–14]. Corresponding to the

transverse THz magnetic field in the Voigt configuration, we calculate the transverse dynamic structure factor,

$$D^{xx}(\omega, q=0) = \sum_{n=0}^{\infty} \int_{-\infty}^{+\infty} \frac{d\theta_1 \cdots d\theta_n}{N(2\pi)^{n-2}} |\langle 0|\sigma^x|A_{a_1}(\theta_1)A_{a_2}(\theta_2)$$

$$\times \cdots A_{a_n}(\theta_n)\rangle|^2 \delta(\omega - E\{a_i\})\delta(P\{a_i\}), \quad (2)$$

for energy transfer ω and zero momentum transfer $q = 0$, as the wavelength of THz spectroscopy is much greater than the lattice constants of $BaCo_2V_2O_8$. In Eq. (2), $N = \prod_{i=1}^{8} n_i!$, $a_i(i = 1, \cdots, n)$ labels a particle with a corresponding mass among $\mathbf{m}_1$ to $\mathbf{m}_8$, θ_i is the corresponding rapidity, and σ^x is the Pauli matrix associated with the spin component $S^x = \sigma^x/2$. The ground state and the n-particle excited state are denoted by $\langle 0|$ and $|A_{a_1}(\theta_1)A_{a_2}(\theta_2)\cdots A_{a_n}(\theta_n)\rangle$, respectively, for $n = 1, 2, 3 \cdots$. The total energy and momentum of the n-particle excited state are $E\{a_i\} = \sum_{i=1}^{n} a_i \cosh \theta_i$ and $P\{a_i\} = \sum_{i=1}^{n} a_i \sinh \theta_i$, respectively (see Supplemental Material [22]). In particular, we derive the dynamical response in the two-particle channels, $|A_{a_1}(\theta_1)A_{a_2}(\theta_2)\rangle$, $\{a_1a_2\} = \{m_1m_1, m_1m_2, m_1m_3, m_2m_2\}$, and in the three-particle channel, $|A_{a_1}(\theta_1)A_{a_2}(\theta_2)A_{a_3}(\theta_3)\rangle$, $\{a_1a_2a_3\} = \{m_1m_1m_1\}$ (see Table I).

The obtained dynamic structure factor is presented in Fig. 3(c) up to the energy of $3.3\mathbf{m}_1$ with the peaks broadened by a full width at half maximum of $0.1\mathbf{m}_1$, which is in accord with the spectral range of our experiment. The lowest-energy $\mathbf{m}_1$ scaling with the perturbative longitudinal field is set as unit. The contributions of the single-particle excitations ($\mathbf{m}_1$ to $\mathbf{m}_6$) and of the two-particle continua ($2\mathbf{m}_1$ and $\mathbf{m}_1 + \mathbf{m}_2$) are separately plotted as dashed and dotted lines, respectively, while the higher-energy continua with smaller spectral weight are omitted for clarity [22]. The analytical results disclose very peculiar many-body dynamic characteristics. First and foremost, the multiparticle continua are not overwhelming but possess even smaller spectral weight compared with the high-energy E_8 single particles. Thus, the single-particle excitations with clearly recognized peaks stand well above the multiparticle continua, profoundly in contrast with the conventional intuitive understanding [34]. Hence, the higher-energy E_8 single particles above $2\mathbf{m}_1$ should be experimentally resolvable. Furthermore, the multiparticle continuum is not featureless, but exhibits a relatively narrow peaklike maximum just above the onset energy, which is followed by an extended tail. While the peak of $2\mathbf{m}_1$ merges coincidently with that of $\mathbf{m}_3$ into a single peak and thus cannot be discriminated experimentally, a pronounced peak due to $\mathbf{m}_1 + \mathbf{m}_2$ is clearly discernible. Although the higher-energy multiparticle continua exhibit a

similar feature, their spectral weight is very small and hardly recognized in the overall dynamic-structure-factor spectrum [22].

As compared in Figs. 3(b) and 3(c), overall excellent agreement is achieved between the experimentally observed spectrum at $B_\perp^{c,1D} = 5$ T and the precise dynamic structure factor of the E_8 dynamics for the single- and two-particle excitations. We emphasize that there are no free-tuning parameters in the field-theory calculation. The agreement between experiment and theory is achieved not only on the energy ratios but also on the relative spectral weights. Although the intensity of the observed $\mathbf{m}_1$ peak seems to be relatively low due to the splitting, the ratio of the integrated spectral weight $I_{m2}/I_{m1} \approx 0.61$ is in good agreement with the theoretically predicted value of 0.52 [see Fig. 1(a)].

These results show that the E_8 dynamic spectrum is realized in the quasi-one-dimensional antiferromagnetic chain $BaCo_2V_2O_8$ at 5 T, where a 1D transverse-field Ising quantum critical point is evidenced to be hidden under the 3D ordered phase. Our results also imply that the E_8 spectrum can generally exist near the quantum critical points of the universality class of the transverse-field Ising chain [33]. The identification of the E_8 particles and their multiparticle excitations demonstrates the emergence of the complex symmetry in the vicinity of a quantum critical point and the power of the integrable quantum field theory to describe the complex quantum critical dynamics. Our results in general shed light on the studies of nonequilibrium dynamics in the 1D models [12,18], the quantum simulations in an optical lattice [19], and the deterministic manipulation of quantum many-body states [5].

Note added in Proof. A recent inelastic neutron scattering experiment provided further evidence for the E_8 spectrum in $BaCo_2V_2O_8$ [35].

---

[1] S. Sachdev, *Quantum Phase Transitions*, 2nd ed. (Cambridge University Press, Cambridge, 2011).

[2] B. Keimer, S. A. Kivelson, M. R. Norman, S. Uchida, and J. Zaanen, From quantum matter to high-temperature superconductivity in copper oxides, Nature (London, U. K.) **518**, 179 (2015).

[3] T. Giamarchi, Ch. Rüegg, and O. Tchernyshyov, Bose-Einstein condensation in magnetic insulators, Nat. Phys. **4**, 198 (2008).

[4] F. H. L. Essler and R. M. Konik, in *From Fields to Strings: Circumnavigating Theoretical Physics*, edited by M. Shifman, A. Vainshtein, and J. Wheater (World Scientific, Singapore, 2005), Vol. 1, pp. 684–830.

[5] L. Amico, R. Fazio, A. Osterloh, and V. Vedral, Entanglement in many-body systems, Rev. Mod. Phys. **80**, 517 (2008).

[6] G. Mussardo, *Statistical Field Theory* (Oxford University Press, New York, 2010).

[7] S. Suzuki, J. Inoue, and B. K. Chakrabarti, *Quantum Ising Phases and Transitions in Transverse Ising Models*, 2nd ed. (Springer, New York, 2013).

[8] A. Dutta, G. Aeppli, B. K. Chakrabarti, U. Divakaran, T. F. Rosenbaum, and D. Sen, *Quantum Phase Transitions in Transverse Field Spin Models: From Statistical Physics to Quantum Information* (Cambridge University, Cambridge, UK, 2015).

[9] P. Pfeuty, The one-dimensional Ising model with a transverse field, Ann. Phys. (N. Y.) **57**, 79 (1970).

[10] W. Lenz, Beitrag zum verständnis der magnetischen erscheinungen in festen körpern, Phys. Z. **21**, 613 (1920).

[11] E. Ising, Beitrag zur theorie des ferromagnetismus, Z. Phys. **31**, 253 (1925).

[12] A. B. Zamolodchikov, Integrals of motion and *S*-matrix of the (scaled) $T = T_c$ Ising model with magnetic field, Int. J. Mod. Phys. A **4**, 4235 (1989).

[13] G. Delfino and G. Mussardo, The spin-spin correlation function in the two-dimensional Ising model in a magnetic field at $T = T_c$, Nucl. Phys. B **455**, 724 (1995).

[14] G. Delfino and P. Simonetti, Correlation functions in the two-dimensional Ising model in a magnetic field at $T = T_c$, Phys. Lett. B **383**, 450 (1996).

[15] P. Calabrese and J. Cardy, Time Dependence of Correlation Functions Following a Quantum Quench, Phys. Rev. Lett. **96**, 136801 (2006).

[16] J. A. Kjäll, F. Pollmann, and J. E. Moore, Bound states and E_8 symmetry effects in perturbed quantum Ising chains, Phys. Rev. B **83**, 020407 (2011).

[17] J. Wu, M. Kormos, and Q. Si, Finite-Temperature Spin Dynamics in a Perturbed Quantum Critical Ising Chain with an E_8 Symmetry, Phys. Rev. Lett. **113**, 247201 (2014).

[18] M. Kormos, M. Collura, G. Takács, and P. Calabrese, Real-time confinement following a quantum quench to a non-integrable model, Nat. Phys. **13**, 246 (2017).

[19] J. Simon, W. S. Bakr, R. Ma, M. E. Tai, P. M. Preiss, and M. Greiner, Quantum simulation of antiferromagnetic spin chains in an optical lattice, Nature **472**, 307 (2011).

[20] R. Wichmann and Hk. Müller-Buschbaum, Neue Verbindungen mit SrNiVO-struktur: $BaCo_2V_2O_8$ und $BaMg_2V_2O_8$, Z. Anorg. Allg. Chem. **534**, 153 (1986).

[21] S. K. Niesen, G. Kolland, M. Seher, O. Breunig, M. Valldor, M. Braden, B. Grenier, and T. Lorenz, Magnetic phase diagrams, domain switching, and quantum phase transition of the quasi-one-dimensional Ising-like antiferromagnet $BaCo_2V_2O_8$, Phys. Rev. B **87**, 224413 (2013).

[22] See Supplemental Material at http://link.aps.org/supplemental/10.1103/PhysRevB.101.220411 for detailed quantum field-theory calculations and more data of transmission measurements [36–38].

[23] W. Yang, J. Wu, S. Xu, Z. Wang, and C. Wu, One-dimensional quantum spin dynamics of Bethe string states, Phys. Rev. B **100**, 184406 (2019).

[24] Z. Wang, M. Schmidt, A. Loidl, J. Wu, H. Zou, W. Yang, C. Dong, Y. Kohama, K. Kindo, D. I. Gorbunov, S. Niesen, O. Breunig, J. Engelmayer, and T. Lorenz, Quantum Critical Dynamics of a Heisenberg-Ising Chain in a Longitudinal Field: Many-Body Strings versus Fractional Excitations, Phys. Rev. Lett. **123**, 067202 (2019).

[25] Z. Wang, J. Wu, W. Yang, A. Kumar Bera, D. Kamenskyi, A. T. M. Nazmul Islam, S. Xu, J. M. Law, B. Lake, C. Wu, and A. Loidl, Experimental observation of Bethe strings, Nature (London, U. K.) **554**, 219 (2018).

[26] A. Kumar Bera, J. Wu, W. Yang, R. Bewley, M. Boehm, J. Xu, M. Bartkowiak, O. Prokhnenko, B. Klemke, A. T. M. Nazmul Islam, J. M. Law, Z. Wang, and B. Lake, Dispersions of many-body Bethe strings, Nat. Phys. **16**, 625 (2020).

[27] S. Kimura, H. Yashiro, K. Okunishi, M. Hagiwara, Z. He, K. Kindo, T. Taniyama, and M. Itoh, Field-Induced Order-Disorder Transition in Antiferromagnetic $BaCo_2V_2O_8$ Driven by a Softening of Spinon Excitation, Phys. Rev. Lett. **99**, 087602 (2007).

[28] B. Grenier, S. Petit, V. Simonet, E. Canévet, L.-P. Regnault, S. Raymond, B. Canals, C. Berthier, and P. Lejay, Longitudinal and Transverse Zeeman Ladders in the Ising-Like Chain Antiferromagnet $BaCo_2V_2O_8$, Phys. Rev. Lett. **114**, 017201 (2015).

[29] Q. Faure, S. Takayoshi, S. Petit, V. Simonet, S. Raymond, L.-P. Regnault, M Boehm, J. S. White, M. Månsson, C. Rüegg, P. Lejay, B. Canals, T. Lorenz, S. C. Furuya, T. Giamarchi, and B. Grenier, Topological quantum phase transition in the Ising-like antiferromagnetic spin chain $BaCo_2V_2O_8$, Nat. Phys. **14**, 716 (2018).

[30] Z. Wang, M. Schmidt, A. K. Bera, A. T. M. N. Islam, B. Lake, A. Loidl, and J. Deisenhofer, Spinon confinement in the one-dimensional Ising-like antiferromagnet $SrCo_2V_2O_8$, Phys. Rev. B **91**, 140404 (2015).

[31] Z. Wang, J. Wu, S. Xu, W. Yang, C. Wu, A. Kumar Bera, A. T. M. Nazmul Islam, B. Lake, D. Kamenskyi, P. Gogoi, H. Engelkamp, Na. Wang, J. Deisenhofer, and A. Loidl, From confined spinons to emergent fermions: Observation of elementary magnetic excitations in a transverse-field Ising chain, Phys. Rev. B **94**, 125130 (2016).

[32] A. Okutani, S. Kimura, T. Takeuchi, and M. Hagiwara, High-field multi-frequency ESR in the quasi-1D $S = 1/2$ Ising-like antiferromagnet $BaCo_2V_2O_8$ in a transverse field, Appl. Magn. Reson. **46**, 1003 (2015).

[33] H. Zou, R. Yu, and J. Wu, Universality of Heisenberg-Ising chain in external fields, J. Phys.: Condens. Matter **32**, 045602 (2020).

[34] R. Coldea, D. A. Tennant, E. M. Wheeler, E. Wawrzynska, D. Prabhakaran, M. Telling, K. Habicht, P. Smeibidl, and K. Kiefer, Quantum criticality in an Ising chain: Experimental evidence for emergent E_8 symmetry, Science **327**, 177 (2010).

[35] H. Zou, Y. Cui, X. Wang, Z. Zhang, J. Yang, G. Xu, A. Okutani, M. Hagiwara, M. Matsuda, G. Wang, G. Mussardo, K. Hódsági, M. Kormos, Z. Z. He, S. Kimura, R. Yu, W. Yu, J. Ma, J. Wu, Exceptional E_8 symmetry in spin dynamics of quasi-one-dimensional antiferromagnet $BaCo_2V_2O_8$, arXiv:2005.13302 (2020).

[36] A. B. Zamolodchikov and A. B. Zamolodchikov, Factorized S-matrices in two dimensions as the exact solutions of certain relativistic quantum field theory models, Ann. Phys. **120**, 253 (1979).

[37] F. A. Smirnov, *Form Factors in Completely Integrable Models of Quantum Field Theory* (World Scientific, Singapore, 1992).

[38] G. Delfino, Integrable field theory and critical phenomena: The Ising model in a magnetic field, J. Phys. A: Math. Gen. **37**, R45 (2004).

Appendix 3

III

K. Amelin, J. Engelmayer, J. Viirok, U. Nagel, T. Rõõm, and Z. Wang, "Experimental observation of quantum many-body excitations of E_8 symmetry in the Ising chain ferromagnet CoNb$_2$O$_6$," *Phys. Rev. B*, vol. 102, p. 104431, Sep 2020

Experimental observation of quantum many-body excitations of E_8 symmetry in the Ising chain ferromagnet CoNb$_2$O$_6$

Kirill Amelin [ORCID],[1] Johannes Engelmayer,[2] Johan Viirok,[1] Urmas Nagel [ORCID],[1] Toomas Rõõm [ORCID],[1]
Thomas Lorenz,[2] and Zhe Wang [ORCID][2,*]

[1]*National Institute of Chemical Physics and Biophysics, 12618 Tallinn, Estonia*
[2]*Institute of Physics II, University of Cologne, 50937 Cologne, Germany*

Close to the quantum critical point of the transverse-field Ising spin-chain model, an exotic dynamic spectrum was predicted to emerge upon a perturbative longitudinal field. The dynamic spectrum consists of eight particles and is governed by the symmetry of the E_8 Lie algebra. Here we report on high-resolution terahertz spectroscopy of quantum spin dynamics in the ferromagnetic Ising-chain material CoNb$_2$O$_6$. At 0.25 K in the magnetically ordered phase we identify characteristics of the first six E_8 particles, m$_1$ to m$_6$, and the two-particle (m$_1$ + m$_2$) continuum in an applied transverse magnetic field of $B_c^{1D} = 4.75$ T, before the three-dimensional magnetic order is suppressed above $B_c^{3D} \approx 5.3$ T. The observation of the higher-energy particles (m$_3$ to m$_6$) above the low-energy two-particle continua features quantum many-body effects in the exotic dynamic spectrum.

I. INTRODUCTION

Since its invention in 1920 the Ising spin-chain model [1–3] has been demonstrated to be extremely useful to rigorously illustrate basic concepts, thus the study of Ising spin chains is still a very lively research field [4–36]. For example, a quantum phase transition occurs in the transverse-field Ising-chain model

$$H = -J \sum_i S_i^z S_{i+1}^z - B \sum_i S_i^x \qquad (1)$$

when the spin gap Δ is closed at the critical field $B_c = J/2$ with J being the exchange interaction between the nearest-neighbor spin-1/2 magnetic moments $\mathbf{S}_i$ on a chain (see Fig. 1). The transverse-field Ising-chain quantum critical point is characterized by a peculiar thermodynamic property: With decreasing temperature at the critical field, the Grüneisen parameter converges [29,37,38], in contrast to the divergent behavior for a generic quantum critical point [39].

The quantum spin dynamics also exhibits exotic features close to this quantum critical point. When the transverse-field Ising chain is perturbed by a small longitudinal field B_z via the Zeeman interaction $-B_z \sum_i S_i^z$, it was predicted that an exotic dynamic spectrum emerges around B_c, exhibiting eight particles with specific mass ratios (see Fig. 4) [9]. This exotic spectrum is uniquely described by a quantum integrable field

theory with the symmetry of the E_8 Lie algebra [9,10]. (Introductory discussions of the E_8 Lie algebra in mathematics and in the relevant context of quantum field theory can be found in Refs. [40,41].) As this model cannot be represented by single-particle states but is featured by many-body interactions, it is challenging to find an exact analytical solution beyond the quantum critical point.

Despite its celebrity in mathematics [40,41], the E_8 symmetry has rarely been explored experimentally. Until 2010 the first piece of experimental evidence for the E_8 dynamic spectrum was reported based on inelastic neutron scattering measurements of the ferromagnetic Ising chains in CoNb$_2$O$_6$ [15]. Constituted by edge-shared CoO$_6$ octahedra, the effective spin-1/2 chains in CoNb$_2$O$_6$ run along the crystallographic c axis in a zigzag manner (see inset of Fig. 1), with the Ising easy axes lying in the crystallographic ac plane [12,13,23]. Due to small but finite interchain couplings, a three-dimensional (3D) magnetic order develops below $T_C = 2.85$ K, which can be suppressed by an applied transverse field of $B_c^{3D} \approx 5.3$ T along the b axis (see Fig. 1 for an illustration) [12,13,23,42]. By following the low-lying spin excitations in the transverse field ($B \parallel b$), two modes were found with an energy ratio being the golden ratio $(1 + \sqrt{5})/2 \approx 1.618$ at 5 T [15], which corresponds to the predicted mass ratio m$_2$/m$_1$ of the first two E_8 particles [9]. The two excitations were interpreted as the low-lying E_8 particles, although the higher-energy E_8 particles were not resolved [15]. The required effective longitudinal field for realizing the E_8 dynamic spectrum is provided by interchain interactions in the ordered phase, and the corresponding one-dimensional (1D) quantum critical point at $B_c^{1D} \approx 5$ T [15] is located below the 3D quantum phase transition at $B_c^{3D} \approx 5.3$ T (see Fig. 1) [19,23].

The absence of the higher-energy E_8 particles m$_3$ to m$_8$ in the inelastic neutron scattering spectra was assumed to
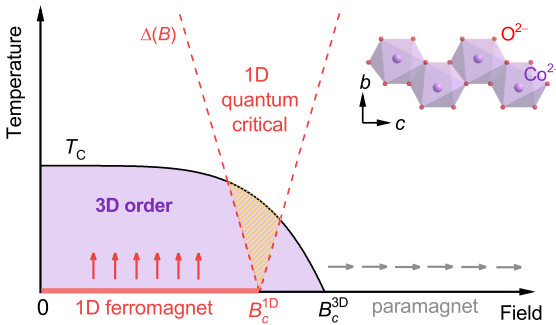
FIG. 1. Illustration of phase diagram for a quasi-one-dimensional (quasi-1D) ferromagnetic Ising-chain system in an applied transverse field. For a 1D ferromagnet, a long-range order is formed only at zero temperature, whereas a 3D order can be stabilized at a finite temperature T_C in the presence of interchain couplings. The 1D and 3D long-range orders can be suppressed by an applied transverse field at B_c^{1D} and B_c^{3D}, respectively. When $B_c^{1D} < B_c^{3D}$ the E_8 dynamic spectrum could be realized around B_c^{1D} as illustrated by the dashed area. Inset shows the zigzag spin chain constituted by edge-shared CoO_6 octahedra in $CoNb_2O_6$.

be a consequence of an overwhelming $(m_1 + m_1)$ continuum [15], since it is energetically more favorable to excite two m_1 particles, as $m_3 \lesssim 2m_1 < m_4$, m_5, m_8. This notion may be more natural for noninteracting particles, but it is not necessarily applicable to the concerned quantum many-body system [17,35,36]. Using the time-evolving block decimation, a numerical study [17] showed that the higher-energy E_8 particles up to m_5 should stand out as sharp peaks in the dynamic spectrum, whereas the $(m_1 + m_1)$ continuum contributes a relatively small background. Moreover, the two-particle continuum $(m_1 + m_2)$ was found to be characterized by a peaklike maximum at the onset energy, and thus potentially resolvable on top of the $(m_1 + m_1)$ continuum.

Very recently the findings of the numerical simulations were supported by rigorous quantum field theory analysis of the dynamic spectra of the two-particle continua [35,36], which revealed that the spectral weight of the $(m_1 + m_1)$ continuum decreases considerably with increasing energy, becoming relatively weak particularly at the energies where the higher-energy particles are predicted to appear. Moreover, it showed that the two-particle continua, such as $(m_1 + m_1)$ and $(m_1 + m_2)$, are not featureless but characterized by a peaklike maximum at the onset energies which is followed by an extended tail towards higher energies [35,36]. These theoretical results clearly showed the exotic dynamic features of this quantum many-body system, in contrast to the conventional understanding drawing from a single-particle picture. Motivated by these theoretical results, we experimentally revisited the spin dynamic spectrum in $CoNb_2O_6$ by performing high-resolution terahertz spectroscopy in an applied transverse magnetic field. We identify not only the two lowest E_8 particles but also the higher-energy ones up to m_6, as well as the peaklike maximum of the two-particle continuum $(m_1 + m_2)$, confirming the theoretical predictions of the 1D quantum many-body system [17,35,36].

II. EXPERIMENTAL DETAILS

Single crystals of $CoNb_2O_6$ were grown by the floating-zone technique, following the procedure reported in Ref. [43], with few modifications. We used polycrystalline powders of Co_3O_4 (chemical purity 99.9985%) and Nb_2O_5 (99.9985%) as starting materials. Two powder reactions were performed in air at 1200°C and 1250°C, respectively, each for 12 h. The powder was pressed to a cylindrical rod at 50 MPa, then sintered at 1275°C. A centimeter-sized single crystal was grown in an atmosphere of 80% O_2/20% Ar and small overpressure with a growth speed of 3 mm/h and a relative rotation of the rods of 30 rpm. X-ray powder diffraction measurements verified phase purity. Laue images confirmed single crystallinity, and were used for cutting b-axis-oriented platelike samples of about 3 mm in diameter and a thickness of 0.5 mm for the optical measurements. On smaller samples magnetic susceptibility measurements were performed in a 100-mT field $B \parallel b$ down to 1.8 K confirming the magnetic transitions at 2.9 and 1.9 K [13,23].

Using a Sciencetech SPS200 Martin-Puplett-type spectrometer, field-dependent terahertz transmission measurements were carried out at 4 K (above T_C) and 0.25 K (below T_C) with a liquid-helium bath cryostat and a ^{3}He - ^{4}He dilution fridge, respectively, using bolometers operating at 0.3 and 0.4 K as detectors. For the 4 K experiment, a rotatable polarizer was placed in front of the sample for tuning polarization of the terahertz waves [35,44]. For the 0.25 K measurements the sample cell was attached to the cold finger of the dilution fridge (Oxford Instruments), which was equipped with a superconducting solenoid for applying a magnetic field. The sample cell was filled with ^{4}He gas at room temperature to provide cooling of the sample. The radiation was filtered with a 0.6-THz low-pass filter at 4 K before the radiation entered the vacuum can of the dilution unit. A frequency resolution of 6 GHz was achieved in the measurements. For the optical experiments, the terahertz radiation propagated in the direction of the external magnetic field which was applied parallel to the b axis of the $CoNb_2O_6$ single crystals.

III. EXPERIMENTAL RESULTS AND DISCUSSION

Zero-field absorption spectra are displayed in Fig. 2 for 0.25 K with unpolarized terahertz radiation, and for 4 K with the terahertz electric field $e^\omega \parallel c$ and the terahertz magnetic field $h^\omega \parallel a$, and with the polarization ($e^\omega \parallel a$, $h^\omega \parallel c$). At 4 K the spectrum of ($e^\omega \parallel c$, $h^\omega \parallel a$) exhibits two peaks at 0.22 and 0.48 THz, respectively, which are denoted by M and $2M$. The nomenclature hereafter for the zero-field excitations is discriminated from that of the E_8 particles. Around the $2M$ peak one can observe a broad continuumlike feature which extends towards higher frequency. These features are similar to those reported for a different polarization ($e^\omega \parallel a$, $h^\omega \parallel b$) in Ref. [18], where the M and $2M$ peaks were assigned as the one- and two-pair spinon excitations, respectively. In contrast, these features are absent for the polarization ($e^\omega \parallel a$, $h^\omega \parallel c$) (see Fig. 2).

Compared with the 4 K spectrum, the 0.25 K one below T_C exhibits more peaks, which are labeled by M_i ($i = 1, 2, 3, \ldots, 7$) with increasing frequency. The energies of M_i
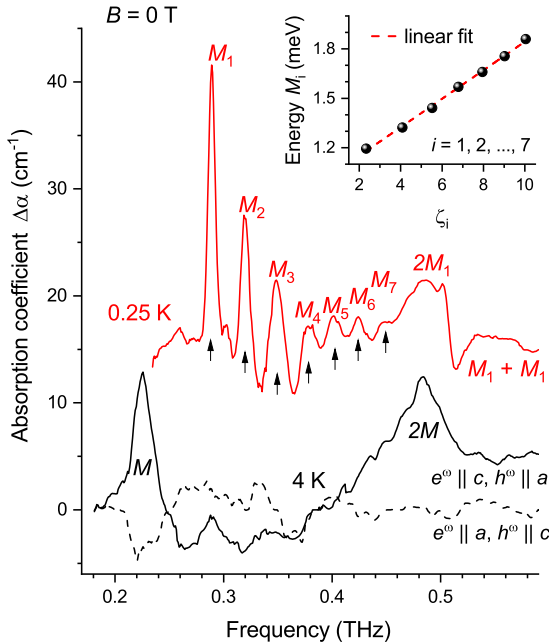
FIG. 2. Absorption spectra measured in zero field at 0.25 K (below T_c) with unpolarized terahertz radiation, and at 4 K (above T_c) for the terahertz polarizations ($e^\omega \parallel c$, $h^\omega \parallel a$) and ($e^\omega \parallel a$, $h^\omega \parallel c$). Inset shows that the eigenenergies of the modes M_1 to M_7 observed at 0.25 K follow a linear dependence on ζ_i which are the negative zeros of the Airy function $Ai(-\zeta_i) = 0$. The linear dependence is expected for confined-spinon excitations. The different nomenclature for these zero-field excitations is used in order to discriminate them from the E_8 particles close to the 1D critical field $B_c^{1D} = 4.75$ T (see below).

are shown in the inset of Fig. 2 as a function of ζ_i, the negative zeros of the Airy function $Ai(-\zeta_i) = 0$. The linear dependence on ζ_i reflects the spinon confinement in a linear confining potential [8,31], which is set up by the interchain couplings in the magnetically ordered phase [15,18,24,27–29,35]. Above M_7 one can see a broader peak around 0.49 THz (labeled $2M_1$) and a broad continuum at higher energy (labeled $M_1 + M_1$), consistent with the observation in Ref. [18]. The $2M_1$ peak corresponds to a kinetic bound state of two pairs of spinons in neighboring chains, which is located below the excitation continuum of two independent pairs of spinons ($M_1 + M_1$) [15,18]. This bound state was found at the Brillouin zone boundary $q = \pi$ by inelastic neutron scattering [15]. Due to the zigzag configuration of the chains (see inset of Fig. 1) [34], this mode is folded to the zone center ($q = 0$) and thus detected by the terahertz spectroscopy. We emphasize that the spinon dynamics and the E_8 spectrum are about very different physics. The former is about the spin dynamics of the gapped phase at zero field, whereas the latter emerges only around the field-induced quantum critical point.

An ideal way to study the E_8 dynamic spectrum would be to first drive an Ising-chain system with an applied transverse field to the quantum critical point, and then monitor the evaluation of the spin dynamics by switching on and

tuning a perturbative longitudinal field. However, such tuning can hardly be realized in a solid-state material, where an effective longitudinal field is an internal field determined by the interchain couplings. Since the transverse field will compete with the interchain couplings, the 1D quantum critical point may not be reached before the 3D order is suppressed (e.g., in $SrCo_2V_2O_8$ [24,32]). To realize the E_8 spectrum, the 1D quantum critical point should be hidden in the 3D ordered phase as illustrated in Fig. 1, which is fulfilled in the Ising-chain ferromagnet $CoNb_2O_6$ [15,19] and in the Ising-chain antiferromagnet $BaCo_2V_2O_8$ [28,35,36]. This also indicates that the observation of a spinon confinement in zero field does not necessarily imply a realization of the E_8 dynamic spectrum around the quantum critical field. Therefore, it is necessary to carry out field-dependent measurements below T_c.

The evolution of the absorption spectra of $CoNb_2O_6$ in an applied transverse field along the b axis is presented in Fig. 3 for fields just below 5 T, at which the inelastic neutron scattering experiment [15] revealed the lowest two E_8 particles, m_1 and m_2. With far more than two peaks, the absorption spectra exhibit very rich features. At 4.75 T one observes several well-defined sharp peaks at 0.16, 0.26, 0.32, 0.40, 0.47, and 0.51 THz, which are labeled m_1, m_2, ..., m_6, respectively, as indicated by the arrows. A relatively broad peak is observed at 0.43 THz as marked by the asterisk. The frequencies of m_1 and m_2 are slightly greater than the reported values of 0.12 and 0.18 THz, respectively, for the finite q-vector (3.6,0,0) by the inelastic neutron scattering experiment [15]. This difference may result from a weak dispersion perpendicular to the chain direction.

The field dependence of these modes can be clearly tracked, as indicated by the arrows in Figs. 3(a) and 3(b). Normalized to the m_1 energy in each field, the eigenenergies of these modes are presented as a function of the applied field in Fig. 4. The energy ratios of these modes increase monotonically with increasing field. At 4.75 T the predicted ratios (dashed lines, see Refs. [9,10]) for the E_8 particles up to m_6 and for the onset energies of the two-particle continua ($m_1 + m_1$) and ($m_1 + m_2$) are simultaneously reached, evidencing the observation of the E_8 dynamic spectrum. The onset of the ($m_1 + m_1$) continuum is very close to the m_3 peak ($\approx 1.989 m_1$) [9], so they cannot be distinguished from each other in the experimental spectrum. The observed features are consistent with the previous predictions from the numerical simulations [17] and the quantum field-theory analysis [35,36]. Moreover, the field-theory analysis [35,36] showed that the two-particle continua are not featureless but characterized by a peaklike maximum at the onset energies followed by a continuous decrease of spectral weight towards higher energy, which allows the identification of the continua by their peaklike maxima. Therefore, these experimental results provide unambiguous evidence for the observation of the high-energy E_8 particles, which also points to a hidden 1D quantum critical point at $B_c^{1D} = 4.75$ T confirming the scenario illustrated in Fig. 1 and discussed above. The value of B_c^{1D} is close to the reported 5 T in Ref. [15].

Previous theoretical analysis also predicted that the intensity of the E_8 particles decreases monotonically with increasing energy [10,11,17,35,36]. Indeed, this trend is
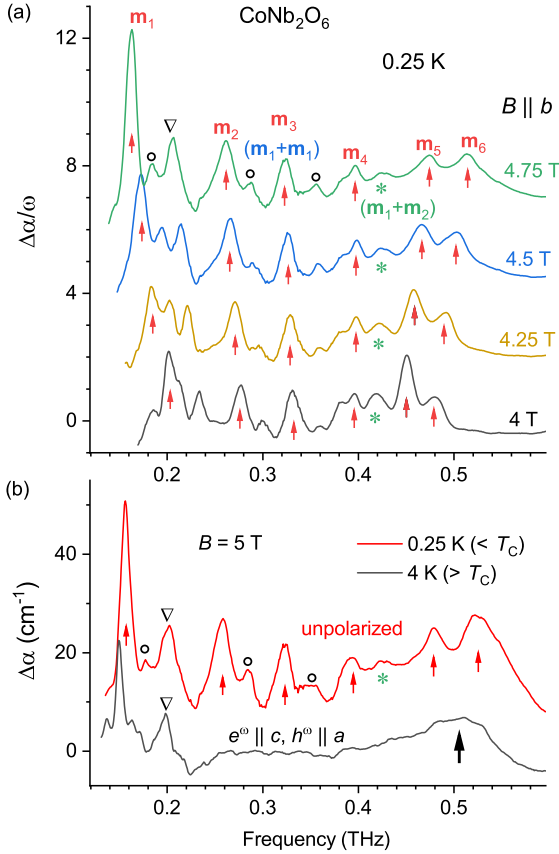
FIG. 3. (a) Absorption spectra of $CoNb_2O_6$ measured at 0.25 K in various applied transverse magnetic fields, $B \parallel b$. $\Delta\alpha$ and ω denote absorption coefficient and wave number, respectively, in the unit of cm^{-1}. The arrows indicate the modes $m_1, m_2, \ldots, m_6$ at 4.75 T and their field-dependent evolution. The asterisk ($*$) marks the onset of the $(m_1 + m_2)$ continuum. At 4.75 T the circles ($\circ$) mark the satellite peaks. The spectra in higher fields are shifted upward by a constant for clarity. (b) Absorption spectra measured at 5 T for 0.25 and 4 K below and above T_C, respectively. For 0.25 K the arrows indicate those modes marked by arrows in (a). The black arrow at the 4 K spectrum marks a broader band observed due to the zone-folding effect. The down-pointing triangle ($\triangledown$) indicates a mode which similar to m_1 is present both above and below T_C. The 0.25 K spectrum is shifted upward for clarity.

FIG. 4. Field dependence of the energies of the observed modes $m_1, \ldots, m_6$ and of the maxima for $(m_1 + m_1)$ and $(m_1 + m_2)$, normalized to the m_1 energy in each field. All the ratios exhibit a monotonic increase with increasing field. The predicted ratios (dashed lines; see Refs. [9,10]) for the E_8 particles are simultaneously reached at $B_c^{1D} = 4.75$ T, evidencing the observation of the high-energy E_8 particles in $CoNb_2O_6$.

obeyed by the first four particles (m_1 to m_4), as shown in the 4.75 T spectrum in Fig. 3(a). However, the m_5 and m_6 peaks appear to be slightly stronger. This cannot be simply attributed to the underlying continua ($m_1 + m_3$) or ($m_2 + m_2$) whose spectral weight is even smaller than the high-energy tails of the $(m_1 + m_1)$ and $(m_1 + m_2)$ continua [17,35,36]. The apparent enhancement of the m_5 and m_6 peaks is contributed by the low-lying spin excitation at the Brillouin-zone boundary ($q = \pi$) [21,22]. This relatively broad band is detected also in the disordered phase above T_c, as indicated by the arrow in the 4 K spectrum in Fig. 3(b), which is observed

due to the zone-folding effects [34]. It is a coincidence that this band is located in the energy range around the m_5 and m_6 peaks. The substantially reduced intensity of the high-energy E_8 particles could be below the resolution limit of the previous inelastic neutron scattering experiment [15], which thus were not resolved at that time. For the same reason the m_7 and m_8 modes are not resolved here either.

The field dependence of the relatively small satellite peaks, marked by the circles in Fig. 3(a), can be clearly followed as well. With decreasing field from 4.75 T one can see a reduction of the satellite-peak intensity and a concomitant merging of these peaks into the corresponding main ones. Above T_c in the disordered phase [Fig. 3(b)], these satellite peaks disappear; thus, they reflect dynamic properties of the 3D ordered phase in the transverse field. In addition, as marked by the triangles in Fig. 3(b), one can observe a peak at 0.2 THz both in the ordered and in the disordered phases. Thus, this mode should result from the 1D spin fluctuations possibly as a zone-boundary excitation observed due to subleading interactions within the zigzag chain [34].

To conclude, by performing high-resolution terahertz spectroscopy of the Ising-chain compound $CoNb_2O_6$ below and above the magnetic ordering temperature in an applied transverse field, we have revealed the dynamic features that were predicted to emerge around the transverse field-induced quantum critical point governed by the E_8 symmetry. In particular, the high-energy E_8 particles, which would be unresolvable according the picture of noninteracting particles, have been identified above the low-energy two-particle continua, featuring the quantum many-body effects. We have also observed features beyond the E_8 dynamics, which appeals for a theoretical study of a realistic model for $CoNb_2O_6$.

[1] W. Lenz, Phys. Z. **21**, 613 (1920).

[2] E. Ising, Z. Phys. **31**, 253 (1925).

[3] S. G. Brush, Rev. Mod. Phys. **39**, 883 (1967).

[4] S. Sachdev, *Quantum Phase Transitions*, 2nd ed. (Cambridge University Press, New York, 2011).

[5] A. Dutta, G. Aeppli, B. K. Chakrabarti, U. Divakaran, T. F. Rosenbaum, and D. Sen, *Quantum Phase Transitions in Transverse Field Spin Models: From Statistical Physics to Quantum Information* (Cambridge University Press, Cambridge, 2015).

[6] G. Mussardo, *Statistical Field Theory* (Oxford University Press, New York, 2010).

[7] P. Pfeuty, Ann. Phys. (NY) **57**, 79 (1970).

[8] B. M. McCoy and T. T. Wu, Phys. Rev. D **18**, 1259 (1978).

[9] A. B. Zamolodchikov, Int. J. Mod. Phys. A **4**, 4235 (1989).

[10] G. Delfino and G. Mussardo, Nucl. Phys. B **455**, 724 (1995).

[11] G. Delfino and P. Simonetti, Phys. Lett. B **383**, 450 (1996).

[12] E. Husson, Y. Repelin, N. Q. Dao, and H. Brusset, Mater. Res. Bull. **12**, 1199 (1977).

[13] T. Hanawa, K. Shinkawa, M. Ishikawa, K. Miyatani, K. Saito, and K. Kohn, J. Phys. Soc. Jpn. **63**, 2706 (1994).

[14] T. Kunimoto, K. Nagasaka, H. Nojiri, S. Luther, M. Motokawa, H. Ohta, T. Goto, S. Okubo, and K. Kohn, J. Phys. Soc. Jpn. **68**, 1703 (1999).

[15] R. Coldea, D. A. Tennant, E. M. Wheeler, E. Wawrzynska, D. Prabhakaran, M. Telling, K. Habicht, P. Smeibidl, and K. Kiefer, Science **327**, 177 (2010).

[16] S. Lee, R. K. Kaul, and L. Balents, Nat. Phys. **6**, 702 (2010).

[17] J. A. Kjäll, F. Pollmann, and J. E. Moore, Phys. Rev. B **83**, 020407(R) (2011).

[18] C. M. Morris, R. Valdés Aguilar, A. Ghosh, S. M. Koohpayeh, J. Krizan, R. J. Cava, O. Tchernyshyov, T. M. McQueen, and N. P. Armitage, Phys. Rev. Lett. **112**, 137403 (2014).

[19] A. W. Kinross, M. Fu, T. J. Munsie, H. A. Dabkowska, G. M. Luke, S. Sachdev, and T. Imai, Phys. Rev. X **4**, 031008 (2014).

[20] J. Wu, M. Kormos, and Q. Si, Phys. Rev. Lett. **113**, 247201 (2014).

[21] I. Cabrera, J. D. Thompson, R. Coldea, D. Prabhakaran, R. I. Bewley, T. Guidi, J. A. Rodriguez-Rivera, and C. Stock, Phys. Rev. B **90**, 014418 (2014).

[22] N. J. Robinson, F. H. L. Essler, I. Cabrera, and R. Coldea, Phys. Rev. B **90**, 174406 (2014).

[23] T. Liang, S. M. Koohpayeh, J. W. Krizan, T. M. McQueen, R. J. Cava, and N. P. Ong, Nat. Commun. **6**, 7611 (2015).

[24] Z. Wang, M. Schmidt, A. K. Bera, A. T. M. N. Islam, B. Lake, A. Loidl, and J. Deisenhofer, Phys. Rev. B **91**, 140404(R) (2015).

[25] Z. Wang, J. Wu, S. Xu, W. Yang, C. Wu, A. K. Bera, A. T. M. Nazmul Islam, B. Lake, D. Kamenskyi, P. Gogoi, H. Engelkamp, N. Wang, J. Deisenhofer, and A. Loidl, Phys. Rev. B **94**, 125130 (2016).

[26] Z. Wang, T. Lorenz, D. I. Gorbunov, P. T. Cong, Y. Kohama, S. Niesen, O. Breunig, J. Engelmayer, A. Herman, J. Wu, K. Kindo, J. Wosnitza, S. Zherlitsyn, and A. Loidl, Phys. Rev. Lett. **120**, 207205 (2018).

[27] Z. Wang, J. Wu, W. Yang, A. K. Bera, D. Kamenskyi, A. N. Islam, S. Xu, J. M. Law, B. Lake, C. Wu, and A. Loidl, Nature **554**, 219 (2018).

[28] Q. Faure, S. Takayoshi, S. Petit, V. Simonet, S. Raymond, L.-P. Regnault, M. Boehm, J. S. White, M. M. C. Rüegg, P. Lejay, B. Canals, T. Lorenz, S. C. Furuy, T. Giamarchi, and B. Grenier, Nat. Phys. **14**, 716 (2018).

[29] Z. Wang, M. Schmidt, A. Loidl, J. Wu, H. Zou, W. Yang, C. Dong, Y. Kohama, K. Kindo, D. I. Gorbunov, S. Niesen, O. Breunig, J. Engelmayer, and T. Lorenz, Phys. Rev. Lett. **123**, 067202 (2019).

[30] W. Yang, J. Wu, S. Xu, Z. Wang, and C. Wu, Phys. Rev. B **100**, 184406 (2019).

[31] A. J. A. James, R. M. Konik, and N. J. Robinson, Phys. Rev. Lett. **122**, 130603 (2019).

[32] Y. Cui, H. Zou, N. Xi, Z. He, Y. X. Yang, L. Shu, G. H. Zhang, Z. Hu, T. Chen, R. Yu, J. Wu, and W. Yu, Phys. Rev. Lett. **123**, 067203 (2019).

[33] A. K. Bera, J. Wu, W. Yang, R. Bewley, M. Boehm, J. Xu, M. Bartkowiak, O. Prokhnenko, B. Klemke, A. T. M. N. Islam, J. M. Law, Z. Wang, and B. Lake, Nat. Phys. **16**, 625 (2020).

[34] M. Fava, R. Coldea, and S. A. Parameswaran, arXiv:2004.04169.

[35] Z. Zhang, K. Amelin, X. Wang, H. Zou, J. Yang, U. Nagel, T. Rõom, T. Dey, A. A. Nugroho, T. Lorenz, J. Wu, and Z. Wang, Phys. Rev. B **101**, 220411(R) (2020).

[36] H. Y. Zou *et al.*, arXiv:2005.13302.

[37] J. Wu, L. Zhu, and Q. Si, Phys. Rev. B **97**, 245127 (2018).

[38] L. Zhang, Phys. Rev. Lett. **123**, 230601 (2019).

[39] L. Zhu, M. Garst, A. Rosch, and Q. Si, Phys. Rev. Lett. **91**, 066404 (2003).

[40] D. Vogan, North Am. Math. Soc. **54**, 1022 (2007).

[41] D. Borthwick and S. Garibaldi, North Am. Math. Soc. **58**, 1055 (2011).

[42] K. Matsuura, P. T. Cong, S. Zherlitsyn, J. Wosnitza, N. Abe, and T.-h. Arima, Phys. Rev. Lett. **124**, 127205 (2020).

[43] D. Prabhakaran, F. Wondre, and A. Boothroyd, J. Cryst. Growth **250**, 72 (2003).

[44] Z. Wang, S. Reschke, D. Hüvonen, S.-H. Do, K.-Y. Choi, M. Gensch, U. Nagel, T. Rõõm, and A. Loidl, Phys. Rev. Lett. **119**, 227202 (2017).

Appendix 4

IV

K. Amelin, Y. Alexanian, U. Nagel, T. Rõõm, J. Robert, J. Debray, V. Simonet, C. Decorse, Z. Wang, R. Ballou, E. Constable, and S. de Brion "Terahertz magneto-optical investigation of quadrupolar spin-lattice effects in magnetically frustrated $Tb_2Ti_2O_7$," *Phys. Rev. B*, vol. 102, p. 13442, Oct 2020

Terahertz magneto-optical investigation of quadrupolar spin-lattice effects in magnetically frustrated Tb₂Ti₂O₇

K. Amelin [1] Y. Alexanian [2] U. Nagel [1] T. Rõõm [1] J. Robert,[2] J. Debray,[2] V. Simonet [2] C. Decorse [3]
Z. Wang,[4,5,†] R. Ballou [2] E. Constable [6] and S. de Brion [2,*]

[1]*National Institute of Chemical Physics and Biophysics, Tallinn 12618, Estonia*
[2]*Université Grenoble Alpes, CNRS, Institut Néel, 38000 Grenoble, France*
[3]*ICMMO, Université Paris-Saclay, CNRS, 91400 Orsay, France*
[4]*Institute of Radiation Physics, Helmholtz-Zentrum Dresden-Rossendorf, 01328 Dresden, Germany*
[5]*Institute of Physics II, University of Cologne, 50937 Cologne, Germany*
[6]*Institute of Solid State Physics, TU Wien, 1040 Vienna, Austria*

Condensed matter magneto-optical investigations can be a powerful probe of a material's microscopic magnetoelectric properties. This is because subtle interactions between electric and magnetic multipoles on a crystal lattice show up in predictable and testable ways in a material's optical response tensor, which dictates the polarization state and absorption spectrum of propagating electromagnetic waves. Magneto-optical techniques are therefore strong complements to probes such as neutron scattering, particularly when spin-lattice coupling effects are present. Here we perform a magneto-optical investigation of vibronic spin-lattice coupling in the magnetically frustrated pyrochlore Tb₂Ti₂O₇. Coupling of this nature involving quadrupolar mixing between the Tb³⁺ electronic levels and phonons in Tb₂Ti₂O₇ has been a topic of debate for some time. This is particularly due to its implication for describing the exotic spin-liquid phase diagram of this highly debated system. A manifestation of this vibronic effect is observed as splitting of the ground and first excited crystal field doublets of the Tb³⁺ electronic levels, providing a fine structure to the absorption spectra in the terahertz (THz) frequency range. In this investigation, we apply a static magnetic field along the cubic [111] direction while probing with linearly polarized THz radiation. Through the Zeeman effect, the magnetic field enhances the splitting within the low-energy crystal field transitions revealing new details in our THz spectra. Complementary magneto-optical quantum calculations including quadrupolar terms show that indeed vibronic effects are required to describe our observations at 3 K. A further prediction of our theoretical model is the presence of a novel magneto-optical birefringence as a result of this vibronic process. Essentially, spin-lattice coupling within Tb₂Ti₂O₇ may break the optical isotropy of the cubic system, supporting two different electromagnetic wave propagations within the crystal. Together our results reveal the significance of considering quadrupolar spin-lattice effects when describing the spin-liquid ground state of Tb₂Ti₂O₇. They also highlight the potential for future magneto-optical investigations to probe complex materials where spin-lattice coupling is present and reveal new magneto-optical activity in the THz range.

I. INTRODUCTION

Interplay between spin and lattice degrees of freedom is the premise behind a range of intriguing phenomena in condensed matter systems. When we consider the fundamental role lattice geometry plays in the formation of conventional periodic magnetic order, this notion is perhaps unsurprising. Nevertheless, when energetically favorable compensations between these degrees of freedom occur, we often find novel and potentially functional material properties emerge. A case in point is found in the spin-Peirls transition of antiferromagnetic quantum spin chains where—in order to lower the total energy of the system—the lattice periodically contracts or dimerizes,

thus favoring the formation of spin singlets, along with a global energy gap of their excitations [1]. Another example is that of type II multiferroics, where the lattice reacts to a low-symmetry magnetic ordering by breaking its inversion symmetry and inducing a polar ferroelectric phase as a result of concomitant structural deformations [2]. Spin-lattice effects are also present in magnetically frustrated systems where relaxations in the elastic degrees of freedom can lift the degeneracy of magnetic configurations promoting a long-range Néel order [3,4]. On the other hand, a dynamic interplay between the spins and lattice of a frustrated system can be perpetually destabilizing, inhibiting any type of order [5]. Indeed, this scenario seems to be the case in magnetically frustrated Tb₂Ti₂O₇, which fails to develop any long-range magnetic order or static frustrated configuration. Rather, a fluctuating spin liquid behavior is observed, persisting down to temperatures as low as 50 mK [6]. A precise description of this peculiar magnetic ground state remains a hotly debated

*sophie.debrion@neel.cnrs.fr
†Present address: Fakultät Physik, Technische Universität Dortmund, 44221 Dortmund, Germany
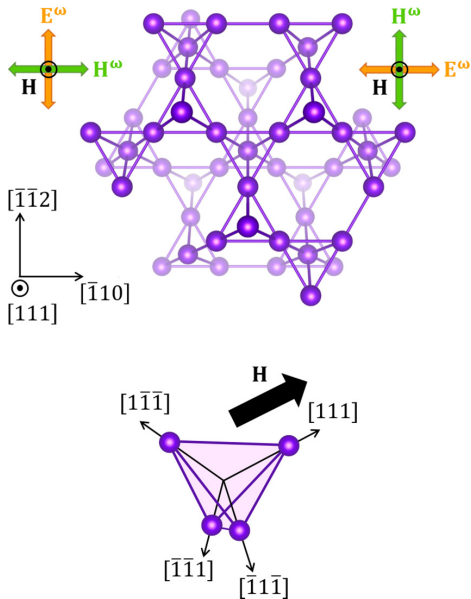
FIG. 1. $Tb_2Ti_2O_7$ cubic structure with the Tb^{3+} network. Upper part: Cross section viewed along the [111] direction showing the connection between tetrahedra. Lower part: one single tetrahedron. Two orthogonal linear polarizations of the incident light beam with **k** ∥ [111] are shown in the upper corners, where the electric field vector $\mathbf{E}^\omega$ and magnetic field vector $\mathbf{H}^\omega$ oscillate parallel to [$\bar{1}\bar{1}2$] or [$\bar{1}10$]. The static magnetic field H, shown in black, is applied perpendicular to the THz polarization plane along one of the diagonals of the cube, the [111] direction.

topic, although it is believed that spin-lattice effects play an important role [7–10].

In $Tb_2Ti_2O_7$, magnetic Tb^{3+} ions are arranged in a network of corner-sharing tetrahedra, forming the so-called pyrochlore lattice shown in Fig. 1. Among rare-earth pyrochlores, $Tb_2Ti_2O_7$ is possibly the least understood, despite having been studied for over two decades. It certainly exhibits noticeable spin-lattice coupling effects. These are observable in x-ray diffraction experiments [11] and manifest as giant magnetostriction [12], elastic softening [7], and pressure-induced magnetic ordering [13]. More recently, inelastic neutron scattering [9,10,14] and THz spectroscopy [15] measurements have highlighted the presence of vibronic coupling as a result of symmetry-allowed hybridization between phonons and the Tb^{3+} crystal electric field (CF) states both within the ground and first excited doublets. In particular, these couplings involve quadrupolar operators that depend on the phonon mode inducing the local dynamical strains. Additionally, it is now well established that the phase diagram of $Tb_2Ti_2O_7$ is extremely sensitive to off-stoichiometry compositions [16] and that $Tb_{2+x}Ti_{2-x}O_{7+y}$ enters a quadrupolar ordered phase below 500 mK for $x \geqslant -0.0025$ [16]. Evidently, quadrupolar and spin-lattice effects play an important role in the ground state of $Tb_2Ti_2O_7$ and should be considered in any attempt to understand the spin-liquid behavior of this compound.

In this study we focus on transitions between the low energy Tb^{3+} CF excitations in $Tb_2Ti_2O_7$, performing magneto-optical observations of their modulation by an applied magnetic field. The first excited CF doublet is separated from the ground state doublet by $\Delta \approx 1.5$ meV (0.37 THz, 12 cm^{-1}) [17–19], and several other higher energy CF excitations also fall within the THz energy range [20]. To the best of our knowledge, no extensive magnetic-field dependence of the CF levels in $Tb_2Ti_2O_7$ has been previously performed. Our experimental results are compared to quantitative theoretical magneto-optical calculations incorporating a quantum mechanical vibronic coupling model. Magneto-optical studies of vibronic processes in magnetic molecules have a long history within the physical chemistry community [21–23]. Within condensed matter physics, magneto-optical investigations are routinely applied to the study of coupled dielectric and magnetic order parameters of multiferroics [24–26]. Yet the combination of these ideas to probe novel spin-lattice effects in frustrated magnets has so far remained largely unexplored. The aim of this paper is to provide better insight into the magnetoelastic couplings and emerging hybrid excitations in frustrated $Tb_2Ti_2O_7$ using magneto-optical and quantitative theoretical techniques. Hence, we aim at broadening our knowledge on the microscopic mechanisms responsible for the spin liquid and quadrupolar phases it exhibits while highlighting the potential for further magneto-optical investigations of complex magnetic materials.

II. EXPERIMENTAL DETAILS

A large single crystal of $Tb_2Ti_2O_7$ was grown by the floating zone method using similar experimental parameters as in Ref. [27]. A plaquette, 220 μm thick and 4 mm in diameter, was shaped with the [111] direction of the cubic pyrochlore lattice normal to the sample surface. A wedge with an angle of $\sim 2°$ was used to avoid interference fringes in the spectra. Another piece of the single crystal cut in close proximity to the plaquette was used for specific heat measurements. The specific heat data revealed a behavior similar to results published for a $Tb_{2+x}Ti_{2-x}O_7$ composition with $x = 0.0025$ [16]—quite close to the spin liquid phase but with a quadrupolar ordering temperature of 400 mK.

Terahertz transmission magneto-optical measurements were performed by Fourier transform spectroscopy using a Martin-Puplett interferometer based at the National Institute of Chemical Physics and Biophysics in Tallinn. The $Tb_2Ti_2O_7$ sample was mounted inside of a superconducting magnet within a liquid helium bath cryostat. The transmitted THz signal was detected by a sensitive Si bolometer cooled to 300 mK using pumped ^{3}He in a separate cryogenic closed circuit. The spectral bandwidth of the setup is 3–200 cm^{-1} (0.4–25 meV). The bandwidth was further limited to 80 cm^{-1} due to strong sample absorption at high energies.

The polarization of the incident THz radiation is controlled by an aluminum wire-grid polarizer in front of the sample. The spectra were measured in the Faraday configuration with a static magnetic field up to 15 T applied along the [111] axis and the wave vector **k** ∥ [111] to the magnetic field vector **H**. At each field value, the spectrum was measured with two orthogonal polarizations, where the oscillating electric and

magnetic fields $\{\mathbf{E}^\omega, \mathbf{H}^\omega\}$ were either along $\{[\bar{1}\bar{1}2], [\bar{1}10]\}$ or $\{[\bar{1}10], [\bar{1}\bar{1}2]\}$, as shown in Fig. 1.

The spectral absorption α of a sample with thickness d is determined by $\alpha = -(1/d)\ln[(1-R)^{-2}I/I_0]$ where I_0 is the incident light intensity, I is the transmitted intensity at the detector, and R is the reflection coefficient at the sample surface. To reveal excitations that have magnetic-field dependent energies and/or intensities, a differential absorption is calculated by $\alpha_i - \alpha_{\mathrm{ref}} = -(1/d)\ln(I_i/I_{\mathrm{ref}})$. Here I_i and I_{ref} are the transmitted light intensities detected at two different values of the magnetic field strength. Here, for I_{ref} we use a reference spectrum measured at 0 T. The primary contribution to the reflection coefficient is the dielectric response of the phonon spectrum in the infrared range (100–1000 cm^{-1}) [15]. We can then safely assume that the reflection coefficient is independent of the magnetic field strength. Therefore, the reflectivity in the differential absorption $\alpha_i - \alpha_{\mathrm{ref}}$ naturally cancels out in the THz range for Tb$_2$Ti$_2$O$_7$. To deal with negative values in $\alpha_i - \alpha_{\mathrm{ref}}$ generated by spectral features in the reference spectrum (α_{ref}) that disappear under magnetic field, we subtract a statistically calculated baseline from all of the measured spectra. The baseline is created by taking the lowest value intensity at each frequency point from the set of measured spectra. Performing the baseline subtraction then corrects for any negative artifacts. The collection of baseline-corrected spectra together with the reference spectrum is what we define as the differential absorption $\Delta\alpha(H)$ that depends on the magnetic field strength.

III. THz SPECTROSCOPY RESULTS

The magnetic-field dependence of the differential absorption spectrum of Tb$_2$Ti$_2$O$_7$ is shown in Fig. 2 at two different temperatures, 3 K and 60 K. The two different THz polarizations do not show any significant differences and are only plotted at 3 K. A wide absorption band (designated ν_1) is observed centered at 14 cm^{-1}, in agreement with previous THz studies [15,20]. It corresponds to the transition between the Tb^{3+} ground state doublet and the first excited CF doublet. When the magnetic field is increased above 5 T, the absorption band appears to broaden with a slight decrease in amplitude and a shift to higher energy. At approximately the same field value, weaker excitations emerge. Two of them (ν_3 above 20 cm^{-1} and ν_4 around 10 cm^{-1}) harden with increasing magnetic field, while another one (ν_5) softens and disappears below 5 cm^{-1}. Another broad absorption band (ν_2) is seen at 75 cm^{-1} at fields below 6 T, which most likely corresponds to a transition from the ground-state level to the second excited CF level.

At 60 K, ν_1 is still present but with a lower intensity due to thermal depopulation of the ground state. It splits into two different branches in high fields. On the other hand, ν_3, ν_4, and ν_5 are no longer observed at 60 K, while ν_2 has a new component (ν_6) that softens with magnetic field.

Combined intensity maps of the field dependence of the differential absorption are shown in Figs. 3(a) and 3(b) for the measurements at 3 K and 60 K, respectively. Together the results demonstrate a high degree of modulation in the CF energy-level scheme of Tb^{3+} ions in Tb$_2$Ti$_2$O$_7$ within a magnetic field. In order to better understand this modulation
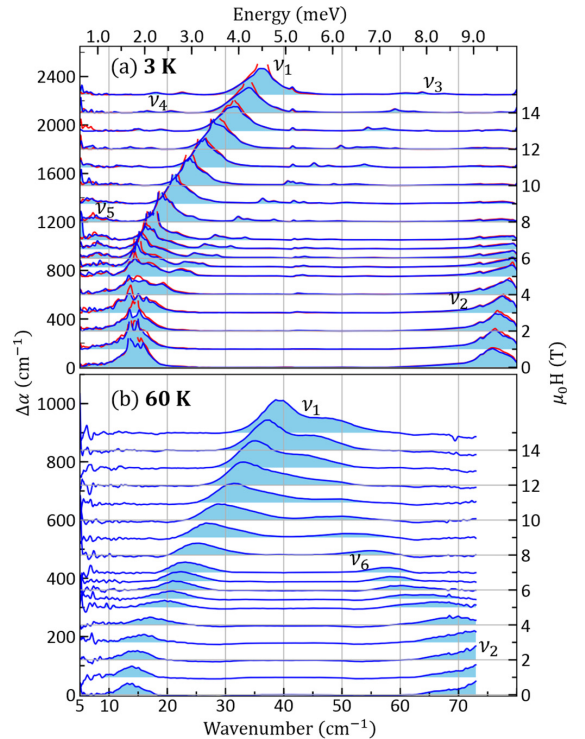
FIG. 2. $\mathbf{H} \parallel [111]$ magnetic-field dependence of the differential absorption $\Delta\alpha(H)$ in Tb$_2$Ti$_2$O$_7$ measured at (a) 3 K and (b) 60 K, with the reference absorption measured in zero field for two different THz polarizations (blue: $\mathbf{H}^\omega$ along $[\bar{1}\bar{1}2]$, red: $\mathbf{H}^\omega$ along $[\bar{1}10]$). The spectra are offset vertically in proportion to H. Shaded areas below the curves are included as a guide to the eye to highlight the different absorption bands.

and to determine the contribution from spin-lattice effects, we now turn to a comparison with theoretically calculated spectra.

IV. THEORETICAL ABSORPTION CALCULATIONS

In order to understand the Tb$_2$Ti$_2$O$_7$ absorption spectra, we use linear response theory, where the sample response to the THz wave of angular frequency ω is described by the complex magnetic susceptibility tensor $[\chi(\omega)]$. Here only the magnetic part of the THz wave is considered. Omitting possible electric effects is valid here since all the relevant CF transitions occur within the first multiplet, i.e., between states of the same parity. Without vibronic coupling, the compound remains in the cubic symmetry and the susceptibility tensor is diagonal. The absorption of a propagating THz wave with wave vector $\mathbf{k}$ is then written [28]

$$\Delta\alpha(\omega) = 2k''(\omega) \approx \frac{n\omega}{c}\chi''(\omega) \qquad (1)$$

as derived by solving Maxwell equations in an isotropic medium with weak dissipation. Here c is the speed of light in vacuum, n is the refractive index of the medium, and k is
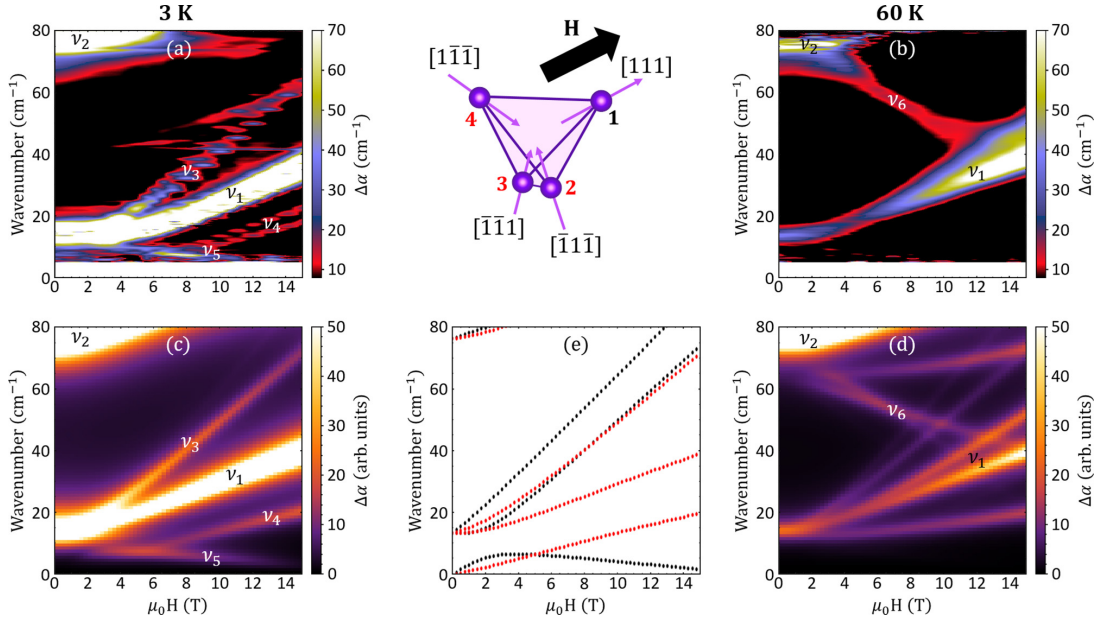
FIG. 3. Experimental and calculated THz absorption as a function of magnetic field applied along the [111] direction of $Tb_2Ti_2O_7$. The panels show the experimental results for 3 K (a) and 60 K (b), and the theoretical calculations for 3 K (c) and 60 K (d). The four Tb^{3+} sites on the tetrahedron (one with the field along its threefold axis shown in black and the three remaining sites shown in red) and the corresponding field dependence of the calculated energy of their absorption branches at 3 K are presented in the middle panels (e). The different observed branches are labeled ν_1 to ν_6.

the wave number. Here and further, the notations prime and double prime refer, respectively, to the real and imaginary part of a quantity. The wave vector can be written as $\mathbf{k} = k\mathbf{u}$ where $\mathbf{u}$ is a vector perpendicular to the wavefront. In the isotropic case that includes the cubic symmetry relevant to pyrochlore compounds, the Poynting vector of the electromagnetic wave $\mathbf{S} = \mathrm{Re}[\mathbf{E}^\omega \times \overline{\mathbf{H}}^\omega]$ is collinear with $\mathbf{k}$ outside and inside the material. Here $\overline{\mathbf{H}}^\omega$ stands for the complex conjugate of $\mathbf{H}^\omega$. The refractive index n is considered constant since the main contribution comes from optical phonons that are at energies higher than the measured THz range (see Ref. [15] and supplementary material therein). This is generally the case in oxides below 80 cm^{-1} where absorption is low and very few phonons are present. In our calculations we used $n = 7.7$ as deduced from the dielectric constant of $Tb_2Ti_2O_7$ at 6 K [15].

We now introduce vibronic couplings, which arise from dynamical strains that break the local symmetry. Thus, the four Tb^{3+} sites of a tetrahedron become inequivalent and the whole tetrahedron has to be considered. At this scale, the magnetic susceptibility tensor remains diagonal but becomes slightly anisotropic, quite similarly to birefringent crystals in optics. When a static magnetic field is applied along the [111] cubic direction, nondiagonal components appear in the susceptibility tensor. Two normal modes (indexed by $\alpha = \{1, 2\}$ with different absorption are then derived from the Maxwell's equations. They are characterized by their wave vectors $\mathbf{k}_\alpha$ and their Poynting vectors $\mathbf{S}_\alpha = \mathrm{Re}[\mathbf{E}^\omega_\alpha \times \overline{\mathbf{H}}^\omega_\alpha]$ that are no longer collinear. The THz wave polarization in the material characterized by the magnetic induction $\mathbf{B}^\omega =$

$\mu_0(1 + [\chi(\omega)])\mathbf{H}^\omega$ is no longer collinear with $\mathbf{H}^\omega$. This is illustrated in Fig. 4. A similar effect has been predicted by considering electric quadrupole and magnetic dipole mixing in antiferromagnets [29]. To our knowledge, this example involving vibronic processes in a frustrated magnet has not been previously reported.

The total absorption in the crystal will then contain contributions of these two modes. The transmitted intensity is given
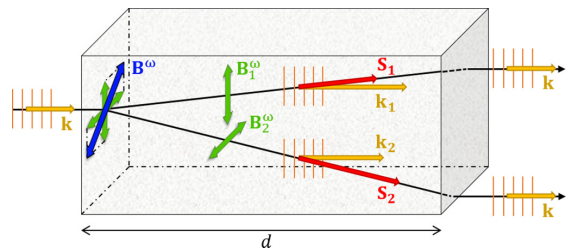
FIG. 4. THz wave propagation in an anisotropic medium. The wave, linearly polarized along $\mathbf{B}^\omega$ (blue), is decomposed into the two—orthogonal and linearly polarized for simplicity of the picture—normal modes polarized along $\mathbf{B}^\omega_1$ and $\mathbf{B}^\omega_2$ (green). Inside the crystal the two waves are normal modes, and the rays propagate independently in the direction of their Poynting vector $\mathbf{S}_1$ and $\mathbf{S}_2$ (red) with wave vector $\mathbf{k}_1$ and $\mathbf{k}_2$, respectively, which have the same direction (orange). At the output face, in vacuum, the Poynting vectors are collinear again.

by

$$I = e^{-2k_1''d}\text{Re}[\mathbf{s_{11}}] + e^{-2k_2''d}\text{Re}[\mathbf{s_{22}}]$$
$$+ e^{-(k_1''+k_2'')d}\text{Re}[e^{i\Delta k'd}\mathbf{s_{12}} + e^{-i\Delta k'd}\mathbf{s_{21}}], \quad (2)$$

where $\Delta k' = k_1' - k_2'$ and $\mathbf{s_{ij}} \propto \mathbf{E}_i^\omega \times \overline{\mathbf{H}_j^\omega}$. The last term in Eq. (2) is similar to an interference term when the two normal modes are not orthogonal. The case of orthogonal modes has been developed in Ref. [30] and the associated absorption is written as:

$$\Delta\alpha(\omega) = \frac{2k_1''(\omega)\text{Re}[\mathbf{s_{11}}] + 2k_2''(\omega)\text{Re}[\mathbf{s_{22}}]}{\text{Re}[\mathbf{s_{11}}] + \text{Re}[\mathbf{s_{22}}]}. \quad (3)$$

When $k_1 = k_2 \equiv k$, the isotropic case [equation (1)] is recovered.

Equation (3) allows us to calculate the differential absorption for the wave vector of the two normal modes k_α. These are functions of the complex magnetic susceptibility tensor components χ_{ij} which are given by:

$$\chi_{ij}(\omega) = \frac{\mu_0(g_J\mu_B)^2}{V}\sum_{mn}\frac{P_n - P_m}{(E_m - E_n - \hbar\omega)^2 + \Gamma^2}$$
$$[i\Gamma + (E_m - E_n - \hbar\omega)]J_{nm}^i J_{mn}^j, \quad (4)$$

where g_J is the Landé factor, V is the sample volume, E_m and E_n is the energy of the different electronic levels, P_n and P_m are the thermal populations of initial and final states, and J_{nm}^i is the matrix element of the angular momentum in the i direction between electronic states $|n\rangle$ and $|m\rangle$ of their angular momentum in the i direction. One single linewidth Γ is used for simplicity. The energy levels are determined by diagonalizing the corresponding Hamiltonian. We will consider only those levels that fall within the THz energy range at low temperatures—i.e., the ground, first, and second levels. The Hamiltonian consists of several terms. The first one, the CF Hamiltonian, describes the effects of the charges surrounding each Tb^{3+} ion on its electronic states in its local D_{3d} symmetry. These ions generate four Bravais lattices from each of the four vertices of an initial Tb tetrahedron, the basic element of the pyrochlore structure. The axis of the threefold symmetry for each ion is parallel to a distinct member of the family of $\langle 111\rangle$ diagonals of the cubic structure characterizing the global symmetry of the material. By selecting this local threefold axis as the quantization z axis and the local twofold axis as the x axis which gives rise to the point group D_{3d}, the CF Hamiltonian is written for each ion in the same form

$$\widehat{\mathcal{H}}_{\text{CF}} = B_2^0\widehat{\mathcal{O}}_2^0 + B_4^0\widehat{\mathcal{O}}_4^0 + B_4^3\widehat{\mathcal{O}}_4^3 + B_6^0\widehat{\mathcal{O}}_6^0 + B_6^3\widehat{\mathcal{O}}_6^3 + B_6^6\widehat{\mathcal{O}}_6^6, \quad (5)$$

where the expansion in Stevens equivalent operators (quadrupolar $\widehat{\mathcal{O}}_2^0$, hexadecapolar $\widehat{\mathcal{O}}_4^0$, $\widehat{\mathcal{O}}_4^3$, and hexacontatetrapolar $\widehat{\mathcal{O}}_6^0$, $\widehat{\mathcal{O}}_6^6$) terms is given by the local D_{3d} symmetry of the Tb^{3+} ions. For correspondence with Wybourne and angular momentum operators, see Appendices A and B.

When a static magnetic field **H** is applied along the [111] direction of the pyrochlore cubic lattice, one Tb^{3+} ion out of four has its threefold axis along the magnetic field, while the three remaining sites have their threefold axes at the same colatitude (polar angle) from the magnetic field and behave

TABLE I. CF parameters used in the CF Hamiltonian.

B_k^q	meV	K
B_2^0	-0.26	-3.0
B_4^0	4.5×10^{-3}	5.2×10^{-2}
B_4^3	-4.1×10^{-2}	-4.8×10^{-1}
B_6^0	-4.5×10^{-6}	-5.2×10^{-5}
B_6^3	-1.2×10^{-4}	-1.4×10^{-3}
B_6^6	-1.4×10^{-4}	-1.6×10^{-3}

similarly. The corresponding Zeeman Hamiltonian is given by

$$\widehat{\mathcal{H}}_Z = -g_J\mu_B\mu_0\mathbf{H}\cdot\widehat{\mathbf{J}}, \quad (6)$$

where $g_J\mu_B\widehat{\mathbf{J}}$ is the Tb^{3+} ion's total magnetic moment ($J = 6$). Finally, the total Hamiltonian for noninteracting tetrahedra is given by

$$\widehat{\mathcal{H}} = \sum_{k=1}^4 \widehat{\mathcal{H}}_{\text{CF}}^k + \widehat{\mathcal{H}}_Z^k. \quad (7)$$

As shown in Eq. (5), the CF Hamiltonian is described in a local frame for each Tb^{3+} ion, while the Zeeman term is better described in the global cubic frame. Therefore, the Stevens equivalent operators must be rotated from the local frame associated to each Tb ion, to the global cubic frame.

The results of the calculations using the Hamiltonian of Eq. (4) (without vibronic coupling) are shown in Fig. 3. The CF parameters were chosen from the literature [14] except for B_2^0 and B_2^4 which were slightly adjusted to match the 14 cm^{-1} transition observed at 3 K and 0 T (see Table I and Appendix B). Wave functions for the ground and first excited doublets are given in Appendix C. An effective Landé factor $g_J \approx 1.4$ is deduced from the magnetic-field dependence of the measured spectra. The obtained value is slightly lower than $g_J = 1.5$ expected for a pure Tb^{3+} ion ground multiplet and reveals the J-mixing effects seen in the intermediate coupling regime [14]. A single linewidth of 2.4 cm^{-1} is used, in agreement with the zero-field data. We find no significant dependence on the polarization of the THz radiation in the calculated spectra, consistent with experiment. The calculated absorption has two contributions when the applied static magnetic field is varied [see panel (e) in Fig. 3]: one from the Tb^{3+} site (1) that has its local threefold axis along the magnetic field direction, the other one from the three other sites (2–4) on the tetrahedron that have their local threefold axes at 109.5 degrees relative to the applied magnetic field. When the magnetic field is increased, the ground and first excited CF levels—both of which are doublets—split into two branches: a softening lower-frequency branch and a hardening higher-frequency branch that decreases (respectively increases) in energy with increased magnetic field. The second CF level is a singlet and its energy increases with the magnetic field.

As seen in Fig. 3, the agreement with the experimental data is already remarkable. The field dependence of the main excitations ν_1 and ν_2 is well reproduced at 3 K. The first one originates entirely from sites 2–4 and corresponds to the transition to their first CF level. The second one has contributions from all sites and is the transition to the second CF level.
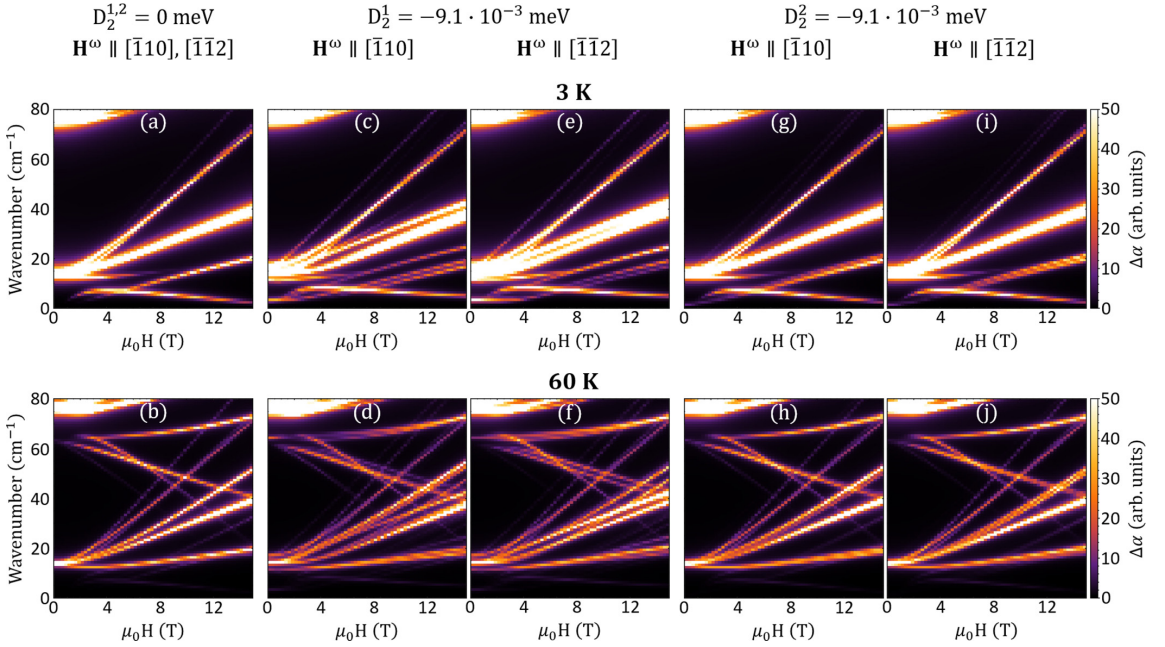
FIG. 5. Calculated absorption as a function of magnetic field applied along [111] at 3 K and 60 K for two THz polarizations with no vibron [(a),(b)], with a vibron associated with $\mathcal{O}_2^1$ [(c)–(f)], and a vibron associated with $\mathcal{O}_2^2$ [(g)–(j)] quadrupolar operators.

Weaker features in the absorption maps are also reasonably well reproduced: ν_3 for the transition to the first CF level (upper branch for sites 2–4 and lower branch for site 1) and ν_4 for the transition within the initial ground doublet for sites 2–4. Also note the peculiar magnetic-field dependence of ν_5: For a field lower than 3 T it is the equivalent of ν_4 for site (1), but above 3 T, the transition to the first excited CF level occurs, producing the only excitation decreasing in energy with the magnetic field. A third branch starting at 14 cm^{-1} and increasing more rapidly under magnetic field than the other branches [visible in Fig. 3(e)] is calculated to be very weak in intensity. It is not visible in either of the calculated or measured absorption maps [Figs. 3(c) and 3(a)].

With our theoretical basis for the field dependence of the CF energy scheme we also reproduce the 60 K results: the main branches, ν_1 at 14 cm^{-1} and ν_2 at 70 cm^{-1}, as well as a new branch decreasing from 75 cm^{-1} (ν_6). Noticeably, two additional weak and rather flat branches are calculated around 65 cm^{-1} and 14 cm^{-1} but not observed in the THz absorption spectra.

As the next step, we have performed calculations including spin-lattice effects through vibronic couplings between the Tb^{3+} crystal field excitations and transverse phonon modes. It has been shown that there are two vibronic processes present: one that couples the first excited Tb^{3+} CF level with a silent optical phonon of T_{2u} symmetry and another one that involves an acoustic phonon coupled to both the ground and first excited CF levels [15]. In particular, these spin-lattice couplings were shown to involve the Tb^{3+} quadrupolar degrees of freedom and give rise to the following symmetry-constrained

vibronic Hamiltonian

$$\widehat{\mathcal{H}}_{\text{vib}} = D_2^0 \widehat{\mathcal{O}}_2^0 + D_2^1 \big(\widehat{\mathcal{O}}_2^1 + \widehat{\mathcal{O}}_2^{-1}\big) + D_2^2 \big(\widehat{\mathcal{O}}_2^2 + \widehat{\mathcal{O}}_2^{-2}\big) \quad (8)$$

when the vibronic coupling is assumed isotropic in the plane perpendicular to the threefold axis. Note that the quadrupolar operator $\widehat{\mathcal{O}}_2^0$ is already present in the CF Hamiltonian. It accounts for the coupling to the silent optical phonon and will not change the symmetry of the system but will simply renormalize its energy eigenvalues. On the other hand, $\widehat{\mathcal{O}}_2^m$ operators with $m = \pm 1, \pm 2$, associated with the acoustic phonons, are not present in the CF Hamiltonian. They induce a splitting of the ground and first excited CF doublets as described in Ref. [15]. The associated wave functions are given in Appendix C. The resulting susceptibility tensor is no longer diagonal and the crystal becomes slightly birefringent.

The influence of both terms (D_2^1 and D_2^2) of the acoustical vibronic coupling on the calculated absorption spectra is presented in Fig. 5. A smaller linewidth of 0.5 cm^{-1} was used in the calculation to better distinguish the different branches that appear due to the vibronic coupling. The Tb^{3+} sites 2–4 are no longer equivalent and the associated branches are split into two or three components that are more or less distinguishable. This is particularly true for the lower-energy branch at 3 K just below ν_1, where two groups of lines are now clearly observed in agreement with the experimental data for ν_4. At 60 K absorption branches are more spread out and therefore less intense. We suspect this could be an explanation for the absence of the flatter bands in the experimental data. Their combination of weak intensity and moderate field dependence would cancel them out in our back-

ground subtraction analysis method. Furthermore, we also note the slight polarization dependence that shows up at both temperatures.

V. DISCUSSION

A comparison of the experimental and the simulated magneto-optical THz spectra demonstrates that the low-energy dynamics of $Tb_2Ti_2O_7$ is well captured by a simple Hamiltonian with only CF and Zeeman contributions. However, our results also indicate that including spin-lattice effects by way of vibronic coupling provides an improved agreement between theory and experiment with the addition of several weaker branches at both 3 K and 60 K. Although subtle, these features are clearly evident in the experimental data, particularly for the transition assigned ν_4. They provide strong evidence that spin-lattice coupling is at play within the energy and time scales relevant to the ground state of this quantum spin liquid. In particular, the vibronic couplings of quadrupolar origin will lower the symmetry of the dynamical susceptibility tensor, which, without external magnetic field, becomes slightly orthorhombic. This implies a dynamic modulation of the local CF environment that describes the magnetic behavior including the potential for entanglement between the different CF levels.

Our results confirm that entanglement between the ground and first excited CF states through the vibronic process is of utmost importance in understating the phase diagram of $Tb_2Ti_2O_7$ at lower temperatures, as was already suggested in Ref. [15]. It is difficult to unambiguously quantify the strength of the quadrupolar couplings associated with $\mathcal{O}_2^1$ and $\mathcal{O}_2^2$. However, according to the observed splittings of the different branches, the D_2^1 and/or D_2^2 terms fall within the energy range 0–10 μeV. Note that these operators, having E_g symmetry in the local D_{3d} environment, have $E_g \oplus T_{1g} \oplus T_{2g}$ symmetry in the global cubic environment. From a symmetry point of view, they are equivalent to a combination of tetragonal and trigonal stress. Nothing clearly distinguishes one operator from the other, except for their strength. As can be seen in Figs. 5(c), 5(e) 5(g), and 5(h), operator $\mathcal{O}_2^{\pm1}$ has a larger effect on the splitting of the different branches than $\mathcal{O}_2^{\pm2}$ does. As a matter of fact, the matrix elements of $\mathcal{O}_2^{\pm1}$ between the ground and first excited states are five times larger than those of $\mathcal{O}_2^1$ at zero applied magnetic field, which would imply five times larger vibronic effects for equal D_2^1 and D_2^2 parameters. This is consistent with the oscillator strength associated with each of the quadrupolar operators, which depends on the structure of the ground and excited doublet states. Note that all of these operators act on the transverse components of the Tb^{3+} angular momentum. It is then possible that these vibronic couplings have some role to play in the low temperature phase diagram of $Tb_{2+x}Ti_{2-x}O_{7+y}$ below 1 K, where a spin liquid or a quadrupolar ordered phase is observed [31].

Finally, due to the high magnetic fields used in this study, we have been able to refine with greater precision the crystal field parameters (see Table I) and the Landé factor $g_J \approx 1.4$. Within the energy range probed, there is no sign of spin waves down to 3 K, which could be present due to a possible ordered magnetic state as observed by neutron diffraction at 40 mK

TABLE II. Values of λ_n^m parameters involved in the CF Hamiltonian of the studied pyrochlore.

λ_2^0	λ_4^0	λ_4^3	λ_6^0	λ_6^3	λ_6^6
1/2	1/8	$-\sqrt{35}/2$	1/16	$-\sqrt{105}/8$	$\sqrt{231}/16$

[32]. Indeed our analysis is in perfect agreement with the measured "3-in/1-out, 3-out/1-in" spin orientation per tetrahedron induced by the magnetic field applied along [111] as well as the proposed dynamical Jahn-Teller model [32]. Our results and analysis allow us to give a more precise description of these spin-lattice couplings.

VI. CONCLUSION

By performing magneto-optical THz spectroscopy measurements of $Tb_2Ti_2O_7$, we have showed the magnetic field dependent evolution of the low energy CF level scheme for Tb^{3+}. Using a simple-model Hamiltonian that incorporates CF and Zeeman contributions, we were able to reproduce the overall field-dependent trends observed in the experiments, in particular the multiple branches that can be attributed to transitions between the different levels for each site in the elementary tetrahedra. However, finer structure observed in the experiment cannot be captured by the simple model and is only reproduced after the inclusion of a vibronic spin-lattice coupling process where the ground and first excited CF doublets are hybridized with acoustic phonons by way of quadrupolar Stevens equivalent operators. The results add further support to the growing evidence that spin-lattice coupling and quadrupolar terms are important when describing the frustrated ground state of $Tb_2Ti_2O_7$, a topic that is still under debate. Finally, we also predict that under an external magnetic field, these couplings induce a novel birefringent response of this otherwise cubic pyrochlore. While this effect has not been tested, a direct measurement would provide further support to the vibronic model. We suggest that this highlights the potential for future magneto-optical investigations aimed at probing complex magnetic phases where spin and lattice degrees of freedom are present. It also open new routes to design magneto-optically active materials.

TABLE III. Matrix element $\theta_n(J)$ for Tb^{3+} ($J = 6$).

θ_2	θ_4	θ_6
$-1/99$	$2/16335$	$-1/891891$

TABLE IV. CF B_n^m parameters (in meV) refined in different recent studies, together with those used in this work. *LS-coupling scheme. **Intermediate coupling scheme.

	B_2^0	B_4^0	B_4^3	B_6^0	B_6^3	B_6^6
Ref. [37]	−0.34	4.9×10^{-3}	4.3×10^{-2}	$−7.9 \times 10^{-6}$	1.3×10^{-4}	$−1.1 \times 10^{-4}$
Ref. [38]	−0.28	5.0×10^{-3}	3.4×10^{-2}	$−7.5 \times 10^{-6}$	1.1×10^{-4}	$−1.2 \times 10^{-4}$
Ref. [39]	−0.73	4.1×10^{-3}	5.9×10^{-2}	$−12 \times 10^{-6}$	$−5.0 \times 10^{-4}$	$−8.5 \times 10^{-4}$
Ref. [42]	−0.28	5.7×10^{-3}	4.6×10^{-2}	$−8.0 \times 10^{-6}$	1.6×10^{-4}	$−1.3 \times 10^{-4}$
Ref. [14]*	−0.28	4.7×10^{-3}	4.1×10^{-2}	$−4.5 \times 10^{-6}$	1.2×10^{-4}	$−1.4 \times 10^{-4}$
Ref. [14]**	−0.27	5.6×10^{-3}	3.9×10^{-2}	$−6.9 \times 10^{-6}$	1.7×10^{-4}	$−1.4 \times 10^{-4}$
This work	−0.26	4.5×10^{-3}	$−4.1 \times 10^{-2}$	$−4.5 \times 10^{-6}$	$−1.2 \times 10^{-4}$	$−1.4 \times 10^{-4}$

ject No. B05). SciPy library [33] for Python was used for the data analysis and representation, and the crystal structure was modeled in Vesta software [34].

K.A. and Y.A. contributed equally to this work. K.A.,T.R., and U.N. performed the THz measurements, K.A. analyzed the experimental data. Y.A. developed the THz calculations with inputs from R.B., J.R., V.S., and S.deB. C.D. grew the single crystal, Y.A. and J.D. prepared the plaquettes. Z.W., E.C., and S.deB. have coordinated the project. K.A., Y.A., E.C., and S.deB. prepared the figures and wrote the paper with inputs from all authors.

APPENDIX A: STEVENS EQUIVALENT OPERATORS

The Stevens equivalent operators $\widehat{\mathcal{O}}_n^m$ used in equations (5) and (8) can be expressed as functions of the angular momentum operators $\widehat{J}_{x,y,z}$ and $\widehat{J}_{+,-}$ of the rare earth ground multiplet. Here we give their correspondence together with the one for Stevens equivalent operators using the x, y, z, notation. These operators are tabulated in Refs. [35,36]. We will use

$$\widehat{X} = J(J+1)\widehat{I},$$

where $\widehat{I}$ is the identity operator. It follows that

$$\widehat{\mathcal{O}}_2^0 = \widehat{\mathcal{O}}_{z^2} = 3\widehat{J}_z - \widehat{X}$$

$$\widehat{\mathcal{O}}_2^1 = \widehat{\mathcal{O}}_{xz} = \frac{1}{2}(\widehat{J}_z\widehat{J}_x + \widehat{J}_x\widehat{J}_z)$$

$$\widehat{\mathcal{O}}_2^{-1} = \widehat{\mathcal{O}}_{yz} = \frac{1}{2}(\widehat{J}_z\widehat{J}_y + \widehat{J}_y\widehat{J}_z)$$

$$\widehat{\mathcal{O}}_2^2 = 2\widehat{\mathcal{O}}_{x^2-y^2} = \frac{1}{2}(\widehat{J}_+^2 + \widehat{J}_-^2) = \widehat{J}_x^2 - \widehat{J}_y^2$$

$$\widehat{\mathcal{O}}_2^{-2} = 2\widehat{\mathcal{O}}_{xy} = -\frac{i}{2}(\widehat{J}_+^2 - \widehat{J}_-^2) = \widehat{J}_x\widehat{J}_y + \widehat{J}_y\widehat{J}_x$$

$$\widehat{\mathcal{O}}_4^0 = 35\widehat{J}_z^4 - [30\widehat{X} - 25\widehat{I}]\widehat{J}_z^2 + [3\widehat{X}^2 - 6\widehat{X}]$$

$$\widehat{\mathcal{O}}_4^3 = \frac{1}{4}[\widehat{J}_z(\widehat{J}_+^3 + \widehat{J}_-^3) + (\widehat{J}_+^3 + \widehat{J}_-^3)\widehat{J}_z]$$

$$\widehat{\mathcal{O}}_4^4 = \frac{1}{2}(\widehat{J}_+^4 + \widehat{J}_-^4)$$

$$\widehat{\mathcal{O}}_6^0 = 231\widehat{J}_z^6 - [315\widehat{X} - 735\widehat{I}]\widehat{J}_z^4$$
$$+ [105\widehat{X}^2 - 525\widehat{X} + 294\widehat{I}]\widehat{J}_z^2$$
$$- [5\widehat{X}^3 - 40\widehat{X}^2 + 60\widehat{X}]$$

$$\widehat{\mathcal{O}}_6^3 = \frac{1}{4}[\{11\widehat{J}_z^3 - (3\widehat{X} + 59\widehat{I})\widehat{J}_z\}(\widehat{J}_+^3 + \widehat{J}_-^3)$$
$$+ (\widehat{J}_+^3 + \widehat{J}_-^3)\{11\widehat{J}_z^3 - (3\widehat{X} + 59\widehat{I})\widehat{J}_z\}]$$

$$\widehat{\mathcal{O}}_6^6 = \frac{1}{2}(\widehat{J}_+^6 + \widehat{J}_-^6)$$

APPENDIX B: CRYSTAL FIELD PARAMETERS LITERATURE REVIEW

In the pyrochlore literature, there exists mainly two ways to write the crystal field (CF) Hamiltonian of the rare earth element: with Stevens equivalent operators $\widehat{\mathcal{O}}_n^m$ as in this study and in Refs. [37–39] and with the Wybourne operators [40,41] $\widehat{\mathcal{C}}_m^n$, as in Refs. [14,17,19,42]. The Wybourne operators are defined as

$$\widehat{\mathcal{C}}_m^n = \sqrt{\frac{4\pi}{2n+1}}\widehat{Y}_n^m, \tag{B1}$$

where $\widehat{Y}_n^m$ are the spherical harmonics operators. The CF Hamiltonian for the D_{3d} point group relevant for the rare earth element in the pyrochlore compounds is then

$$\widehat{\mathcal{H}}_{CF}^{(Wy)} = W_0^2\widehat{\mathcal{C}}_0^2 + W_0^4\widehat{\mathcal{C}}_0^4 + W_3^4(\widehat{\mathcal{C}}_{-3}^4 - \widehat{\mathcal{C}}_3^4) + W_0^6\widehat{\mathcal{C}}_0^6$$
$$+ W_3^6(\widehat{\mathcal{C}}_{-3}^6 - \widehat{\mathcal{C}}_3^6) + W_6^6(\widehat{\mathcal{C}}_{-6}^6 + \widehat{\mathcal{C}}_6^6), \tag{B2}$$

TABLE V. Wave functions of the ground and first excited doublets, obtained by diagonalization of the CF Hamiltonian [equation (5)] without vibronic coupling ($D_2^1 = D_2^2 = 0$). The value in brackets following the wave-function name is its associated eigenenergy.

	$|\psi_+^0\rangle$(0.0)	$|\psi_-^0\rangle$(0.0)	$|\psi_+^1\rangle$(13.5)	$|\psi_-^1\rangle$(13.5)
$|6\rangle$				
$|5\rangle$	0.35		−0.89	
$|4\rangle$		−0.91		−0.37
$|3\rangle$				
$|2\rangle$	0.18		−0.25	
$|1\rangle$		−0.13		−0.14
$|0\rangle$				
$|-1\rangle$	−0.13		−0.11	
$|-2\rangle$		−0.18		0.25
$|-3\rangle$				
$|-4\rangle$	0.91		0.37	
$|-5\rangle$		0.35		−0.89
$|-6\rangle$				

TABLE VI. Wave functions of the ground and first excited doublets, obtained by diagonalization of the CF Hamiltonian [equation (5)] with a vibronic coupling parameter $D_2^1 = -9.1 \times 10^{-3}$ meV. The value in brakets following the wave-function name is its associated eigenenergy. Only coefficients of wave functions $> 10^{-2}$ are shown.

	$\|\psi_1\rangle(0.0)$	$\|\psi_2\rangle(2.76)$	$\|\psi_3\rangle(13.8)$	$\|\psi_4\rangle(16.6)$
$\|6\rangle$				
$\|5\rangle$	-0.30	$-0.09 - 0.12i$	$-0.14 + 0.64i$	$-0.13 - 0.59i$
$\|4\rangle$	$-0.44 - 0.43i$	$-0.09 + 0.67i$	$-0.14 + 0.09i$	$-0.17 + 0.27i$
$\|3\rangle$	$-0.01i$			-0.02
$\|2\rangle$	-0.14	$-0.06 - 0.08i$	$-0.04 + 0.19i$	$-0.03 - 0.16i$
$\|1\rangle$	$-0.06 - 0.06i$	$-0.01 + 0.10i$	$-0.06 + 0.04i$	$-0.05 + 0.08i$
$\|0\rangle$				
$\|-1\rangle$	0.08	$0.06 + 0.08i$	$-0.02 + 0.07i$	$-0.02 - 0.09i$
$\|-2\rangle$	$-0.10 - 0.10i$	$-0.01 + 0.11i$	$0.16 - 0.10i$	$0.09 - 0.14i$
$\|-3\rangle$	0.01			-0.02
$\|-4\rangle$	-0.62	$-0.41 - 0.54$	$0.04 - 0.17i$	$0.07 + 0.31i$
$\|-5\rangle$	$0.21 + 0.20i$	$0.02 - 0.15i$	$-0.55 + 0.36i$	$-0.33 + 0.51i$
$\|-6\rangle$				

where W_m^n are the Wybourne crystal field parameters. Note that, in the literature, these quantities are often denoted B_m^n, the same way (except with an index exchange) as the Stevens crystal field parameters B_n^m. Here, we prefer a different notation to avoid confusion.

The Stevens operators $\widehat{\widehat{\mathcal{O}}}_n^m$ are then derived from the Wybourne operators [43]

$$\widehat{\widehat{\mathcal{O}}}_n^m = (\lambda_n^m)^{-1}\big(\widehat{C}_{-m}^n + (-1)^m \widehat{C}_m^n\big), \tag{B3}$$

where the proportionality factors λ_n^m are reproduced in Table II for those which are involved in the CF Hamiltonian of the studied pyrochlore. Then, within the Hilbert space restricted to the ground multiplet J, this Stevens operator can be expressed as a function of the associated Stevens equivalent operators $\widehat{\mathcal{O}}_n^m$ used in this study and reproduced in

Appendix A

$$\widehat{\widehat{\mathcal{O}}}_n^m = \theta_n(J)\widehat{\mathcal{O}}_n^m, \tag{B4}$$

where the matrix element $\theta_n(J)$ are tabulated for the ground multiplet of all trivalent $4f$ ions in Refs. [35,36] and reproduced here for Tb^{3+} in Table III. The relationship between the Stevens and Wybourne crystal field parameters is then

$$B_n^m = \lambda_n^m \theta_n(J) W_q^m. \tag{B5}$$

We can now compare the CF parameters obtained in different studies for $Tb_2Ti_2O_7$ (Table IV).

One can be surprised that the sign of our B_4^3 and B_6^3 parameters are different from those of most of the literature. However, as pointed out by Bertin *et al.* [37], when the sign of these two parameters are exchanged, there is no effect on the Hamiltonian eigenvalues. This property is only true without magnetic field, which is the case for all the

TABLE VII. Wave functions of the ground and first excited doublets, obtained by diagonalization of the CF Hamiltonian [equation (5)] with a vibronic coupling parameter $D_2^2 = -9.1 \times 10^{-3}$ meV. The value in brakets following the wave-function name is its associated eigenenergy. Only coefficients of wave functions $> 10^{-2}$ are shown.

	$\|\psi_1\rangle(0.0)$	$\|\psi_2\rangle(1.07)$	$\|\psi_3\rangle(13.7)$	$\|\psi_4\rangle(14.3)$
$\|6\rangle$				
$\|5\rangle$	$-0.23 + 0.12i$	$0.14 - 0.19i$	$-0.44 - 0.46i$	$-0.19 + 0.59i$
$\|4\rangle$	$-0.19 + 0.61i$	$0.10 + 0.64i$	$-0.26 - 0.01i$	$-0.12 - 0.25i$
$\|3\rangle$				-0.01
$\|2\rangle$	$-0.12 + 0.07i$	$0.07 - 0.10i$	$-0.12 - 0.13i$	$-0.05 + 0.16i$
$\|1\rangle$	$-0.03 + 0.08i$	$0.01 + 0.09i$	-0.08	$-0.04 - 0.07i$
$\|0\rangle$				
$\|-1\rangle$	$0.08 - 0.04i$	$-0.05 + 0.07i$	$-0.05 - 0.06i$	$-0.03 + 0.08i$
$\|-2\rangle$	$-0.04 + 0.13i$	$0.02 + 0.12i$	0.18	$0.07 + 0.15i$
$\|-3\rangle$				-0.01
$\|-4\rangle$	$-0.56 + 0.30i$	$0.38 - 0.53i$	$0.17 + 0.18i$	$0.08 - 0.26i$
$\|-5\rangle$	$0.07 - 0.25i$	$-0.04 - 0.23i$	$-0.63 - 0.03i$	$-0.27 - 0.56i$
$\|-6\rangle$				

previous neutrons and optical studies, but does not hold under an applied magnetic field. Indeed, we find much better agreement between our experimental results and calculations with $B_4^3 < 0$ and $B_6^3 > 0$; the eigenenergies at zero magnetic field are strictly identical when changing the sign of these two parameters.

APPENDIX C: WAVE FUNCTIONS FOR CRYSTAL-FIELD STATES

The wave functions for the ground and first excited doublets are given in the included Tables V, VI, VII, without and with the vibronic coupling.

[1] R. Comès, M. Lambert, H. Launois, and H. R. Zeller, Evidence for a peierls distortion or a kohn anomaly in one-dimensional conductors of the type $K_2Pt(CN)_4Br_{0.30} \cdot xH_2O$, Phys. Rev. B **8**, 571 (1973).

[2] D. Khomskii, Classifying multiferroics: Mechanisms and effects, Physics **2**, 20 (2009).

[3] S.-H. Lee, C. Broholm, T. H. Kim, W. Ratcliff, and S-W. Cheong, Local Spin Resonance and Spin-Peierls-Like Phase Transition in a Geometrically Frustrated Antiferromagnet, Phys. Rev. Lett. **84**, 3718 (2000).

[4] O. Tchernyshyov, R. Moessner, and S. L. Sondhi, Order by Distortion and String Modes in Pyrochlore Antiferromagnets, Phys. Rev. Lett. **88**, 067203 (2002).

[5] J. S. Gardner, M. J. P. Gingras, and J. E. Greedan, Magnetic pyrochlore oxides, Rev. Mod. Phys. **82**, 53 (2010).

[6] J. S. Gardner, A. Keren, G. Ehlers, C. Stock, E. Segal, J. M. Roper, B. Fåk, M. B. Stone, P. R. Hammar, D. H. Reich, and B. D. Gaulin, Dynamic frustrated magnetism in $Tb_2Ti_2O_7$ at 50 mK, Phys. Rev. B **68**, 180401 (2003).

[7] Y. Nakanishi, T. Kumagai, M. Yoshizawa, K. Matsuhira, S. Takagi, and Z. Hiroi, Elastic properties of the rare-earth dititanates $R_2Ti_2O_7$ (R = Tb, Dy, and Ho), Phys. Rev. B **83**, 184434 (2011).

[8] P. Bonville, I. Mirebeau, A. Gukasov, S. Petit, and J. Robert, Tetragonal distortion yielding a two-singlet spin liquid in pyrochlore $Tb_2Ti_2O_7$, Phys. Rev. B **84**, 184409 (2011).

[9] S. Guitteny, J. Robert, P. Bonville, J. Ollivier, C. Decorse, P. Steffens, M. Boehm, H. Mutka, I. Mirebeau, and S. Petit, Anisotropic Propagating Excitations and Quadrupolar Effects in $Tb_2Ti_2O_7$, Phys. Rev. Lett. **111**, 087201 (2013).

[10] T. Fennell, M. Kenzelmann, B. Roessli, H. Mutka, J. Ollivier, M. Ruminy, U. Stuhr, O. Zaharko, L. Bovo, A. Cervellino, M. K. Haas, and R. J. Cava, Magnetoelastic Excitations in the Pyrochlore Spin Liquid $Tb_2Ti_2O_7$, Phys. Rev. Lett. **112**, 017203 (2014).

[11] J. P. C. Ruff, Z. Islam, J. P. Clancy, K. A. Ross, H. Nojiri, Y. H. Matsuda, H. A. Dabkowska, A. D. Dabkowski, and B. D. Gaulin, Magnetoelastics of a Spin Liquid: X-Ray Diffraction Studies of $Tb_2Ti_2O_7$ in Pulsed Magnetic Fields, Phys. Rev. Lett. **105**, 077203 (2010).

[12] I. V. Aleksandrov, B. V. Lidskiǐ, L. G. Mamsurova, M. G. Neǐgauz, K. S. Pigal'skiǐ, K. K. Pukhov, N. G. Trusevich, and L. G. Shcherbakova, Crystal field effects and the nature of the giant magnetostriction in terbium dititanate, Sov. Phys. JETP **62**, 1287 (1985).

[13] I. Mirebeau, I. N. Goncharenko, P. Cadavez-Peres, S. T. Bramwell, M. J. P. Gingras, and J. S. Gardner, Pressure-induced crystallization of a spin liquid, Nature (London) **420**, 54 (2002).

[14] M. Ruminy, E. Pomjakushina, K. Iida, K. Kamazawa, D. T. Adroja, U. Stuhr, and T. Fennell, Crystal-field parameters of the rare-earth pyrochlores $Tb_2Ti_2O_7$ (R = Tb, Dy, and Ho), Phys. Rev. B **94**, 024430 (2016).

[15] E. Constable, R. Ballou, J. Robert, C. Decorse, J.-B. Brubach, P. Roy, E. Lhotel, L. Del-Rey, V. Simonet, S. Petit, and S. deBrion, Double vibronic process in the quantum spin ice candidate $Tb_2Ti_2O_7$ revealed by terahertz spectroscopy, Phys. Rev. B **95**, 020415(R) (2017).

[16] T. Taniguchi, H. Kadowaki, H. Takatsu, B. Fåk, J. Ollivier, T. Yamazaki, T. J. Sato, H. Yoshizawa, Y. Shimura, T. Sakakibara, T. Hong, K. Goto, L. R. Yaraskavitch, and J. B. Kycia, Long-range order and spin-liquid states of polycrystalline $Tb_{2+x}Ti_{2-x}O_{7+y}$, Phys. Rev. B **87**, 060408(R) (2013).

[17] M. J. P. Gingras, B. C. den Hertog, M. Faucher, J. S. Gardner, S. R. Dunsiger, L. J. Chang, B. D. Gaulin, N. P. Raju, and J. E. Greedan, Thermodynamic and single-ion properties of Tb^{3+} within the collective paramagnetic-spin liquid state of the frustrated pyrochlore antiferromagnet $Tb_2Ti_2O_7$, Phys. Rev. B **62**, 6496 (2000).

[18] J. S. Gardner, B. D. Gaulin, A. J. Berlinsky, P. Waldron, S. R. Dunsiger, N. P. Raju, and J. E. Greedan, Neutron scattering studies of the cooperative paramagnet pyrochlore $Tb_2Ti_2O_7$, Phys. Rev. B **64**, 224416 (2001).

[19] I. Mirebeau, P. Bonville, and M. Hennion, Magnetic excitations in $Tb_2Sn_2O_7$ and $Tb_2Ti_2O_7$ as measured by inelastic neutron scattering, Phys. Rev. B **76**, 184436 (2007).

[20] T. T. A. Lummen, I. P. Handayani, M. C. Donker, D. Fausti, G. Dhalenne, P. Berthet, A. Revcolevschi, and P. H. M. van Loosdrecht, Phonon and crystal field excitations in geometrically frustrated rare earth titanates, Phys. Rev. B **77**, 214310 (2008).

[21] Dennis J. Caldwell, Vibronic theory of circular dichroism, J. Chem. Phys. **51**, 984 (1969).

[22] Timothy A. Keiderling, Observation of magnetic vibrational circular dichroism, J. Chem. Phys. **75**, 3639 (1981).

[23] M. Pawlikowski and T. A. Keiderling, Vibronic coupling effects in magnetic vibrational circular dichroism. a model formalism for doubly degenerate states, J. Chem. Phys. **81**, 4765 (1984).

[24] A. M. Kalashnikova, R. V. Pisarev, L. N. Bezmaternykh, V. L. Temerov, A. Kirilyuk, and Th. Rasing, Optical and magneto-optical studies of a multiferroic $GaFeO_3$ with a high Curie temperature, J. Exp. Theor. Phys. Lett. **81**, 452 (2005).

[25] A. Pimenov, A. A. Mukhin, V. Yu. Ivanov, V. D. Travkin, A. M. Balbashov, and A. Loidl, Possible evidence for electromagnons in multiferroic manganites, Nat. Phys. **2**, 97 (2006).

[26] S. Miyahara and N. Furukawa, Theory of magneto-optical effects in helical multiferroic materials via toroidal magnon excitation, Phys. Rev. B **89**, 195145 (2014).

[27] S. Petit, P. Bonville, J. Robert, C. Decorse, and I. Mirebeau, Spin liquid correlations, anisotropic exchange, and symmetry breaking in $Tb_2Ti_2O_7$, Phys. Rev. B **86**, 174403 (2012).

[28] Laura Chaix, Dynamical magnetoelectric coupling in multiferroic compounds : iron langasites and hexagonal manganites, Ph.D. thesis, Université de Grenoble (2014).

[29] E. B. Graham and R. E. Raab, Magnetic effects in antiferromagnetic crystals in the electric quadrupole-magnetic dipole approximation, Philosophical Magazine B **66**, 269 (1992).

[30] B. E. A. Saleh and M. C. Teich, *Fundamentals of Photonics* (John Wiley & Sons, Ltd, 1991).

[31] H. Takatsu, S. Onoda, S. Kittaka, A. Kasahara, Y. Kono, T. Sakakibara, Y. Kato, B. Fåk, J. Ollivier, J. W. Lynn, T. Taniguchi, M. Wakita, and H. Kadowaki, Quadrupole Order in the Frustrated Pyrochlore $Tb_{2+x}Ti_{2-x}O_{7+y}$, Phys. Rev. Lett. **116**, 217201 (2016).

[32] A. P. Sazonov, A. Gukasov, H. B. Cao, P. Bonville, E. Ressouche, C. Decorse, and I. Mirebeau, Magnetic structure in the spin liquid $Tb_2Ti_2O_7$ induced by a [111] magnetic field: Search for a magnetization plateau, Phys. Rev. B **88**, 184428 (2013).

[33] P. Virtanen, R. Gommers, T. E. Oliphant, M. Haberland, T. Reddy, D. Cournapeau, E. Burovski, P. Peterson, W. Weckesser, J. Bright, S. J. van der Walt, M. Brett, J. Wilson, K. J. Millman, N. Mayorov, A. R. J. Nelson, E. Jones, R. Kern, E. Larson, C. J. Carey, İ. Polat, Y. Feng, E. W. Moore, J. VanderPlas, D. Laxalde, J. Perktold, R. Cimrman, I. Henriksen, E. A. Quintero, C. R. Harris, A. M. Archibald, A. H. Ribeiro, F. Pedregosa, P. van Mulbregt, and SciPy 1.0 Contributors, SciPy 1.0: fundamental algorithms for scientific computing in python, Nature Methods **17**, 261 (2020).

[34] K. Momma and F. Izumi, VESTA 3 for three-dimensional visualization of crystal, volumetric and morphology data, J. Appl. Cryst. **44**, 1272 (2011).

[35] K. W. H. Stevens, Matrix elements and operator equivalents connected with the magnetic properties of rare earth ions, Proc. Phys. Soc. Sec. A **65**, 209 (1952).

[36] M. T. Hutchings, Point-charge calculations of energy levels of magnetic ions in crystalline electric fields, Solid State Phys. **16**, 227 (1964).

[37] A Bertin, Y Chapuis, P Dalmas de Réotier, and A Yaouanc, Crystal electric field in the $R_2Ti_2O_7$ pyrochlore compounds, J. Phys.: Condens. Matter **24**, 256003 (2012).

[38] V. V. Klekovkina and B. Z. Malkin, Crystal field and magnetoelastic interactions in $Tb_2Ti_2O_7$, Optics and Spectroscopy **116**, 849 (2014).

[39] J. Zhang, K. Fritsch, Z. Hao, B. V. Bagheri, M. J. P. Gingras, G. E. Granroth, P. Jiramongkolchai, R. J. Cava, and B. D. Gaulin, Neutron spectroscopic study of crystal field excitations in $Tb_2Ti_2O_7$ and $Tb_2Sn_2O_7$, Phys. Rev. B **89**, 134410 (2014).

[40] G. Racah, Theory of complex spectra. II, Phys. Rev. **62**, 438 (1942).

[41] B. G. Wybourne, *Spectroscopic Properties of Rare Earths* (Interscience Publishers, New York, 1965).

[42] A. J. Princep, H. C. Walker, D. T. Adroja, D. Prabhakaran, and A. T. Boothroyd, Crystal field states of Tb^{3+} in the pyrochlore spin liquid $Tb_2Ti_2O_7$ from neutron spectroscopy, Phys. Rev. B **91**, 224430 (2015).

[43] A. J. Kassman, Relationship between the coefficients of the tensor operator and operator equivalent methods, J. Chem. Phys. **53**, 4118 (1970).

Curriculum Vitae

1. Personal data

Name	Kirill Amelin
Date and place of birth	23 May 1991, Tallinn, Estonia
Nationality	Estonian

2. Contact information

Address	National Institute of Chemical Physics and Biophysics (KBFI)
	Akadeemia tee 23, 12618 Tallinn, Estonia
Phone	+372 55515006
E-mail	kirill.amelin@kbfi.ee

3. Education

2017–...	Tallinn University of Technology, School of Science, Engineering Physics, PhD
2014–2016	KTH Royal Institute of Technology, School of Electrical Engineering, Electrophysics, MSc
2010–2014	Tallinn University of Technology, Faculty of Science, Engineering Physics, BSc

4. Language competence

Russian	native
Estonian	fluent
English	fluent
Swedish	intermediate

5. Professional employment

2017– ...	National Institute of Chemical Physics and Biophysics (KBFI), Junior Researcher
2017	The European Organization for Nuclear Research (CERN), Trainee
2016–2017	National Institute of Chemical Physics and Biophysics (KBFI), Engineer
2014–2016	KTH Royal Institute of Technology, Technician

6. Computer skills

- Operating systems: Windows, MacOS, Linux

- Document preparation: Microsoft Office, Latex

- Programming languages: Python, Matlab, Wolfram Mathematica

- Scientific packages: matplotlib, NumPy, SciPy, Pandas, Origin

7. Defended theses

- 2016, Analysis of ICRH of H and He-3 minorities in D and D-T plasmas in JET, MSc, supervisor Prof. Thomas Jonsson, KTH Royal Institute of Technology, Division of Fusion Plasma Physics

- 2014, The influence of different surface treatments on heterojunction properties in Cu_2ZnSnS_4/CdS solar cells, supervisor Prof. Jüri Krustok, Tallinn University of Technology, Department of Materials Science

10. Field of research

- FIELD OF RESEARCH: 4. Natural Sciences and Engineering; 4.10. Physics and Technical Physics; CERCS SPECIALITY: P260 Condensed matter: electronic structure, electrical, magnetic and optical properties, supraconductors, magnetic resonance, relaxation, spectroscopy; SPECIALITY: THz spectrometry of low dimensional and strongly correlated electron and spin systems, high magnetic fields, low temperature

11. Scientific work

Papers

1. K. Amelin, U. Nagel, R. S. Fishman, Y. Yoshida, Hasung Sim, Kisoo Park, Je-Geun Park, and T. Rõõm, "Terahertz absorption spectroscopy study of spin waves in orthoferrite $YFeO_3$ in a magnetic field," *Phys. Rev. B*, vol. 98, p. 174417, Nov 2018.

2. Z. Zhang, K. Amelin, X. Wang, H. Zou, J. Yang, U. Nagel, T. Rõõm, T. Dey, A. A. Nugroho, T. Lorenz, J. Wu, and Z. Wang, "Observation of E_8 particles in an Ising chain antiferromagnet," *Phys. Rev. B*, vol. 101, p. 220411, Jun 2020.

3. K. Amelin, J. Engelmayer, J. Viirok, U. Nagel, T. Rõõm, and Z. Wang, "Experimental observation of quantum many-body excitations of E_8 symmetry in the Ising chain ferromagnet $CoNb_2O_6$," *Phys. Rev. B*, vol. 102, p. 104431, Sep 2020.

4. K. Amelin, Y. Alexanian, U. Nagel, T. Rõõm, J. Robert, J. Debray, V. Simonet, C. Decorse, Z. Wang, R. Ballou, E. Constable, and S. de Brion "Terahertz magneto-optical investigation of quadrupolar spin-lattice effects in magnetically frustrated $Tb_2Ti_2O_7$," *Phys. Rev. B*, vol. 102, p. 13442, Oct 2020.

Conference presentations

1. K. Amelin. *Ion cyclotron resonance heating of plasma in a fusion reactor*, Graduate School of Functional Materials and Technology (GSFMT) Scientific Conference, 7–8 March 2017, Tartu, Estonia

2. K. Amelin. *Study of magnetism-driven order by THz absorption spectroscopy*, 3rd Grandmaster PhD Workshop in Physics, 19–23 February 2018, Vienna, Austria

3. K. Amelin. *THz absorption spectroscopy study of spin waves in orthoferrite $YFeO_3$*, American Physics Society March Meeting, 5–9 March 2018, Los Angeles, USA

4. K. Amelin. *THz absorption spectroscopy study of spin waves in orthoferrite $YFeO_3$ in a magnetic field*, The European Magnetic Field Laboratory (EMFL) summer school, 26–30 September 2018, Arles, France

5. K. Amelin. *THz absorption spectroscopy study of spin waves in orthoferrite YFeO$_3$ in a magnetic field*, Graduate School of Functional Materials and Technology (GSFMT) Scientific Conference, 1–2 February 2019, Tartu, Estonia

6. K. Amelin. *Spin structure models of YFeO$_3$ from THz spectroscopy study*, American Physics Society March Meeting, 4–8 March 2019, Boston, USA

7. K. Amelin. *"Special frequency region": opportunities and limitations behind Fourier-transform terahertz spectroscopy*, Centre of Excellence "Emerging orders in quantum and nanomaterials" EQUiTANT Seminar, 14–15 June 2019, Vehendi, Estonia

8. K. Amelin. *THz absorption spectroscopy study of spin waves in orthoferrite YFeO$_3$*, 4th Grandmaster PhD Workshop in Physics, 1–7 September 2019, Split, Croatia

9. K. Amelin. *THz spectroscopy study of the rare-earth pyrochlore Tb$_2$Ti$_2$O$_7$*, Graduate School of Functional Materials and Technology (GSFMT) Scientific Conference, 4–5 February 2020, Tallinn, Estonia

10. K. Amelin. *THz spectroscopy study of the rare-earth pyrochlore Tb$_2$Ti$_2$O$_7$*, American Physics Society March Meeting (CANCELLED), 2–6 March 2020, Denver, USA

11. K. Amelin. *Magnetoelectric SmFe$_3$(BO$_3$)$_4$ as a model system of quantum optics*, International Conference on Low Energy Electrodynamics in Solids (CANCELLED), 27 June–2 July 2020, Portland, ME, USA

Elulookirjeldus

1. Isikuandmed

Nimi	Kirill Amelin
Sünniaeg ja -koht	23.05.1991, Tallinn, Eesti
Kodakondsus	Eesti

2. Kontaktandmed

Aadress	Keemilise ja Bioloogilise Füüsika Instituut
	Akadeemia tee 23, 12618 Tallinn, Eesti
Telefon	+372 55515006
E-post	kirill.amelin@kbfi.ee

3. Haridus

2017–…	Tallinna Tehnikaülikool, Loodusteaduskond, Tehniline Füüsika, doktoriõpe
2014–2016	KTH Royal Institute of Technology, School of Electrical Engineering, Electrophysics, MSc
2010–2014	Tallinna Tehnikaülikool, Matemaatika-loodusteaduskond, Tehniline Füüsika, BSc

4. Keelteoskus

vene keel	emakeel
eesti keel	kõrgtase
inglise keel	kõrgtase
rootsi keel	kesktase

5. Teenistuskäik

2017–…	Keemilise ja Bioloogilise Füüsika Instituut, Nooremteadur
2017	Euroopa Tuumauuringute Keskus (CERN), Praktikant
2016–2017	Keemilise ja Bioloogilise Füüsika Instituut, Insener
2014–2016	KTH Royal Institute of Technology, Tehnik

6. Arvutioskus

- Operatsioonisüsteemid: Windows, MacOS, Linux

- Kontoritarkvara: Microsoft Office, Latex

- Programmeerimiskeeled: Python, Matlab, Wolfram Mathematica

- Teadustarkvara paketid: matplotlib, NumPy, SciPy, Pandas, Origin

7. Kaitstud lõputööd

- 2016, Analysis of ICRH of H and He-3 minorities in D and D-T plasmas in JET, MSc, juhendaja Prof. Thomas Jonsson, KTH Royal Institute of Technology, Division of Fusion Plasma Physics

- 2014, Erinevate pinnatöötluste mõju heteroülemineku omadustele Cu_2ZnSnS_4/CdS päikesepatareides, BSc, juhendaja Prof. Jüri Krustok, Tallinna Tehnikaülikool, Materjaliteaduse Instituut

10. Teadustöö põhisuunad

- VALDKOND: 4. Loodusteadused ja tehnika; 4.10. Füüsika; CERCS ERIALA: P260 Tahke aine: elektrooniline struktuur, elektrilised, magneetilised ja optilised omadused, ülijuhtivus, magnetresonants, spektroskoopia; PÕHISUUND: madalamõõduliste ja tugevalt korreleeritud elektron- ja spinnsüsteemide infrapuna ja THz-spektromeetria, tugevad magnetväljad, madalad temperatuurid

11. Teadustegevus

Teadusartiklite, konverentsiteeside ja konverentsiettekannete loetelu on toodud ingliskeelse elulookirjelduse juures.